TESIS DE LA UNIVERSIDAD DE ZARAGOZA
2026
63

Amaiur Mendi Altube

Dynamic Electromagnetic and Thermal Effects on Nonlinear Induction Heating Loads Driven by a Flexible Power Converter for Industrial Applications

Director/es
Villar Iturbe, Irma
Carretero Chamarro, Claudio

ISSN 2254-7606

Prensas de la Universidad
Universidad Zaragoza

Universidad de Zaragoza
Servicio de Publicaciones

ISSN 2254-7606

Universidad Zaragoza
1542

Tesis Doctoral

DYNAMIC ELECTROMAGNETIC AND THERMAL EFFECTS ON NONLINEAR INDUCTION HEATING LOADS DRIVEN BY A FLEXIBLE POWER CONVERTER FOR INDUSTRIAL APPLICATIONS

Autor

Amaiur Mendi Altube

Director/es

Villar Iturbe, Irma
Carretero Chamarro, Claudio

UNIVERSIDAD DE ZARAGOZA
Escuela de Doctorado

2026

Universidad Zaragoza

1474

Doctoral Thesis

Dynamic Electromagnetic and Thermal Effects on Nonlinear Induction Heating Loads Driven by a Flexible Power Converter for Industrial Applications

Candidate

Amaiur Mendi Altube

Supervisors

Irma Villar Iturbe
Claudio Carretero Chamarro

Programa de Doctorado en Ingeniería Electrónica
Escuela de Doctorado

2025

This is an Industrial Doctorate funded by and developed at:

Modeling and Design of Induction Heating Systems

ABSTRACT

Induction heating is a non-contact heat transfer process applied to materials with good electrical conductivity, typically metals. Using a variable magnetic field, induced currents are generated in the material, which dissipate heat due to the Joule effect. Furthermore, the efficiency of the energy transfer process is greatly influenced by the presence of magnetic properties in the material.

This technology is utilized in various fields, including industrial, medical, and domestic applications. Its main characteristics include efficiency, heating speed, safety, and precision in process control. Its efficiency is primarily defined by the relationship between the power delivered to the workpiece, i.e., the material to be heated, and the losses that occur in the winding that generates the variable magnetic field. Another critical parameter is the distribution of power delivered to the workpiece, which is determined by the geometry of the coil. In general, the combination of the physical and geometric characteristics of the induction system makes it challenging to analyze.

In industrial applications, which are the subject of this thesis, various processes exist depending on the treatment required for the material. Industrial processes that utilize induction heating can be categorized into three groups, as outlined below. First, among the induction heat treatments, we can list hardening, tempering, annealing, and normalizing. Next, we can mention the applications of induction heating, including forging, forming, extrusion, stretching, sealing, straightening, and melting. Finally, we should mention special applications, such as soft soldering, brazing, welding, and bonding.

In this work, the induction heating process in surface hardening applications will be studied. In this case, the physical properties of the workpiece change considerably as the temperature increases, even exceeding the Curie temperature, at which the magnetic properties disappear. To obtain a comprehensive description of the system's behavior, an electromagnetic-thermal model must be developed that simultaneously accounts for the dependence of all parameters using an approach based on the application of nonlinear boundary conditions. This approach allows for a realistic description of the phenomena

involved at a reduced computational cost.

In a subsequent step, the results obtained in the previous section will be integrated to create a simulation model of the complete induction system, comprising the inductor-workpiece system and its associated electronics. In this way, the results of the electromagnetic-thermal model obtained by FEM simulation will be integrated into a circuit simulation program.

Finally, experimental measurements will be carried out to validate the results obtained. First, measurements will be taken in the small-signal regime to verify that the electromagnetic simulation models are correct. Subsequently, measurements will be taken in an experimental setup under real working conditions delivering high power levels.

Key words – Induction heating, resonant inverter, nonlinear load, dynamic modeling, Curie temperature, finite elements.

Modelado y Diseño de un Sistema de Calentamiento por Inducción

RESUMEN

El calentamiento por inducción es un proceso de transferencia de calor sin contacto, que se aplica a materiales con una buena conductividad eléctrica, normalmente, a metales. Utilizando un campo magnético variable, se generan corrientes inducidas en el material, las cuales disipan el calor, como consecuencia del efecto Joule. Además, la eficiencia del proceso de transferencia de energía se ve muy influenciada por la presencia de propiedades magnéticas del material.

Dicha tecnología se utiliza en diversos campos, como pueden ser tanto las aplicaciones industriales, como las médicas y las domésticas. Sus principales características son la eficacia, la velocidad de calentamiento, la seguridad y la precisión en el control del proceso. Su eficiencia se define principalmente por la relación entre la potencia suministrada a la pieza, es decir, el material a calentar, y las pérdidas que se producen en el bobinado que genera el campo magnético variable. Otro parámetro crítico es la distribución de la potencia suministrada a la pieza, que viene determinada por la geometría de la bobina. En general, la combinación de las características físicas y geométricas del sistema de inducción dificulta su análisis.

En las aplicaciones industriales, que son el objeto de esta tesis, existen diversos procesos en función del tratamiento que requiera el material. Los procesos industriales, que utilizan el calentamiento por inducción, pueden clasificarse en tres grupos, los cuales se describen a continuación. En primer lugar, entre los tratamientos térmicos por inducción, podemos enumerar el temple, el revenido, el recocido y la normalización. A continuación, mencionaremos las aplicaciones del calentamiento por inducción, entre las que se incluyen, la forja, el conformado, la extrusión, el estirado, el sellado, el enderezado y la fusión. Por último, caben destacar las aplicaciones especiales, tal y como los procesos de soldadura o de unión.

En este trabajo se analizará, así mismo, el proceso de calentamiento por inducción, den-

tro de las aplicaciones de temple superficial. En dicho caso, las propiedades físicas de la pieza varían considerablemente a medida que aumenta la temperatura, superando incluso la temperatura de Curie, a partir de la cual desaparecen las propiedades magnéticas. Para obtener una descripción completa del comportamiento del sistema, es necesario desarrollar un modelo electromagnético-térmico que dé cuenta simultáneamente de la dependencia de todos los parámetros, mediante un enfoque basado en la aplicación de las condiciones de frontera no lineales. El mencionado enfoque permite obtener una descripción realista de los fenómenos implicados, con un coste computacional reducido.

En un paso posterior, se integrarán los resultados obtenidos en el apartado anterior, con el objetivo de crear un modelo de simulación del sistema de inducción completo, que se encuentra compuesto por el conjunto inductor-pieza y su electrónica asociada. De esta forma, los resultados del modelo electromagnético-térmico, obtenidos mediante simulación FEM, se integrarán en un programa de simulación de circuitos.

Finalmente, se realizarán medidas experimentales, con el objeto de validar los resultados obtenidos. En primer lugar, se realizarán medidas en el régimen de pequeña señal, de cara a verificar que los modelos de simulación electromagnética son correctos. Y, posteriormente, se ejecutarán mediciones dentro de un montaje experimental, basados en condiciones reales de trabajo con altos niveles de potencia.

Palabras clave – Calentamiento por inducción, inversor resonante, carga no-lineal, modelado dinámico, temperatura de Curie, elementos finitos.

Indutzio Bidezko Berokuntza Sistemen Modelatzea eta Diseinua

LABURPENA

Indukzio bidezko berokuntza prozesu bat da, non beroa kontakturik gabe transferitzen den. Eroankortasun elektriko ona duten materialei aplikatzen zaie, normalean, metalei. Eremu magnetiko aldakor baten bidez, materialean induzitutako korronteak agertzen dira, Joule efektuaren ondorioz beroa barreiatzen dutenak. Gainera, materialaren propietate magnetikoek eragin handia dute energia transferitzeko prozesuaren eraginkortasunean.

Teknologia hori hainbat arlotan erabiltzen da; hala nola, industriako, medikuntzako eta sukaldeko aplikazioetan. Prozesuaren kontrolaren eraginkortasuna, berotze abiadura, segurtasuna eta zehaztasuna dira haren ezaugarri nagusiak. Prozesu horren efizientzia piezari, hots, berotu beharreko materialari, transferitutako potentziaren eta eremu magnetiko aldakorra sortzen duen induktorearen galeren arteko erlazioak definitzen du, nagusiki. Beste parametro kritiko bat da piezaren zeharreko potentziaren distribuzioa, eta hori bobinaren geometriak zehazten du. Oro har, indukzio sistemaren ezaugarri fisikoen eta geometrikoen konbinazioak erronka bihurtzen du bere analisia.

Tesi honen xede diren industria aplikazioetan, materialak behar duen tratamenduaren araberako hainbat prozesu daude. Indukzio bidezko berokuntza erabiltzen duten industria prozesuak hiru multzotan sailka daitezke, eta horiek jarraian deskribatzen dira. Lehenik eta behin, indukzio bidezko tratamendu termikoen artean, tenplatzea, iraoketa, suberaketa eta normalizazioa kokatzen dira. Ondoren, indukzio bidezko berokuntzaren aplikazioak bereizten dira, besteak beste, forja, konformazioa, estrusioa, tenkatzea, zigilatzea, zuzentzea eta fusioa. Azkenik, aplikazio bereziak daude, hainbat soldadura mota eta lotura, esaterako.

Lan honetan, era berean, indukzio bidezko berokuntza prozesua aztertuko da gainazaleko tenplatze aplikazioetarako. Kasu honetan, piezaren propietate fisikoak nabarmen aldatzen dira materiala berotu ahala; Curieren tenperatura gainditzean, propietate magnetikoak desagertzen dira. Sistemaren portaera bere osotasunean ulertzeko, beharrezkoa

da parametro guztien mendekotasuna aintzat hartuko duen modelo elektromagnetiko-termiko bat garatzea, mugalde-baldintza ez-linealak aplikatuz. Ikuspegi horrek aukera ematen du prozesuan inplikatutako fenomenoen deskribapen errealista bat egiteko; eta, gainera, kostu konputazional txikiarekin.

Jarraian, aurreko atalean lortutako emaitzak integratuko dira, indukzio-sistema osoaren simulazio-eredu bat sortzeko helburuarekin; eta azken hori induktore-pieza sistemaz eta hari lotutako elektronikaz dago osatua. Modu horretan, FEM simulazioen bidez lortutako modelo elektromagnetiko-termikoaren emaitzak integratuko dira zirkuituak simulatzeko programa batean.

Azkenik, tesian garatutako modeloak baliozkotzeko jomugarekin neurketa esperimentalak gauzatuko dira. Lehenengo eta behin, seinale txikiaren erregimenean egingo dira neurketak, modelo elektromagnetikoak zuzenak direla ziurtatzeko. Eta, ondoren, muntaia esperimental bat baliatuko da simulazioak lan baldintza errealetan, hau da, potentzia maila handiagoekin balioztatzeko.

Hitz gakoak – Indukzio bidezko berokuntza, erresonantzia inbertsorea, karga ez-lineala, modelatze dinamikoa, Curie tenperatura, elementu finituak.

Acknowledgements

This journey didn't truly begin in 2021, but rather in 2018, when I first met you, Irma – the one who has stood by my side since the very first day I set foot in IKERLAN.

Eskerrik asko, esan bezala, hasiera-hasieratik ondoan egoteagatik, laguntzeagatik, eta, nola ez, eman dizkidazun aukera guztiak emateagatik. Esan daiteke zuri esker naizela gaur naizena, zuk bidean utzitako ogi zatitxoak jasotzen joan bainaiz. Bide batez, Luisi eta Alexi ere esker eta zorion bereziak, hiruok gidatu duzuen talde bikainarengatik.

The early stages of this journey were about finding a university that could support us – professionals with a background in induction heating technology. That led us to the University of Zaragoza, pioneers in induction heating for cooking applications. Irma reached out to Jesús, who then suggested Claudio as co-supervisor.

Os estoy muy agradecida. Claudio, gracias por las innumerables videoconferencias, tu sabiduría y tu constante ayuda. Gracias por todo lo que me has enseñado. Jesús, gracias a tus gestiones, sugerencias y revisiones. Ha sido un verdadero placer haberte tenerte a mi lado en este camino. Tampoco me olvido de los compañeros de UNIZAR con los que he ido coincidiendo a lo largo de estos años, tanto en mis viajes a Zaragoza como en congresos. Muchas gracias por hacerme sentir una más. Os deseo lo mejor, lo merecéis.

To my teammates at IKERLAN – the professional people who shared not only their knowledge, but also their patience and good humor throughout this journey.

Esker mila, PEL, hasiera-hasieratik etxean bezala sentiarazteagatik, eta, beste mila esker, BPE, sortu dugun ekipo berezi honengatik. Zuekin ikasitakoa ez da gradu batean jasotzen, master batek ere ez du ematen, zuekin eta bertatik bertara bizi behar da horretarako. Asko balio duzue, kristonak zarete, bai profesionalki, eta baita pertsonalki ere. Mila milioi esker, ekipo. IKERLANen ezagututako beste guztioi ere eskerrak; modu batera edo bestera, baina tesi honek zuen izenak ere badaramatza. Gaztetxoenentzat itxaropen hitzak besterik ez, zuek ematen diozue bizia honi. Segi horrela!

Altzuri eta Ixi, Ixi eta Altzuri, bidaia honek egin didan oparirik polit eta ederrena, zuek ezagutzea. 2021eko irailera itzuli eta berriz nire bidea aukeratu beharko banu, bizitakoak bizita, ezin beste biderik hartu. Ez dut ezer berririk esateko zuentzat, dena dago esanda, eta zerbait falta bada, denborak azaleratuko du. Sortu dugun harreman hau mantentzea izango da zuek niri egin diezadakezuen oparirik politena (orain ere eskean, kar-kar).

To my group of friends 'Ardauzaliak', who kept trying to understand what my work was all about – though perhaps I don't deserve this PhD, since I never quite managed to explain

it properly during all those years.

Zenbat juerga eta parranda, zenbat barre eta algara, tartean baita eztabaida eta haserreak ere, baina beti maitasunez. Horrelako lagun talde handi batean, oso gertuko, gertuko eta ez hain gertuko pertsonak bereiz daitezke; baina ausartzen naiz esatera, bakoitzak bere neurrian jarri diola aletxoa lan honi, eman didala aurrera egiteko bultzada niri. Horregatik, bihotzez eskerrak, neskak.

To Oñatz, the Basque traditional dance group I proudly belong to – my other family of friends.

Eltzian pasatu ditugun ordu luze horiengatik. Eltzian eta Eltziatik kanpo, bizitzako edozein unetan garelako dantzari/dantzakide/lagun. Erreferente izan zareten beteranoei, eta erreferentziatzat gauzkaten gaztetxoenei. Segi dezagun dantzan! Eta ez daudenak gogoan, nola ez, Txutxin.

To all the people I've met along the way – unexpected encounters that made the journey richer.

Lau urte hauetan nire bide korapilatsuan nola edo hala gurutzatu zareten horiei guztioi ere eskerrak eman gabe ezin nintzen gelditu; batzuk hemen jarraitzen duzue, beste batzuk hor egon zarete momenturen batean. Izan ere, bizipen guztietatik ikasten da zerbait, inoizko ezbeharrik handiena gertatu zaizula uste duzunean, zorigaitz horrek argitzen du aurrera egiteko bidea, gauzak hobeto egiteko modua. Eta denbora igaro ahala, konturatzen zara ez zela hainbesterako izan; hemendik urte batzutara tesi hau ikusiko dudan bezala, garai batean ezinezkoa zirudiena.

Family is made up of people you don't get to choose – and yet, they are often both our greatest support and our greatest challenge.

Abenidako zein Sanpedroko familiei, biak ala biak alboan beti. Bi etxeetan eman didazue jaten, lagundu hazten, irakatsi maitatzen, eskerrik asko. Ama, aitta, zuek gabe ez nintzen existituko, ez zen ikerketa lan hau irtengo. Zuek zarete honen guztiaren sustrai. Milioi bat esker. Bukatzeko, etxeko txikia, etxeko printzesa. Eskerrik asko, Ekhi, azkenengo bi urte hauetan – batez ere – nire ondoan egoteagatik, nire zaintzaile izateagatik, finean, ahizpa zaharrarena egiteagatik. Erori ez banaiz, zuri esker izan da.

Thank you!
Eskerrik asko!

Maite zaituztet,
Amaiur

List of Figures

List of Tables

Acronyms

AC	alternating current
AC-AC	AC to AC converter
AC-DC	AC to DC converter
ASC	Analytic Saturation Curve
BEM	Boundary Element Method
CSI	Current Source Inverter
DC	direct current
DC-AC	DC to AC converter
DC-DC	DC to DC converter
EMC	electromagnetic compatibility
EMF	electromotive force
EV	Electric Vehicle
FB	full-bridge
FDM	Finite Difference Method
FEM	Finite Element Method
FPGA	Field Programmable Gate Array
GVOVC	Grid-Voltage Oriented Vector Control
HB	half-bridge
HEMT	high electron mobility transistor
IBC	Impedance Boundary Condition
IGBT	insulated gate bipolar transistor
IH	Induction Heating
LES	Large Eddy Simulation
LFH	longitudinal flux heating
MAS	microalloyed steel
MFC	magnetic flux concentrator
MOSFET	metal-oxide-semiconductor field-effect transistor
PDC	Peak Detector Circuit
PDM	Pulse Density Modulation
PFC	Power Factor Corrector
PFM	pulse frequency modulation
PhD	Doctor of Philosophy
PI	proportional-integral

PID	proportional-integral-derivative
PLL	phase-locked loop
PSM	Phase-Shift Modulation
PWM	Pulse Width Modulation
rms	root mean square
SoA	State-of-the-Art
TFH	transversal flux heating
VLSI	very large-scale integration
VSI	Voltage Source Inverter
WBG	wide-bandgap
WPT	Wireless Power Transfer
ZCS	Zero Current Switching
ZVS	Zero Voltage Switching

Symbols

ΔT	Temperature difference	°C
$\Delta i_{L,max}$	Maximum inductor current ripple	A
Φ_{shift}	Phase shift between current and voltage	°
α	Temperature coefficient of resistivity	1/°C
δ	Penetration depth	m
γ	Power coefficient for temperature dependence function of the magnetic characteristic	-
$\mathbf{A}$	Magnetic potential vector	V·s/m
$\mathbf{B}$	Magnetic flux density	T
$\mathbf{D}$	Electric flux density	C/m^2
$\mathbf{E}$	Electric field	V/m
$\mathbf{H}$	Magnetic field	A/m
$\mathbf{J}_D$	Displacement current	A/m^2
$\mathbf{J}_{coil}$	Current distribution in the turn section of the winding	A/m^2
$\mathbf{J}_{ind}$	Induced current density in the workpiece	A/m^2
$\mathbf{J}$	Current density	A/m^2
$\hat{\mathbf{n}}$	Unit normal vector pointing outward the conductor material	-
$\hat{\mathbf{r}}$	Path unit vector	-
$\mathbf{r}$	Path vector	m
$\mathbf{v}_g$	Grid-side voltage vector	V
BW	Bandwidth	Hz
B_s	Saturation magnetic field	T
B	Magnetic flux density	T
$C'_{L_T,i}$	Proportionality factor of the polynomial function for the temperature-dependent inductance above Curie point	-
$C'_{R_T,i}$	Proportionality factor of the polynomial function for the temperature-dependent resistance above Curie point	-
C'_{T_E}	Proportionality factor of the quadratic function for the energy-dependent temperature above Curie point	-
$C_{L_I,i}$	Proportionality factor of the polynomial function for the current-dependent inductance below Curie point	-

$C_{L_T,i}$	Proportionality factor of the polynomial function for the temperature-dependent inductance below Curie point	-
C_P	Heat capacity	J/ºC
$C_{R_I,i}$	Proportionality factor of the polynomial function for the current-dependent resistance below Curie point	-
$C_{R_T,i}$	Proportionality factor of the polynomial function for the temperature-dependent resistance below Curie point	-
C_{T_E}	Proportionality factor of the potential function for the energy-dependent temperature below Curie point	-
$C_{T_I,i}$	Proportionality factor of the polynomial function for the current-dependent temperature below Curie point	-
C_{oss}	Output parasitic capacitance	F
C_r	Resonant capacitance	F
C	Factor controlling the temperature dependence of the magnetic properties	ºC
C	Capacitance	F
$E_{\|\|}$	Electric field longitudinal to the turns of the coil	V/m
E_φ	Azimuthal component of the electric field along the wire	V/m
E_{OFF}	Switching-off energy losses	J
E_{brk}	Cumulative energy to reach the Curie temperature	J
H_a	Parameter used on the function of the analytic saturation curve with knee adjustment	-
H_v	Voltage gain	-
H	Magnetic field	A/m
I_{IH}	Induction load current amplitude	A
I_{L1}	Output current through the inductance of the first branch	A
I_{L2}	Output current through the inductance of the second branch	A
I_L	Current through inductor	A
I_{coil}	Current amplitude flowing through the winding	A
I_{dc}	DC current	A
I_{ref}	Reference temperature to fit the reduced-order temperature and impedance current-dependent curves	A
I_{rms}	rms current	A
I	Current	A
K_i	Integral constant of a PI regulator	-
K_p	Proportional constant of a PI regulator	-
L_1	First inductive component of the impedance equivalent network	H
L_2	Second inductive component of the impedance equivalent network	H
L_3	Third inductive component of the impedance equivalent network	H

L_{I}	Inductance's current-dependent term	H
L_{T}	Inductance's temperature-dependent term	H
L_{eq}	Equivalent inductance	H
L_{f}	Inductance of the converter side of the filter	H
L_{g}	Inductance of the grid side of the filter	H
L_{n}	n-th inductive component of the impedance equivalent network	H
L_{stray}	Stray inductance	H
L	Inductance	H
M_{an}	Anhysteretic magnetization	A/m
M_{s}	Saturation magnetization	A/m
P_{cond}	Conduction power losses	W
P_{ind}	Induced power to the load	W
$P_{\mathrm{inv,in}}$	Active power at the inverter's input	W
$P_{\mathrm{inv,out}}$	Active power at the inverter's output	W
P_{in}	Input active power	W
P_{loss}	Power losses	W
P_{nom}	Nominal power	W
P_{out}	Output active power	W
$P_{\mathrm{r,IBC}}$	Radial power flow employing IBC	W/m^2
$P_{\mathrm{r,pk}}$	Radial power flow's peak value	W/m^2
P_{r}	Radial power flow	W/m^2
$P_{\mathrm{sw,off}}$	Switching-off power losses	W
$P_{\mathrm{sw,on}}$	Switching-on power losses	W
P_{sw}	Switching power losses	W
P	Active power	W
Q_{out}	Output reactive power	VAR
Q_{p}	Quality factor for a parallel equivalent circuit	-
Q_{s}	Quality factor for a series equivalent circuit	-
Q	Quality factor	-
Q	Reactive power	VAR
R_1	First resistive component of the impedance equivalent network	Ω
R_2	Second resistive component of the impedance equivalent network	Ω
R_3	Third resistive component of the impedance equivalent network	Ω
R_{DS}	Drain-source resistance	Ω
R_{I}	Resistance's current-dependent term	Ω
R_{T}	Resistance's temperature-dependent term	Ω
R_{dc}	DC resistance	Ω
R_{eq}	Equivalent resistance	Ω
R_{n}	n-th resistive component of the impedance equivalent network	Ω

R	Resistance	Ω
S_a, S_b, S_c	Pulses for the controlled three-phase rectifier switches	-
S_{turn}	Cross-sectional area of a turn	m^2
T_0	Ambient temperature	ºC
T_C	Curie temperature	ºC
$T_{bnd,avg}$	Average temperature of the billet's vertical surface	ºC
T_{brk}	Tendency-breaking temperature close to Curie point	ºC
T_i	Integral time of a PI regulator	s
T_m	Temperature of the superficial central point of the billet	ºC
T_s	Surface temperature	ºC
T_s	Switching period	s
T	Period	s
T	Temperature	ºC
V_1	Voltage value for the fundamental frequency	V
V_{LL}	Line-to-line voltage	V
$V_{dc,1}$	DC-bus 1 voltage	V
$V_{dc,2}$	DC-bus 2 voltage	V
V_{dc}	DC-bus voltage	V
V_{ind}	Induced voltage in the winding	V
V_n	*n*th harmonic voltage	V
V_o	Output voltage	V
V_{rms}	rms voltage	V
V	Electric potential	V
X_C	Capacitive reactance	Ω
X_L	Inductive reactance	Ω
Z_{IBC}	Boundary impedance condition at the material's surface	Ω
$Z_{eq,IBC}$	Equivalent impedance employing IBC	Ω
Z_{eq}	Equivalent impedance	Ω
Z	Impedance	Ω
$\widehat{E}_{IH}$	Estimation of the induced energy	J
$\widehat{I}_{IH}$	Induction load current's peak value	A
$\widehat{T}_E$	Estimated temperature's energy-dependent term	ºC
$\widehat{T}_I$	Estimated temperature's current-dependent term	ºC
$\widehat{T}_m$	Estimated temperature of the superficial central point of the billet	ºC
a_1	Constant multiplying factor	-
a_2	Constant multiplying factor	-
a	Factor governing the slope of the Langevin curve	-
a	Constant multiplying factor	-
c_p	Specific heat	J/kg·ºC
d_1	Duty cycle of the first DC-DC branch	%
d_2	Duty cycle of the second DC-DC branch	%
d_{ext}	Turn external diameter	m
d_{int}	Turn internal diameter	m

d_t	Separation between turns along a common rotational axis	m
d	Duty cycle	%
d	Depth from the surface	m
$e(t)$	Input error of a regulator	-
e_{df}	d component of the coupling terms for the LCL filter	V
e_{qf}	q component of the coupling terms for the LCL filter	V
f_1	Frequency at point 1	Hz
f_2	Frequency at point 2	Hz
f_{3-ph}	Frequency of the 3-phase rectifier	Hz
f_{IH}	Specified frequency for the induction heating process	Hz
f_{buck}	Buck frequency	Hz
f_{grid}	Grid frequency	Hz
f_r	Resonant frequency	Hz
f_{sw}	Switching frequency	Hz
f_s	Switching frequency of the square-wave train	Hz
f	Frequency	Hz
h	Convection coefficient	$W/m^2 \cdot ^oC$
$i_{\alpha g}$	α component of the grid side current	A
$i_{\beta g}$	β component of the grid side current	A
i_{CH}	Channel current	A
i_{Coss}	Current through the output parasitic capacitance	A
$i_{Cr/2,b}$	Resonant capacitor current through the bottom half-bridge branch	A
$i_{Cr/2,t}$	Resonant capacitor current through the top half-bridge branch	A
$i_{Cr/2}$	Resonant capacitor current through a half-bridge branch	A
i_{Cr}	Resonant capacitor current	A
i_C	Transient current through capacitor	A
i_D	Drain current	A
i_{IH}	Current delivered to the load	A
$i_{L,sw}$	Switching current from the inductance	A
i_{RL}	Current through the load	A
i_{ac}	AC current	A
i_{af}, i_{bf}, i_{cf}	Output currents of the converter	A
i_{ag}, i_{bg}, i_{cg}	Currents flowing through the grid side of the filter	A
i_{df}	d component of the converter side current	A
i_{dg}	d component of the grid side current	A
i_f	Converter-side current	A
i_g	Grid-side current	A
i_{qf}	q component of the converter side current	A
i_{qg}	q component of the grid side current	A
k	Thermal conductivity	$W/m \cdot ^oC$

l_{coil}	Length of the coil	m
l	Length	m
n_{T_E}	Exponent factor of the potential function for the energy-dependent temperature below Curie point	-
n	Exponent	-
n	Number of harmonic	-
n	Transformation ratio	-
n	Coil's turn number	-
q_{cond}	Heat flux by conduction	W/m^2
q_{conv}	Heat flux by convection	W/m^2
q_{ind}	Heat flux by induction	W/m^2
q_{rad}	Heat flux by radiation	W/m^2
r_{int}	Ring's inner radius	m
r	Path	m
r	Radius	m
t	Time	s
$u(t)$	Output response of a regulator	-
$v_{\alpha f}$	α component of the converter voltage	V
$v_{\beta f}$	β component of the converter voltage	V
$v_{Cr/2,b}$	Resonant capacitor voltage in bottom half-bridge branch	V
$v_{Cr/2,t}$	Resonant capacitor voltage in top half-bridge branch	V
$v_{Cr/2}$	Resonant capacitor voltage in a half-bridge branch	V
v_{Cr}	Resonant capacitor voltage	V
$v_{DS,L}$	Voltage on the device	V
v_{DS}	Drain-source voltage	V
v_L	Voltage on the stray inductance	V
v_{ac}	AC voltage	V
v_{af}, v_{bf}, v_{cf}	Output voltages of the converter referred tot hte neutral point of the load n	V
v_{ag}, v_{bg}, v_{cg}	Grid voltages with electric angular speed in rad/s	V
v_{coil}	Volume of the coil	m^3
v_{df}	q component of the converter voltage	V
v_{dg}	d component of the grid voltage	V
v_f	Converter-side voltage	V
v_g	Grid-side voltage	V
v_{load}	Voltage in the induction load	V
v_o	Transient output voltage	V
v_{qf}	q component of the converter voltage	V
v_{qg}	q component of the grid voltage	V
z	Position in the z axis	m
μ_0	Magnetic permeability of free space ($4\pi \cdot 10^{-7}$ $W/m^2 \cdot K^4$)	H/m
$\mu_{r,i}$	Initial relative magnetic permeability	-
μ_r	Relative magnetic permeability	-

μ	Magnetic permeability	H/m
∇T	Temperature gradient	ºC/m
ω_r	Angular resonant frequency	rad/s
ω_s	Angular frequency of the square-wave train	rad/s
ω	Angular frequency	rad/s
ρ_0	Resistivity at ambient temperature	Ω·m
ρ_r	Specific electrical resistivity	Ω·m
ρ	Density	kg/m^3
ρ	Electrical resistivity	Ω·m
σ	Gaussian bell deviation	m
σ	Stefan-Boltzmann constant (5.6703 $W/m^2 \cdot K^4$)	$W/m^2 \cdot K^4$
σ	Electrical conductivity	S/m
$\dot{Q}$	Heat source	W/m^3
θ	Phase angle	º
ε_Z	Impedance error	%
ε	Emissivity	-

Contents

Chapter 1

Introduction

This chapter is a State-of-the-Art (SoA) study of the Induction Heating (IH) technology, which is the general topic of this thesis. It includes the historical evolution and prospects of IH systems, the fundamental principles of induction heating, including main definitions, the comparative advantages of induction heating over other heating methods, and an overview of various induction heating processes, with a focus on industrial applications. This SoA compiles power electronic topologies employed in literature and methods to model IH systems; a brief overview of some dynamic models is also added. Finally, the thesis will be framed, describing its objectives and scope, and the structure of the document will be introduced.

1.1 Introduction to Induction Heating Technology

Human beings have always invented various tools to survive in their existence. These inventions have evolved alongside humanity and influenced our understanding of life. One of the most significant discoveries in the history of mankind is fire, which was discovered more than seven hundred thousand years ago, [1]. Around four hundred thousand years ago, traces of fire became significantly more common at various archaeological sites, [2]. This natural phenomenon affects many animal species, but only humans have learned to control and create fire.

Figure 1.1. Metal under treatment on burning fire.

Throughout history, people have utilized various heat sources for their everyday requirements and industrial purposes; in Fig. 1.1, a metal under treatment on a burning fire is captured. The use of fire for melting, casting, and forging metals, particularly during the Iron Age, represented a significant advancement in human technological progress. The progression of fire technology facilitated the creation of a wide array of heat-based industrial processes, such as furnaces, kilns, and ovens. It was not until the beginning of the twentieth century that the electric furnace was introduced into the iron and steel industries, [3]. Even if initially it was not very desirable, it has now become a valuable tool in the industry, increasing the application range.

Indeed, the use of electromagnetic induction for heating is a relatively recent innovation, dating back to the late 19th century. Michael Faraday discovered the basics of electromagnetic induction heating, which James Maxwell afterward developed, describing it by four famous equations named after him. Figure 1.2 captures the plaque showing Maxwell's equations.

In 1831, Faraday found a close connection between magnetism and electricity. As a result, an electric current was induced simply by moving a magnet near a coil: electromagnetic induction. At the end of the 19th century, in 1865, Maxwell published his famous equations based on Faraday's and other scientists' discoveries. These equations, which

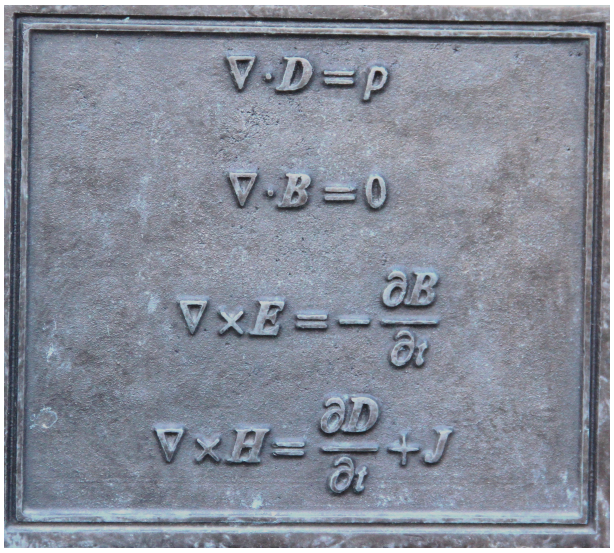

Figure 1.2. *Plate detailing equations affixed to rear of plinth on which statue of James Clerk Maxwell statue sits* by Impensustained, [4].

describe the link between electricity and magnetism, are the induction heating principle. Then, in the 1920s, that induction heating technology developed enough to expand its applications, becoming the most important one in the industry, especially in the manipulation of metals. In the Second World War, induction heating was used for military purposes. Nowadays, various applications use this technology, such as cooking appliances and medicine, [5].

Even if induction heating technology has developed significantly, its potential is far from limited. The demand for this technology is remarkably increasing, and the reason is simple: induction equipment improves constantly, and the systems are studied every day by researchers; induction heating processes are optimized continuously. It remains among the most popular heating methods, guaranteeing security and reliability. It is crucial to continue in this line. In the near future, induction heating might be essential for the research and development of similar but more efficient technologies.

1.1.1 Fundamentals of Induction Heating Technology

Electromagnetic induction heating (IH) is a process in which an electrically conductive material, usually a metal, is heated by means of an alternating magnetic field. Induced currents are generated inside the mentioned metal, and its resistivity tends to heat the material due to the Joule effect. In case of materials with significant values of relative permeability, the heat transfer due to induced currents becomes more effective. Energy is transferred from the source coil to the heated part through the magnetic field, so no physical contact is needed to carry out such a process, [6].

IH is used in several fields, such as industrial, medical, and domestic applications. This technology stands out for its efficiency, heating velocity, security, and very precise con-

trol. Its efficiency depends mainly on the ratio between the resistance of the coil and the equivalent resistance of the material to be heated; generally, the former being the DC component and the latter the AC one due to eddy currents induced within it. Moreover, the optimization of the coils' geometry is important when it comes to the homogeneity of the heated parts. Even more, the material's magnetic and electric behaviors must be known for a correct measurement of the system, [7].

Electromagnetism and heat transfer are closely related, as the strength of the magnetic field and the temperature of the material define its physical properties. Additionally, the metallurgical phenomenon is a nonlinear function of process characteristics such as temperature, heating intensity, cooling speed, and the material's chemical composition. Therefore, electromagnetic induction heating can be described as a complex combination of electromagnetic, heat transfer, and metallurgical phenomena, [6].

1.1.1.1 Electromagnetism principles of induction heating

Induction heating processing system consists of three basic elements: an alternating current generator, the material to be heated, and a coil through which a current is driven, generally located around the workpiece to be heated, [8]. The first one is often referred to as the inverter or generator, which is used to convert the mains frequency and increase it to anywhere between a few hundred hertz to megahertz. The workpiece consists of a metallic material where the eddy currents are induced through an electromagnetic field generated by the coil, which carries the AC current.

When an alternating current passes through a coil, a magnetic field of the same frequency appears around the material being heated. If the electrically conductive workpiece is placed in the proximity, this magnetic field will be able to heat it thanks to the Joule effect and hysteresis losses, which are respectively represented by Fig. 1.3a and Fig. 1.3b.

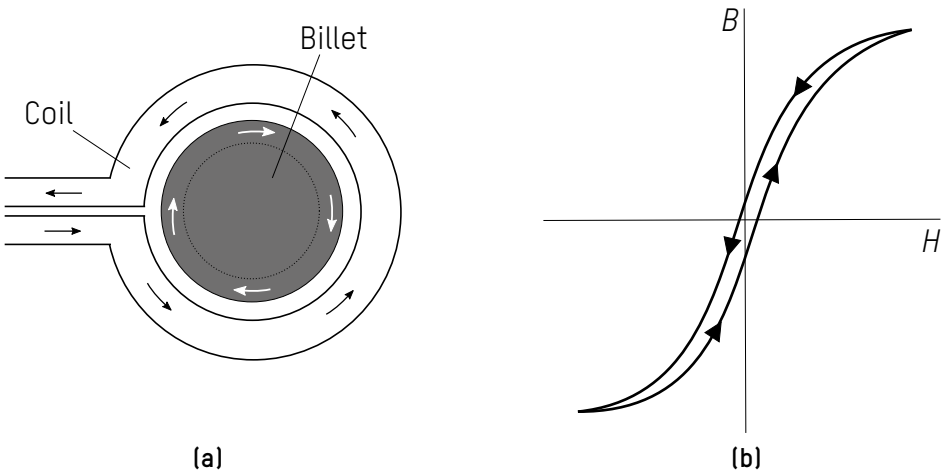

Figure 1.3. Effects responsible for induction heating: (a) Joule effect, and (b) hysteresis.

Undoubtedly, the primary phenomenon for heat dissipation through electromagnetic

induction is the Joule effect caused by eddy currents induced by the applied variable magnetic field on the material's surface. All metals are electrically conductive, and the power losses occur due to their resistance to the flow of electricity they conduct, resulting in heat generation. This occurs in both ferromagnetic and non-ferromagnetic materials. Some metals have low resistivity and are consequently good conductors, e.g., silver and copper; others, which are worse conductors of electricity, have higher resistivity, such as steel. Therefore, more heat is lost when electric currents circulate through materials like steel.

Hysteresis losses, which are only found in magnetic materials, such as steel and nickel, are lower than those of the Joule effect and are considered only in ferromagnetic materials below Curie temperature. In the process of induction heating of magnetic materials, when the magnetic field H is applied, the magnetic domains of the material begin to oscillate, delaying the magnetic response of the B-field. This process is called hysteresis, and the heat generated is the result of the energy released in the process of reorienting the magnetic domains. While hysteresis losses may not be significant, the characteristics related to the BH-curve of the material greatly influence the performance of the induction heating process. This influence can arise from the effects of permeability or the magnetic saturation of the material.

When alternating current flows through a conductor, the current distribution across the cross-section is not uniform. The highest current density value appears at the surface of the piece and weakens towards the center. This is known as the skin effect. This effect is also reflected in a workpiece surrounded by the coil, causing eddy currents to appear on the workpiece's surface. As a result, less or null current flow will be detected in the center of the part, [9].

The power dissipation will be concentrated in the surface layer due to the skin effect because the fields exponentially decay inside the material with the characteristic distance given by the penetration depth, δ, for linear material, which depends on the frequency and the material's electrical and magnetic properties, [10]. This penetration depth depends inversely on the electrical conductivity, magnetic permeability, and excitation frequency.

The electrical conductivity is the ability of the material to conduct electric current and corresponds to the inverse of the material's resistivity. At higher temperatures, metals offer higher resistivity, so the higher the impedance reflected on the load. Besides, the magnetic permeability is the ability of the material to conduct magnetic flux, which decreases with temperature. It gives the relation between the magnetic flux density, B, and the magnetic field, H, as $B = \mu H$.

Therefore, while the workpiece is being heated, the electrical resistivity will usually increase, and the magnetic permeability will decrease to a greater extent. For this reason, the penetration depth will be higher with temperature. Thus, it can be deduced that when the temperature of a metal increases and it becomes paramagnetic, the eddy currents will reach areas closer to the core.

Induction heating systems can be classified as transversal flux heating (TFH) or longitudinal flux heating (LFH) based on the flux direction, [11]. In transversal flux heating, the material to be heated is often positioned over an inductor located below the workpiece as

in Fig. 1.4a. The electromagnetic field caused by the alternating current in the induction coils is orthogonal to the material's surface to be heated; therefore, eddy currents induced in the plane of the object produce Joule losses and heat in its surface. Magnetic flux concentrators are often used with this technology, [12]. According to [13], the TFH concept offers very high electrical efficiency.

Figure 1.4b depicts the longitudinal flux heating typical case, where the material to be heated is surrounded by the induction coil. The current through the coil creates an electromagnetic field with orthogonal flux to the cross section of the piece. Therefore, eddy currents are induced close to the surface. For example, [14] analyses the effects on blanks for a press hardening process with longitudinal flux heating.

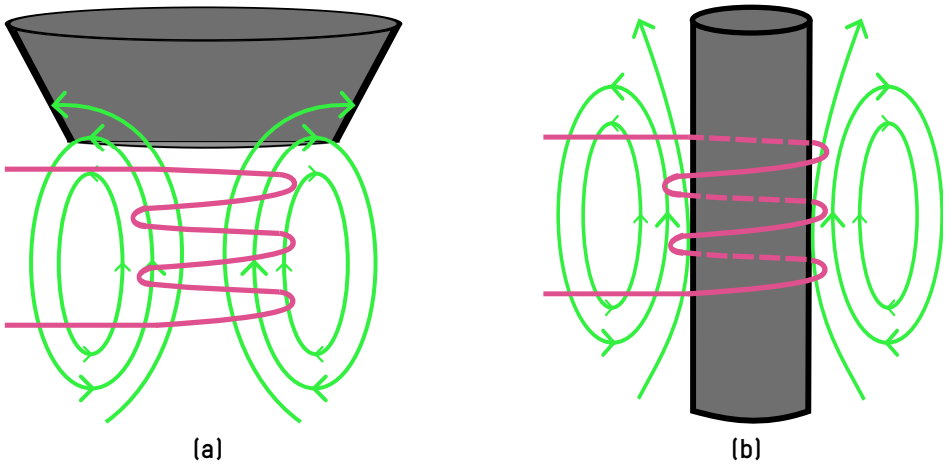

Figure 1.4. Inductors for (a) transverse flux heating, and (b) longitudinal flux heating.

1.1.2 Induction Heating Applications

Eddy current and dielectric losses, once considered problematic for radio engineers, are now employed as effective heating methods. These techniques have expanded the scope of induction heating, allowing for a wider range of processes and operations to benefit from this versatile technology. Induction heating is increasingly being developed and employed in diverse fields. It is primarily used in industrial, household, and medical applications [5], [15], but its potential is far from limited, [8].

(a)

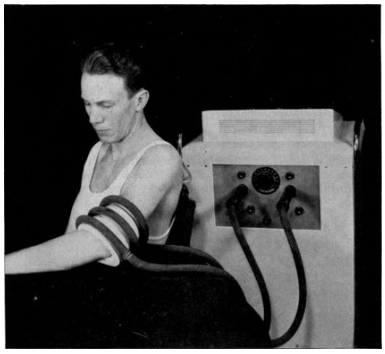

(b)

(c)

(d)

(e)

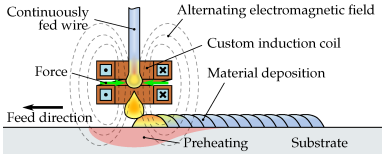

(f)

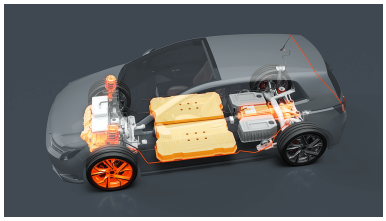

(g)

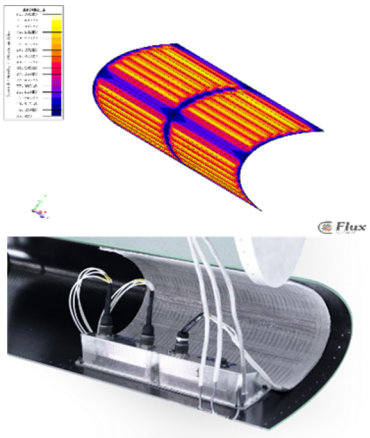

(h)

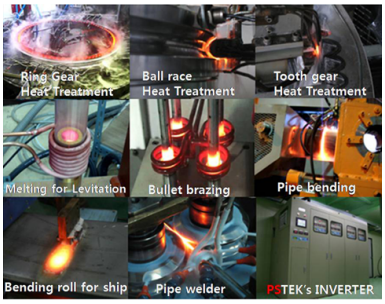

(i)

Figure 1.5. Applications of induction heating technology: (a) induction cooking, (b) diathermy treatment, (c) agriculture, [16], (d) crystal growing, (e) textile industry, [17], (f) 3D printing, (g) automotion, [18], (h) aeronautics, and (i) metal industry.

Induction heating is a remarkably versatile technology with applications in various fields,

as it can be seen in Fig. 1.5. This process, which utilizes electromagnetic induction to generate heat within a conductive material, has become increasingly dominant in multiple industries, from manufacturing to automotive engineering, domestic to biomedical applications. Some of these are described below:

- It is commonly employed in domestic appliances, such as induction cooktops where their efficiency and precise temperature control make IH an attractive alternative to traditional heating methods (Fig. 1.5a), [19].
- Biomedical applications of IH include, among others, its use in hyperthermia cancer treatments, where the controlled heating of targeted tumor tissues can enhance the efficacy of radiation therapy or chemotherapy, [20]. Electromagnetic induction for hyperthermia therapy was first proposed in 1957, [21]. In Fig. 1.5b, a diathermy treatment is captured. Furthermore, electromagnetic induction is also proposed to clean the biofilm seeded on orthopaedic implants, [22].
- Electromagnetic heating has also been studied for potential applications in agriculture. This technique has been investigated for treating grains and forages, controlling stored-product insects and plant pathogens. For example, in [16], a large-scale induction heating system is designed for organic waste digesters to produce fertilizer (Fig. 1.5c).
- Induction heating is also used in specific applications such as nanoparticle research, crystal growing, and enhancement of diamonds, [23]. Silicon growing process by IH in 1956 is captured in Fig. 1.5d.
- The textile industry has shifted from electric heating to more efficient alternatives like induction heating to reduce costs and improve fuel utilization, [24]. Even [17] proposes an iron that works with electromagnetic induction (Fig. 1.5e).
- Induction heating technique is also suggested for additive manufacturing or 3D printing in [25] (Fig. 1.5f).
- In the automotive industry, induction heating is utilized within a variety of fields in the production of electric vehicles, [18]. In Fig. 1.5g, an electric vehicle is shown with highlighted parts that have been produced by IH technology. Moreover, in [26], thermal management of electric vehicle batteries is proposed by employing induction heating technology.
- According to the aerospace domain, induction heating is employed in the heat treatment of aircraft components, allowing precise control over the thermal characteristics of critical parts. For example, in [27], aeronautical gears are hardened through induction heating. Additionally, [28] proposes IH for de-icing critical areas of aircraft wings (Fig. 1.5h).
- One of the primary applications of induction heating is in the heat treatment of metallic materials, [6]. The focus in the following lines will be on IH for the metal industry. Figure 1.5i captures different industrial processes employing electromagnetic induction.

All these applications highlight the versatility of induction heating and its ability to address a diverse range of heating needs. However, it is worth mentioning that electromag-

netic induction is not only used for transferring heat but also for transmitting power for other uses, such as Electric Vehicle (EV) wireless charging in [29].

1.1.3 Advantages of Induction Heating Systems

In the dynamic manufacturing sector, efficiency, precision, and sustainability are critical. Consequently, induction heating has acquired significant popularity in various industrial sectors. Induction heating systems have gained relevant attention in recent years due to their remarkable advantages over traditional heating methods for conductive materials. These systems are contactless and easy-to-control. Induction heating technology provides rapid heating, particularly beneficial in industrial and commercial applications where time is crucial. It is durable, capable of withstanding harsh environments and prolonged use, and efficient, enabling precise temperature regulation and effective energy utilization.

Furthermore, only a specific part of the piece can be heated with this technology, i.e. the part that needs to be treated, unlike traditional ovens, where the entire piece is heated. This significantly improves the efficiency of the entire system, [30].

To sum up, it offers numerous advantages over other traditional heating methods, [31]. The following advantages further demonstrate the effectiveness and appeal of IH technology:

- Enhanced mechanical properties are obtained. As the heating is more precise than with traditional methods, the risk of overheating or uneven heating is minimized, and fewer defects are caused.
- High-efficiency process leads to reduced energy consumption – resulting in cost savings – because the whole piece no longer needs to be heated. This high efficiency is due to the precise heating of specific areas, minimizing unwanted heat zones.
- IH is a rapid and direct heating method that significantly reduces processing times compared to other traditional heating methods.
- Induction heat treatment processes can be automated; it is very suitable for large-scale production.
- Moreover, it is a process that allows for precise temperature control and repeatability, with consistent results. Thus, it is a reliable choice for batch-based production, reducing manufacturing variability.
- IH systems have few moving parts, unlike traditional furnaces. Therefore, the equipment life is lengthened, and there is less downtime; maintenance costs are also reduced.
- It is relatively easy to move without any particular infrastructure.
- Environmentally friendly. Induction heating uses electricity instead of fossil fuels, increasing energy efficiency up to 90 % and reducing carbon footprint.
- IH is a flame-free process that creates a safer working environment. Therefore, the

risk of burns and harmful airborne particles is eliminated, ensuring safe and comfortable conditions.

- Suitable for several applications, as detailed in the previous section.

1.1.4 Induction Heating in Metal Industry

Induction heating is a widely adopted technology in several industrial sectors, offering versatile and efficient heat treatment techniques, [32]. The inherent advantages of IH, such as its speed, precision, and energy efficiency, have made it an attractive alternative to traditional heating methods, particularly in the context of industrial processes.

As the popularity of heat treatment techniques is rising, the use of induction heating in this area has become increasingly extended, particularly for the treatments focused on steel components like tubes, pipes, or pressure vessels.

In [33], recent applications and future development trends for efficient heating and melting by electrothermal technologies in metallurgical processes are described.

In the following lines, some industrial fields of induction heating technology are summarized from [34]:

- **Hardening** is one of the most common applications of IH. It consists of heating the workpiece and suddenly cooling it, in order to give the material the necessary hardness and flexibility.
- **Tempering** is a supplementary treatment after the hardening, to increase the material's tenacity and to reduce the stresses created in the previous process.
- The **annealing** process returns properties that the material lost in some previous process: eliminating internal stresses, removing the hardness, obtaining a specific microstructure, etc. First, the material is heated to the austenization temperature and then cooled slowly.
- **Normalizing** takes place before hardening or tempering; it is about balancing internal stresses. To do so, the billet is heated up above the critical temperature and cooled with ambient air.
- In a **welding** process, two or more pieces are heated up to their melting temperature.
- **Forging** is realized at high power and low frequencies. In essence, a preheated piece is shaped as its resistance to deformation is weakened when heated.
- In **fusion** metals are melted inside a crucible. Afterward, the molten metal is poured into a cast to give the desired shape.

1.1.4.1 Induction hardening

As mentioned previously, one of the most typical applications of induction heating in the metal industry is the hardening of steel or cast iron. In Fig. 1.6, an induction heating process of a gear is rendered.

Figure 1.6. *Inducteur à roue dentée* by Leflambela, [35].

The purpose of the hardening process is for the material to obtain certain properties, including hardness and resistance to erosion. The workpiece to be hardened is heated to the temperature of austenization and immediately cooled.

Thus, the process is divided into at least two stages. The first is induction heating, in which the billet is heated while the alternating current circulates through the inductor. There are three critical temperatures: Curie's temperature (in steels, around 700-800 ºC) determines the ferromagnetic limit, and AC1 and AC3 temperatures, respectively, determine the beginning and end of austenization. Once the areas to be hardened exceed the AC3 temperature (as a general rule, about 50 ºC further), it is crucial to immediately cool them. This fast cooling is realized by putting the workpiece into oil or a shower with aqueous polymers. Then the austenite parts will become martensite – below 400 ºC –, hardening even more, but becoming more fragile.

Figure 1.7 depicts the isothermal transformations (left) and phase diagram (right) of carbon steels, [35]; the isothermal transformation is also named as Time-Temperature-Transformation (TTT). Martensitic transformation begins at a temperature called Ms, which depends on the chemical composition of the material. To calculate this temperature, there are several equations developed by various authors, [36]. Due to the fast nature of induction hardening, it is usually considered that only martensite and bainite are generated, [37].

Finally, if needed, a tempering treatment would be applied to reduce this fragility and weaken internal stresses. To do so, the piece is heated below the AC1 temperature, kept at that temperature for as long as necessary, and cooled with ambient air.

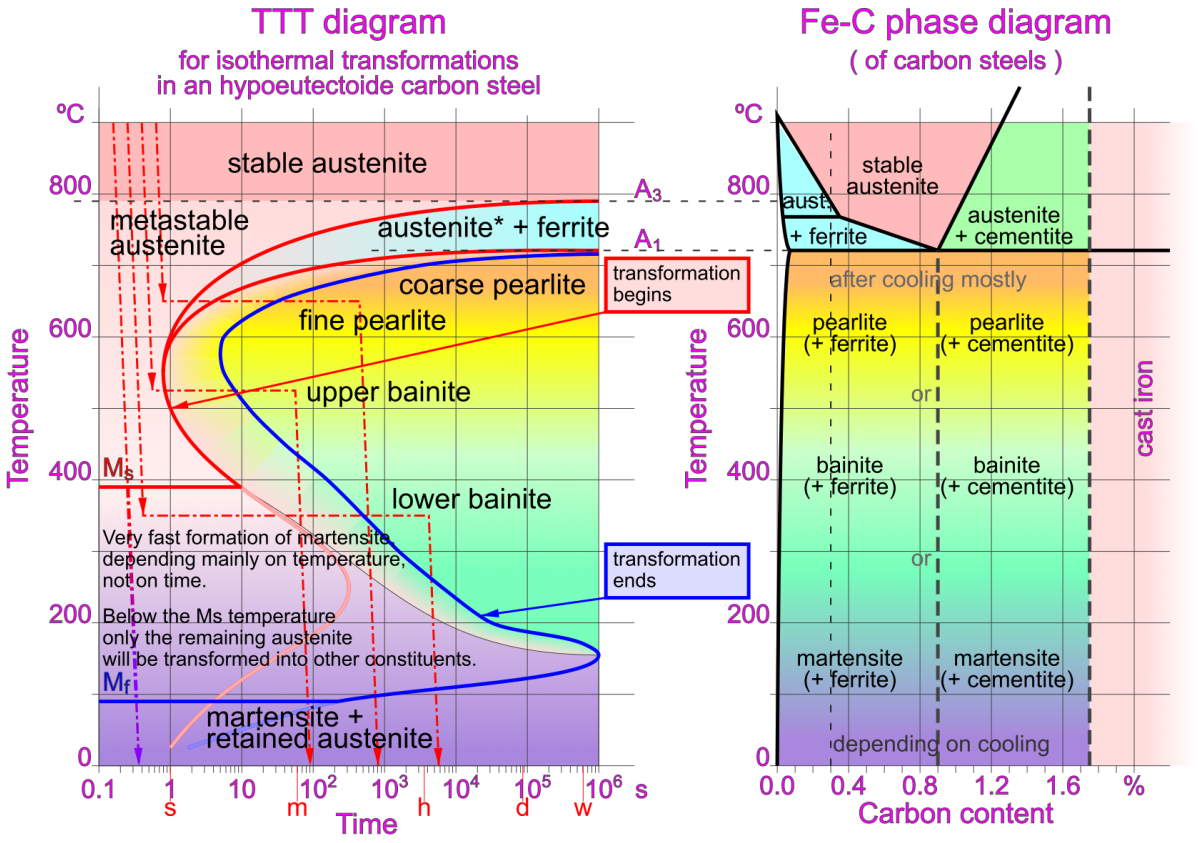

Figure 1.7. *TTT diagram of the isothermal transformations of a hypoeutectoid carbon steel* by Jon Peli Oleaga, [38].

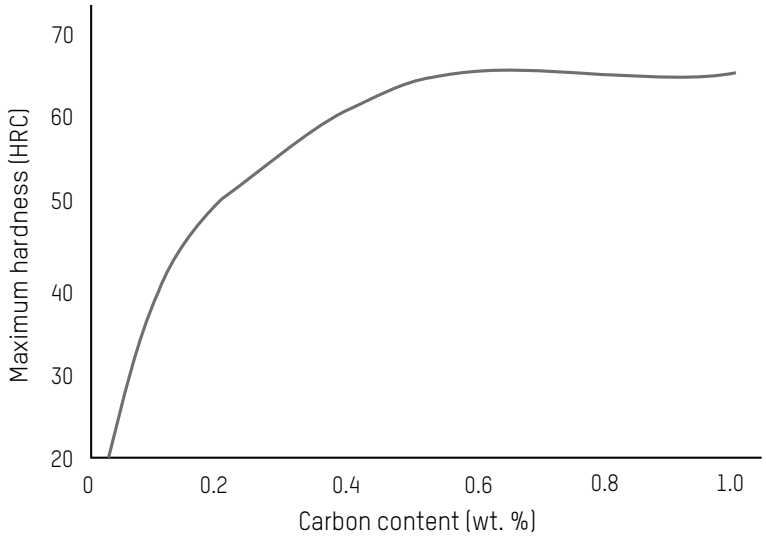

Figure 1.8. Maximum steel hardness depending on the amount of carbon, [30].

If the heating process of the industrial hardening is executed by induction, the martensite layer is formed in the desired areas of the billet, keeping intact the zones that do not

need the treatment, because they will not exceed the AC1 temperature, and their mechanical properties shall not be altered.

The induction hardening is distinguished by its high accuracy in the areas treated with heat. Induction allows distortion to be as small as possible, due to the speed of the process and the ability of the heat source to concentrate on the surface layer, which is directly related to the aforementioned penetration depth of the current.

Steel alloys are often used in induction hardening processes. The type of steel is chosen according to the working conditions defined by the degree of hardness and profile of the surface, plus the cost of the system. Pure carbon steel and low alloys are the cheapest, used in a variety of hardening applications, with a carbon content of between 0.2 and 0.7 %. The amount of carbon in steel determines the maximum hardness obtained on the surface, see Fig. 1.8, [30].

Depending on the specifications of the thermal treatment or the geometry of the workpiece, the induction hardening may be a simple device or a more complex machine. The first step in designing an induction hardening system is to determine the hardness profile, depth, and transition zone of the surface. The factors involved in the hardness through the radius or thickness of the billet are temperature distribution, metallic microstructure and chemical composition, cooling conditions, grain size, and the material's hardening capacity, [6].

Compared to other traditional heating systems, the induction technique is noticeably influenced by changes in the chemical composition of metals, [39]. That is why it is essential to control these changes adequately. It is important to have homogeneous and fine grains, rapid metal response to heat treatment, and as little distortion as possible. This initial microstructure will ensure greater hardness at a wider depth. Softer surfaces also improve the conditions of heat treatment, such as fatigue, resistance, and durability.

According to the temperature distribution, the geometry, power density, and frequency of the workpiece and coil are designed, [6]. Complex designs, holes, and sharp edges, among others, determine the success of the process. In addition, as the process requires short heating cycles for proper execution, it is necessary to work with high power densities. Frequency is the first control variable to be considered in induction hardening systems, which will determine the hardness profile, depth, and transition zone of that surface.

It is important that the heating and cooling times are respectively long and short enough. Otherwise, a phenomenon called superhardening may occur. As its name suggests, it consists of hardening a piece more than is necessary, and there are two reasons: to heat too quickly or to cool too slowly. This phenomenon occurs mainly in steel with 0.35-0.6 % carbon, [34], [40].

1.2 Induction Heating Systems Structure

As it was previously stated, the fundamental structure of an induction heating system comprises three key components: the inductor-workpiece assembly, the power converter, and the control system.

The inductor-workpiece system serves as the heart of the induction heating process. In this critical component, electrical energy is converted into a magnetic field that induces alternating current directly within the material being heated. This efficient transfer of energy allows for accurate control over the heating process, making it ideal for various applications, from metal hardening to melting.

The power converter plays a significant role in the overall cost and effectiveness of the system. It transforms input electrical energy into the precise frequency and voltage required for induction heating. A well-engineered power converter is vital, as it directly influences the efficiency, performance, and reliability of the entire system.

Finally, the control system manages and monitors the operation of the induction heating system. Typically designed with advanced digital components, the control system regulates the power delivery, adjusts parameters based on real-time feedback, and ensures that the heating process is both efficient and safe. Together, these components work in harmony to deliver precise and reliable induction heating solutions.

1.2.1 Inductor-Workpiece Assembly

The coil is the primary component of the inductor-workpiece assembly, as it directly impacts key characteristics such as power distribution and heat transfer to the workpiece. Typically, the coil is made by winding several turns of a highly conductive material, usually copper. Depending on the application, the coil may be constructed from solid wire, a tubular structure, or multi-stranded wire. The coil carries the current that generates variable magnetic fields throughout the system. However, it is also influenced by inductive effects, which can be classified into the skin effect, the proximity effect, and the ring effect.

The skin effect in the cross-section of each turn in a coil is related to the tendency of electric and magnetic fields to exponentially decay within a conductor. This phenomenon becomes significant as the frequency increases. Consequently, at certain frequencies, the current in the conductor flows primarily near the surface, as the penetration depth within the material approaches the characteristic size of the cross-section of the conductor. This effect is illustrated in Fig. 1.9a.

The proximity effect is due to the influence of neighboring conductors in the coil. When explaining the skin effect, we often refer to a single conductor, but in most induction systems there are usually several conductors (or induction coils) close to each other. Each of these conductors has its own magnetic field which interacts with the surrounding fields. Therefore, when placing two conductors next to each other, in addition to the surface effect, the proximity effect will also influence the current density distribution (Fig. 1.9b). If the currents passing through the conductors are in opposite directions, more current will be concentrated in the surface areas between the two conductors. On the other hand, if the currents are in the same direction, the outer areas will have a higher current density.

Finally, the ring effect is a combination of the two previous effects. When a conductor is forming a loop, as in Fig. 1.9c, the current lines will be concentrated inside the ring, reducing the current density on the outside. As a result, most of the current will be in the inner surface layer of the ring. The ring effect can have both positive and negative implications

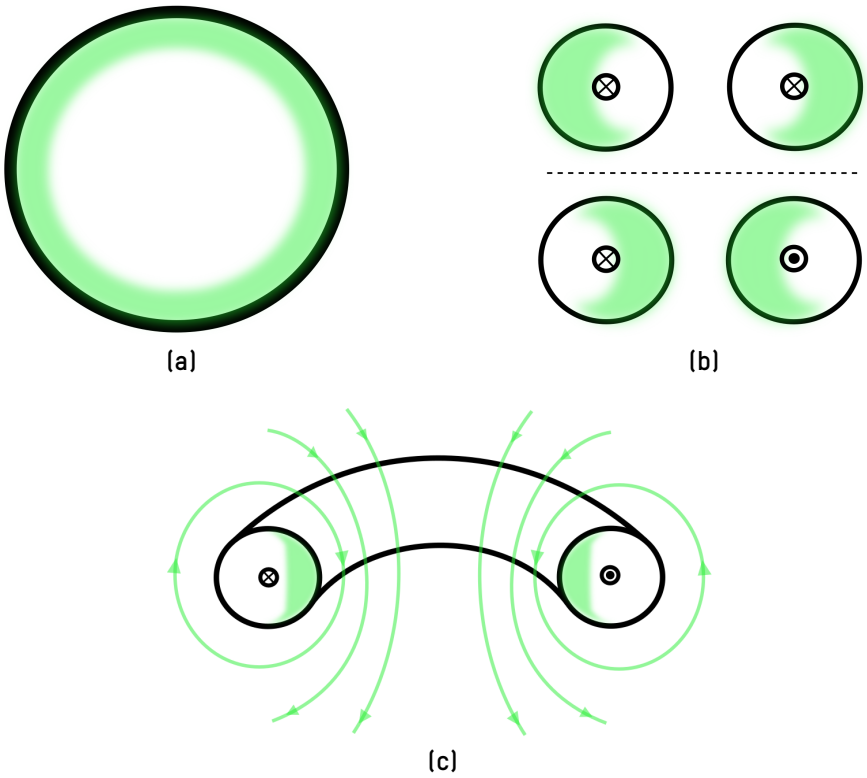

Figure 1.9. Induction phenomena in the coil: (a) skin effect, (b) proximity effect, and (c) ring effect.

depending on the application. In a conventional induction heating system where the part to be heated is surrounded by the wire, the ring effect can be beneficial. Together with the skin and proximity effects, the ring effect will help to concentrate the current inside, thereby increasing the efficiency of the coil. However, it can have a negative impact when the aim is to heat the inner surface of a billet.

In some cases, a magnetic flux concentrator (MFC) made of a magnetic material is added in the construction of the coil. The purpose of these elements is related to their influence on the magnetic field distribution, which can improve the coupling between the coil and the workpiece. Different impeder/flux concentrator materials for induction tube welding systems are demonstrated in [41]. Moreover, numerical simulation and experimental investigation of MFC is realized in [42], where a novel type of MFC is presented, based on ferromagnetic particles embedded in ceramic matrix material, so high-temperature mechanical stability and good magnetic performance are guaranteed.

Due to the importance of the coil in the induction heating system performance, an effective design of these components constitutes a key task to achieve successful results. Different optimization methods and numerical finite element methods for induction coils for surface hardening are exposed in [43]. Moreover, inductive coils for induction hardening are also optimized in [44] to increase their lifetime. The optimal design of the inductor shape for transverse flux heating is described in [13] using numerical modeling and optimization techniques. The peculiarity of this design refers to the very slow movement speed

and the target temperature. A numerical optimization algorithm is used in [45] to design a one-sided transverse flux induction coil.

Focusing more on the electrical behavior of the induction load, this inductor-workpiece system is seen from the electrical equivalent point of view as an inductive impedance, [46]. The simplest way of modeling an IH load is the series, Fig. 1.10a, or parallel, Fig. 1.10b, resistance and inductance equivalent circuit, where the resistance is associated with the total dissipated power – induced power – and the inductance is related to the total energy stored in the system. These two components are named as equivalent resistance, R_{eq}, and equivalent inductance, L_{eq}. Their values depend on the system's geometry and materials, the frequency of the AC current, and other parameters.

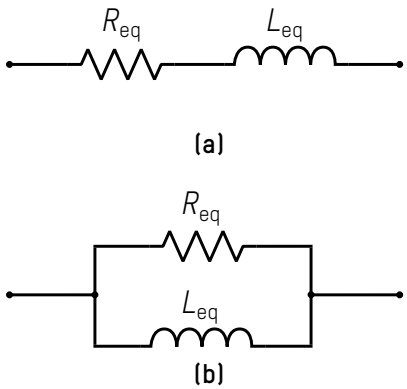

Figure 1.10. Electrical models of an IH load: (a) series, and (b) parallel.

The parameter that best characterizes the RL circuit is the quality factor, Q, which gives the ratio between the reactive power - corresponding to the energy stored in the inductance - and the active power - energy dissipated in the resistance -. In a high-Q circuit the reactive power is small with respect to the active power. Therefore, quality factors for series, $Q_s = \frac{\omega L_{eq}}{R_{eq}}$, and parallel, $Q_p = \frac{R_{eq}}{\omega L_{eq}}$, models are distinguished, [47].

Regardless of the chosen model, the energy behavior of the circuit must always be the same, therefore, the quality factors of both models must be the same. Thus, the parallel resistance value is Q^2 times the series resistance, [48]. The majority of authors choose the series model because it is more intuitive, and the calculations are occasionally more straightforward as the same current circulates through both R_{eq} and L_{eq}.

However, both equivalent impedance circuits are linear models which do not properly catch the frequency response of the IH systems, [49]. Indeed, induction load's equivalent electrical parameters for different frequencies, $R_{eq}(f)$-$L_{eq}(f)$, are computed in [50] by means of FEM simulations, E_φ. Moreover, every inductive load may have a nonlinear behavior that will be further described in Section 1.3.

Alternative passive electrical networks have been proposed by some authors to extend the conditions under which the equivalent response to the IH systems is achieved, always departing from the structures described in Fig. 1.10. Those networks can mainly be divided into equivalent modeling by linear network, to match the frequency response in a given

range, and equivalent modeling by nonlinear models, where it is intended to describe in part the dependence on the response at variable excitation levels.

1.2.1.1 Equivalent modeling by linear network

Linear networks are used to capture the frequency dispersion in the electrical equivalent response. On the one hand, in literature, Foster's impedance equivalent networks (Fig. 1.11) have been employed to model the eddy current effects in different electromagnetic applications. In [51], Foster's series and parallel circuits are analyzed for transformer transients.

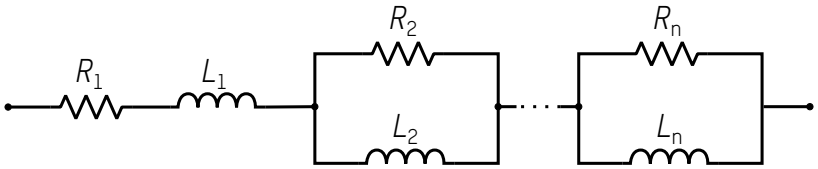

Figure 1.11. Foster's series impedance equivalent network.

The one depicted in Fig. 1.11 has the series configuration and is solved by (1.1).

$$Z(\omega) = (R_1 + j\omega L_1) + (R_2 || j\omega L_2) + ... + (R_n || j\omega L_n) \tag{1.1}$$

Foster's networks are also employed, for example, by [52] to model high-frequency multiwinding magnetic components, or in [53] with inductances for very large-scale integration (VLSI) applications. In [54], Foster's series network is proposed for modeling loads in domestic induction heating applications.

Different electrical IH load models are presented in [55], from the basic series and parallel resistor-inductor equivalent circuits to more improved models taking into account eddy current effects. In [49], this improved circuit in Fig. 1.12 is explained, where R_1 and L_1 are the series resistor and leakage inductance, and R_2, R_3, L_2, and L_3 are the parameters corresponding to the magnetic losses and to the flux.

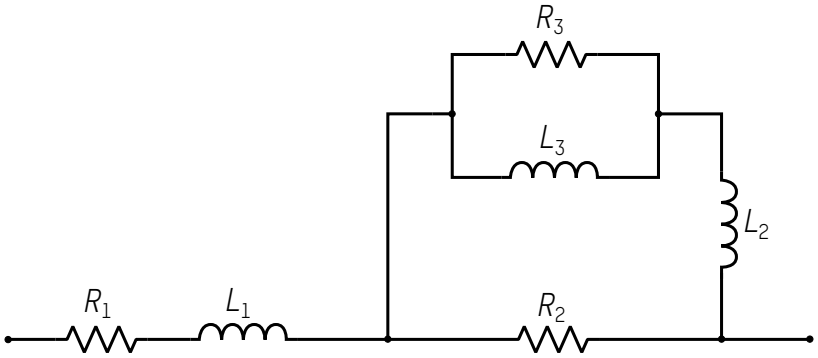

Figure 1.12. Equivalent impedance network proposed in [55].

This circuit can be computed by the equation (1.2).

$$Z(\omega) = (R_1 + j\omega L_1) + (R_2 || (R_2 || (R_3 || j\omega L_3) + j\omega L_2)) \tag{1.2}$$

This equivalent network of passive elements proposed by Forest et al. in [55] and [49] is also employed in other research works to model domestic IH loads, [56], where the values of the components of the equivalent network are adjusted to the equivalent impedance computed from numerical simulations by FEM.

In Fig. 1.11 and Fig. 1.12, R_1 and L_1 represent, respectively, the DC resistance and infinite inductance values, both independent of frequency.

In those equivalent networks, series connections of the rest *R-L* paralleled pairs reflect the effect of frequency; the more *R-L* pairs, the more accurate the fitting will be, but the more complex the analysis. This model is not very precise at low frequencies, but it works well at higher frequencies.

1.2.1.2 Equivalent modeling by nonlinear elements

Because of the nonlinear nature of induction loads and the dependence of the equivalent impedance on excitation, a Foster's series nonlinear network is employed in [54] to model both frequency and current-dependent behavior of IH loads.

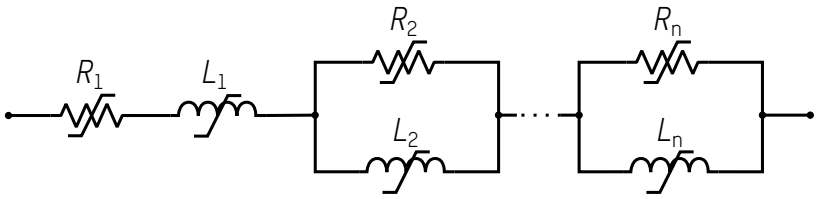

Figure 1.13. Foster's equivalent nonlinear network.

The circuit depicted in Fig. 1.13 is the same as Fig. 1.11 but employing nonlinear elements; this model has potential for improvement.

In [57], the equivalent impedance of a domestic IH load is also modeled depending on excitation current and frequency.

There is a third factor that affects the electrical performance of the IH load: temperature. In [58], the temperature dependence of domestic induction heating systems is studied with analytical expressions.

In conclusion, R_{eq} and L_{eq} values of such load are frequency-, magnetic field-, and temperature-dependent, so electromagnetic-thermal modeling of the inductive load is needed to obtain its complete behavior; among others, [59] couples electromagnetic and temperature fields by FEM. This will be extensively described in Section 1.3.

1.2.2 Power Electronics

The range of power converter topologies used in induction heating systems is very wide, as specifications vary from application to application; they are chosen according to the

frequency and output power needed. Anyway, the main function is the same for each of them. These power converters are essentially frequency modifiers; that is, they convert the mains 50 Hz or 60 Hz single- or three-phase power into a higher-frequency single-phase power. In [60], a review of the state-of-the-art soft-switching power electronics stages is compiled; in the very first part, power converter topologies are classified.

Depending on the application and the material to be heated, the operating frequency of the power converter varies greatly; from a few hertz in high-power systems – melting of metals – to hundreds of kilohertz – surface treatments –. Induction heating systems rely on power electronic converters to generate medium/high-frequency alternating current, which induces heat in electrically conductive materials. The efficiency, reliability, and power density of those systems are directly influenced by the characteristics of power semiconductors, [61].

Traditionally, silicon (Si) has dominated the field of semiconductor materials due to its mature fabrication technology and cost-effectiveness, preparing for significant advancements in solid-state devices. Semiconductor devices employing silicon as the active material, including insulated gate bipolar transistor (IGBT) and metal-oxide-semiconductor field-effect transistor (MOSFET) structures, have become prevalent, particularly in low- and medium-frequency IH applications. However, Si-based devices are subject to limitations in high-frequency and high-temperature operations, primarily due to their inherent material properties.

Indeed, the increasing demand for increasing efficiency, higher operating frequencies, and compact converter designs has facilitated the adoption of wide-bandgap (WBG) semiconductors. The materials silicon carbide (SiC) and gallium nitride (GaN) are increasingly being utilized in power electronics, demonstrating enhanced performance in comparison to conventional Si-based devices, particularly in demanding applications such as induction heating, [61].

SiC devices exhibit superior thermal conductivity, higher breakdown voltage, and lower switching losses. These properties make them well-suited for high-power and high-temperature environments, [62]. Conversely, GaN devices offer distinct advantages, including high switching speeds and low on-resistance, which are particularly beneficial in high-frequency and low/medium-power applications, [63].

Depending on the operating frequency and power level, various power device structures are employed in induction heating inverters. IGBTs are a popular choice in applications up to a few tens of kHz due to their high current capability and ruggedness, although their switching speed is relatively limited. Si MOSFETs are frequently utilized at higher frequencies, ranging from 100 to 500 kHz, where the rate of switching becomes critical. SiC MOSFETs and Schottky diodes are being used more frequently to replace Si devices in high-performance systems. This substitution has the effect of extending the feasible operating range beyond 1 MHz while reducing cooling requirements. GaN high electron mobility transistor (HEMT) is now demonstrating its viability as a promising solution for compact, high-efficiency resonant inverters, particularly within the range of tens to thousands of kilowatts, [64].

It is noteworthy that silicon carbide devices are being adopted more frequently in IH

inverters due to their lower switching losses. Consequently, SiC has emerged as the preferred technology for high-frequency switches. The paper [65] presents a series of pragmatic technical considerations for the practical implementation of SiC devices in resonant inverters for industrial IH applications. Moreover, the paper [66] puts forward several propositions to facilitate the provision of intelligence to IH converters and to advance services for the integration of IH converters in an Industry 4.0 network. Besides, in [67], the implementation of GaN technology is proposed in modular induction heating cells. This approach offers a flexible solution that has the potential to outperform current State-of-the-Art solutions.

The general power conversion scheme for IH systems is shown in Fig. 1.14. The main feature of this type of system is the resonant tank that includes the IH load, composed of a coil and the workpiece, whose electrical equivalent consists of an inductance, *L*, in series with a resistance, *R*, [68]. The frequency of the current exciting the load can be raised either with two-stage conversion stages as in Fig. 1.14a or employing direct conversion as in Fig. 1.14b.

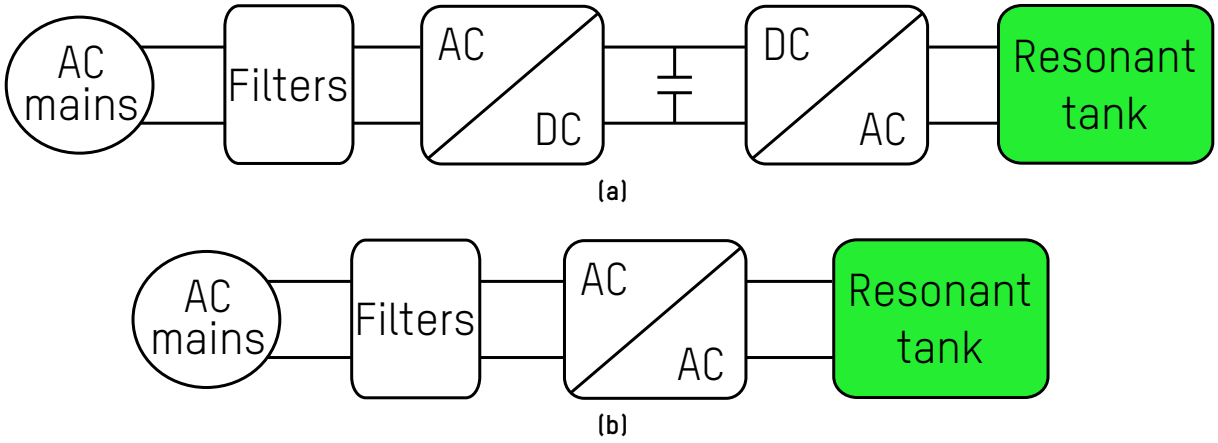

Figure 1.14. Diagram of the power conversion stages with resonant tank including the IH load: (a) typical AC-DC plus DC-AC conversion, [5], and (b) direct AC-AC conversion.

Regarding Fig. 1.14a, the first AC-DC rectifier stage supplies the DC-bus from the AC mains voltage. The most straightforward constructions consist of passive diode bridge rectifiers, although controlled options have advantages. In [69], three-phase Power Factor Corrector (PFC) rectifier topologies with sinusoidal input currents and controlled output voltage are derived from known single-phase PFC rectifier systems and/or passive 3-ph diode rectifiers. Moreover, a comparative evaluation of four three-phase PFC rectifiers for industrial applications is realized in [70].

Additionally, sometimes an intermediate DC-DC converter is implemented further to control the input voltage of the DC-AC inverter stage. For example, [71] employs an intermediate buck converter to adjust the amplitude of the rectifier's output voltage.

Finally, the DC-AC resonant inverter stage generates the medium/high-frequency current that will feed the inductive type load. The different configurations used distinguish between the type of electronics employed, according to the number of switching devices,

either single switch [72], [73], half-bridge [74], or full-bridge topologies,[75].

Depending on the structure of the resonant tank, a distinction can be made between LC-series [76], [77], which stands out for its simplicity; LC-parallel [78], [79], which achieves favorable working conditions for the electronic inverter but increasing the control complexity; and LLC [80]–[82], which features robustness. Depending on the type of the resonant tank, Current Source Inverter (CSI) or Voltage Source Inverter (VSI) topology is employed [83].

Recently, proposals have also been made for direct AC-AC converters applied to induction heating, as appears in Fig. 1.14b, [84], but the more significant number of devices to be switched complicates the generation of gating signals [85]–[87], directly affecting the cost.

Additionally, there are several proposals for multiple output topologies [88]–[90], mainly focused on a specific application with the purpose of obtaining a complex power distribution.

However, our work will focus on the typical stages for power conversion in IH applications depicted in Fig. 1.14b, whose main blocks will be described as follows. This power conversion sequence offers a versatile converter able to supply the required power to loads of varying characteristics while maintaining robust behavior; thus, the control is facilitated compared with direct AC-AC converters.

1.2.2.1 AC-DC rectifier

The mains source provides 50 Hz or 60 Hz of alternating current that needs to be converted into a medium- or high-frequency current required by the induction heating application. For that purpose, the first conversion stage, which generally consists of a bridge configuration topology rectifier, converts the mains AC power into a DC-bus.

This stage can be an uncontrolled/passive – composed of diodes – or controlled/active – thyristors, transistors–. Depending on the specifications, some IH applications require a Power Factor Corrector (PFC) to ensure a sinusoidal input current and/or increase voltage, [91].

1.2.2.2 DC-AC inverter

A comprehensive review of high-frequency converters is presented in [92]. Topology selection, soft-switching technologies, resonant gate drivers, and magnetic components design and optimization are analyzed.

Quasi-resonant single-switch inverters represented in Fig. 1.15a is the simplest structure and are the most typical for low-power IH applications due to their cheapness, [93]. In [94], a quasi-resonant ZVS-PWM inverter with PFC is proposed for a domestic IH application.

In [95], a method to improve the reliability of half-bridge (HB) series-resonant inverter for high-frequency IH applications is presented, as can be seen in Fig. 1.15b.

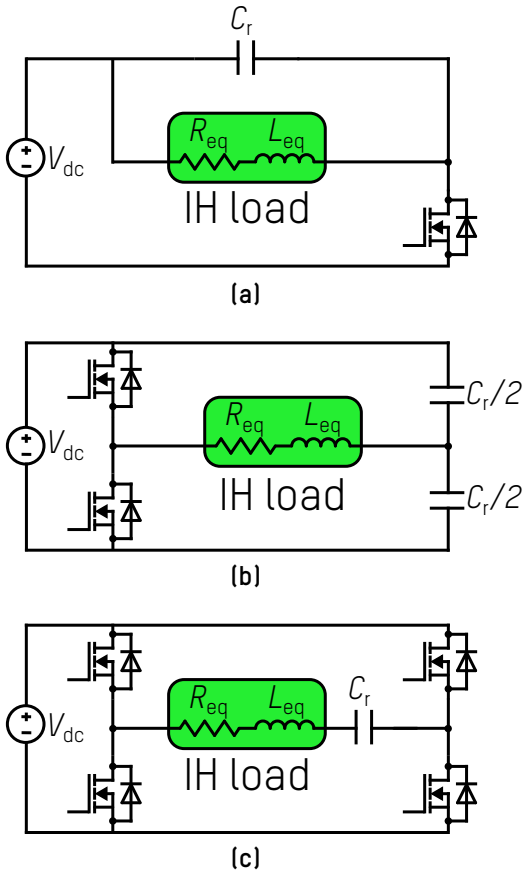

Figure 1.15. Typical inverter topologies for IH systems: (a) quasi-resonant single-switch, (b) half-bridge, and (c) full-bridge.

The full-bridge (FB) topology in Fig. 1.15c is proposed in [96] for induction metal surface hardening. Control techniques for the FB inverter are evaluated in this paper, which is further analyzed afterward.

1.2.2.3 Resonant tanks

Nowadays, all or almost every induction heating system uses resonant circuits [92] at the output of the inverter stage to achieve high efficiency and power densities. The functionality of resonant circuits and the most commonly used topologies are described in the following lines.

An inductor-workpiece load can be modeled with an equivalent resistance, R_{eq}, and inductance, L_{eq}, depending on the model, connected in series or parallel. This IH load depends on the exciting current frequency and envelope, and the temperature of the material. Thus, for complete modeling, equivalent impedance networks are employed, as described in the previous section.

Then, additional capacitors and inductors are added to complete the resonant tank. Capacitive and inductive impedances are balanced by working at a frequency called the res-

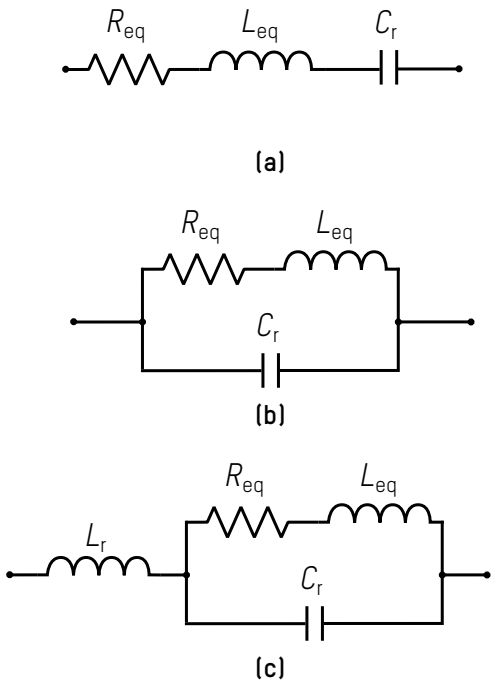

Figure 1.16. Typical IH resonant tanks: (a) series, (b) parallel, and (c) LLC.

onant frequency. At this point, all the power entering the circuit is active, and the system works at maximum efficiency.

The most common structures are second-order circuits connected in series, as shown in Fig. 1.16a, or parallel, Fig. 1.16b, and the combination of both, Fig. 1.16c, would be a third-order resonant circuit. Those resonant circuits are explained and detailed in [97].

A series-resonant circuit is commonly used in VSI topologies; when the switching frequency is above resonance, that is, Zero Voltage Switching (ZVS) is achieved, avoiding the switching on losses. However, parallel resonant circuits are usually used in CSIs, reducing currents through switches and allowing Zero Current Switching (ZCS) operation, [65]. In Table 1.1, the comparison of voltage-fed and current-fed inverters is summarized.

Table 1.1. Characteristics of VSI and CSI topologies.

Voltage-fed	**Current-fed**
Capacitive DC filter	Inductive DC filter
Square voltage	Sinusoidal voltage
Sinusoidal current	Square current
Series resonance	Parallel resonance
Load current = output current	Load voltage = output voltage
Voltage x Q	Current x Q
Low Q loads	High Q loads

Finally, the hybrid series-parallel LLC configuration combines the advantages of the two

previous structures, being the most widely used topology in high-power industrial applications [81], [82].

Additionally, matching transformers are widely used in induction heating applications between the output of the inverter and the resonant tank. The inductive load is placed on the secondary side, and the resonant capacitors can be connected even to the primary or secondary side, depending on the resonance condition, [98]. For example, in [99], the compensated capacitors are distributed between both sides to achieve self-starting switching.

1.2.3 Control Strategies for Induction Heating Power Converters

Focusing on modulation strategies, different methods can be applied to vary the power delivered to the inductor-workpiece system. Taking advantage of the resonance curve of the IH systems, Pulse Density Modulation (PDM) is usually applied, [100]; this control strategy allows the inverter to operate near the resonant frequency for different output power levels, [101]. The PDM inverter makes an induction heating system simple and compact, leading to higher efficiency, [102]. PDM is a form of modulation to represent an analog signal with a binary signal, where the relative density of the pulses corresponds to the analog signal's amplitude. Indeed, Pulse Width Modulation (PWM) is a particular case of PDM with a fixed switching frequency.

On the other hand, in the case of using full-bridge inverters, it is possible to apply Phase-Shift Modulation (PSM), [103]. PSM consists of varying the phase of the carrier between a certain number of discrete values. While in the conventional phase modulation the phase variation is continuous, in PDM, it is a digital signal, so the number of states are limited.

Furthermore, several methods for resonant inverters in IH systems have been proposed regarding control variables; but the general schemes do not vary so much from one method to the other, almost every of them are based on proportional-integral (PI) and phase-locked loop (PLL) regulators.

In control theory, a PI regulator is a type of feedback controller used to maintain a desired output in a system by adjusting the error between the real output and desired setpoint; in this case, proportional and integral controls are combined to eliminate the error. A single proportional regulator can also be employed, or it can also be combined with a derivative controller, composing a proportional-integral-derivative (PID) regulator. Else, a PLL is a feedback control system that adjusts the phase of a generated output signal to suit the phase of an input signal.

In [104], output power and switching frequency are regulated, respectively, based on diagrams depicted in Fig. 1.17 and Fig. 1.18. The power control is realized by regulating the voltage to reach the power reference. Additionally, the switching frequency is taken near resonance by decreasing the phase shift between the voltage and current waveforms, or in other words, making the reactive power close to zero.

In [105], similar controls are proposed to improve the efficiency of parallel LLC resonant inverters, combining both output power control in Fig. 1.17 and phase shift control in Fig. 1.18, which aims to reduce effective current reducing conduction and switching

losses and improve power transfer efficiency; they consider ZVS operation, output power variations, and load changes. In [106], the same scheme is again proposed to control the output power; here, they use a PID regulator. Moreover, in [107] and [108], the output power of a series-resonant inverter is regulated based on online equivalent load estimation.

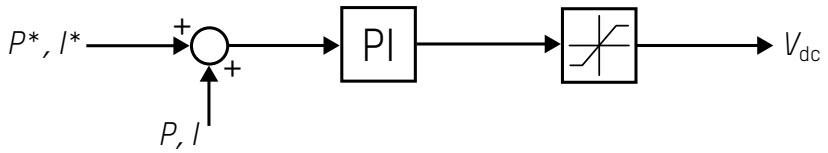

Figure 1.17. Power/current control general diagram.

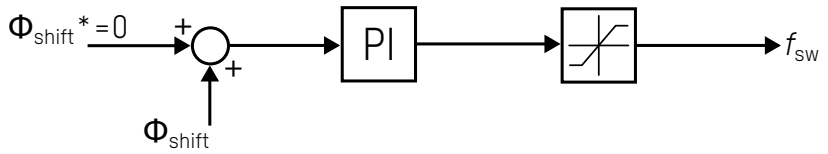

Figure 1.18. Frequency control general diagram.

In [109], the power transmitted to the induction coil is controlled in a single-phase voltage source inverter with LLC resonant load. This power is regulated by means of the inverter's output current or voltage controls employing PI regulators as in Fig. 1.17.

A single-switch quasi-resonant DC inverter is studied in [93] modeling a variable load current, frequency, and temperature dependent. The output power is controlled based on a PI regulator as in Fig. 1.17 but employing the pulse frequency modulation (PFM).

The power control of a full-bridge resonant inverter for an induction hardening process is analyzed in [96]. The control is implemented digitally. Controls based on the input DC voltage and the PDM appear suitable for the surface metal treating for large temperature variations. Moreover, output power is also regulated in [110] for a series-resonant inverter.

Current is controlled in [111] employing a similar similar scheme as in Fig. 1.17, but with current measurement and reference and employing a shift-phase control. A single-phase voltage source inverter feeding a parallel resonant IH load is analyzed.

Regarding multiphase induction heating systems, on the one hand, three concentric inductors supplied by three resonant current inverters for metal sheets is presented in [11]. At the end, a control of the effective current through each coil is proposed employing a similar scheme as in Fig. 1.17, with current inputs. On the other hand, an equal system is analyzed in [112] employing a resonant control to achieve a perfect current reference tracking.

A PLL based on the concept in Fig. 1.18 is employed [113] to track the resonant frequency. A series-resonant DC-DC converter is studied in for high-power density and high-efficiency applications, with an LLC resonant tank.

Billet temperature control is proposed in [114] by using a feedback temperature measured at one point within the volume. An optimal control algorithm is presented for that

purpose. When controlling temperature, one of the difficulties is estimating the temperature of the object being heated. In [115], non-contact temperature measurement is proposed through radiation. A wireless temperature measurement induction heating using an Au-coated ferromagnetic implant is proposed in [116]. The main disadvantage of using thermocouples in IH systems is that they get affected by the electromagnetic field in the surroundings, giving erroneous results. In [117], a K-type thermocouple is used to measure the temperature of the workpiece and compared with a commercial IR sensor. Moreover, a procedure to measure high-temperature gradients during raping heating of an induction dilatometer is proposed in [118].

Other works suggest temperature control based on data obtained from previous analyses. For example, in a hot rolling production line, [119] proposes an artificial neural network to establish the temperature prediction model considering the factors that cause the billet temperature rise concluded from the electromagnetic analysis.

1.3 Electromagnetic-Thermal Modeling of Induction Loads

Especially focusing on industrial applications, the same workpiece can be treated under different operating conditions, e.g., a higher frequency is needed for induction hardening than for melting. The operation point is determined by the current flowing through the inductor. In addition, not only the heat treatment type but the load's characteristics also vary depending on the working frequency and current level. In other words, the equivalent impedance of the inductive load depends on the magnetic field level and frequency due to the BH-curve and skin effect, respectively.

Temperature is also a factor that modifies the properties of materials, particularly at temperatures above Curie point. Such change of properties directly influences the electrical behavior of the inductor-workpiece system, which must be predicted to properly analyze the power converter supplying the heating system. The basis of an industrial hardening process is to exceed the austenizing temperature in the area to be processed and afterward create the martensite layer, the hardened one, through the rapid cooling of the austenite. It is worth mentioning that this austenizing point is above the Curie temperature; therefore, modeling the load at high temperatures is a key factor when designing and foreseeing this type of IH processing.

1.3.1 Electromagnetic-Thermal Modeling

Each IH process is a challenging combination of three phenomena: electromagnetism, heat transfer, and metallurgy. In other words, it is a multiphysical problem, [120]. Electromagnetic-thermal numerical simulations are needed to fully describe this behavior, [121].

The computation of a IH system can be simply done by analytic equations as detailed in [47]. However, numerical modeling has become essential in various fields, and IH systems are one of those, for example, [122]–[124]. Therefore, the focus of this work will be on numerical models. In [125], different electromagnetic-thermal analysis programs and

methods of calculation are mentioned.

There are different methods to apply numerical modeling. The Finite Difference Method (FDM) is a well-known approach where partial differential equations are discretized on a grid, and the derivatives are approximated using finite differences; this method is employed, for instance, in [126]. The Finite Element Method (FEM) is better suited for handling complex geometries and boundary conditions, [127]. It divides the domain into smaller elements and approximates the solution within each node, allowing for a more accurate representation of the problem. The Boundary Element Method (BEM), on the other hand, focuses on transforming the partial differential equation into an integral equation on the boundary of the domain, which can be advantageous for problems with infinite or semi-infinite domains, [128]. Other works, such as [129], [130], propose hybrid FEM-BEM modeling for induction heating processes. Other numerical methods like Large Eddy Simulation (LES) are also used in various industrial processes where liquid metal is driven by electromagnetic forces, but are more intended to compute turbulent recirculating flows, [131].

Numerical computations based on FEM are regularly employed and commonly used to model IH systems, considering the material's nonlinear properties. In this way, accurate modeling is achieved under a wide range of operational conditions so that the control of the supplying power electronics influenced by the variable behavior of the load can be properly designed.

1.3.1.1 FEM-based electromagnetic-thermal modeling

The fundamentals of the electromagnetic modeling are described in [132]. Almost every FEM simulations are based on the very known Maxwell's differential equations in (1.3), which are described in [133].

$$\begin{aligned} \nabla \cdot \mathbf{D} &= \rho \\ \nabla \cdot \mathbf{B} &= 0 \\ \nabla \times \mathbf{E} &= -\frac{\partial \mathbf{B}}{\partial t} \\ \nabla \times \mathbf{H} &= \mathbf{J} + \frac{\partial \mathbf{D}}{\partial t} \end{aligned} \tag{1.3}$$

The general algorithm used by FEM tools to couple the electromagnetic and thermal analyses is depicted in Fig. 1.19. In [134], a coupled electromagnetic-thermal transient finite-element solution for modeling IH of ferromagnetic materials is presented based on the mentioned algorithm.

In three-dimensional domain, the same algorithm is used, for example, by [135] for induction surface hardening, in [136] and [137] for tube welding; moreover, in [138], a commercial FEM tool, ANSYS®, is used to model induction press hardening and heating of complex disks, respectively.

In [140], FEM is used to couple electromagnetic and thermal analyses with hardness fields; they present both mathematical models and experimental results. [141] also studies metallurgical aspects by FEM, apart from electromagnetic-thermal analysis.

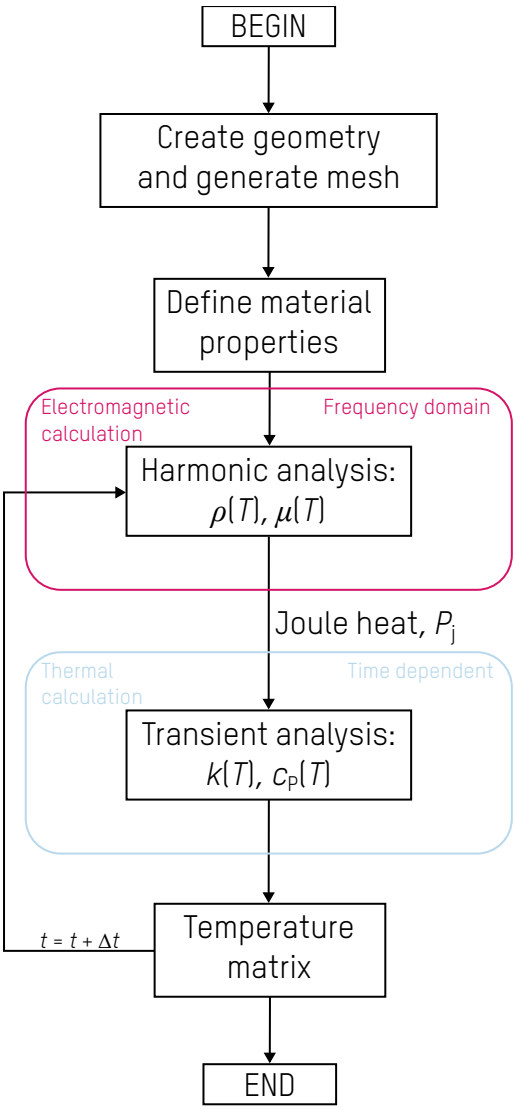

Figure 1.19. Coupled electromagnetic and thermal analyses by FEM, frequency-transient study, [139].

Induction heating for hot metal forming increases the production rate and improves energy efficiency. However, it is a complex task because the heated parts are pre-shaped with holes and cutouts. In [142], a FEM and experimental investigation is carried out to optimize a single-stage IH process for hot forming of pre-shaped blanks.

In [143], an induction hardening problem is divided into simpler ones and the electrical regime is optimized by FEM. Moreover, a multi-surrogate multi-objective decision-making optimization algorithm for IH systems design is presented in [144]. The electromagnetic, thermal, and metallurgical fields are coupled in [145] for a multi-fidelity framework. Induction mass heating is modeled in [146] based on multiple-criteria optimization. In [147], different multi-objective approaches for the design and control of electromagnetic devices are investigated.

1.3.2 Material Properties

Electromagnetic-thermal modeling of the system permits accurate analysis of such behavior, but the computational cost, in that case, is very high and requires precise characterization of the properties of the load. In this subsection, the material's magnetic, electrical, and thermal properties will be briefly described, departing from research works as [148].

1.3.2.1 Magnetic properties

Magnetism is a fundamental property of materials that has been extensively studied and applied in various fields, from electronics to biomedicine. Three main categories are employed to classify the magnetic properties of materials: ferromagnetism, diamagnetism, and paramagnetism.

Each material is classified into one of these groups, considering its relative permeability. Ferromagnetic materials have a relative permeability much higher than 1, meaning they are easily magnetized and exhibit a strong magnetic response to an external magnetic field. However, diamagnetic materials weakly oppose the magnetic fields as their relative permeability is slightly less than 1. In contrast, magnetic fields softly attracted paramagnetic materials due to the relative permeability value a bit greater than 1. But for practical application, diamagnetic and paramagnetic materials are considered non-magnetic.

Hysteresis has been mentioned as one of the properties of magnetic materials; in literature, there are different models of magnetic hysteresis. The Preisach model of hysteresis, which was first proposed in 1935, describes a ferromagnetic material as a network of independent small magnetized domains [149]. The Stoner-Wohlfarth model (1948) is widely used for modeling small magnetic particles, as it is a suitable model for the magnetization of ferromagnetic material with single domains [150]. In 1984, the Jiles-Atherton model was introduced [151], which consists of calculating hysteresis parameters from experimental magnetization measurements departing from the anhysteretic susceptibility, the coercivity, remanence, and the coordinates of the hysteresis loop [152].

When modeling IH systems, anhysteretic BH-curves are employed, but the complexity comes from the nonlinearity of the material's magnetic properties according to field levels and temperature. In the past, some efforts have been devoted to measuring BH-curves of magnetic materials at different temperatures, [153]–[155]. Moreover, [156] measures the magnetic saturation of steels through a vibration sample magnetometer and proposes a method to extrapolate the BH-curve.

Departing from the measurements, different equations have been proposed in the literature to compute the equivalent nonlinear magnetization characteristic of materials, [157].

According to IH systems, going from the simplest to the more complex ones, three BH-curve equations are compared in [158]: simple potential model, Fröhlich model, and inverse tangent approximation. Fröhlich approximation of the nonlinear BH-curve is also employed in [159], [160], emphasizing its accuracy and simplicity. The Langevin function, which is used to determine anhysteretic magnetization in the Jiles-Atherton model, is em-

ployed by [161] to describe the magnetic properties of soft materials. A more complex approximation is named Analytic Saturation Curve (ASC), whose equation was employed for the first time in [162]. In [153]–[155], temperature dependence is added to this expression as an exponential function. Furthermore, the ASC with knee adjustment is proposed by [163]. [164] also proposes this same equation, identifying the magnetic properties using neural networks. In Appendix A, all the mentioned BH-curve models are detailed and compared between them.

On the other hand, there are works [161], [165], [166] that compute a nonlinear equivalent magnetic permeability to assure the same performance with IBC method.

1.3.2.2 Electrical properties

Electrical resistivity or specific electrical resistance, ρ, is a specific property that measures how strongly a material opposes electrical current. In fact, electrical conductivity, σ, is the reciprocal of ρ.

Regarding how the electrical resistivity behaves with temperature, it is often simplified as a linearized approximation:

$$\rho(T) = \rho_0 (1 + \alpha (T - T_0)), \tag{1.4}$$

where ρ is the electrical resistivity, α is the temperature coefficient of resistivity, T_0 is a fixed temperature reference – usually ambient temperature–, and ρ_0 is the resistivity at temperature T_0. The temperature coefficient α is an empirical parameter obtained from measured data, and it differs for different reference temperatures.

According to metals, in general, electrical resistivity increases with temperature. At low-mid temperatures, the resistivity follows a power law function of temperature, which can be mathematically approximated with the Bloch-Grüneisen formula proposed in [167].

However, in [153], the temperature dependence of the electrical resistivity is simplified for an IH process, in which two linear equations are proposed changing the slope at the phase transition near the Curie temperature.

Prediction of electrical resistivity from the chemical composition of a plain carbon manganese steel is performed in [168], employing regression-based and artificial neural network-based models.

1.3.2.3 Thermal properties

The thermal properties of interest in induction heating systems are the heat capacity, C_P, and the thermal conductivity, k. The former is a property that indicates how much a material resists temperature changes, while the latter, as its name suggests, describes the ability of such material to conduct heat. In [169], these two parameters are obtained depending on temperature for the different materials, from ambient temperature to beyond the Curie point. The heat capacity is principally affected by the phase transition of the material; its temperature-dependent graph shows a significant peak value around the Curie point.

Convection and radiation heat fluxes at the surfaces might also be considered, as they are the reason for dissipating part of the heat, [170]. Heat convection is the transfer of heat from one place to another through fluid movement. Heat radiation, on the other hand, is caused by the electromagnetic radiation emitted from a surface into its environment.

On the other hand, especially for hardening processes, the numerical simulation of the metal quenching process is performed in [171], using FEM to couple temperature, phase transformation, and stress-strain fields. Heat transfer coefficients for quenching processes are obtained in [172]. Precisely, quenching in water using steel probes for a variety of iron alloys is studied in [173].

1.3.2.4 Mechanical properties

The induction heating process involves the aforementioned three phenomena. The mechanical properties will be briefly mentioned, due to their reduced importance for this thesis, to conclude this section.

The mechanical properties of microalloyed steel (MAS) are established in a comprehensive database by [174], at temperature ranges from room to 550 ºC. First, chemistry, hardness, and microstructure are analyzed; then, physical and tensile properties are studied; effect of long term thermal exposure is also evaluated; and, finally, oxidation and engine testings are realized. Moreover, in [175] a mechanical model is developed to be employed in FEM simulations of an IH system. [176] also models the mechanical phenomena, but in this case, to study a hard turning process.

1.4 Dynamic Modeling

The general scheme of a dynamic simulation model is depicted in Fig. 1.20. It is usually based on a dynamic load highlighted in green, which is dependent on output parameters obtained by parameter sensing. The dynamic load may be preceded or followed by structural systems.

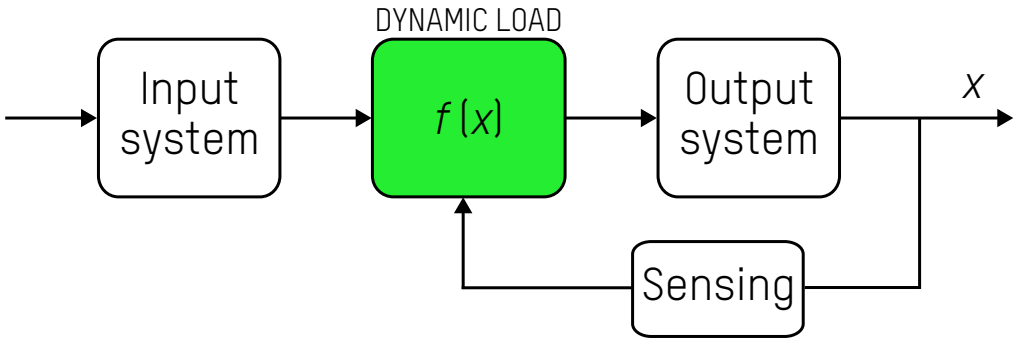

Figure 1.20. General scheme of a dynamic simulation model.

The dynamic behavior of the inductor-workpiece load has been described in some works, although it is not fully captured due to the complex dependencies of the physical proper-

ties of the inductor, [177]. On the other hand, some works have been devoted to studying the dynamics of power converters applied to induction heating. An analysis based on experimental results is proposed in [178].

In [179], the dynamics of the induction load is studied by applying phase shift control, and in [180], an analysis of the dynamics of a matrix power converter is performed but both focused exclusively on the circuit behavior of the IH load, which need to be properly identified.

Other research fields regularly employ dynamic models. For example, in [181], a power hardware-in-the-loop is simulated to analyze the effects of real variable speed heat pump and battery energy storage systems in a building. A data-driven rolling optimization control approach is presented in [182] to handle the dynamics of the virtual energy storage system. Moreover, a variable refrigerant flow system is modeled in [183] to predict its performance for model-based control, fault diagnosis, and detection. Furthermore, a model predictive control strategy is proposed in [184] to reduce the cost of installing energy storage to islanded microgrids.

1.5 Objectives and Scope

In a few words, induction heating is a heating process of an electrically conductive object, usually a metal, by means of electromagnetic induction. Induced currents are generated inside the aforementioned conductive object and tend to heat the material due to the Joule effect. In case of magnetic materials with significant values of relative permeability, the heating process can become more effective.

Induction heating is used in several fields, such as industrial, medical, and domestic applications. This technology stands out for its efficiency, heating velocity, security, and very precise control. Its efficiency depends mainly on the ratio between the resistance of the coil and the equivalent resistance of the material to be heated. Moreover, the optimization of the coils' geometry is important when it comes to the homogeneity of the heated parts. Even more, the material's magnetic and electric behaviors should be properly described for a correct characterization of the system.

Coming back to induction heating processes, many impedance equivalent network models have been suggested in previous literature to model the load depending on the magnetic field's frequency, which have been described in previous pages. However, the magnetic field level's influence on the load behavior, caused by the heated material's nonlinear BH-curve and reflected in the coil current's envelope dependence, is less analyzed. Furthermore, the induction load's temperature dependence is also critical as it directly influences the behavior of the power converter's control dynamics.

1.5.1 Thesis Framework and Methodology

This thesis is framed in the industrial applications of induction heating. In this framework, we will study induction heating application conditions that are not very usual in this

field but can be expected to provide improved heat treatments with respect to the present ones. These conditions may include the use of lower frequencies than usual in this field.

The proposed methodology includes both finite-element study and electrical simulation activities as well as experimental developments. As for the simulation activities, the problem will be approached from a multiphysical point of view by coupling the electromagnetic and thermal aspects of the problem. In this way, the aim is to explore the benefits that the use of non-standard working conditions could bring to the thermal treatments.

As for the experimental activities, the development of a versatile test bench is planned, including a variable current generator, a sensor system, and the automation necessary for the verification of the planned heat treatments.

1.5.2 General Objectives

The working method of this research project will be a combination of simulations and experimental tests. First, a combination of electromagnetic-thermal finite-element simulations and electrical software simulations will be developed. Moreover, those simulations will be validated in an induction hardening testbench.

These are the general objectives that arise under the main goal:

Goal 1: Obtain technical knowledge about induction heating systems.

That is, SoA of induction heating technology; analyze at which stage is the investigation about IH systems. Gain knowledge about its history and future, basics (definitions, equations), advantages (compared to other heating methods), and different processes (focus on industrial ones). Study thoroughly the power electronics technologies needed for IH (different converter topologies, control strategies, etc.). Also find information about the fundamentals of FEM simulations and other calculation methods.

Goal 2: Ability to simulate different induction heating processes by finite-element method.

Different FEM models will be employed to foresee the performance of the system. A coupled electromagnetic-thermal model of the induction load will be developed.

Goal 3: Optimize the operating point of the power electronic converter that feeds the inductor.

The FEM models will be coupled with an electrical circuits simulator to better study the behavior of the power converter and its control dynamics.

Goal 4: Carry out induction heating tests.

One of the aims of this thesis is to employ the induction hardening testbench to validate the assumptions and simulations carried out during the development of the PhD studies.

1.5.3 Chapters Overview

This thesis document is structured as follows: first, the thesis topic has been introduced in this Chapter 1. Now, the nonlinear load will be modeled by a commercial FEM tool in Chapter 2, where electromagnetic and thermal models of induction loads will be developed step by step. In Chapter 3, the power electronics of the analyzed system will be described. Then, in Chapter 4, the proposed dynamic model of the nonlinear induction load under study will be detailed, followed by the electrical simulation of the heating process. To validate the model, the simulation results will be compared with some experimental measurements in Chapter 5. Finally, the work will be summarized with the most meaningful conclusions in Chapter 6, and some interesting future lines will be proposed.

Chapter 2

Electromagnetic-Thermal Modeling of the Induction Heating System by Finite Element Method

This chapter presents a thorough examination of the numerical modeling of the induction heating system analyzed in this thesis. The main purpose of the industrial induction system under study is to conduct metallurgical treatment on a cylindrical steel component, which represents a typical load in industrial environments. Initially, the chapter will detail the computational characterization of the system's electromagnetic behavior. This will be followed by an overview of the key aspects of the thermal modeling process. Subsequently, an integrated electro-thermal model will be developed to effectively couple both electromagnetic and thermal behaviors. Finally, the chapter will focus on the system as it pertains to the specific material of interest, namely 42CrMo4 steel, also referred to as AISI 4140. This material is widely recognized in the industry for its applications in the manufacture of various machine components across a broad spectrum of uses.

2.1 Modeling of Induction Heating Systems

The process of material treatment through induction heating involves the interaction among three primary phenomena: electromagnetic behavior, heat transfer, and metallurgy techniques. Achieving accurate results in computational analyses necessitates a careful consideration of these multifaceted effects and their interconnections. This complexity often results in significant computational costs, and various challenges must be addressed due to the coupling between different behaviors. To effectively manage these challenges, the focus of numerical modeling will be on finite element analysis, which is a well-established methodology specifically suited for this application and is widely utilized in the modeling of induction heating systems. Initially, the uncoupled phenomena will be explored individually before advancing to the development of a coupled model. The final outcome will be a comprehensive simulation model that integrates specific behaviors relevant to the process.

The electromagnetic phenomenon is the fundamental reason behind the inductive heating of a workpiece, acting as the primary source of heat generated at its surface. In induction heating systems, power is transferred from a coil, which generates a variable electromagnetic field when supplied with a periodic current. This electromagnetic field induces currents in the workpiece—in this case, typically a metal billet—resulting in heat generation due to Joule heating, where energy is dissipated as heat due to electrical resistivity of the material under treatment.

A defining feature of IH systems is their capacity to transfer heat without any direct physical contact with the workpiece, particularly at the surface level. This capability is predominantly due to the skin effect, a phenomenon where the induced currents tend to flow near the surface of the conductor, thereby allowing for localized heating. This unique heating method enables the application of high power levels to specific regions of the material almost instantaneously, facilitating complex thermal treatments and processes such as hardening, annealing, or melting, tailored to the material's requirements.

A typical IH system consists of a coil and a power electronic converter. The coil is essential for generating the electromagnetic field necessary for inducing currents in the workpiece. To accurately model the electrical behavior of the workpiece-coil system, we often use a simple equivalent circuit composed of an equivalent resistance and an equivalent inductance, which can be configured either in series or in parallel.

The equivalent resistance represents the power transferred from the coil to the workpiece, capturing the fundamental energy flow. However, it also accounts for minor contributions from power losses occurring in the coil itself, which can be due to resistive heating and other inefficiencies. Conversely, the equivalent inductance is associated with the magnetic energy stored within the system. The workpiece significantly influences this inductance, as its presence modifies the magnetic field distribution generated by the coil.

Both the equivalent resistance and inductance are highly sensitive to the geometry and physical characteristics of the workpiece, including its dimensions, shape, and material properties. Additionally, the characteristics of the external electromagnetic field—such as frequency and intensity—further affect these parameters. It is particularly noteworthy

that the magnetic properties of the load exhibit linear responses at low excitation levels; however, as excitation levels increase, nonlinear effects, such as saturation phenomena, become critically important. These nonlinearities can introduce complex behaviors in the system, making detailed analysis and modeling increasingly challenging and demanding a more nuanced understanding of the electromagnetic interactions at play.

After the electromagnetic heat dissipation is obtained, the system's thermal analysis is carried out. Here, conductive heat transfer is the dominant process. The thermal conductivity defines the rate at which heat diffuses through the conductive areas, while the specific heat capacity determines the energy needed to increase the temperature a degree per mass unit. Both thermal parameters depend on the material's temperature and microstructure. It is worth mentioning that during both heating and quenching, there are various microstructural phase changes, so that the thermal properties can change abruptly. However, to a lesser extent, some of the power is dissipated on the workpiece surface due to convection and radiation heat losses but it just reduces the effectiveness of the heat transfer to the workpiece, that is, the net power delivered into the load is almost the totally power transferred by the induction process.

Regarding the metallurgical aspects, during a phase transformation of a material, at least one new phase is formed with different structural properties and physical characteristics from the parent phase. Most transformations do not happen immediately; instead, they start with forming many small particles of the new phase, which gradually increase in size until the transformation is complete. However, this analysis is beyond the scope of this thesis.

Various methods are used to analyze the behavior of the inductor-workpiece system, and they can be broadly categorized into two main groups: analytical methods and numerical methods. Analytical methods have been used since the early days of IH for simple geometries and linear materials. However, as the processes and geometries became more complex, these analytical methods proved insufficient for further analysis. Numerical computing is increasingly utilized in industry, and its role is expected to expand. Some numerical methods have been described and cited in Chapter 1. In this work, a commercial finite-element method tool, COMSOL Multiphysics®, [185], is employed to simulate the numerical model of the induction system under study.

2.2 Computational Model of the Induction Load

The industrial application of induction heating involves the integration of electromagnetism, heat transfer, and metallurgy. Consequently, numerical simulation tools that utilize multiphysics analysis are essential for developing an electrical model of the inductor-workpiece system. This modeling is necessary to describe and optimize both the system and the associated power electronics.

In this thesis, electromagnetic modeling will be conducted using frequency domain simulations, which provide a good balance between result accuracy and computational cost. For the heat transfer and metallurgy processes, we will employ transient thermal modeling.

This approach incorporates the properties of the workpiece by defining the temperature dependence of thermal conductivity and capacity, as the phase transitions related to the microscopic internal structure of the material show a strong dependence on these parameters.

Initially, we will separately describe both types of simulations using simplified characteristics. Subsequently, incremental models will be developed to construct a comprehensive electric-thermal coupled model. Finally, specific characteristics will be included to achieve a complete model that captures the main features of the induction heating system. A key focus will be on determining the equivalent impedance of the induction heating system.

2.2.1 Electromagnetic Modeling

The electromagnetic model of the workpiece-inductor system will be based on several key assumptions specific to this configuration. First, capacitive effects will be ignored, as they only become significant at frequencies much higher than those typically used in this type of system. Instead, we will focus solely on inductive effects, which are associated with current densities within the system. No current discontinuities will be observed because no current accumulation are allowed under the assumptions taken for the simulation.

The physical properties of the materials in the system will influence the characteristics of the electromagnetic fields. In particular, if any of the materials exhibit magnetic properties, indicated by their relative permeability in linear form, the fields in the system will be enhanced. Moreover, as is typical in induction systems, currents will be induced in materials with electrical conductivity. These induced currents will be affected by the skin effect, which causes them to concentrate near the surface of the conductive materials.

Obviously, the starting point of electromagnetic modeling is Maxwell's equations, [133]. Because of the characteristics of the problem, it is appropriate to use the decomposition using the electric potential, V, and the magnetic vector potential, $\mathbf{A}$, as given below, [134], [163]:

$$\mathbf{E} = -\nabla V - \frac{\partial \mathbf{A}}{\partial t} \tag{2.1}$$

and

$$\mathbf{B} = \nabla \times \mathbf{A}. \tag{2.2}$$

It is important to understand that electric charge densities create electric potential, V, while magnetic vector potential is generated by electric current densities. Since the inductive behavior is fully described by the magnetic vector potential, $\mathbf{A}$, we can disregard the electric potential in our analysis. Consequently, the electric and magnetic fields relevant to the IH system can be expressed as $\mathbf{E} = -\frac{\partial \mathbf{A}}{\partial t}$ and the magnetic field is given by $\mathbf{B} = \nabla \times \mathbf{A}$, respectively.

In addition, a magneto-quasi-static approach can be applied to the IH system, as the contribution from radiation is less significant. This assumption implies that the displace-

ment current in Ampère's law can be considered negligible, which means that $\mathbf{J}_\mathrm{D} = \frac{\partial \mathbf{D}}{\partial t} = 0$. Under these conditions, the electromagnetic model of the system simplifies to solving the following partial differential equation throughout the entire system, derived from Maxwell's equations, [36], [186]:

$$\frac{1}{\mu}\nabla^2\mathbf{A} - \sigma\frac{\partial \mathbf{A}}{\partial t} = -\mathbf{J}_\mathrm{coil} \tag{2.3}$$

where σ is the electrical conductivity and μ is the magnetic permeability of the material media. The field's sources of the magnetic vector potential are given by the external current density in the coil $\mathbf{J}_\mathrm{coil}$, which typically corresponds to the homogenized distribution of the current in the cross-sectional area of the coil's turns.

The preceding expression relates to a parabolic diffusion equation that is solved in the transient regime. The computational cost associated with this time-domain simulation is exceptionally high, often leading to convergence issues or prolonged simulation times. However, given the characteristics of the power electronics and the resonant tank employed, the current supplied to the coil aligns with the fundamental harmonic of the operating frequency. Therefore, we can utilize a frequency domain approach, resulting in a significant reduction in computational cost. In the context of eddy current problems, obtaining results in the frequency domain is generally more straightforward. Under this regime, the fields are substituted by a complex amplitude, and the time derivative operator is replaced by the operator $j\omega$, where ω is the angular frequency associated with the working frequency of the power converter, simplifying the solution to the following equation:

$$\frac{1}{\mu}\nabla^2\mathbf{A} - j\omega\sigma\mathbf{A} = -\mathbf{J}_\mathrm{coil}, \tag{2.4}$$

where the angular frequency is $\omega = 2\pi f$.

One of the aims of the finite-element modeling of induction heating systems is to obtain the electrical equivalent of the induction load. For that purpose, first, the induced voltage in the coil V_ind is calculated by integrating the electrical field on the coil's turns, as it is given as follows:

$$V_\mathrm{ind} = -\int_\mathrm{coil} \mathbf{E}\cdot d\mathbf{r} \tag{2.5}$$

By defining the longitudinal electric field along the turns as $E_\parallel = \mathbf{E}\cdot\widehat{\mathbf{r}}$, equation (2.5) can now be rewritten as:

$$V_\mathrm{ind} = -\int_\mathrm{coil} E_\parallel dr \tag{2.6}$$

It should be noted that the effect of induced currents in conductive materials has two significant implications. First, the induced voltage in the coil is complex valued, with the real component exceeding zero. Second, this induced voltage is indeed frequency dependent, meaning its value varies based on the operating frequency of the converter.

The previous expression corresponds to coils made up of filiform turns. However, considering turns with a cross-sectional area denoted by S_{turn}, it can be convenient to rewrite the equation as:

$$V_{\text{ind}} = -\frac{1}{S_{\text{turn}}} \int_{v_{\text{coil}}} E_{\parallel} dv \tag{2.7}$$

where v_{coil} corresponds to the whole volume of the coil.

Dividing such induced voltage by the coil's excitation current, the complex impedance is obtained. The equivalent resistance and inductance values are directly calculated due to $Z_{\text{eq}} = R_{\text{eq}} + j\omega L_{\text{eq}}$. This calculation is analytically expressed as [50]:

$$Z_{\text{eq}} = \frac{V_{\text{ind}}}{I_{\text{coil}}} = -\frac{1}{I_{\text{coil}}} \frac{1}{S_{\text{turn}}} \int_{v_{\text{coil}}} E_{\parallel} dv, \tag{2.8}$$

where I_{coil} is the current amplitude flowing through the coil and $E_{\parallel}$ is the aforementioned longitudinal electric field to the turns of the coil.

Typically, the electrical properties of an induction heating system are characterized numerically by the frequency-dependent equivalent resistance, $R_{\text{eq}}(\omega)$, and the equivalent inductance, $L_{\text{eq}}(\omega)$. These values can be accurately determined through Finite Element Method (FEM) simulation in the frequency domain by varying the excitation frequency.

2.2.2 Thermal Modeling of the IH System

The thermal modeling of the induction heating system must take into account its intrinsic characteristics. First and foremost, the coil and the workpiece can be considered essentially isolated because the space between these two elements is filled with air, which can be assumed to act as a thermal insulator. Additionally, in industrial applications, the thermal behavior of the coil can be largely neglected, as the water-based cooling system prevents any overheating of this component. Consequently, the thermal simulation should focus primarily on the thermal behavior of the workpiece.

When conducting a thermal simulation of a workpiece, two key factors must be considered. Firstly, in induction heating systems, the heat source is related to the induced currents, which are significantly influenced by the skin effect. This means that the heat is concentrated in a thin layer close to the surface of the workpiece. Secondly, the main variable analyzed in this type of simulation is the temperature, T, at each point within the workpiece. Given the high power levels involved, it is common to observe large temperature gradients, which result in rapid heat transfer throughout the component.

According to heat transfer fundamental theory, [170], heat is transferred through three primary mechanisms: conduction, convection, and radiation.

- **Conduction**: also known as heat diffusion, this process involves heat transfer within a solid or fluid, and arises from the exchange of kinetic energy between atoms. The empirical constitutive law of heat conduction is written as:

$$q_{\text{cond}} = -k\nabla T, \tag{2.9}$$

where k is the thermal conductivity, ∇T is the temperature gradient, and q_{cond} is the heat flux by conduction.

- **Convection**: this mode transfers heat from one location to another through mass transfer, and it just happens in fluids. The heat transfer by convection at a surface, q_{conv}, is given by:

$$q_{\text{conv}} = h\left(T_{\text{s}} - T_0\right), \tag{2.10}$$

where h is the convection coefficient, T_{s} is the surface temperature, and T_0 is the ambient temperature. The impact of this process becomes notable when the part is subjected to quenching through a water shower because it is equivalent to a rapid increase in the convection coefficient.

- **Radiation**: it involves electromagnetic radiation emitted from a body to its surroundings. Notably, this is the only mode of heat transfer that does not require a material medium to occur. It holds significant importance at elevated temperatures. Radiation heat losses are given by:

$$q_{\text{rad}} = \varepsilon\sigma\left({T_{\text{s}}}^4 - {T_0}^4\right), \tag{2.11}$$

where σ is the Stefan-Boltzmann constant ($5.67 \cdot 10^{-8}$ W/m$^2 \cdot$ K^4) and ε is the emissivity of the surface.

Heat transfer by conduction is a process that aims to homogenize temperature throughout the workpiece, affecting its entire volume. In contrast, convection and radiation involve the dissipation of heat at the surface of the material but are generally less significant than conduction heat transfer.

The power source to heat the material results from the Joule losses caused by the eddy currents in a thin layer close to the surface of the workpiece to be heated. The energy generated in the material, q_{ind}, is given by:

$$q_{\text{ind}} = \frac{1}{2\sigma}|\mathbf{J}_{\text{ind}}|^2. \tag{2.12}$$

where $\mathbf{J}_{\text{ind}}$ is the complex amplitude of induced current density in the workpiece.

The induced current is given by $\mathbf{J}_{\text{ind}} = \sigma\mathbf{E}$, therefore, including the relationship for the electric field, $\mathbf{E} = -j\omega\mathbf{A}$, we obtain:

$$q_{\text{ind}} = \frac{\sigma\omega^2}{2}|\mathbf{A}|^2. \tag{2.13}$$

Thus, the heat dissipation from the induced current can be straightforwardly calculated from the electromagnetic field simulation.

The thermal behavior of materials heated by induction is primarily determined by the heat diffusion in the workpiece. This is due to the high power levels involved and the efficient thermal conductivity of metals. Additionally, the material's thermal capacity plays a role in the heat transfer process, as it affects the transient response of the temperature distribution within the workpiece. The heat transfer equation, given by (2.14), describes how the temperature distribution in the material changes over time and space.

$$\rho c_{\mathrm{p}} \frac{\partial T}{\partial t} - \nabla \left(k \nabla T \right) = \dot{Q}, \tag{2.14}$$

where ρ is the density of the material , c_{p} is the specific heat, k is the thermal conductivity, and $\dot{Q}$ is the aforementioned heat source arising from eddy currents as well as includes the heat dissipation in the workpiece's surface by convection and radiation.

Unlike its electromagnetic counterpart, the thermal model operates in the time domain. As a result, when significant changes in physical properties arise from updates in temperature distribution, a new electromagnetic simulation must be conducted in the frequency domain. When considering the coupling between electromagnetic and thermal behaviors, it is essential to account for the different dynamics of both systems. Additionally, as explained in the previous section, electromagnetic simulation is carried out in the frequency domain, while thermal modeling is performed in the time domain. Therefore, it is crucial to update the parameters at designated intervals to optimize the results effectively.

2.3 Finite Element Simulations of the Induction Heating Systems

Finite element simulation has been widely used to model industrial induction heating systems. This section outlines an incremental procedure for modeling, aimed at highlighting the key aspects of this type of simulation.

First, we will describe the reference model, which consists of a coil and a metallic workpiece. Although this model is simple, it demonstrates the effectiveness of such an approach, even under simplified conditions. Initially, we will consider linear physical properties to analyze their influence on the final results.

Next, we will explain the uncoupled simulation model, which will include two configurations: one with the coil in air and another with the inductor interacting with linear properties in the workpiece. Following this, we will construct a thermal model with constant physical properties to identify the main aspects of the heat transfer process.

In the final part of this section, we will present the main results of a coupled electrothermal model that also uses linear properties.

The reference system geometry consists of an inductor with a multi-turn spiral coil. To simplify this geometry, it is modeled as a given number of evenly spaced rings with a common axis. This reduction transforms the coils into a two-dimensional axisymmetric structure with rotational symmetry. Such a simplification typically leads to a significant

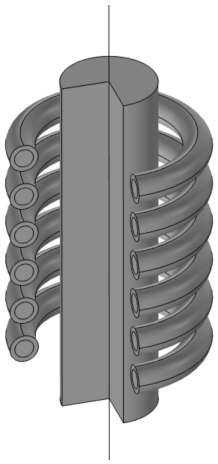

Figure 2.1. Geometry of the induction heating system in a three-dimensional capture by revolving the axisymmetric structure.

reduction in computational costs while enhancing accuracy compared to a fully detailed geometric model.

Additionally, the insertion of the workpiece, which is a single metallic billet, preserves the rotational symmetry of the system. Thus, simplifying the coil's geometry boosts the simulation's performance with minimal impact on the precision of the numerical results. The complete inductor-workpiece geometry is illustrated in Fig. 2.1, as utilized in COMSOL®, the FEM tool employed in this dissertation.

Table 2.1. Inductive load's geometry.

Parameter	Value	Unit
Coil's turn number	6	
Coil's inner radius	15	mm
Turn inner diameter	4	mm
Turn outer diameter	6	mm
Distance between turns	9	mm
Billet radius	10	mm
Billet length	75	mm

The geometrical data for the induction heating load is detailed in Table 2.1. As shown in the table, the coil is constructed with $n = 6$ tubular turns, as a water-cooling system is necessary to limit the maximum working temperature of this component. The tube has a cross-section consisting of an outer circle with a diameter of $d_{ext} = 6$ mm and a hollow section with an inner diameter of $d_{int} = 4$ mm. Water circulates inside the tube to cool the coil. Each turn forms a ring with an inner radius of $r_{int} = 15$ mm, with a separation of $d_t = 9$ mm along a common rotational axis.

The metallic workpiece is a cylindrical billet, with a radius of $r = 10$ mm and a length of $l = 75$ mm. It is important to note that this geometry corresponds to the prototype used in the experimental setup designed to characterize induction heating in the subsequent

chapters. However, the conclusions drawn in this section can easily be extended to alternative configurations.

2.3.1 Electromagnetic Simulation Modeling

As it was stated, the starting point to explain the FEM-tool simulation model is to consider just electromagnetic simulation. Linear physical properties are considered for these simulations. Moreover, due to time-domain simulations requiring a high amount of resources, it can be adequate to perform the simulation in the frequency domain, which provides good results at a moderate computational cost. The central assumption taken in the frequency domain simulation refers to the excitation waveform, which corresponds to a perfect single harmonic of a given frequency. The validity of the preceding condition is beyond any doubt because the power converter feeds a resonant tank close to resonance with a high-quality factor load. In that case, the diffusion equation is reduced to a simplest form because, as was aforementioned, the operator for the derivative is substituted by an operator $j\omega$, and the parabolic equation is transformed into a most straightforward elliptic equation.

The simulation will cover a larger range of excitation frequencies, from 10 Hz to 100 kHz, in order to capture the electromagnetic behavior under a wide variety of situations. In this study, three different configurations are examined. First, the coil in air is modeled to determine its inductance and the resistance associated with power dissipation due to the current driven by the device. In this case, the frequency dependence of these parameters will be examined. Next, a billet with specific physical linear properties is included in the simulation to extract the main characteristics of the induction heating system. Finally, the method for incorporating nonlinear physical properties related to the BH-loop of the material is explained. It is important to note that these characteristics introduce additional challenges to the electromagnetic analysis.

2.3.1.1 Coil in air

The billet is removed from the model to simulate the coil in air. As previously mentioned, the coil is a hollow tube made of copper, whose electrical conductivity at ambient temperature is $\sigma = 58$ MS/m. Actually, during the process, the coil dissipates heat, and cooling water circulates through the inner hole of the inductor, but in this analysis, the temperature is not taken into account; the coil is supposed to be at ambient temperature. In this configuration, magnetic properties do not play any important role because both air and coil are non-magnetic.

The geometry of the coil in air is relatively straightforward, benefiting from the axial symmetry of its simplified structure. The main challenge in modeling this type of system lies in the reconfiguration of the current distribution as the excitation frequency increases. This is due to the induced currents that arise from the conductivity of the material used in the turns. To effectively simulate the influence of these induced current densities, it is important to consider key parameters related to the so-called penetration depth, δ. For linear media, this penetration depth can be analytically defined as follows:

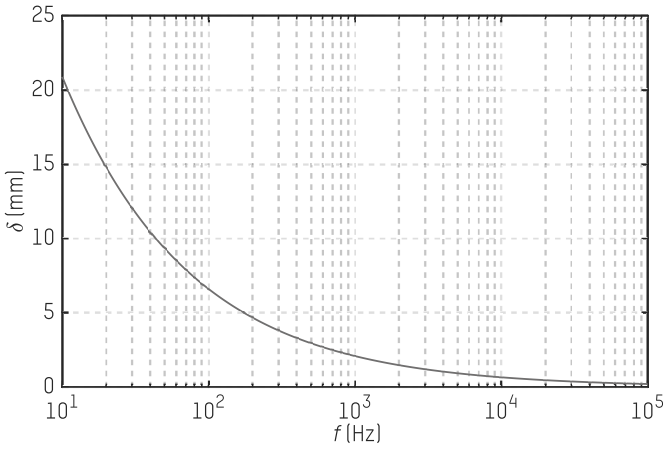

Figure 2.2. Skin depth, δ, in the coil's section for an excitation frequency range of interest.

$$\delta = \sqrt{\frac{2}{\omega\mu\sigma}}, \tag{2.15}$$

where σ and μ are, respectively, the electrical conductivity and the magnetic permeability of the material, and ω is the exciting current's angular frequency.

According to the penetration depth's expression, increasing the excitation frequency δ is reduced, resulting in a more pronounced effect. The frequency-dependent coil's skin depth is plotted in Fig. 2.2, where it is clearly observed that the penetration depth decreases as the frequency is increased.

It is noteworthy that at an intermediate frequency of 1 kHz, the penetration depth measures approximately 2 mm, closely matching the characteristic dimensions of a single turn's cross-section. This penetration depth is crucial, as it clearly defines how electromagnetic fields diminish within conductive media. At the turn level, two prominent phenomena arise due to current distribution. First, we observe the definitive ring effect, which occurs largely because the spiral design of the turn channels current densities toward its inner side. This effect intensifies when the penetration depth aligns precisely with the turn's diameter. Additionally, at higher frequencies, we see a significant shift in current distribution: current densities increasingly gather at the external surface of the turns. This shift arises because the penetration depth is less than the thickness of the turns' cross-section, defined by the difference between the outer and inner radii.

With the purpose of accurately visualizing the distribution of induced currents at the turn level, it is important to apply an appropriate spatial discretization, or meshing, to the coil's geometry in air. Generally, the mesh elements used in numerical simulations should be smaller than the characteristic distances over which the modeled fields vary, i.e., the penetration depth value at the higher excitation frequency. In Fig. 2.3, the mesh of the coil is displayed, with particular attention to the mesh of each turn's outer boundary layer. This fine mesh is crucial for accurately modeling the skin effect on the coil's turns. In that case, a total of eighteen layers are utilized at the surface of the turn with an exponential

growth factor slightly higher than one, and the remainder geometry is meshed with free triangular elements. This meshing can be more clearly observed in the zoomed-in view of a turn's mesh. The surrounding air is meshed using free triangular grids.

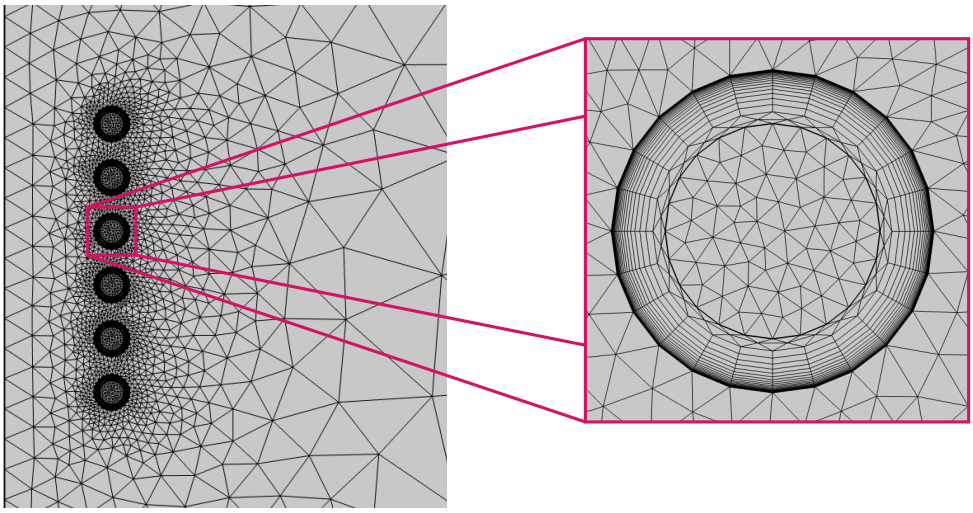

Figure 2.3. Meshing applied to the coil in air structure.

Due to the linear physical properties of this configuration, the simulation results are proportional to the applied excitation level. Consequently, the equivalent resistance derived from the simulation is independent of this excitation level. This independence allows for the selection of any value for the excitation. In this thesis, two different current excitation levels are considered: the small-signal regime, which is related to the current level used in high-precision measurements with an LCR meter, and the large-signal level that occurs when the system operates under typical working conditions. For the small-signal level, we consider a harmonic current level of 10 mA. This value is selected because, even with a workpiece inserted, the system's behavior can still be described by media with linear properties.

In Fig. 2.4, the current density distribution at the turn level in the coil is shown. At lower frequencies, the current distribution is uniform. As expected, at intermediate frequencies, the ring effects lead to an asymmetric current distribution across the cross-sectional area of the turn. Finally, at higher frequencies, the skin effect on the external surface of the turn is clearly evident, as well as proximity and ring effects also modify $\mathbf{J}_{\text{coil}}$.

In Fig. 2.5, the equivalent resistance and inductance of the coil in air are plotted with respect to the excitation frequency. At lower frequencies, both the equivalent resistance and inductance remain relatively constant and show little dependence on the excitation frequency. However, around 1 kHz, an increase in the equivalent resistance and a decrease in the equivalent inductance can be observed. This alteration is associated with changes in the current distribution due to the skin effect. At higher frequencies, the skin effect becomes particularly significant on the outer surface of the coil. As a result, the increase in equivalent resistance becomes more pronounced, while the change in equivalent inductance is less significant. This is because the magnetic energy stored in the

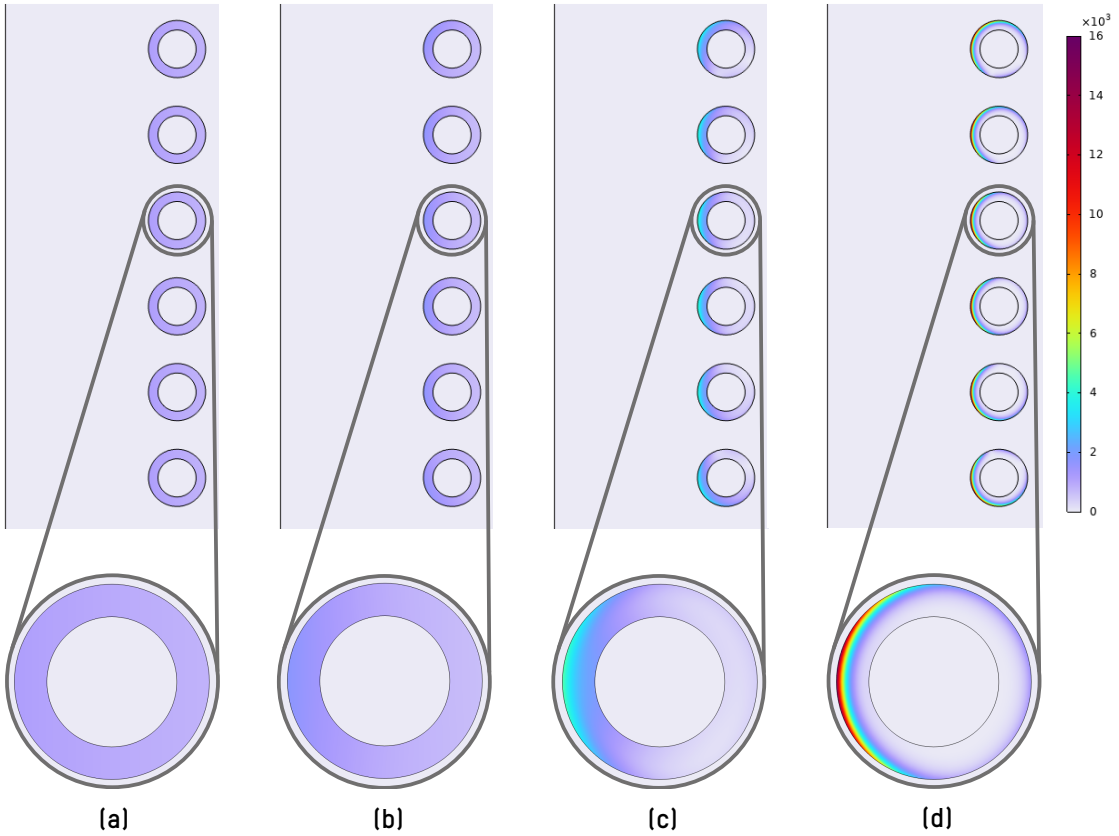

Figure 2.4. Current density in the coil's turn section for different excitation frequency values: (a) 100 Hz, (b) 1 kHz, (c) 10 kHz, and (d) 100 kHz.

system is primarily located in the surrounding air, making the inductance within the cross-section of the coil's turns negligible. Finally, it is important to note that at lower frequencies, where the current distribution is uniform, the equivalent resistance of the coil is determined by its direct current (DC) resistance value. This value can be easily calculated analytically from:

$$R_{\text{dc}} = \rho \frac{l_{\text{coil}}}{S_{\text{turn}}}, \tag{2.16}$$

where ρ is the electrical resistivity inverse of the electrical conductivity ($\rho = 1/\sigma$) and S_{turn} and l_{coil} are the turn's cross-section area and coil's length, respectively. As a result, for the geometry under study, the analytical R_{dc} value is 0.75 mΩ.

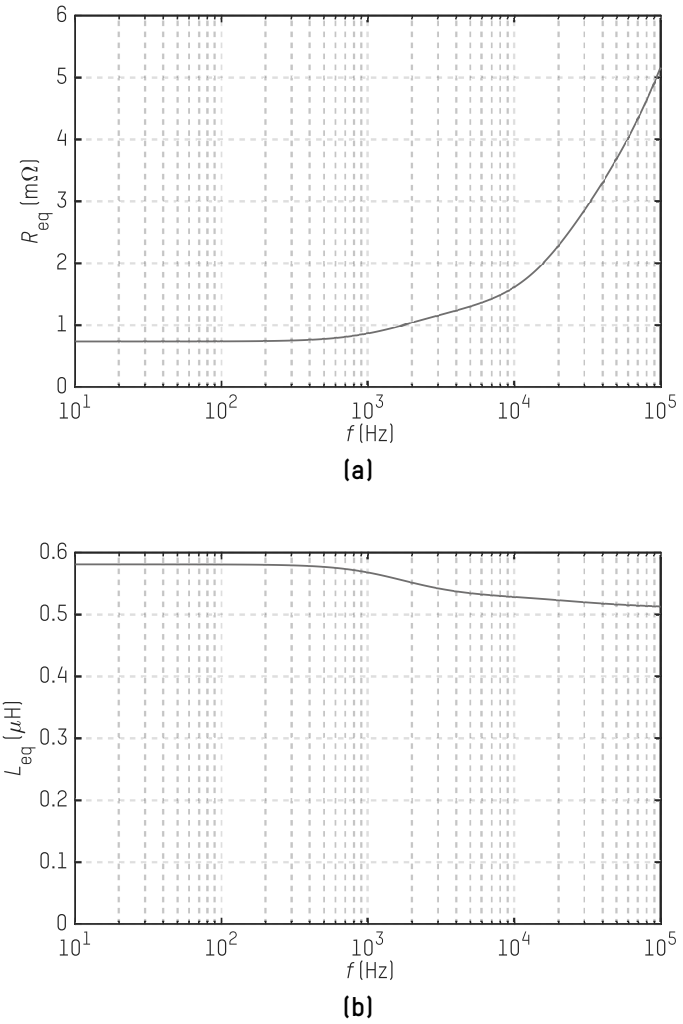

Figure 2.5. Simulated equivalent impedance of the induction coil: (a) equivalent resistance, R_{eq}, and (b) equivalent inductance, L_{eq}.

2.3.1.2 Induction system with linear workpiece material

After analyzing the coil in air, a cylindrical billet is placed inside the copper turns. To address the diffusion equation, (2.3), a crucial step involves discretizing the system's geometry using a mesh. In the case of electromagnetic simulations involving induction loads, there is a rapid exponential variation when the fields enter a conductive material, which is determined by the characteristic distance also known as the penetration depth, δ, [126]. Therefore, it is essential to include several mesh elements that are a fraction of the penetration depth when modeling the induction charge. This requirement leads to a high number of degrees of freedom that need to be solved, resulting in increased computational costs.

The workpiece inside the coil consists of a metallic ferromagnetic material. For illustration purposes, we will select typical linear properties: electrical conductivity $\sigma = 1$ MS/m and relative magnetic permeability $\mu_r = 100$. These values are representative of iron when excited at small signal levels, where the behavior of the induction heating system can be approximated using linear properties. Under these conditions, the penetration depth within the workpiece is significantly smaller than that in the copper of the coil. Therefore, a finer spatial discretization will be applied at the external surface of the workpiece, particularly on the side facing the coil's turns.

The meshing applied to the IH system is illustrated in Fig. 2.6. The coil remains unchanged as shown in Fig. 2.3, while the billet is meshed with a structured grid that becomes noticeably finer in the area corresponding to the skin depth, as detailed in Fig. 2.6. More nodes are concentrated at the outer boundary of the workpiece due to the skin effect, ensuring that there are always at least two layers throughout the penetration depth. The meshing in the workpiece implies a large increase in the computational cost of the simulation, because capturing the rapid variation of the fields inside the workpiece is a challenge to achieve accurate results.

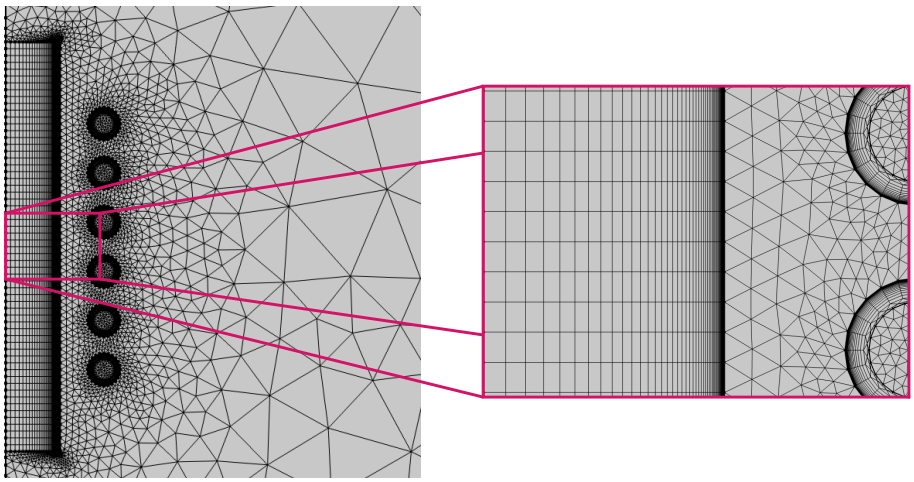

Figure 2.6. Meshing of the IH system including workpiece.

In Fig. 2.7, the simulated equivalent resistance of the complete induction heating system is displayed. As seen in the figure, the equivalent resistance is significantly influenced by the excitation frequency. At higher frequencies, the energy transfer to the workpiece becomes much more effective. Conversely, at low frequencies, the equivalent inductance is greater than the inductance of the coil in air. This increase is due to the high permeability of the load, which enhances the magnetic fields throughout the system. However, as the excitation frequency rises, the induced current densities within the load cause the equivalent inductance to decrease. Both parameters depend on frequency, as is expected in any induction heating system.

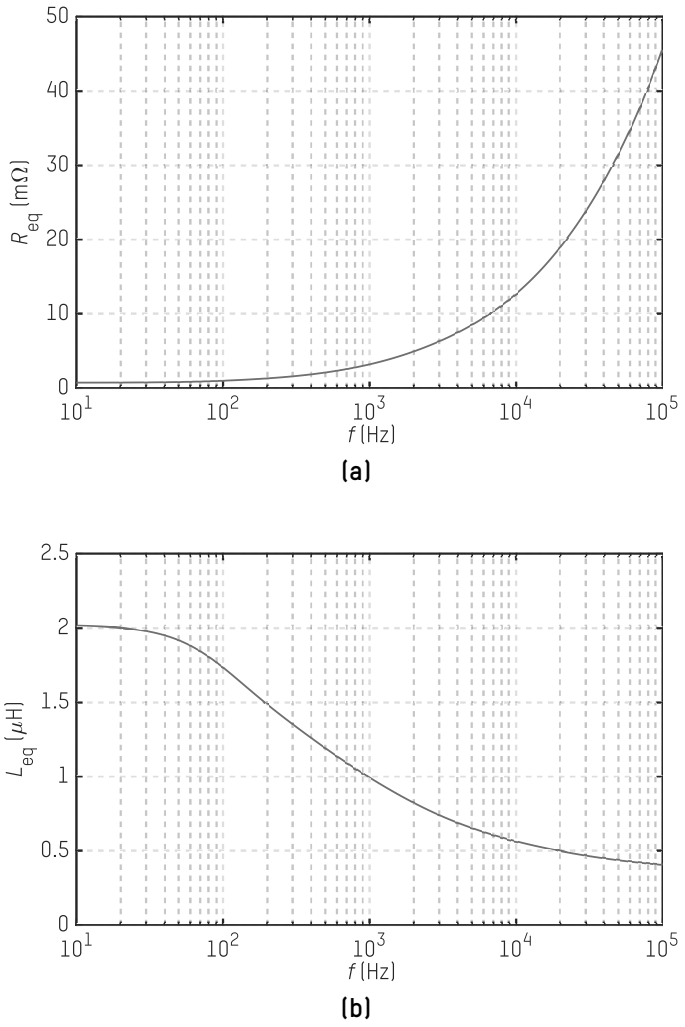

Figure 2.7. Equivalent impedance of the induction load for $\sigma = 1$ MS/m and $\mu_r = 100$: (a) equivalent resistance, R_{eq}, and (b) equivalent inductance, L_{eq}.

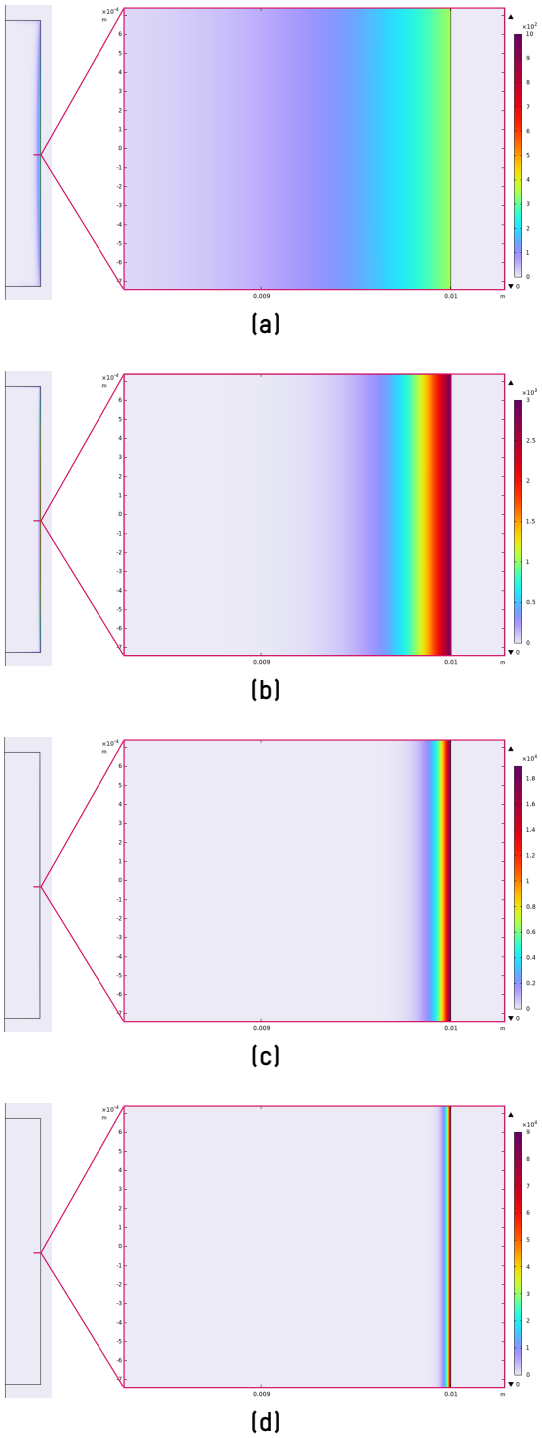

Figure 2.8. Current density in the induction load's vertical cross-section at selected frequencies: (a) 100 Hz, (b) 1 kHz, (c) 10 kHz, and (d) 100 kHz.

The previously mentioned skin effect in the workpiece significantly influences the behavior of the induction heating system. As shown in Fig. 2.8, the current densities concentrate near the surface of the workpiece as the excitation frequency increases. In fact,

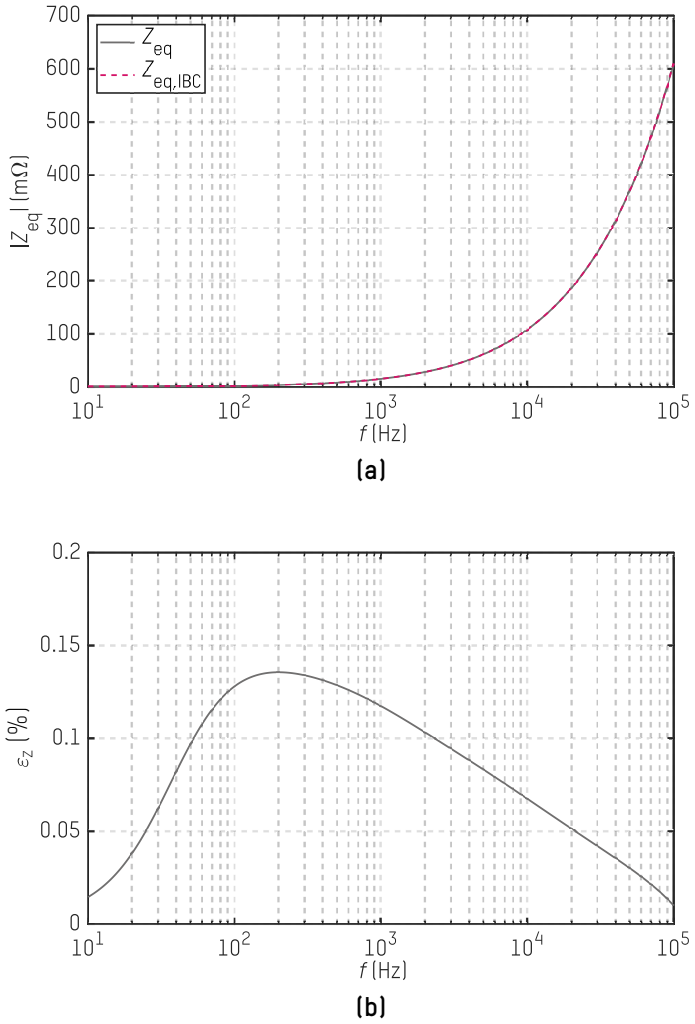

Figure 2.9. Comparison of the simulated induction load's equivalent impedance meshing the billet, Z_{eq}, and using meshless with IBC technique, $Z_{eq,IBC}$: (a) impedance module, and (b) the error between both results.

at typical working frequencies in industrial induction heating systems, which can reach several kilohertz, the current densities can often be modeled as a surface current density. From an electromagnetic perspective, this means that the surface of the workpiece acts as a discontinuous boundary for the fields, effectively causing them to vanish within the material. This behavior can be modeled using the Impedance Boundary Condition (IBC), which establishes a specific relationship between the tangential components of the electric and magnetic fields at the workpiece's surface, [187]. Applying this IBC allows us to avoid meshing within the workpiece, resulting in a significant reduction in computational costs while maintaining a negligible loss of precision in the results. Particularly, when the penetration depth is smaller than the typical dimensions of the system, the accuracy of the simulation using the impedance boundary condition is very high.

Then, a linear Impedance Boundary Condition (IBC) has been implemented to this model.

As recently mentioned, it is imperative to employ more minor mesh elements in regions characterized by significant spatial field variations, particularly evident in induction heating systems near material surfaces. The penetration depth serves as a key metric for field variation. In the pursuit of minimizing computational costs while upholding precision in linear media, the meshing of the workpiece is substituted by a boundary impedance condition at the material's surface, denoted as Z_{IBC}. With this strategy, the abruptly varying fields near the conductor's surface are replaced by the following relationship on the boundary, [161]:

$$\widehat{\mathbf{n}} \times \mathbf{E} = Z_{\text{IBC}} \left(\widehat{\mathbf{n}} \times \mathbf{H} \right) \times \widehat{\mathbf{n}}, \tag{2.17}$$

where $\widehat{\mathbf{n}}$ is the normal vector to the surface, and $\mathbf{E}$ and $\mathbf{H}$ are, respectively, the aforementioned electric and magnetic fields complex amplitudes.

This condition establishes the relationship between the tangential components of the electric and magnetic fields expressed as [161]:

$$Z_{\text{IBC}} = \frac{1+j}{\sigma\delta} \tag{2.18}$$

The aim is to secure the effectiveness of this technique by comparing the IBC model with the complete one. For a general comparison, a relative permeability of 100 and an electrical conductivity of 1 MS/m were set to the steel workpiece. The resulting equivalent impedance is plotted in Fig. 2.9a, comparing the complete model with the IBC. The equivalent impedance error, ε_Z, between both models is computed by means of (2.19) and plotted in Fig. 2.9b.

$$\varepsilon_Z(\%) = 100 \cdot \frac{|Z_{\text{eq}} - Z_{\text{eq,IBC}}|}{|Z_{\text{eq}}|} \tag{2.19}$$

As the frequency increases, the difference between the complete model and the one with IBC diminishes. This happens due to the pronounced skin effect at higher frequencies; the billet's current penetration depth according to frequency is computed by (2.15) and plotted in Fig. 2.10. Therefore, the more eddy currents flow through the boundary, the lesser the error of the IBC model. The error values in Fig. 2.9b are acceptable in line with the reduction in computational cost. In the case of a linear load in electromagnetic analyses, the computational cost is not very large, but the number of degrees of freedom is reduced from 111917 to 32017 employing IBC; corresponding, respectively, to simulation times of 513 seconds comparing with 134 seconds employing IBC.

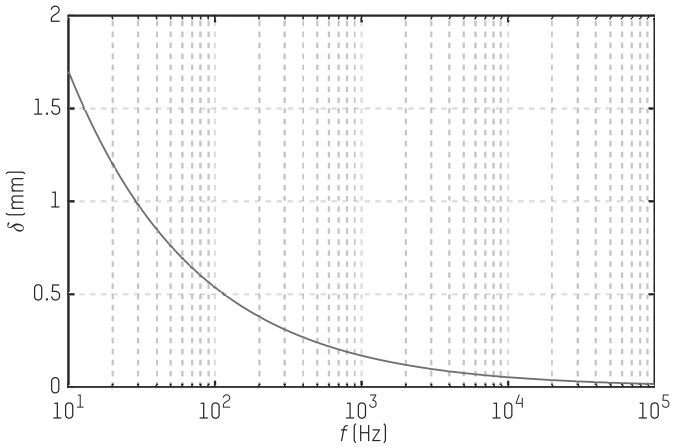

Figure 2.10. Skin depth, δ, in the billet's section for an excitation frequency range according to (2.15).

In conclusion, by using this IBC, it is possible to achieve accurate simulation results while significantly reducing computational costs. Thus, given that the characteristic dimensions of the system are on the order of millimeters, it can be confirmed that the results derived from applying the IBC are accurate.

Additionally, the application of the IBC reveals an important aspect of the behavior of induction heating systems that is related to the physical properties of the load. From the internal structure outlined in the definition of the IBC, it can be observed that the electromagnetic fields outside the workpiece—responsible for determining the equivalent impedance through the integration of the electric field along the coil turns—do not depend independently on the values of electrical conductivity and magnetic permeability. Instead, they are influenced by a single reduced factor, which is the ratio of electrical conductivity to magnetic permeability, σ/μ_{r}. This ratio dependence can be observed in Fig. 2.11.

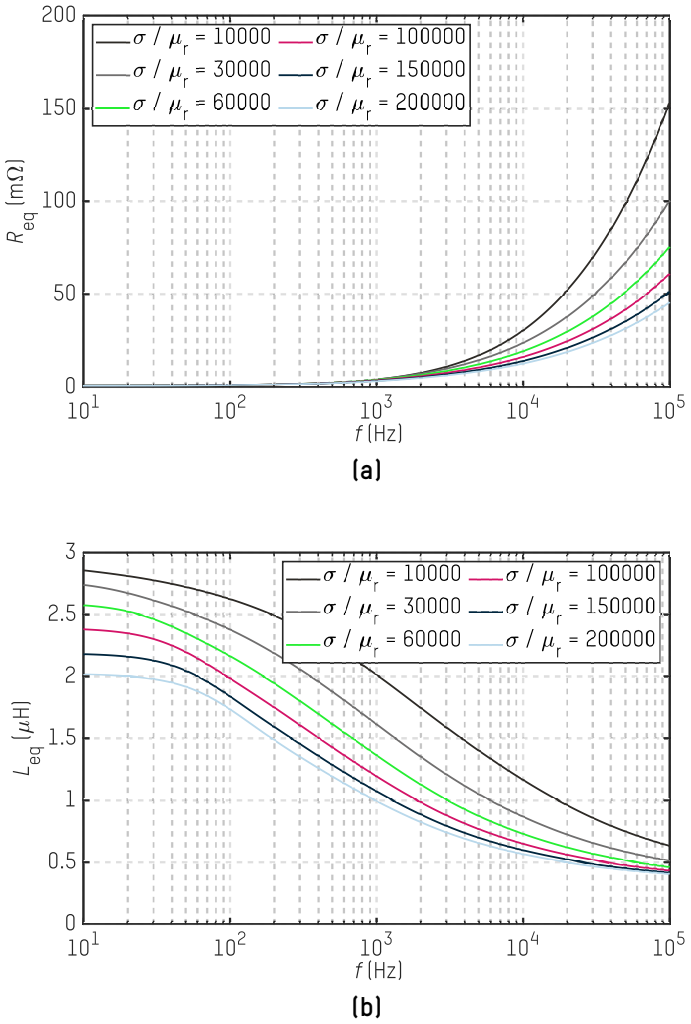

Figure 2.11. Equivalent impedance of the induction load (coil-billet pair) depending on σ/μ_r: (a) equivalent resistance, R_{eq}, and (b) equivalent inductance, L_{eq}.

In Fig. 2.12, the radial power flow on the vertical surface in the billet is plotted for an excitation effective current of 10 mA and different frequencies; it is worth mentioning that the resulting values are very low due to the small-signal excitation. Figure 2.12a shows P_r curves for different frequencies relatively near each other, while in Fig. 2.12b, three distant frequencies are represented in logarithmic scale for the *y* axis. It is concluded that the excitation frequency significantly changes the power flux value, but the profile with respect to the *z* axis is always maintained. As expected, higher power flow is given at the central areas of the billet's surface because the magnetic flux density is higher in such zones.

Moreover, in those figures, the power fluxes simulated with the complete model and employing IBC are compared, and a close agreement is observed.

Figure 2.13 captures the power flux distribution through the superficial area of the billet for the frequencies used in Fig. 2.12b. No difference is observed between the fully meshed

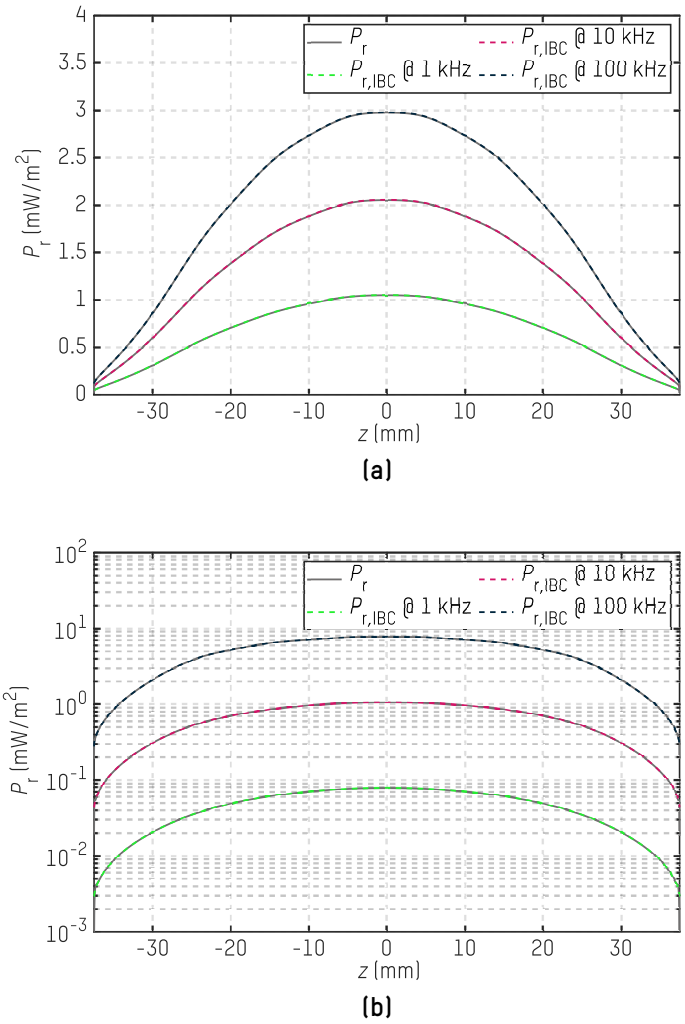

Figure 2.12. Comparison of the simulated radial power flow through the billet's vertical surface meshing the whole workpiece at, P_r, vs. employing IBC technique, $P_{r,IBC}$, for frequencies: (a) 10, 20 and 30 kHz, and (b) 1, 10, and 100 kHz with logarithmic scale on the y axis.

model and the IBC one.

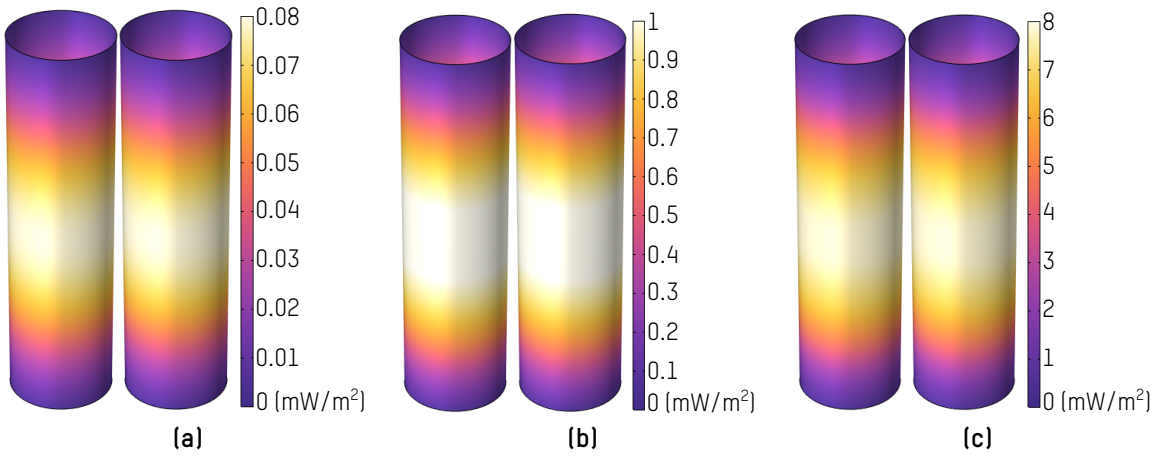

Figure 2.13. Comparison of the simulated radial power flow, P_r, in through the billet's vertical surface meshing the whole workpiece (left) vs. employing IBC technique (right) for frequencies: (a) 1 kHz, (b) 10, and (c) 100 kHz.

2.3.2 Heat Transfer Modeling

The induction heating process delivers high power density to specific workpiece surface areas, resulting in significant temperature gradients. Additionally, heat capacity values play a crucial role in influencing temperature distribution since they relate to the amount of energy required to raise the temperature at each point, as well as the energy needed to increase the temperature of the entire workpiece. Therefore, accurately modeling the transient behavior of temperature requires considering both thermal conductivity and heat capacity, as they are essential factors.

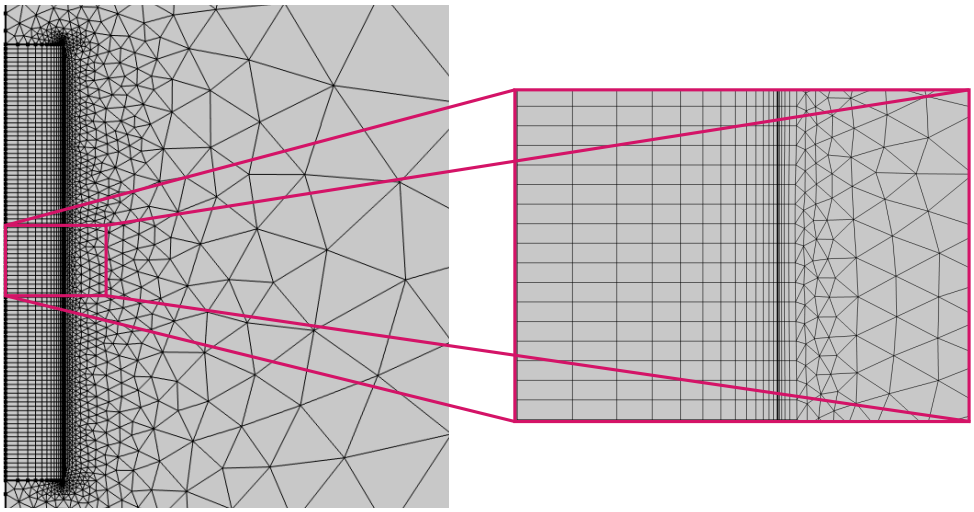

Figure 2.14. Workpiece thermal model meshing.

The spatial dependence of the thermal phenomenon is smooth compared to the electromagnetic one, so a less dense meshing can be used in that case, as can be seen in

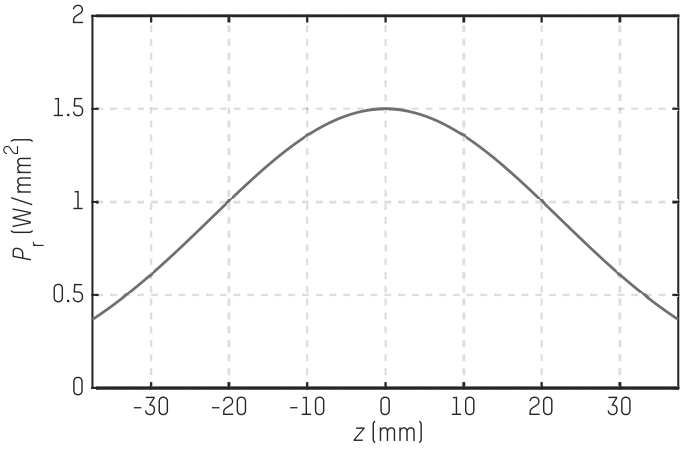

Figure 2.15. Gaussian bell-shaped input surface power flow.

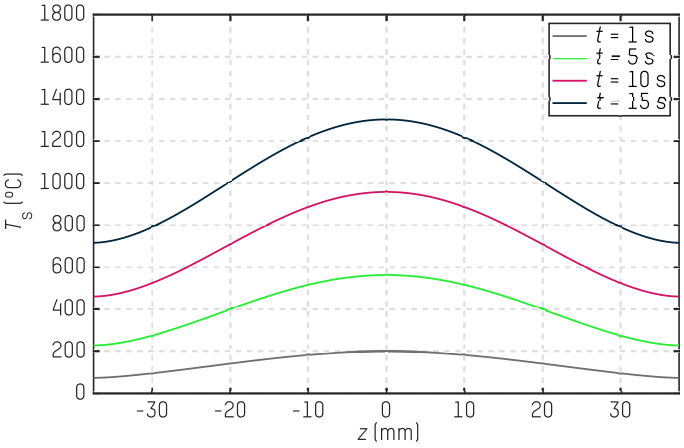

Figure 2.16. COMSOL®-based temperature distribution through the billet's vertical surface at different time instants for the reference model with $c_p = 400$ J/kg·°C and $k = 40$ W/m·°C.

Fig. 2.14. In this system, 5727 degrees of freedom are sufficient to obtain accurate results. The transient simulation of a thermal process lasting 15 seconds takes approximately 5 seconds.

A single thermal system is modeled in a transient study, departing from a vertically distributed radial power flow, P_r, in the curved surface of the billet. Regarding the previously simulated radial power flows, bell-shaped surface power flows are obtained; therefore, the power distribution in this thermal simulation is modeled as a Gaussian equation described in (2.20).

$$P_r(z) = P_{r,pk} e^{-z^2/\sigma}, \tag{2.20}$$

where $P_{r,pk}$ is the maximum value of the Gaussian bell and σ is the spatial standard deviation. The values given to each of them are 1.5 W/mm^2 and 1 mm, respectively. The power distribution profile imposed by this equation (2.20) is displayed in Fig. 2.15. Therefore, the

steel billet is heated with a power of around 4.5 kW, which is a typical value in an industrial induction heating system employing light loads.

This thermal study was realized to understand the effect of the specific heat capacity, c_p, and thermal conductivity, k, effects of the material. For this purpose, some different cases were simulated, varying those two parameters. As a reference model, constant $c_p = 400$ J/kg·°C and $k = 40$ W/m·°C are selected, respectively. Figure 2.16 depicts the billet's vertical surface temperature evolution for this reference model; temperature curves throughout the z axis are plotted for different time instants.

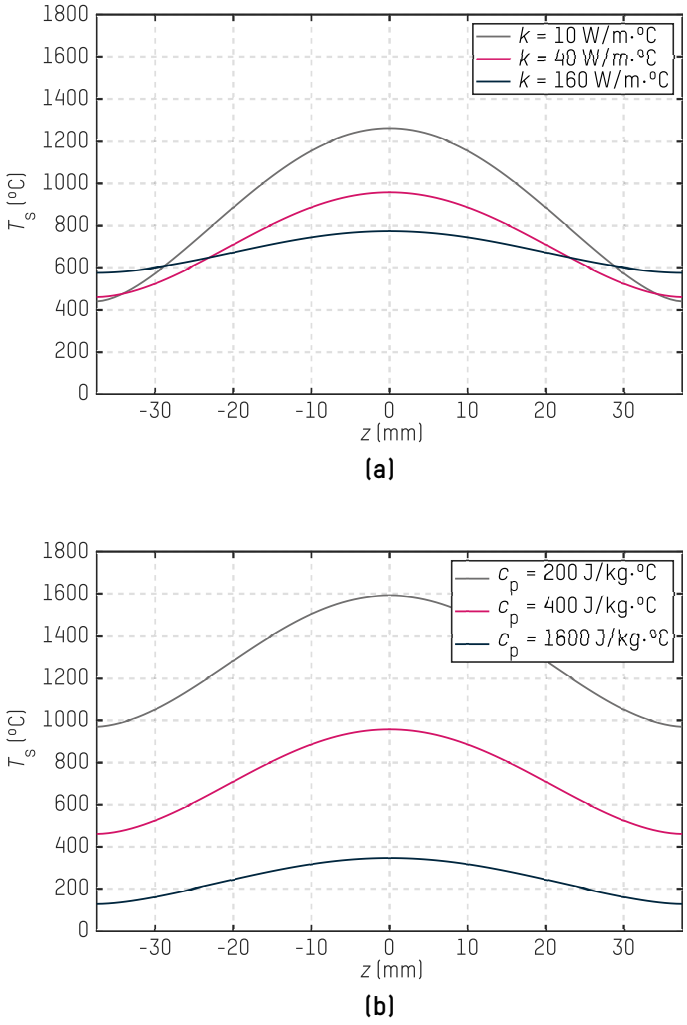

Figure 2.17. COMSOL®-based temperature distribution through the billet's vertical surface, at $t = 10$ s for different c_p-k combinations: (a) constant $c_p = 400$ J/kg·°C, and (b) constant $k = 40$ W/m·°C.

The bell-shaped temperature distribution through the billet's superficial z axis is observed in this Fig 2.16, which is strictly linked to the input heat source shape in Fig 2.15.

Then, some other cases are compared in Fig. 2.17, where different models' temperatures are plotted for a specific time instant. First, maintaining the heat capacity constant

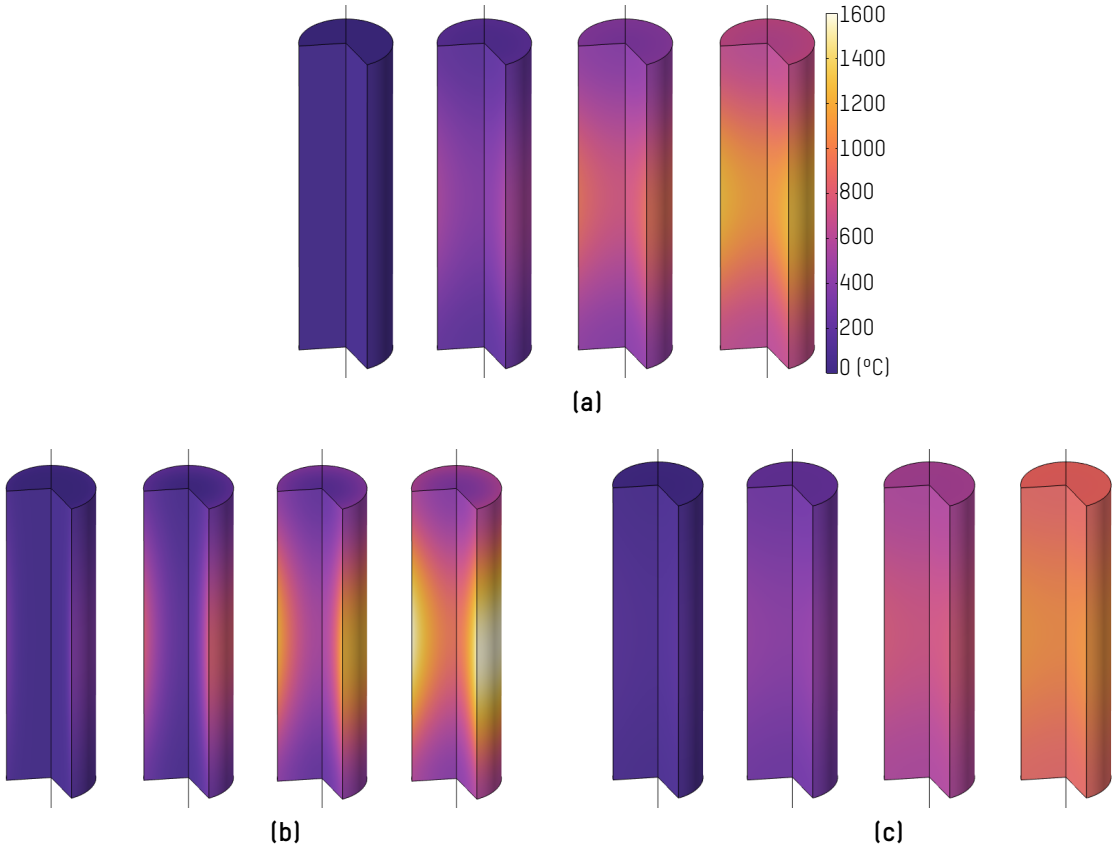

Figure 2.18. COMSOL®-based temperature distribution in the billet, respectively, at selected times t = 1, 5, 10, and 15 s for $c_p = 400$ J/kg·°C and different k combinations: (a) $k = 40$ W/m·°C, (b) $k = 10$ W/m·°C, and (c) $k = 160$ W/m·°C.

and varying the thermal conductivity parameter; then, vice versa, maintaining k as in the reference model and varying c_p. Some simulation results of the mentioned models are presented in the next lines.

Figure 2.17a shows three cases that notably vary the thermal conductivity value. For lower k values, the material shows more resistance to heat conduction, so more heat is accumulated in the central areas of the billet, exactly where more power flow is applied; the heat gradient through the billet's vertical surface becomes higher. This happens because lower thermal conductivities entail accumulating more heat in the heat source areas, making it more difficult to circulate such heat. The temperature at the extremities of the billet is higher for the model with a quarter of the thermal conductivity value, while its peak temperature is higher. Instead, with higher conductivity values, the temperature tends to be more uniform throughout the billet's vertical surface.

On the other hand, in Fig. 2.17b, the specific heat capacity, c_p, value is varied, maintaining the thermal conductivity constant. Therefore, it is clearly seen that when the heat capacity of the material increases significantly, much more power is needed to heat the billet. Multiplying the heat capacity by four times shows that the heat source is not strong enough to elevate the temperature of the billet's surface.

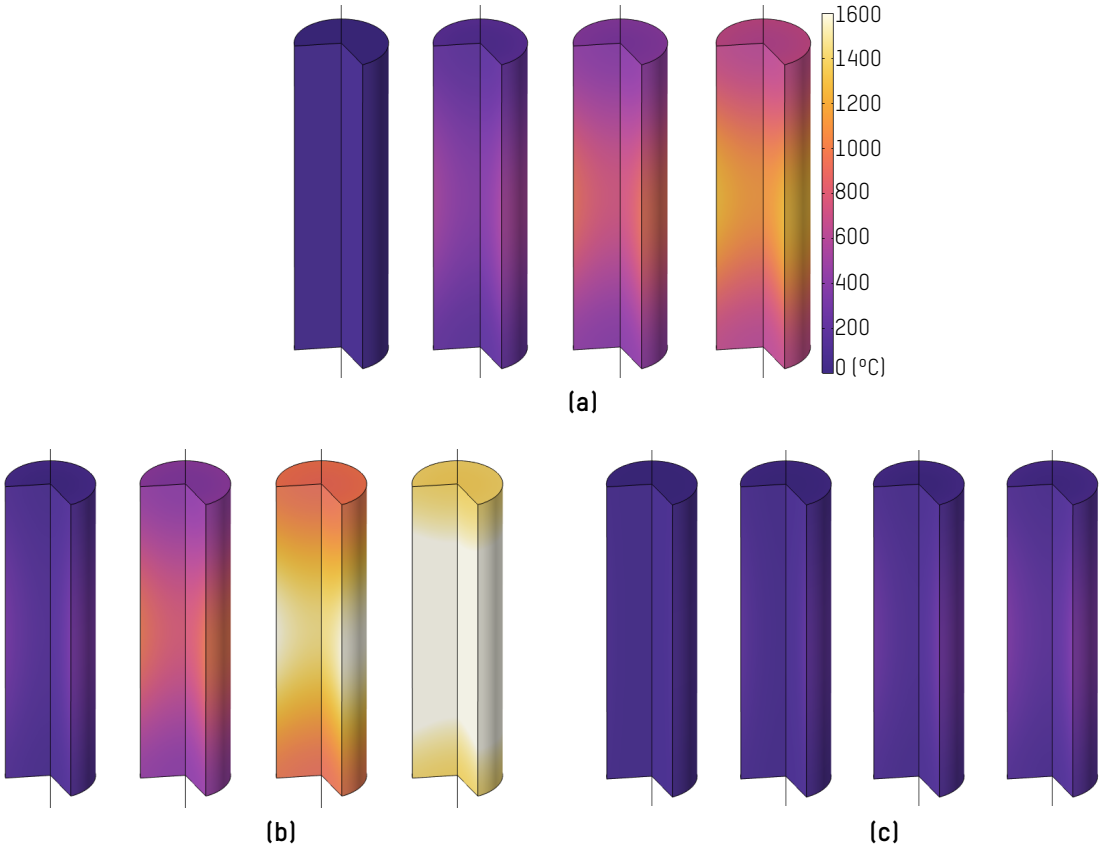

Figure 2.19. COMSOL®-based temperature distribution in the billet, respectively, at selected times t = 1, 5, 10, and 15 s for $k = 40$ W/m·°C and different c_p combinations: (a) $c_p = 400$ J/kg·°C, (b) $c_p = 200$ J/kg·°C, and (c) $c_p = 1600$ J/kg·°C.

In Fig. 2.18 and Fig. 2.19, the same information is displayed in a different format. Temperature distribution on the billet's surface is depicted for different time instants in a more visual way. The same conclusions are extracted, seeing the same effect of varying c_p and k values. Moreover, in those figures, not only is the heat's vertical distribution shown, but also how it penetrates the billet's cross-section, again obtaining the same conclusions.

2.3.3 Electromagnetic-Thermal Simulation Model

Now, the recently described models are coupled in COMSOL Multiphysics® tool; a coupled electromagnetic-thermal model is developed. For that purpose, the frequency-transient study domain is simulated.

The coil is excited with a sinusoidal current of 400 A rms and 10 kHz, thus heating the steel billet with about 5 kW; 15 seconds are needed to reach around 1400 °C at the hottest point of the billet. The material does not saturate, so the temperature continues to increase, resulting in such a high temperature; indeed, all the electromagnetic and thermal parameters are assumed linear and the same as employed in the previous single models, exactly, relative permeability of $\mu_r = 100$, electrical conductivity of $\sigma = 1$ MS/m, heat

capacity of $c_p = 400$ J/kg·°C, and thermal conductivity of $k = 40$ W/m·°C.

In Table 2.2, electrical equivalent parameters, resistance and inductance, are computed comparing the meshed-billet model and the one employing IBC. As the material is assumed linear, there is no dependence on current envelope and temperature, so they are maintained constant during the whole process. Instead, they do depend on the excitation frequency, these values are computed for a frequency of 10 kHz. The error between the completely meshed and the impedance boundary models is very little, so that the IBC use is legitimate when simplifying the model.

Table 2.2. Comparison of electrical parameters between simulation models for $f = 10$ kHz.

Electrical parameter	Meshed model	IBC model	Error
R_{eq}	33.1 mΩ	33.2 mΩ	0.3 %
L_{eq}	1.6393 μH	1.6403 μH	0.03 %
$\lvert Z_{eq}\rvert$	108.2 mΩ	108.3 mΩ	0.09 %

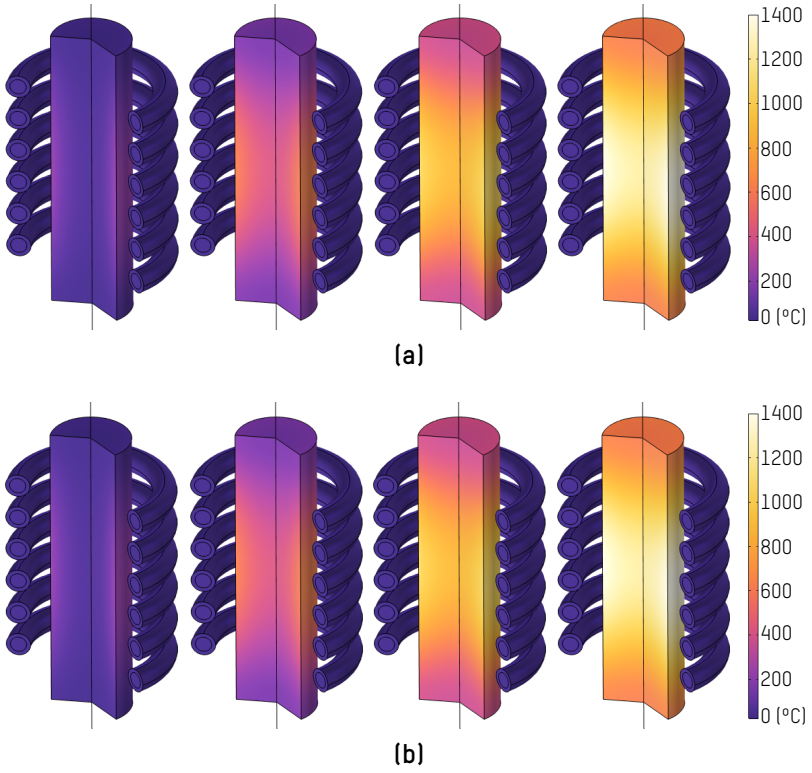

Figure 2.20. COMSOL®-based temperature distribution through the billet at $t = 1$, 5, 10, and 15 s: (a) meshed billet for the electromagnetic simulation vs. (b) meshless IBC for the electromagnetic simulation.

In Fig. 2.20, the simulated temperature distribution through the billet is captured during the transient process of 15 seconds. Comparing at a glance the meshed billet model for the electromagnetic simulation with the one using IBC, no significant differences are

observed. Note that meshing inside the load is required for the thermal simulation in both cases.

Moreover, this Fig. 2.20 is represented in Fig. 2.21 with linear plots; again reinforcing the conclusion that the IBC model is taken as a good alternative to reduce the degrees of freedom. Furthermore, the same affirmation is made according to Fig. 2.22; as the material is modeled with linear properties, the power flow in the superficial boundary of the billet is maintained constant during the heating process.

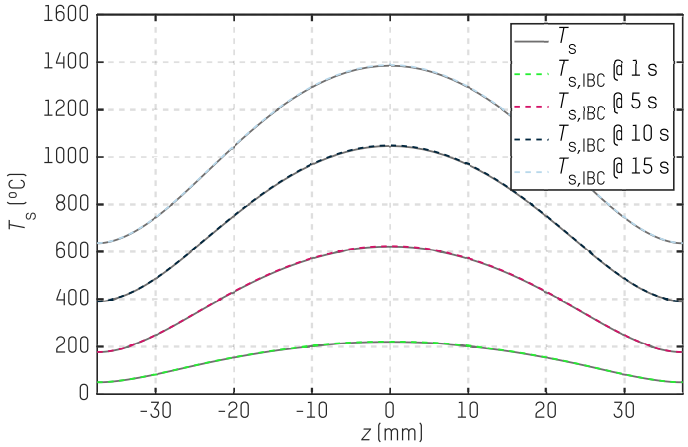

Figure 2.21. COMSOL® -based temperature distribution in the billet's vertical surface, T_s, at different time instants for the coupled electromagnetic-thermal model with linear material properties.

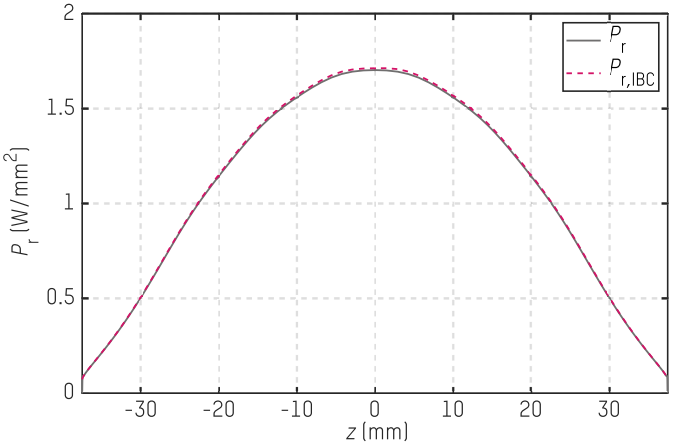

Figure 2.22. COMSOL® based power flow distribution through the billet's vertical surface, P_r, at different time instants for the coupled electromagnetic-thermal model with linear material properties.

2.4 Electromagnetic-Thermal Model with Nonlinear Properties Workpiece

2.4.1 Description of the Induction Load

The inductor-workpiece system under analysis has the exact geometrical dimensions as in Table 2.1. The current flows through a solenoid-shaped coil of 6 turns of radius 18 mm, spaced 9 mm apart. Copper tubing has been used in its construction to allow liquid cooling by circulating water so that at all times, its operating temperature is guaranteed to be below the boiling point of water. The copper tube has an outer diameter of 6 mm and an inner diameter of 4 mm. The metallic part to be heated consists of a 42CrMo4 - AISI 4140 steel cylinder of radius 10 mm and length 75 mm.

42CrMo4 steel is a low-alloy, high-strength steel that is extensively utilized in various industrial metallurgical processes due to its exceptional adaptability to multiple treatment options before machining different parts and components. This alloy is characterized by its favorable mechanical properties, making it suitable for applications that require durability and toughness, [176].

The widespread use of 42CrMo4 steel in the industrial sector is further reinforced by a substantial body of research that examines its behavior under various conditions. Numerous publications have emerged, detailing the findings of studies conducted on this material, which have contributed to a deep understanding of its characteristics and performance, [153].

Research has addressed different aspects of 42CrMo4 steel, including its heat treatment methods, fatigue resistance, and overall mechanical performance, [175]. This extensive characterization under diverse working conditions allows engineers and researchers to predict how this steel will perform in practical applications, providing valuable insights for its utilization in design and manufacturing.

Physical properties of 42CrMo4 - AISI 4140 steel can be found in the literature. The temperature of the material considerably influences all the physical properties of importance; however, the disappearance of the magnetic properties from the Curie temperature, $T_C = 783$ ºC, which is reflected, in turn, in a substantial variation of the thermal capacity of the material, stands out especially. From the analytical expression of the BH-curve with respect to temperature presented in [162], it is straightforward to apply the methodology proposed in [161] to obtain the equivalent magnetic permeability of the material with respect to field and temperature.

In summary, the combination of extensive research, comprehensive characterization, and effective processing methods, particularly through induction heating, highlights the importance of 42CrMo4 steel in advancing mechanical engineering practices and optimizing the performance of components used in a wide range of industrial applications.

2.4.2 Physical Properties of 42CrMo4 Steel

Given its notable properties and the depth of knowledge available, 42CrMo4 steel presents significant potential for processing through induction heating. This innovative technique allows for precise temperature control and rapid heating, which can lead to various heat treatment processes designed to optimize its mechanical behavior. Induction heating treatments can improve hardness, strength, and tire resistance, making 42CrMo4 steel even more desirable for applications in demanding environments.

In the metalworking industry, 42CrMo4 carbon steel is extensively used, but manufacturers do not usually provide complete information about its physical and mechanical properties, which are often given at ambient temperature. Even though, in [153] and [169], the temperature-dependent parameters can be found under certain conditions of interest. An adequate characterization of the characteristics of the load is needed for proper modeling of the hardening process due to the high temperature reached. The high-temperature level involved in this kind of process entails relevant changes in the material properties.

2.4.2.1 Electromagnetic properties

In a first step, the characterization of the magnetic properties of the material at elevated temperature levels is a complex task, but it plays an essential role in the complete modeling of the load. Some research have dedicated large efforts to gaining expertise in this kind of measurements, [153], [155]. The characteristics measured in those works correspond to the temperature-dependent BH-curve, neglecting the hysteresis effects in order to simplify the analysis. The BH-curve strongly influences the load modeling due to the presence of nonlinearity, in particular, associated with magnetic saturation, which implies a dependence on the coil current level.

Several anhysteretic equations have been proposed in literature to model the nonlinearities of the magnetic properties, describing the magnetic flux density B depending on the magnetic field H and billet's temperature T. The comparison of those models is realized in Appendix A.

One of the most used model in literature to model nonlinear induction loads is the Analytic Saturation Curve (ASC) in (2.21), which was first proposed in [162]. This magnetic characteristic equation combines the analytic saturation curve in (A.8) with exponential function of temperature in (A.12), representing both nonlinearities.

$$B(H,T) = \mu_0 H + \frac{2B_s}{\pi} \arctan\left(\frac{\pi \mu_{r,i} \mu_0 H}{2B_s}\right)\left(1 - e^{(T-T_C)/C}\right) \tag{2.21}$$

where B is the magnetic flux density, H is the magnetic field, T is the temperature of the sample, μ_0 is the vacuum permeability, B_s is the saturation field, $\mu_{r,i}$ is the initial relative permeability, T_C is the Curie temperature of the material, and C is a factor controlling the temperature dependence of the magnetic properties.

The BH-curves depicted in Fig. 2.23 are obtained by the expression given in (2.21) with coefficients fitted to experimental results provided in [153]. Coefficients for fitting the BH-curves at different temperatures of 42CrMo4 steel are magnetic saturation, $B_s = 1.32$ T,

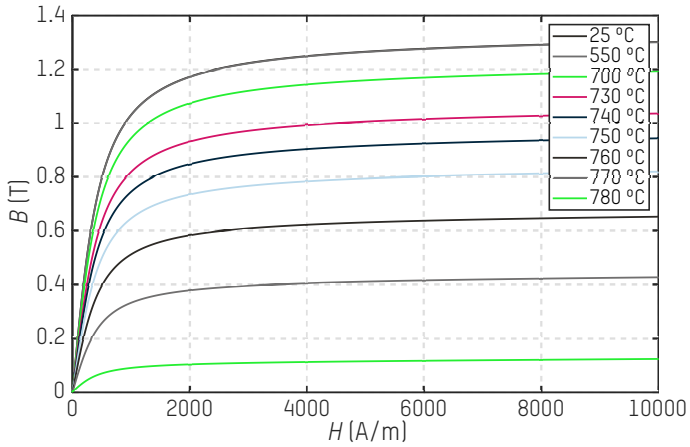

Figure 2.23. BH-curves of 42CrMo4 steel at different temperatures.

initial permeability, $\mu_{r,i} = 1860$, Curie temperature, $T_C = 783$ °C, and factor controlling the temperature dependence, $C = 33.6$ °C, taken from [127].

On the other hand, the selected material is a good electrical conductor, whose temperature-dependent resistivity is given by [153]:

$$\rho(T) = \begin{cases} 1.026\rho_r + 1.4 \cdot 10^{-3} T - 1.3 \cdot 10^{-3} T\rho_r - 0.028, & 20\ °C < T < 800\ °C \\ 3.8 \cdot 10^{-4} T + 0.785, & 800\ °C \leq T < 1200\ °C \end{cases} \tag{2.22}$$

where ρ_r is the specific electrical resistivity at 20 °C of the 42CrMo4 material (0.212 $\mu\Omega$·m), T is the temperature of the material, and $\rho(T)$ is expressed in $\mu\Omega$·m.

Figure 2.24 shows the electrical conductivity of the material obtained by computing the inverse function of (2.22).

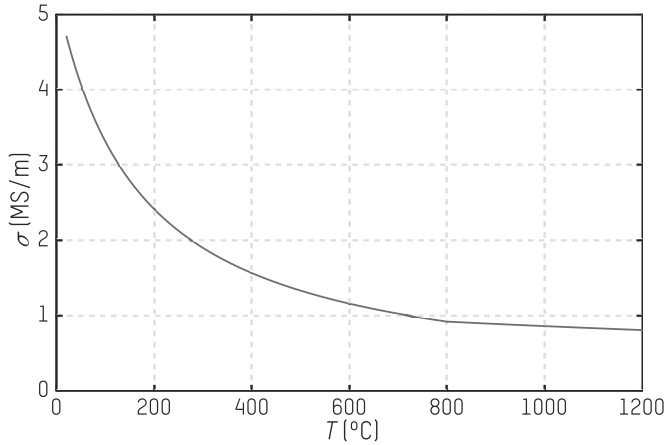

Figure 2.24. Temperature-dependent electrical conductivity in MS/m of 42CrMo4 steel.

There are several studies in the literature that relate the electrical resistivity (at ambient temperature) to the material's chemical composition. For example, [188] proposes an

equation to compute this ambient resistivity depending on the chemical composition of low-carbon steel. However, [168] highlights the effects of carbon, aluminum, and nickel on the resistivity, which are not considered in the former model. Finally, [153] proposes other composition-proportional relation for the 42CrMo4 steel in $\mu\Omega$·m:

$$\begin{aligned}\rho_{\mathrm{r}} = {} & 0.0011 + 0.0283\mathrm{C} + 0.17\mathrm{Si} + 0.0387\mathrm{Mn} - 0.1295\mathrm{S} + 0,0702\mathrm{Al} \\ & +0.0272\mathrm{Cr} + 0.0335\mathrm{Cu} + 0.0333\mathrm{Mo} + 0.0193\mathrm{Ni},\end{aligned} \tag{2.23}$$

where the chemical composition is summarized in Table 2.3.

Table 2.3. Chemical composition of 42CrMo4 steel in wt.-%, [153].

C	Si	Mn	P	S	Cr	Ni	Mo	Sn	Al
0.425	0.309	0.702	0.019	0.013	1.014	0.098	0.198	0.013	0.021

2.4.2.2 Thermal properties

According to the heat conduction (2.14) described at the beginning of this chapter, the complete electromagnetic-thermal modeling also needs to include the thermal properties of the material, namely the thermal conductivity, k, and the heat capacity, c_{p}. The temperature-dependent k and c_{p} parameters for 42CrMo4 steel are obtained from [169] and plotted in Fig. 2.25 and Fig. 2.26, respectively. In both cases, the parameters increase around Curie temperature due to the influence of the phase transition in the material, which is also associated with the structural changes in the hardening processing. The effect of the phase transition mainly affects the heat capacity; therefore, more power has to be provided to increase the temperature around this point.

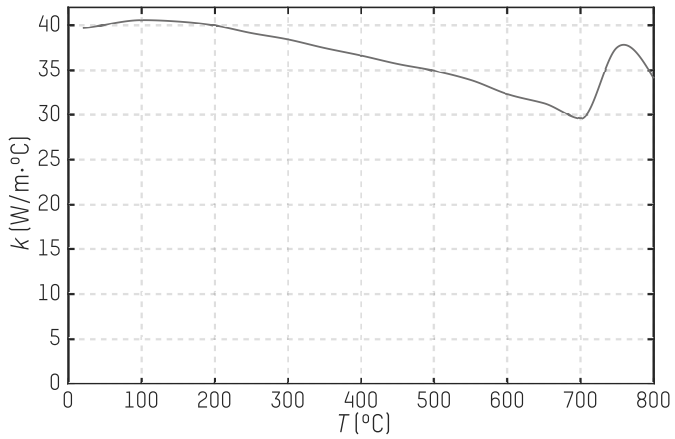

Figure 2.25. Temperature-dependent thermal conductivity of 42CrMo4 steel.

Moreover, convection and radiation heat fluxes, q_{conv} and q_{rad}, might be considered as they are the reason for dissipating part of the heat. The convection coefficient, h, of

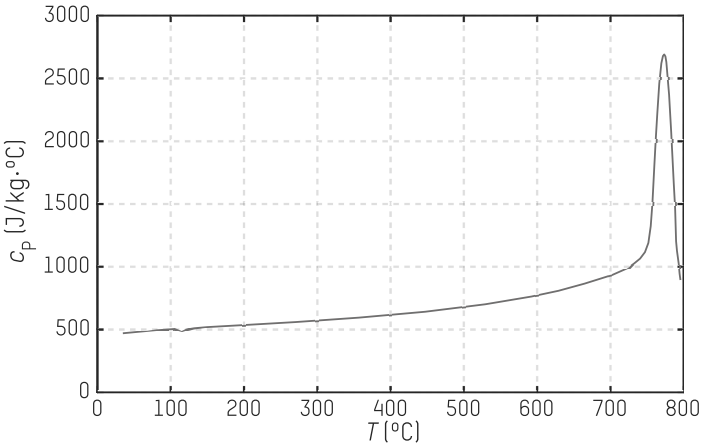

Figure 2.26. Temperature-dependent heat capacity of 42CrMo4 steel.

42CrMo4 steel is determined in [134] and [189], where a value of 10 W/m^2·ºC is given. The emissivity is also assumed constant and is taken from [190]. In this work, the emissivity of AISI 4140 steel is modeled considering the view factor and depending on the ratio of workpiece radius to the inner radius of castable refractory, and an approximate value of $\varepsilon = 0.4$ has been chosen. It is worth mentioning that this value changes while the workpiece changes its surface color with high temperatures, but it has been assumed to be constant throughout the whole heating process.

2.4.3 Nonlinear Electromagnetic Model

The electromagnetic modeling of a nonlinear load is a very complex task due to the BH-curve saturation, but to facilitate the processing, a nonlinear impedance boundary condition has been adopted. This condition allows the replacement of a domain with a boundary with special properties. Therefore, the mesh inside the billet is not required for the electromagnetic analysis, see Fig. 2.27, and the computational cost is simplified as mentioned in the previous analysis.

As mentioned in the previous point, the Impedance Boundary Condition (IBC) is commonly employed to lower the computational cost of electromagnetic simulations in induction heating systems. Generally, this approach yields highly accurate results when the system's characteristic dimensions exceed the penetration depth, δ. This δ is influenced by the physical properties of the workpiece, specifically its electrical conductivity and magnetic permeability, along with the operating frequency, which typically measures a few tens of micrometers. Thus, given that the characteristic dimensions of the system are on the order of millimeters, it can be confirmed that the results derived from applying the IBC are accurate.

Furthermore, because the magnetic properties of the material are significantly nonlinear, an equivalent permeability that depends on temperature and magnetic field strength has been developed. This equivalent permeability, μ, is incorporated into the COMSOL® sim-

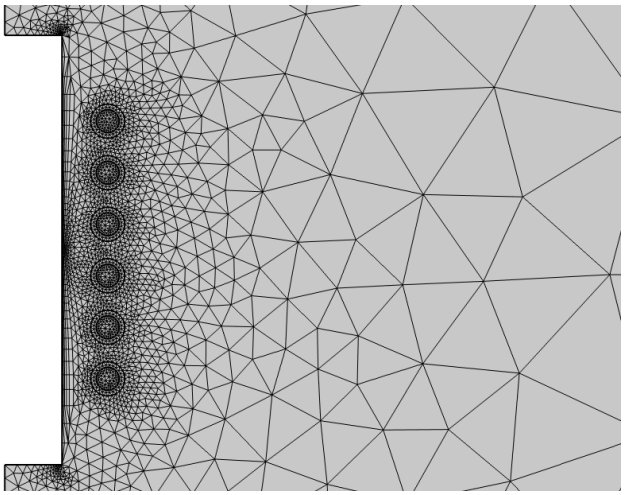

Figure 2.27. Frequency-domain mesh of the entire induction heating system in the axisymmetric two-dimensional geometry with Impedance Boundary Condition (IBC).

ulation following the procedure outlined in the paper [161]. This procedure has also been described for a practical COMSOL® simulation in the paper [191]. The equivalent permeability is obtained by solving the simple one-dimensional equation of magnetic field diffusion within the material.

Figure 2.28 shows the induction heating system's equivalent resistance and inductance values depending on the excitation current's level. In this analysis, the 42CrMo4 steel's properties were introduced; first, obtaining the equivalent magnetic permeability based on this material's anhysteretic BH-curve in Fig. 2.23, then, directly inserting the electrical conductivity value, σ. Regarding the equivalent resistance and inductance simulated, respectively, in Fig. 2.28a and Fig. 2.28b, it is clearly concluded that both parameters decay while the current envelope – field level – increases. This is the reflection of the material's BH property in Fig. 2.23, as the magnetic field, *B*, increases with magnetic flux density, *H*, until the steel saturates. Therefore, the relative magnetic permeability, μ_r, decreases to unity after saturation.

Moreover, in Fig. 2.29, the simulated radial power flow through the billet's vertical boundary is depicted for various current envelopes. The profile is again maintained, and the peak amplitude changes with the value of the exciting current. The power induced in the billet increases with the field level even if the equivalent impedance drops.

2.4.4 Complete Nonlinear Electromagnetic-Thermal Model

As mentioned at the beginning of this Chapter 2, every induction heating process is a combination of three physical phenomena: electromagnetism, heat transfer, and metallurgy. This thesis focuses on the first and second problems. The electromagnetic analysis has already been done in the previous pages. Now, the thermal simulation will be coupled to the electromagnetic one, including the material's nonlinear behavior.

In contrast to the electromagnetic model in Fig. 2.27, the billet mesh is captured in

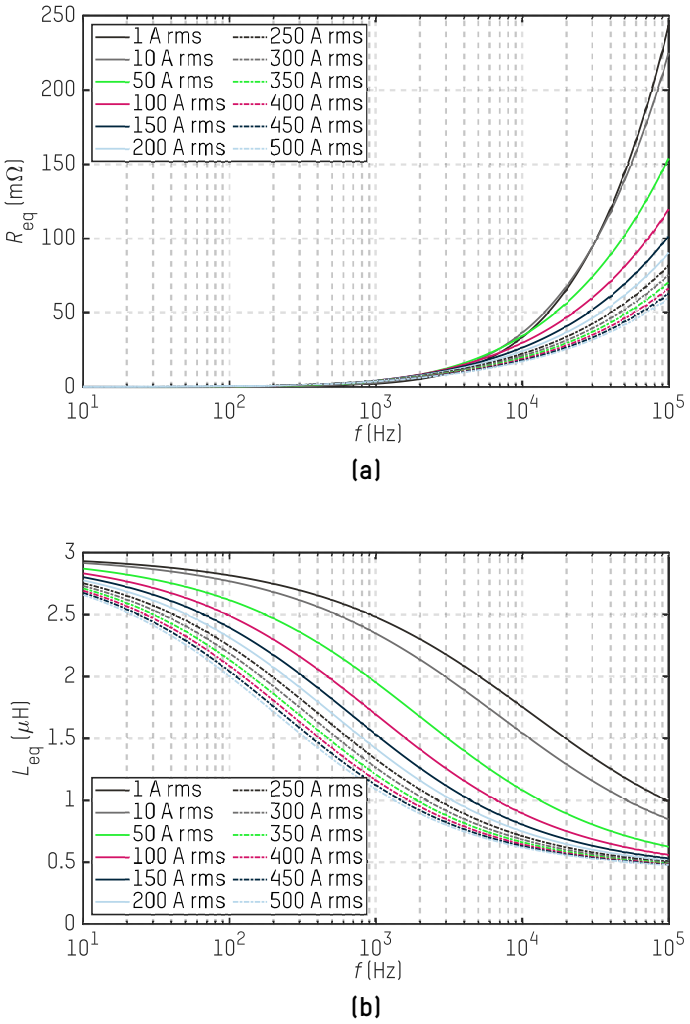

Figure 2.28. Simulated equivalent impedance of the nonlinear induction load (coil-billet pair) under different excitation effective current values: (a) equivalent resistance, R_{eq}, and (b) equivalent inductance, L_{eq}.

Fig. 2.30 for the thermal simulation. This mesh is not so critical as in the electromagnetic analysis, as the dynamics of the thermal nature is slower. Therefore, the complete billet can be meshed with fewer elements that do not involve large computational costs.

According to material properties, the equivalent magnetic permeability is computed by combining the magnetic field and temperature dependencies as expressed in (2.21). The temperature-dependent electrical conductivity is also inserted as the inverse of (2.22). Furthermore, thermal conductivity and heat capacity datasets are included, respectively, from Fig. 2.25 and Fig. 2.26. Finally, the billet's surface heat convection and radiation are modeled; due to the high-power density levels transferred to the load by the induction process, the power losses of the two preceding phenomena have a moderate impact on the final results.

In addition, copper tubing has been used in the construction of the coil to allow liquid

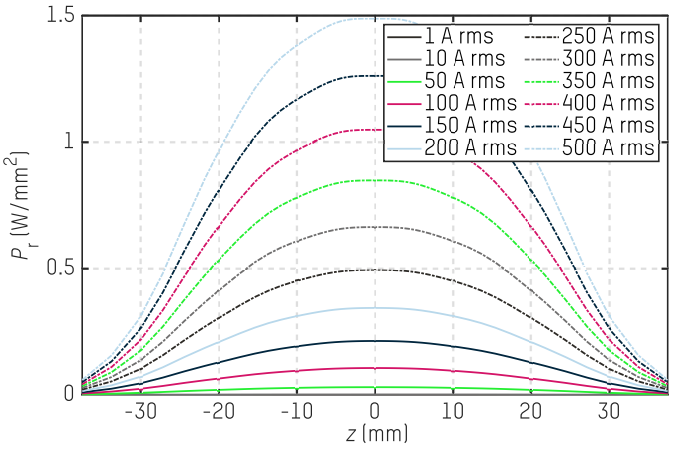

Figure 2.29. Simulated radial power flow, P_r, through the billet's vertical surface at 10 kHz for different current envelopes.

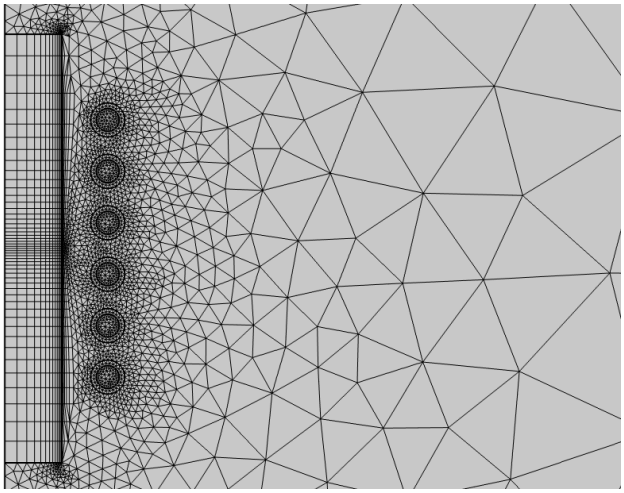

Figure 2.30. Thermal transient simulation mesh of the entire induction heating system.

cooling by circulating water so that at all times, its operating temperature is guaranteed to be below the boiling point of water.

The electromagnetic modeling is performed in the frequency domain, and the thermal modeling is done in the time domain to capture the transient behavior of the load. Both types of simulations can be coupled using two COMSOL Multiphysics® modules. In [192], [193], the complete electromagnetic-thermal modeling of the induction load under study was presented.

2.4.4.1 Simulation procedure

The transient electromagnetic-thermal simulation can be initialized either with fixed values or with an initial electromagnetic simulation. In this case, an initial simulation is realized to define the initial condition of the magnetic field.

This first simulation consists of a frequency-domain study with the same current amplitude and frequency values that will be employed in the induction heating simulation process. There is no heating at all; the initial electromagnetic parameters are computed for the ambient temperature. This initial study is performed in less than 10 seconds.

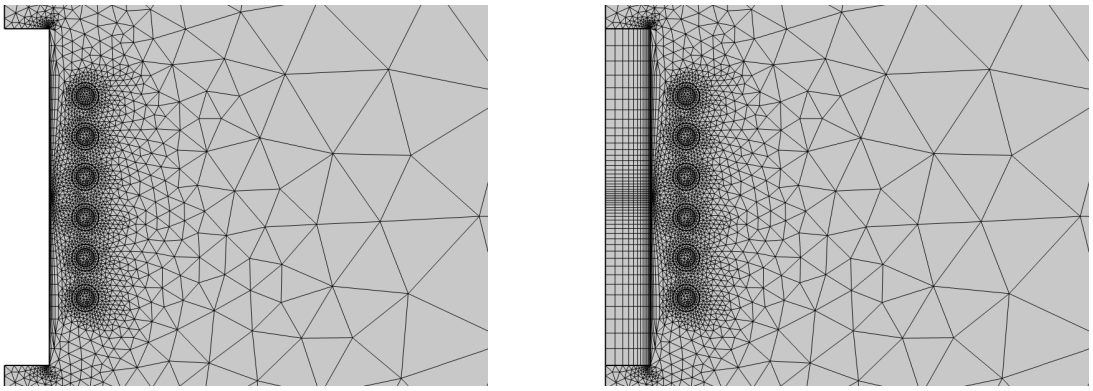

Figure 2.31. Initial mesh of the induction heating system: (a) electromagnetic study employing IBC, and (b) transient thermal model meshing.

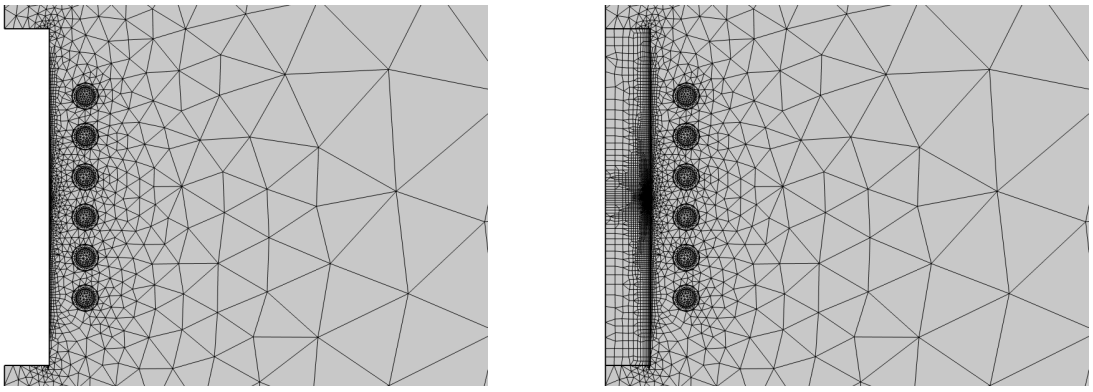

Figure 2.32. Induction heating system meshing in the first step using the adaptive mesh refinement technique: (a) electromagnetic study employing IBC, and (b) transient thermal model meshing.

For this purpose, an initial mesh captured in Fig. 2.31a is created for the electromagnetic model, which makes use of the previously mentioned IBC technique. This condition allows the replacement of a domain with a boundary with special properties; therefore, the mesh inside the billet is not required for the electromagnetic analysis, and the computational cost is simplified. However, a mapped mesh, as can be seen in Fig. 2.31b, is used for the billet in the thermal analysis. It is worth mentioning that the thermal domain mesh could be coarser, but a finer mesh has been employed to gain precision, as the computational cost is not highly elevated.

The simulation with a fixed mesh does not converge properly at some points of the process, especially during the phase transition of the material under treatment. At this point, the workpiece saturates, and convergence problems appear, sometimes resulting in unstable results and other times breaking the simulation.

Luckily, the solver from COMSOL Multiphysics® offers an attribute called adaptive mesh refinement, which consists of, as the name evokes, adapting the mesh during the simulation process; in other words, creates multiple meshes for fixed time steps of a time-dependent simulation [185]. This adaptive mesh solver is employed to simulate the IH process with the aim of obtaining more stable results.

The mesh of the whole geometry is modified for manually defined time steps. One hundred is the maximum number of different meshes allowed by the FEM tool, and all of them have been employed in this study. Therefore, every three seconds, the whole domain's geometry is re-meshed.

In Fig. 2.32, both frequency-domain and thermal-transient respective meshes are shown for the first step at $t = 0.3$ s. Comparing them with the meshes in Fig. 2.31, two significant modifications are observed. On the one hand, the mesh inside the billet is modified to concentrate more nodes in the central inner part. On the other hand, the mesh in the coil's turns is simplified, so fewer nodes need to be computed.

2.4.4.2 Simulation results

Transient simulations of 30 s duration have been performed, starting at room temperature. In each simulation, the coil is fed with a single-harmonic current of 14.2 kHz, and a fixed amplitude ranging from 250 A rms to 500 A rms, covering a wide range of operating conditions. The electromagnetic properties are updated when the temperature distribution changes. Then, some intermediate frequency-domain simulations are done in selected instants by the FEM tool.

In Fig. 2.33, the results of the equivalent impedance of the inductor-workpiece system, $Z_{eq} = R_{eq} + j\omega L_{eq}$, are plotted at the set working frequency. Now, the equivalent impedance of the inductor-workpiece system depends on the time, i.e. on temperature. In Fig. 2.33a, it can be seen how the equivalent resistance, R_{eq}, initially increases due to the temperature increase of the workpiece, but its value starts to decrease, possibly due to the magnetic saturation of a region of the workpiece exceeding the Curie temperature. The volume of this saturated region increases with time. On the other hand, in Fig. 2.33b, a similar behavior of the equivalent inductance, L_{eq}, is observed, although with a smaller relative variation.

Therefore, it is concluded that a local saturation of the material can have a considerable effect on the electrical characteristics of the induction load. This behavior needs to be considered in the power electronics control in order to ensure that the dynamics of the closed-loop current control is capable of handling the change in the electrical properties of the load.

The induction heating process is characterized by a substantial transfer of power to the surface of the workpiece, leading to the development of extremely high-temperature gra-

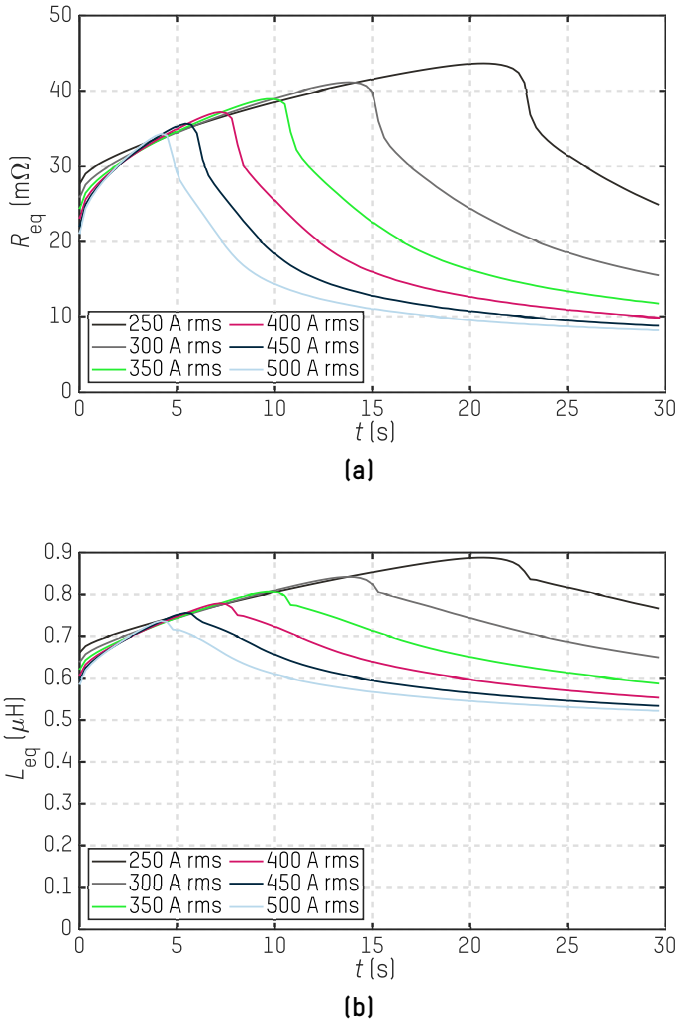

Figure 2.33. Results from COMSOL Multiphysics® simulations during a transient of time of 30 s: (a) equivalent resistance, and (b) equivalent inductance.

dients across its structure. This process typically involves generating heat through electromagnetic induction, causing localized heating that can result in significant variations in temperature within the workpiece. In Fig. 2.34a, the temperature of the central region of the workpiece, T_m, has been plotted to observe its behavior as it approaches close to the Curie point of the material. It is observed that T_m stops increasing abruptly because the efficiency of the induction energy transfer process decreases as the magnetic properties are lost. In Fig. 2.34b, the average temperature of the vertical boundary surface of the billet is plotted during the whole heating process.

Therefore, it has been observed that tracking the temperature at the hottest point of the workpiece, identified as the midpoint, provides a useful approximation of the overall behavior of the heating system. This approach simplifies the analysis, allowing for a more manageable representation of the complex thermal dynamics.

However, it is important to note that the temperature distribution throughout the work-

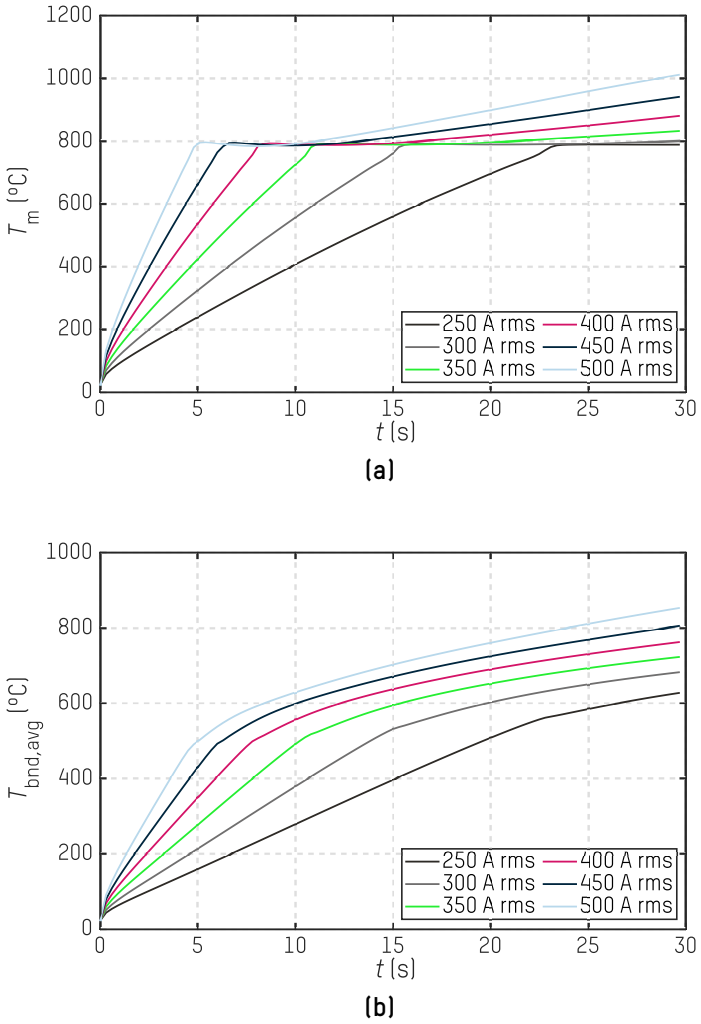

Figure 2.34. Results from COMSOL Multiphysics® simulations during a transient of time of 30 s: (a) temperature in the middle point of the billet's surface, and (b) average temperature of the billet's vertical surface.

piece is highly inhomogeneous, exhibiting considerable variation due to the nature of induction heating. As a result, certain critical characteristics of the heating behavior may be uncertain when the entire process is reduced to the probing of a single temperature point.

Nevertheless, a key finding from the simulations is the significant change in the system's equivalent resistance and equivalent inductance once the reference point at the midpoint reaches the Curie temperature. This temperature marks a critical transition for certain magnetic materials, beyond which their magnetic properties change substantially. Understanding this relation is crucial for optimizing the induction heating process and ensuring effective control over the heating parameters.

The temperature distribution in the load is represented in Fig. 2.35 for some selected times. Higher temperatures are initially reached close to the surface of the middle area of

the billet. Next, the deep regions are also around Curie temperature. Temperatures significantly above the Curie point are not observed due to magnetic saturation or the increase in heat capacity.

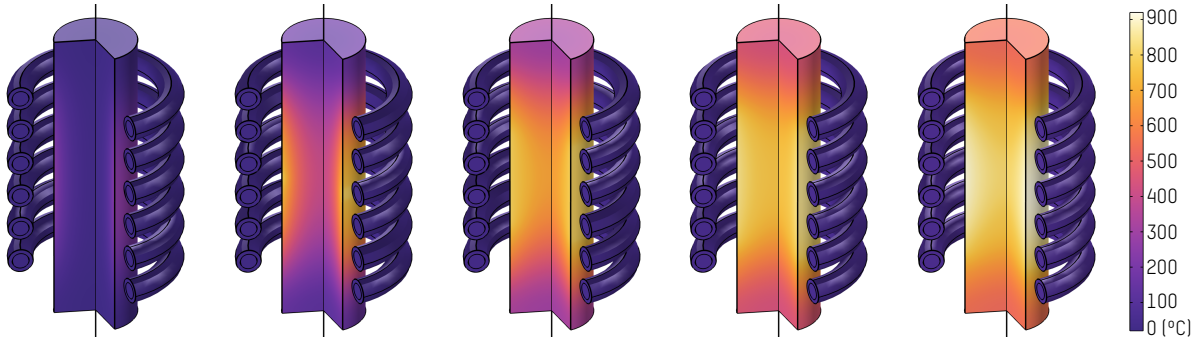

Figure 2.35. COMSOL®-based temperature distribution through the billet for 500 A rms and 14.2 kHz coil's current at $t = 1$, 5, 10, 15, and 20 s, respectively.

The heat flux in the load is represented in Fig. 2.36. As can be observed, at surface temperatures below Curie temperature, the power flux reaches the maximum values, but after the magnetic saturation of the material, the performance of the power transfer by induction clearly reduces. Therefore, the phase transition associated with the magnetic saturation contributes to the homogenization of the temperature profile of the billet.

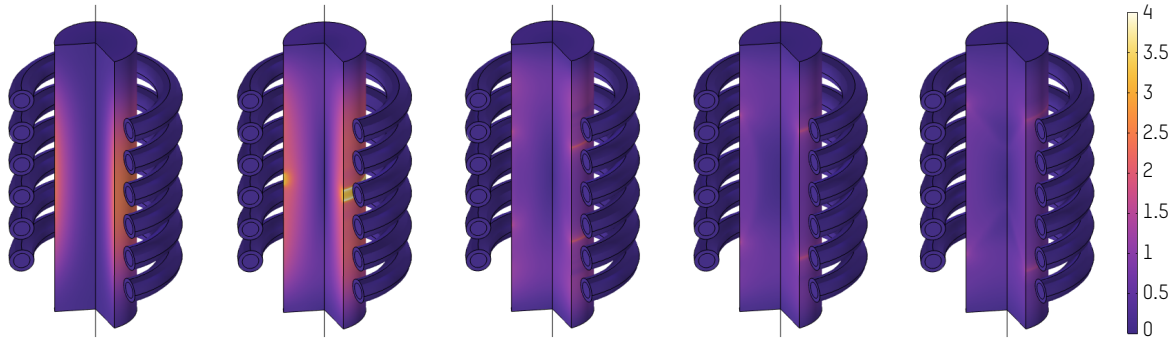

Figure 2.36. COMSOL®-based heat flux distribution in W/mm^2 through the billet for 500 A rms and 14.2 kHz coil's current at $t = 1$, 5, 10, 15, and 20 s, respectively.

In Fig. 2.37, the simulated power exchange in the billet's surface is plotted, exciting the induction coil with 500 A rms and 14.2 kHz current. Figure 2.37a shows that even when stabilizing the value of the current supplied to the inductor, the change in the equivalent resistance implies a time dependence on the power transferred to the load. At the same time, some power losses associated with convection and radiation slightly reduce the net energy accumulated by the load, as can be seen in Fig. 2.37b, but the temperature distribution in the load is mainly determined by the surface power density transferred to the load. The simulation results for the power losses in the load are based on constant convective and emissivity coefficients, but accurate results can be achieved by including temperature dependence.

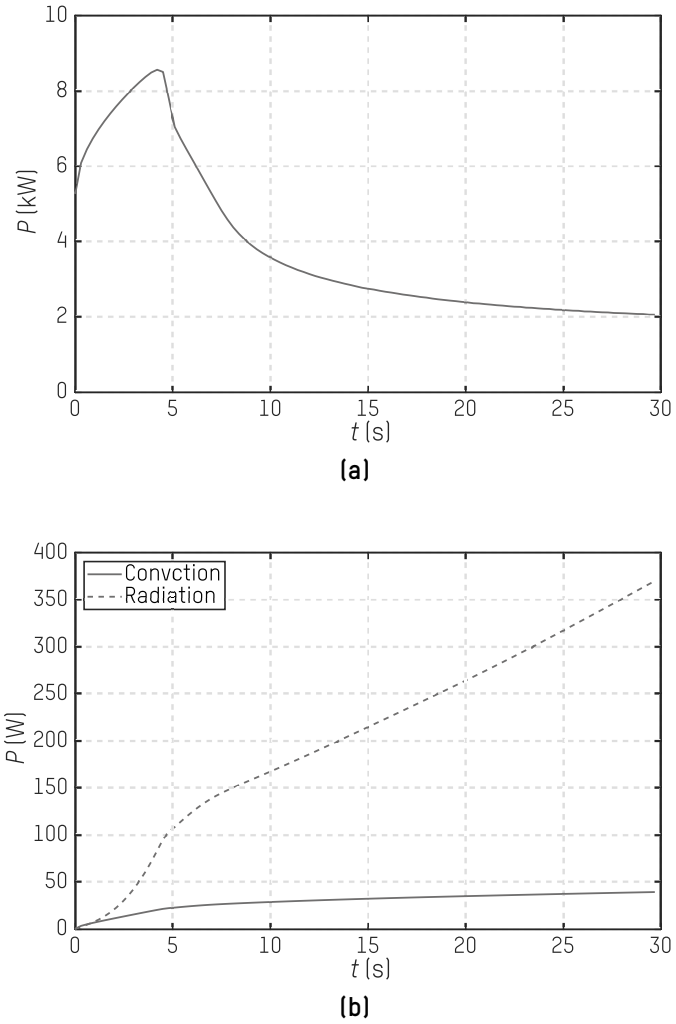

Figure 2.37. Power exchange in the billet's surface during a transient of time of 30 s for 500 A rms and 14.2 kHz coil's current: (a) power induced into the load, and (b) convection and radiation power losses in the billet.

Chapter 3

Power Electronic Converter for Industrial Induction Heating Application

In this chapter, the power converter for industrial induction heating applications is analyzed. This converter is conceived as a versatile instrument for further research activities on the high-temperature heating processes currently demanded by the metal industry. Moreover, a modular hardware design for power electronics is proposed, which allows great flexibility in operation while maintaining simplicity in its control. First, the light induction load is introduced and the power conversion stages of the employed flexible power converter are briefly described. Afterward, the sizing of each stage and the control strategies are related. Finally, the focus is taken to the last inverter stage, which is the one that provides medium-frequency current to the induction load; in the last section, the series-resonant inverter´s versatility study is realized.

3.1 Introduction: Power Electronics Characteristics

The induction heating system required for industrial heat treatments must work under a wide range of conditions to achieve accurate thermal processing of materials. This system involves a nonlinear, light, inductive load, where the equivalent impedance depends on both the workpiece's temperature distribution and the applied excitation level during processing.

Tens of kilowatt power levels are delivered to the load in order to obtain the required elevated temperatures on the billet. The variable induction load consists of a resistive value in the order of tens of milliohms and a few microhenries of inductance. As a result, relatively elevated currents – up to 500 A rms at frequencies around tens of kilohertz – flow through this light load.

In order to facilitate the control of the power converter, a versatile inverter topology able to supply the required power to loads of varying characteristics while maintaining robust behavior is proposed. The power converter must be able to control the power delivered to the load despite the change in its properties, with the purpose of modulating the metallurgical process in the workpiece. Moreover, it should cover various power levels to ensure proper operation. Additionally, the electronics have to be capable of handling inductive loads with the mentioned small resistive component, which may vary considerably throughout the hardening. The main function of this power converter is to obtain the medium-frequency AC current to circulate through the coil that will generate the magnetic field of the same current to inductively heat the steel workpiece on the basis of the 400 V and 50 Hz three-phase mains voltage.

3.1.1 Power Conversion Stages

The basic block diagram of power conversion systems for induction heating systems is illustrated in Fig. 3.1. The AC-DC rectifier supplies de DC-bus from the three-phase AC mains. Then, the following DC-AC stage generates the medium-frequency current that will feed the induction load, which comprises the resistor-inductor pair of the resonant tank.

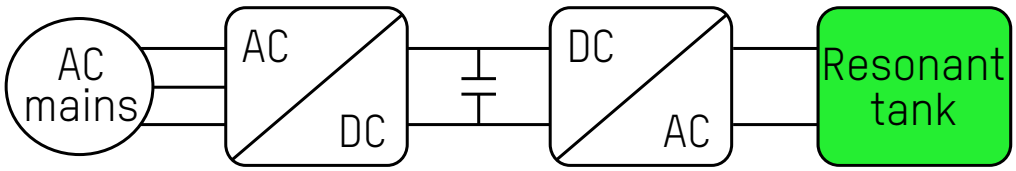

Figure 3.1. Schematic of a power converter for IH purposes.

However, this is not so suitable for light loads like the one under study; it is preferably used with loads with impedances of orders of ohms. In this case, an intermediate DC-DC buck converter is added to further control the voltage at the input of the inverter with this light load that modifies its electrical performance within fractions of seconds. Moreover, with this intermediate converter, the power delivered to the load can be regulated.

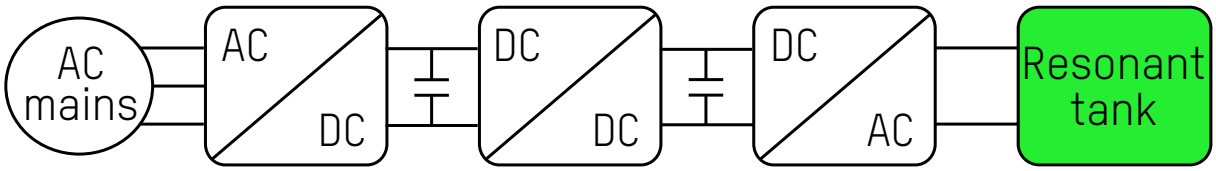

Figure 3.2. Power conversion general scheme including the intermediate DC-DC stage.

In Fig. 3.2, the block diagram of the power conversion system employed in this thesis is depicted.

The electronic stage was designed to prioritize both flexibility and robustness under a wide variety of operational requirements. Its construction is particularly influenced by the necessity to function effectively across an extensive range of frequencies, as well as the ability to supply varying levels of current to loads whose characteristics can change rapidly and unpredictably. To achieve these objectives, a modular approach was adopted, allowing for the separation of different control tasks, which enhances efficiency and reliability.

In a few words, the first component of the system is a controlled boost-type rectifier, which is tasked with the efficient conversion of mains electricity into a usable form. This rectifier is essential for providing a stable input to the subsequent stages of the system. The second modular element is dedicated to the precise control of the current delivered to the loads, ensuring safe operating conditions at all times. This module utilizes a DC-DC converter explicitly designed for this purpose, allowing it to respond swiftly to the dramatic fluctuations in load characteristics that may occur during operation. This responsiveness is critical for maintaining performance and protecting both the system and the connected devices. The final stage of the system is an inverter, which plays an essential role in adapting the DC-bus voltage to the desired output frequency. This adaptation is crucial for ensuring that the power delivered meets the specific requirements of various applications, further enhancing the overall versatility of the system.

Although it is technically feasible to design a more compact system by eliminating the intermediate conversion stage, this would significantly compromise the flexibility and robustness that characterize the proposed topology. The current modular design not only improves functionality but also provides a clear pathway for upgrades and adjustments, making it a practical choice for a wide range of applications.

3.1.1.1 Grid-connected three-phase rectifier

The three-phase, six-pulse, full-bridge rectifier is the most common circuit for mains' rectification purposes, [194]. In this case, the first component of the induction heating power conversion system under study is a controlled three-phase boost rectifier depicted in Fig. 3.3, which is tasked with the efficient conversion of mains electricity into a usable form. This rectifier is essential for providing a stable input to the subsequent stages of the system. Apart from allowing the control of the output voltage on the DC-bus, V_o, it permits sinusoidal current absorption of the phase current from the grid.

This converter is composed of six bidirectional two-quadrant switches, [195]. The in-

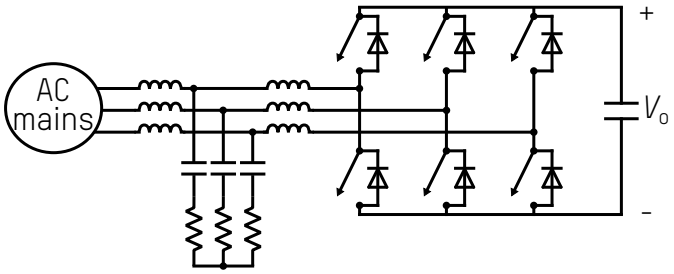

Figure 3.3. Three-phase boost rectifier's switch diagram.

ductors and capacitor – LCL filter – between the mains and the rectifier's input filter the high-frequency switching harmonics; moreover, it facilitates the connection to the mains.

With this topology, the input current is regulated independently of the voltage, and the power factor can be corrected. Moreover, the converter is bidirectional, allowing the current to flow in the opposite direction. Since it is a boost-type converter, the output DC voltage must be greater than the input line-to-line peak voltage.

To sum up, in this stage, the output DC voltage is regulated at a constant value of at least the maximum voltage required at the input of the H-bridge inverter.

3.1.1.2 Intermediate DC-DC buck converter

The second modular element is dedicated to the precise control of the current delivered to the loads, ensuring safe operating conditions at all times. This module utilizes a buck-type synchronous DC-DC converter, whose generic diagram is depicted in Fig. 3.4, designed specifically for this purpose, allowing it to respond swiftly to the dramatic fluctuations in load characteristics that may occur during operation. This responsiveness is critical for maintaining performance and protecting both the system and the connected devices.

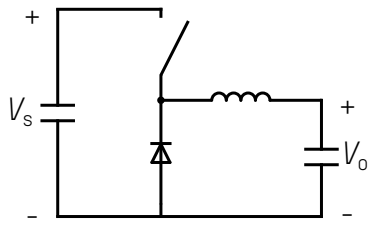

Figure 3.4. DC-DC buck converter's basic diagram.

The energy is transferred to the output when the upper switch is conducting, [194]. In essence, a buck converter generates an average output voltage lower than the input voltage.

3.1.1.3 Series-resonant inverter

The final stage of the system is an inverter, which plays an essential role in adapting the input DC-bus voltage to the desired output frequency. This adaptation is crucial for ensuring that the power delivered meets the specific requirements of various applications, further enhancing the overall versatility of the system.

This inverter will excite a resonant tank that behaves as a filter. The basic structure of an inverter exciting a resonant tank is depicted in Fig. 3.5.

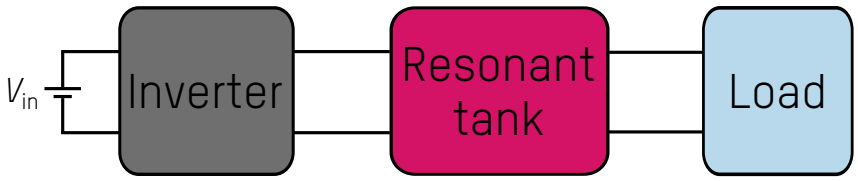

Figure 3.5. Basic structure of an inverter exciting a resonant tank.

A resonant tank is a combination of two or more reactive components – inductors and capacitors – which can be connected in series or parallel; therefore, several combinations can be made. In essence, the resonant tank works as a filter between a converter and the load, and the gain the resonant tank applies to the load depends on the frequency with which it is excited, [195].

In this specific system, the series compensation of the resonant tank is employed to ensure soft switching of the inverter's switches, and thus limit the losses of such stage, see Fig. 3.6.

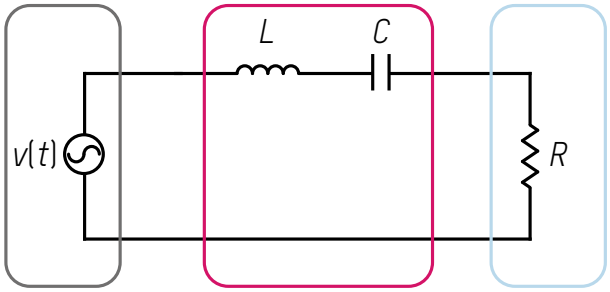

Figure 3.6. Series resonant tank circuit scheme, from left to right: inverter's output, series LC tank, and resistive load.

The series-resonant tank circuit's impedance is given by (3.1), which is frequency-dependent. This expression clearly shows that the real part will always be resistive, R, independently of the excitation frequency. However, reactances – or imaginary parts – are frequency dependent. The inductive reactance, X_L, evolves linearly with the frequency and the capacitive reactance, X_C, is inversely proportional to the frequency, which means that at very low frequencies, there will be almost null inductive reactance and infinite capacitive reactance, and, inversely, at very high frequencies, infinite inductive reactance and almost null capacitive reactance. Moreover, there is a point at which both reactances

intersect, so they eliminate each other; this point happens at a frequency called the resonant frequency, f_r.

$$Z(j\omega) = R + j\left(\omega L - \frac{1}{\omega C}\right). \tag{3.1}$$

Equalizing X_L and X_C, resonant frequency expression is obtained:

$$f_r = \frac{1}{2\pi\sqrt{LC}}. \tag{3.2}$$

This resonant frequency also classifies the inverter's operation modes. At switching frequencies smaller than f_r, the inverter operates in capacitive mode; on the contrary, at higher switching frequencies than f_r, the operation mode is inductive. When the switching frequency is equal to the resonant frequency, the inverter is operating in resonance, and the impedance of the tank is at its lowest value, and it is completely imposed by the resistive component.

The same operation modes can be explained in terms of voltage gain with (3.3). At resonance, the voltage gain, H_v, is 1, which means that the whole voltage inserted is applied to the load; however, in inductive and capacitive operation modes, respectively, the inductive and capacitive reactances appear, so the voltage gain will also be smaller than unity. Moreover, at frequencies close to zero or infinite, H_v will tend to zero.

$$|H_v(j\omega)| = \frac{R}{\sqrt{R^2 + \left(\omega L - \frac{1}{\omega C}\right)^2}} = \frac{\text{real}(Z)}{|Z|} \tag{3.3}$$

The impedance-frequency curve is represented in Fig. 3.7b; in this case, at the resonant frequency, the tank's impedance value will be minimum and fully resistive. On the other hand, in Fig. 3.7a, the voltage gain curve is depicted depending on the exciting frequency, for a series-resonant tank.

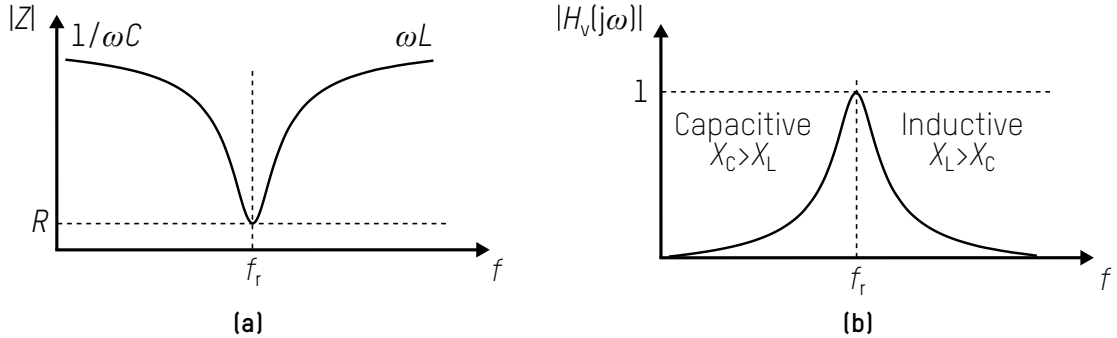

Figure 3.7. Series-resonant tank's characteristic diagrams: (a) impedance, and (b) voltage gain, [195].

Moreover, two other important factors that determine the behavior of resonant tanks shall be considered: quality factor, Q, and bandwidth, BW. By definition, the quality factor

is the ratio between the stored energy and the dissipated energy in a period at the resonant frequency:

$$Q = \frac{\text{Stored energy}}{\text{Dissipated energy}}. \tag{3.4}$$

From (3.4), the quality factor expression for the series-resonant tank can be easily derived, [194]:

$$Q_s = \frac{\omega_r L}{R}, \tag{3.5}$$

where ω_r is the angular resonant frequency.

Instead, the bandwidth, which is the range of frequencies over which at least half of the maximum power is provided, is inversely proportional to the quality factor:

$$BW = \frac{f_r}{Q}. \tag{3.6}$$

The bandwidth can also be expressed as the distance between two cut-off frequencies, $f_2 - f_1$. At those frequency values, 50 % of the maximum output power is obtained, which means the same, the voltage gain is 70.7 %, 3 dB below its maximum. Inside the bandwidth, it is assumed that the power transferred to the load is at least half of the maximum output power.

On the other hand, the quality factor reflects the sharpness of the voltage gain curve's peak. The selectivity term is used to measure the ability to reject frequencies outside the bandwidth. A more selective circuit – higher Q – will have a narrower shape, and for less selective circuits – lower Q –, the shape will be wider.

Voltage gain curves for different R values are depicted in Fig. 3.8, including the quality factor and bandwidth parameters.

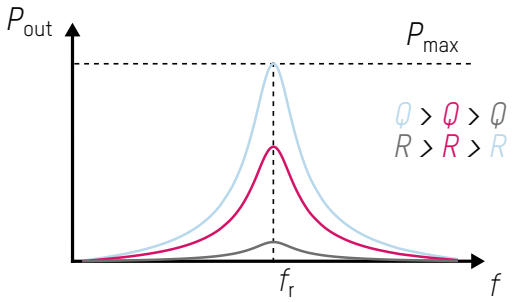

Figure 3.8. Frequency-dependent voltage gains for different R and Q values.

Switched inverters are employed to excite such resonant tanks. Basically, these inverters synthesize square-wave train output voltages, $v_o(t)$, whose Fourier series contains odd harmonics expressed in [195]:

$$v_o(t) = \sum_{n,\text{odd}} \frac{4V_{dc}}{n\pi} \sin n\omega_s t, \tag{3.7}$$

where V_{dc} is the DC-bus voltage, n is the harmonic number and, ω_s the angular frequency of the square wave, $\omega_s = 2\pi f_s$. The amplitude of each voltage term is given by:

$$V_n = \frac{4V_{dc}}{n\pi}. \tag{3.8}$$

While the harmonic number, n, grows, the amplitude of the Fourier voltage component, V_n, reduces. Likewise, according to Fig. 3.7, the voltage gain also decreases, and the impedance increases at higher n values. In conclusion, only the fundamental and a few other terms will take part in the power transfer, and therefore, there will be an almost sinusoidal voltage. In fact, working around f_r, the fundamental harmonic is a good approach.

There are several types of switched inverters, but the most employed ones are bridge-type topologies: half-bridge (HB) and full-bridge (FB). They stand out for good performance and easy control.

On the one hand, there is the half-bridge topology, which consists of a switch branch. It can be either configured with a middle point and the capacitors divided into two equal branches (Fig. 3.9) or with the resonant capacitor in a unique branch, eliminating the middle point.

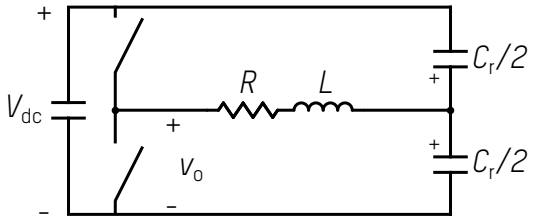

Figure 3.9. Switch diagram of the inverter's half-bridge topology.

In essence, this inverter excites the resonant tank with a square voltage wave depicted in Fig. 3.10a, with values ranging from zero to V_{dc}. The mean value of this square voltage is not null, synthesizing a mean value in the harmonic spectrum in Fig. 3.10b. However, the resonant capacitor will avoid reflecting this mean value on the load, so it will not be problematic.

From Fig. 3.10a, the output voltage can be expressed in two time intervals. For the first half-period, the output voltage will be V_{dc}, and for the next one, zero. Therefore, the fundamental output voltage of a half-bridge inverter is expressed in [196]:

$$V_1 = \frac{2V_{dc}}{\pi} \tag{3.9}$$

To analyze the circuit in Fig. 3.9, the half-period, where the top switch is closed and the one on the bottom is open, will be considered. Note that the other half-period is precisely

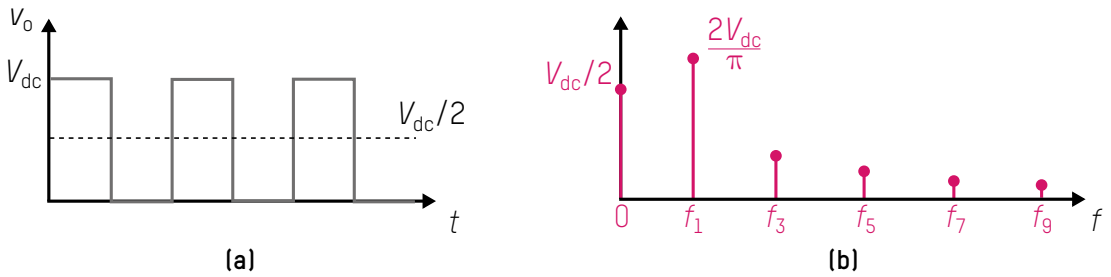

Figure 3.10. Half-bridge inverter's output voltage (a) waveform, and (b) harmonics.

the opposite. So, applying Kirchhoff's current law, we obtain the expression of the load current, i_{RL}:

$$i_{RL} = i_{Cr/2,t} + i_{Cr/2,b}, \tag{3.10}$$

where $i_{Cr/2,t}$ and $i_{Cr/2,b}$ are, respectively, top and bottom resonant capacitor currents, which are equally divided in both branches, $i_{Cr/2,t} = i_{Cr/2,b} = i_{Cr/2}$.

$$i_{Cr/2} = \frac{C_r}{2}\frac{dv_{Cr/2}}{dt} \tag{3.11}$$

In the same way, according to Kirchhoff's voltage law:

$$v_o = -v_{Cr/2,t} + v_{Cr/2,b}, \tag{3.12}$$

where $v_{Cr/2,t}$ and $v_{Cr/2,b}$ are, respectively, voltages on top and bottom resonant capacitors, which are phase-shifted, $v_{Cr/2,t} = v_{Cr/2,b} = v_{Cr/2}$. Then, the voltage value for each capacitor is expressed as:

$$v_{Cr/2} = i_{RL}R + \frac{di_{RL}}{dt}L. \tag{3.13}$$

Therefore, the circuit in Fig. 3.9 can be simplified to the circuit in Fig. 3.11.

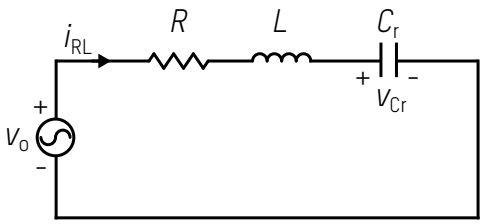

Figure 3.11. Simplified series-resonant inverter's circuit.

On the other hand, there is the full-bridge topology, drawn in Fig. 3.12. This topology synthesizes an output voltage waveform in Fig. 3.13a, without any mean value. Likewise,

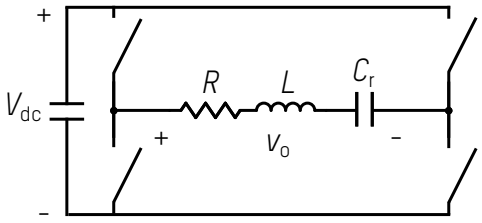

Figure 3.12. Switch diagram of the inverter's full-bridge topology.

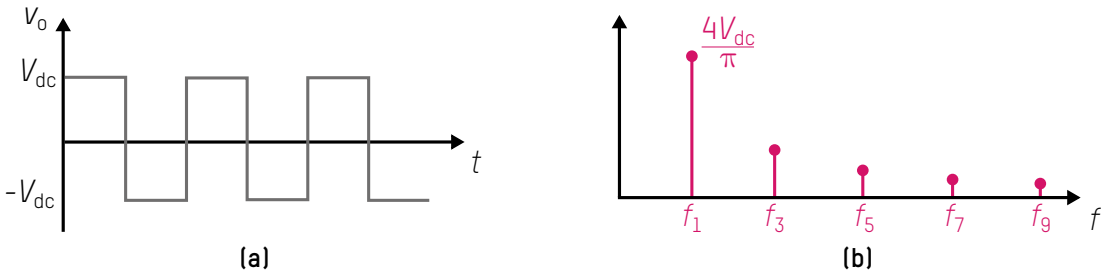

Figure 3.13. Full-bridge inverter's output voltage (a) waveform, and (b) harmonics.

the output voltage is twice the value of the half-bridge output voltage. The harmonic spectrum of the full-bridge output voltage is represented in Fig. 3.13b. In this case, the output voltage at the fundamental frequency is given by (3.14).

$$V_1 = \frac{4V_{dc}}{\pi}. \tag{3.14}$$

The same analysis realized with the half-bridge circuit is now applied to the full-bridge topology. In the first half-period analyzed, the top-left and bottom-right switches are closed, and the other two are opened. In this case, the same current circulates through the induction load and resonant capacitors, which, at the same time, is the same as the current through the closed switches:

$$i_{RL} = i_{Cr}, \tag{3.15}$$

where

$$i_{Cr} = C_r \frac{dv_{Cr}}{dt}. \tag{3.16}$$

Then, v_o is computed with Kirchhoff's voltage law:

$$v_o = i_{RL}R + \frac{di_{RL}}{dt}L + v_{Cr}. \tag{3.17}$$

Overlapping either Fig. 3.10b or Fig. 3.13b in Fig. 3.7b, it is concluded that when exciting the tank with a frequency near resonance, there will be an almost sinusoidal voltage at

the output; because the only one that will take part in the power transfer will be the fundamental component. This is an approximation expressed in Fig. 3.14, where it is clearly observed that beyond the third harmonic, both the amplitude of such harmonic and the voltage gain are reduced until they become null.

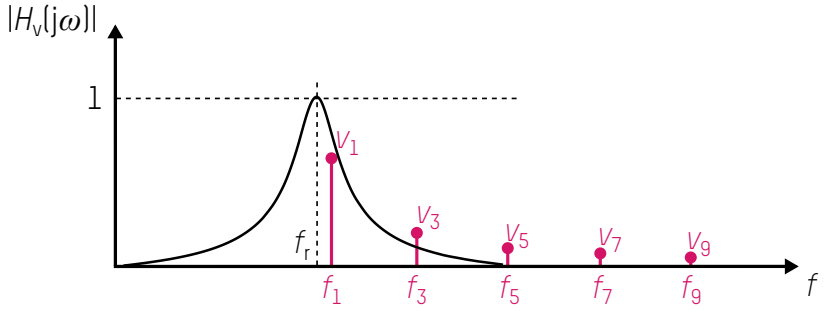

Figure 3.14. Harmonic spectrum expressed on the voltage gain curve.

On the other hand, the resonant tank does also affect on the inverter, indeed, on its power losses. Here again, the three operation modes are differentiated, making mention of the phase shift between the voltage and current waveforms:

$$\Phi_{\text{shift}} = \arctan \frac{X_L - X_C}{R}, \tag{3.18}$$

where X_L and X_C are, respectively, inductive and capacitive reactances.

In an ideal operation, working at resonance, $f = f_r$, there is no phase-shift between the output voltage and current, so the diodes do not conduct, and the only power losses are generated on the solid-state switches. Moreover, as both the voltage and current are in phase, there is no current when switching on and off, so there are no switching losses.

In the inductive operation mode, $f > f_r$, the voltage leads current; current circulates through the transistors and diodes, so the conduction losses are caused by all of them. According to switching losses, when a transistor is switched off, another diode switches on; therefore, there are turn-off losses on the transistors and turn-on losses on the diodes. It is assumed that diode turn-on losses are negligible as they are almost insignificant compared with the turn-off losses. Moreover, when switching on the transistor, the voltage on its terminals is null, as its flying diode was already conducting, so the transistor switches on with zero voltage. This soft switching on of the transistor is known as Zero Voltage Switching (ZVS), [105].

However, at capacitive operation mode ($f < f_r$), the current leads voltage, so here again the transistors and diodes have conduction losses. Here, when switching off a diode, another transistor switches on, so there are turn-off losses on diodes and turn-on losses on transistors. In this case, the transistor switches off when the current is zero, which is called Zero Current Switching (ZCS), [65].

To sum up, see Fig. 3.15. When working at resonance, there only are conduction losses on the transistors. In the inductive operation mode, there are conduction losses on transistors and diodes, and switching-off losses on transistors. And at capacitive operation mode, there are also conduction losses on transistors and diodes, but switching-on

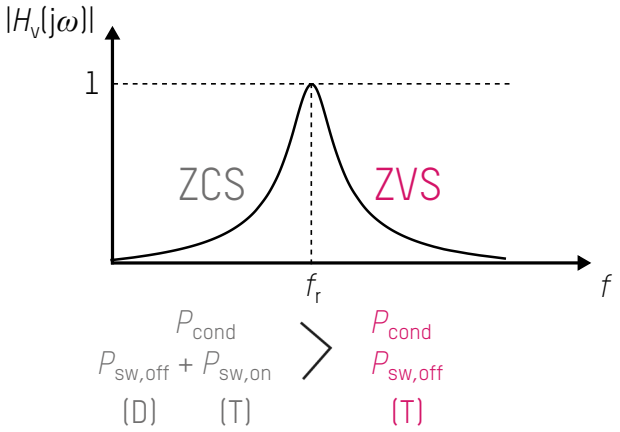

Figure 3.15. ZCS and ZVS switching modes reflected in the frequency-dependent voltage gain curve.

losses on transistors and switching-off losses on diodes. Therefore, if it is aimed to regulate the voltage gain, it is preferable to increase the switching frequency and operate at inductive mode or ZVS.

3.2 Design Parameters of the Selected Topology

This section will further detail the power converter used to feed the induction coil. As described in the previous section, three conversion stages are distinguished, which are integrated with the input filters; the control electronics, the sensors, and other elements. Then, a resonant capacitor bank is implemented in an independent component. And, finally, the induction load is given by the coil-billet impedance, which will be represented as an equivalent resistance-inductance pair's series connection. The scheme of the organization of the power conversion stages is shown in Fig. 3.16.

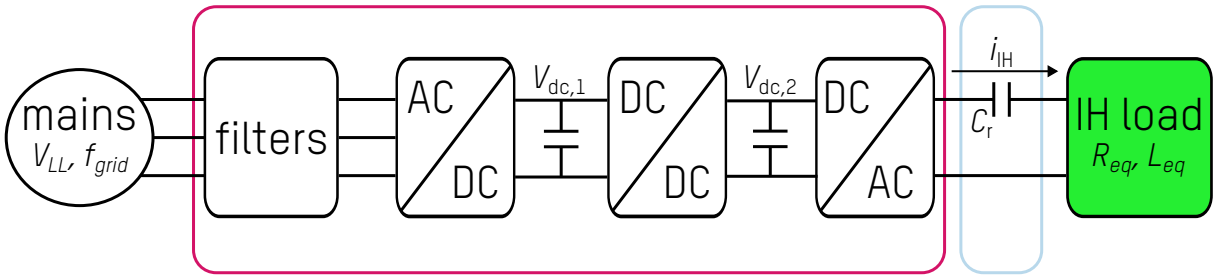

Figure 3.16. Diagram of the power converter of the induction heating system for flexible working condition.

This power converter is connected to a three-phase mains of 400 V and designed to deliver a nominal power of 50 kW. The electrical specifications of the IH power converter are exposed in Table 3.1.

Table 3.1. Electrical specifications of the IH power converter.

Parameter	Value	Unit
Nominal power, P_{nom}	50	kW
Input line-to-line voltage, V_{LL}	400	V
Input three-phase mains frequency, f_{grid}	50	Hz
Maximum voltage in the first DC-bus, $V_{dc,1}$	650	V
Maximum voltage in the second DC-bus, $V_{dc,2}$	600	V
Maximum current through the IH load, i_{IH}	500	A rms

The electrical additional requirements of each stage and passive components to be designed have been defined by performing some calculations according to the specifications in Table 3.1; therefore, the maximum input current per phase is 72.46 A, and the current through the output of the DC-DC converter can reach 200 A.

Now, each of the three power conversion stages will be further detailed with the aid of electrical simulations. PLECS® electrical simulation software, [197], is employed in this section, so that the behavior of every conversion stage will be electrically studied.

The load employed in the simulation is similar to the induction heating load analyzed in this thesis, but in a simplified version, because the aim here is not to model the dynamics of such load but to justify the design parameters of the power converter topology under study. The simulated resonant tank's linear parameters are listed in Table 3.2. The resonant frequency has been fixed to somehow maintain coherence in the whole document; the load's equivalent parameters are measured in Section 3.3, and the resonant capacitance value has been chosen to obtain such resonant frequency value.

Table 3.2. Resonant tank parameters for PLECS® electrical simulation.

Parameter	Value	Value
Resonant frequency, f_r	14	kHz
Equivalent resistance, R_{eq}	50	mΩ
Equivalent inductance, L_{eq}	3.7	μH
Resonant capacitance, C_r	36.4	μF

Moreover, all the commercial and manufactured components used to build the power converter are described in the following lines. The corresponding datasheet references are also included at the end of the document.

3.2.1 Three-Phase Controlled Boost-Type Rectifier

The first electronic stage consists of a three-phase controlled boost-type rectifier that converts the 400 V / 50 Hz three-phase mains voltage into a 650 V DC-bus voltage. In Fig. 3.17, mains grid-side phase voltages, v_{ag}, v_{bg}, v_{cg}, are depicted.

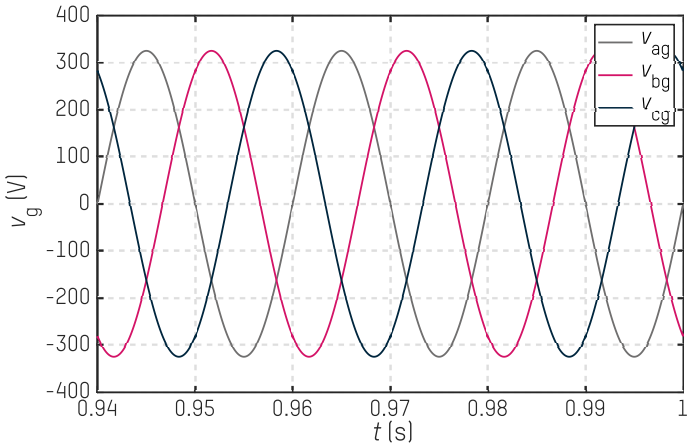

Figure 3.17. Simulated 3-phase mains 50 Hz phase voltage.

3.2.1.1 Sizing of the rectifier

In the following lines, the sizing of the rectifier is realized step by step.

- **Input filters**

  First, there is the input filter, which has two main purposes: filtering the harmonics and facilitating the grid connection. It was designed according to the current regulations for mains connections. The current harmonics will depend on the filter's impedance, which will be responsible for ensuring that the regulations are complied with. Frequency ranges from 10 to 50 kHz are considered to design the filter. An analysis was performed between L and LCL-type filters, and the latter one, which is composed of two inductors and a capacitor, was chosen. The cost, size, and weight of this filter are lower, and was harmonic injection is expected to be better than with a single L per phase.

  Moreover, a dumping resistor is added. Even if it may seem unnecessary, it helps to avoid perturbations and oscillations while connecting and disconnecting the converter.

  The transfer function of an LCL filter is given by [198]:

$$\frac{i_g(s)}{v_f(s)} = \frac{CRs+1}{L_gL_fCs^3 + (L_g+L_f)CRs^2 + (L_g+L_f)s}. \tag{3.19}$$

  This expression is simplified for frequencies above 10 kHz to (3.20) to realize a quick estimation of the required inductances:

$$\frac{i_g(s)}{v_f(s)} = \frac{R}{L_gL_fs^2}. \tag{3.20}$$

  Considering a suitable dumping resistance of 100 mΩ, the established requisite is met with two inductances of 100 μH minimum value. However, it is recommended to use higher values and verify that they are high enough to minimize the grid's fifth and

seventh harmonics, complying with existing regulations. Then, the spectral analysis was realized by simulations, and the LCL filter values per phase were chosen, which are given in Table 3.3.

Table 3.3. Designed LCL filter values.

Component	Value	Unit
Grid-side inductor, L_g	80	μH
Converter-side inductor, L_f	260	μH
Three-phase capacitor, C	78.6	μF
Dumping resistor, R	100	mΩ

Although the choices of possible LCL values are infinite, the values in Table 3.3 have been chosen for a cut-off frequency between 2-4 kHz and maintaining a higher converter-side inductor value to minimize the current ripple (power losses) of the rectifier.

The simulated currents before and after the LCL filter are plotted in Fig. 3.18a and Fig. 3.18b, respectively. Those currents are also known as grid-side currents, i_{ag}, i_{bg}, i_{cg}, and converter-side currents, i_{af}, i_{bf}, i_{cf}.

The grid- and converter-side inductors were ordered from a specialized company in designing and manufacturing electrical transformers, chokes, and other electrical machines, with the specifications calculated in the previous section. A three-phase capacitor with 33 μF on each phase is then placed, with MKP technology for signal filtering. The three dumping resistances are of 100 mΩ and 100 W.

In addition, in order to further comply with existing standards, an EMC filter was placed at the input of the converter. An EMC filter was placed at the input of the converter to meet the established electromagnetic compatibility requirements.

- **Bus capacitor**

  First, the current to be supplied by the capacitor is obtained from (3.21). According to electrical specifications in Table 3.1, the nominal values of the first bus voltage and power are, respectively, 650 V and 50 kW. Therefore, this bus capacitor should provide about 38 A rms.

$$i_C \approx \frac{P}{2V_{dc}} \tag{3.21}$$

  However, computing the minimum capacitance value is complex, and it depends directly on the control dynamics. Some increasing ramps of a few tens of milliseconds have been simulated, and it was concluded that the bus capacitor should have around 600 μF to prevent the bus from under-voltages during the power transient.

  The output of the controlled three-phase rectifier consists of a bus capacitor in a configuration of six KEMET C44U0GT6100A8TK 100 μF capacitors connected in parallel. These capacitors have a nominal voltage of 900 V and a ripple current of 65 A at 10 kHz each.

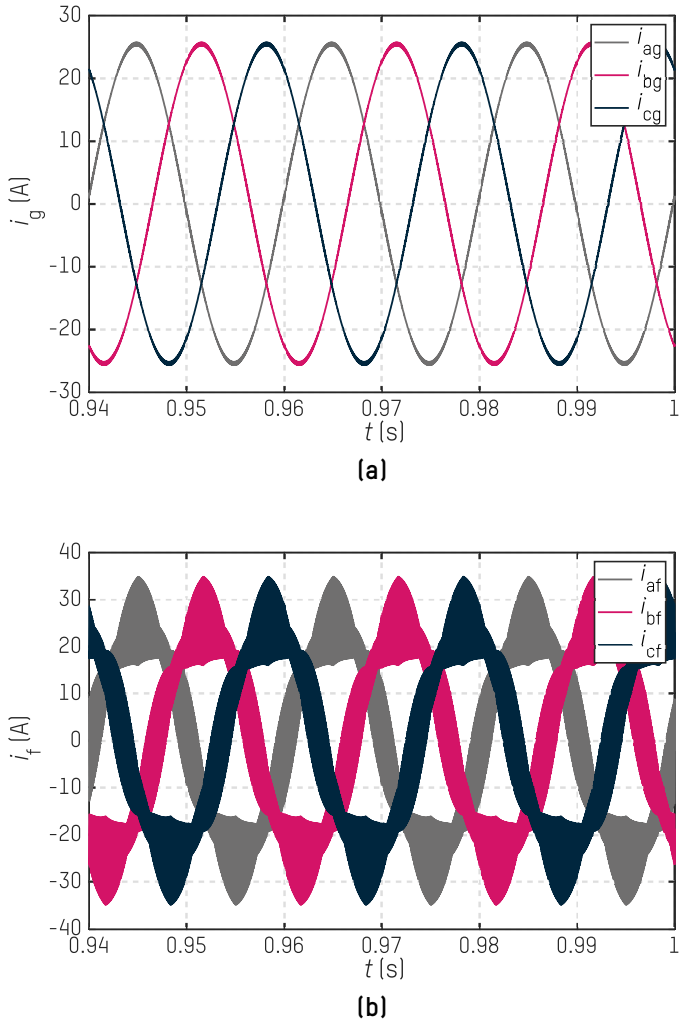

Figure 3.18. Rectifier input currents: (a) grid-side currents i_{ag}, i_{bg}, i_{cg}, and (b) converter-side currents i_{af}, i_{bf}, i_{cf}.

3.2.1.2 Vector control

A vector control integrating a Power Factor Corrector (PFC) has also been included to ensure a low ripple output and power factor close to one at the input by canceling the reactive power consumption.

The vector control strategy of a grid-connected converter is normally developed in *dq* rotating reference frame, aligning the grid voltage vector, $\mathbf{v}_g$, with the *d* axis, [198]. In this way, not only the voltage equations are simplified, but also active and reactive power computations are reduced in, respectively, (3.22) and (3.23):

$$P = \frac{3}{2}\left(v_{dg} i_{dg} + v_{qg} i_{qg}\right), \tag{3.22}$$

and

$$Q = \frac{3}{2}\left(v_{qg} i_{dg} + v_{dg} i_{qg}\right). \tag{3.23}$$

The control of the modules is achieved by applying the Grid-Voltage Oriented Vector Control (GVOVC) strategy in Fig. 3.19. This vector control aligns with the grid voltage space vector and is in charge of regulating the voltage at the output, $V_{dc,1}$, and the reactive power exchange with the grid. On the one hand, controlling the DC-bus voltage will ensure a proper active power exchange. In this case, to ensure unity power factor, the reactive power reference is annulled by setting i_{qg} reference to zero current.

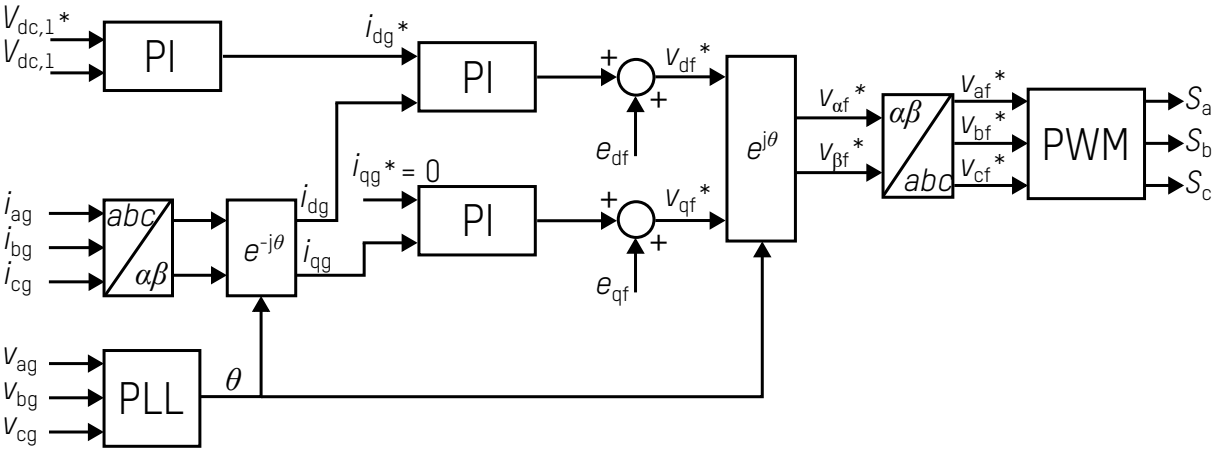

Figure 3.19. Grid-Voltage Oriented Vector Control (GVOVC) block diagram, [198].

The gating signals of the MOSFETs in the 3-phase rectifier are generated from the V_{dc} voltage and i_{qg} current references. i_{dg} current reference is generated by the proportional-integral (PI) regulator corresponding to the DC-bus voltage. Then, the two grid current components references are passed through other two PI regulators, canceling the coupling terms at their outputs. The terms for the cancellation of the LCL filter are the following:

$$e_{df} = -\omega \cdot L_f \cdot i_{qf} - \omega \cdot L_g \cdot i_{qg} + v_{dg} \tag{3.24}$$

$$e_{qf} = \omega \cdot L_f \cdot i_{df} + \omega \cdot L_g \cdot i_{dg} \tag{3.25}$$

Actually, in this case, only the grid-side current is measured, assuming that both i_g and i_f currents have similar fundamental values. Therefore, the coupling terms are minimized:

$$e_{df} \approx -\omega \cdot (L_f + L_g) \cdot i_{qg} + v_{dg} \tag{3.26}$$

$$e_{qf} \approx \omega \cdot (L_f + L_g) \cdot i_{dg} \tag{3.27}$$

Next, voltage references for the three-phase rectifier are obtained by the rotational and Clarke transformations, which are finally transformed into gating signals for the MOSFETs

by Pulse Width Modulation (PWM). The drivers generate the trigger signals at a fixed switching frequency of f_{3-ph} =16.67 kHz. This frequency is relatively high to minimize the inductive components size and avoid any undesired acoustic noise, but without exceeding too much as the efficiency would be penalized due to increasing the switching losses.

The angle of the grid voltage, θ, is estimated by a phase-locked loop (PLL), providing stability and rejecting perturbations. This angle is employed in the voltage and current coordinate transformations.

The first DC-bus voltage control dynamics are shown in Fig. 3.20. First, the bus is precharged passively by the diodes of the rectifier; 4.7 Ω precharge resistors are employed for such purpose. Then, the rectifier and its associated control are enabled to reach the referenced DC voltage of 650 V. The following two stages are also enabled at the same instant as the rectifier.

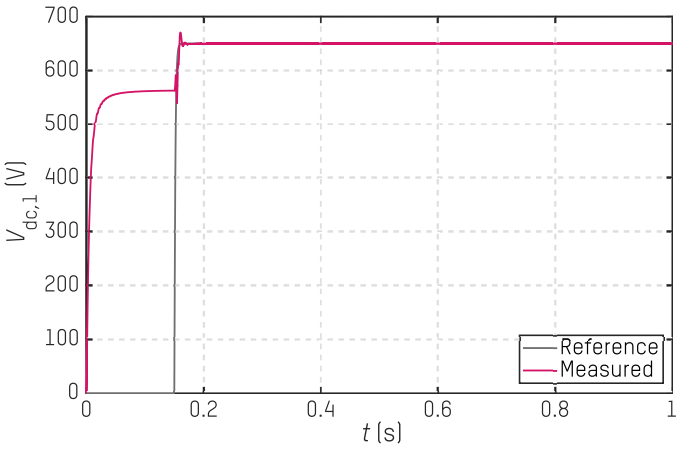

Figure 3.20. Voltage control in the first DC-bus.

3.2.2 Two-Channel Interleaved Synchronous DC-DC Buck-Type Converter

The intermediate power stage consists of a DC-DC buck converter regulating the variable bus voltage $V_{dc,2}$. Its final objective is to control the delivered power to the induction load. Considering the selected series-resonant topology and that the inverter operates at an open loop (uncontrolled), the power will be proportional to the voltage at the output of this DC-DC converter. In other words, the power delivered by the series-resonant inverter will be controlled with this intermediate stage.

3.2.2.1 Sizing of the buck converter

In the design of this DC-DC converter, particular attention has been paid to minimizing the inductive elements at the output. For this reason, considering that the input voltage is always higher than the output one, and the current through the output could reach 200 A, a buck converter with two output channels has been chosen; thus, this current is split into 100 A through each output inductor.

- **Output inductors**

  There are some criteria to consider when designing the output inductors of the buck converter. First, the switching frequency has to be relatively high to reduce the size of the inductors and avoid acoustic noise; at the same time, high frequencies cause switching losses. Therefore, a working frequency of 16.67 kHz has been chosen.

  Then, the maximum current ripple, $\Delta i_{L,max}$, from each of the inductors is established. A very large ripple value means designing an inductance with very high saturation currents, whereas to reduce this ripple, a very large inductive value – a very heavy inductor – is needed. A typical value for this criterion is between 10 and 40 % of the nominal value. After some computations, the inductance value of 330 μH was defined. The circulating currents through the output inductors of 330 μH each are simulated in Fig. 3.21.

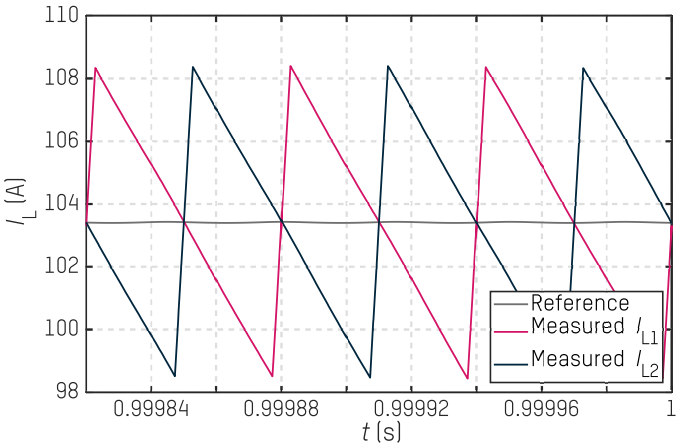

Figure 3.21. Current waveforms through each inductor.

Two 330 μH inductors were placed at the output of the buck converter, one for each branch. To design such inductors, the design software from IKERLAN was employed, which provides a volume-efficiency optimized design. We manufactured those inductors in IKERLAN.

Considering the working frequency of 16.67 kHz, the amorphous material is the one best suited, as it exploits its maximum inductance with acceptable losses, resulting in a smaller inductance size. Standard amorphous cores AMCC from Hitachi were employed. Litz wires were chosen as the wiring technology. It should be noted that at these operating frequencies, using a solid conductor would generate excessive losses.

The design was launched in the mentioned tool, which makes a sweep using the databases composed of standard cores and wires. The characteristics of one of the DC-DC inductors are shown in Table 3.4. Moreover, an air gap was introduced to reach the desired inductive value.

Table 3.4. Characteristics of one of the DC-DC inductors.

Size	126 x 68 x 132 mm
Turn number	47 turns in 3 layers
Core	4 x AMCC-125
Litz wire	0.2 mm x 360

- **Bus capacitor**

  With respect to the DC-bus capacitor, after simulating different values as in the first DC-bus, a capacitance value of 400 μF was chosen.

  The output of the DC-DC buck converter is configured by the four 100 μF capacitors in parallel due to technological issues.

3.2.2.2 DC-bus voltage control

In this case, two inverting synchronous branches working in two-channel interleaved mode are used. Fixed switching frequency modulation at f_{buck} = 16.67 kHz is used, applying asymmetrical voltage control on each branch. PI regulators, whose output response is given by (3.28), are employed, as detailed in Fig. 3.22.

$$u(t) = K_p \left(e(t) + \frac{1}{T_i} \int_0^t e(t)\, dt \right), \tag{3.28}$$

where $e(t)$ is the error at the input of the PI block, K_p is the proportional constant, T_i the integral time, and $u(t)$ is the output response of the regulator. The integral gain is given by: $K_i = K_p/T_i$.

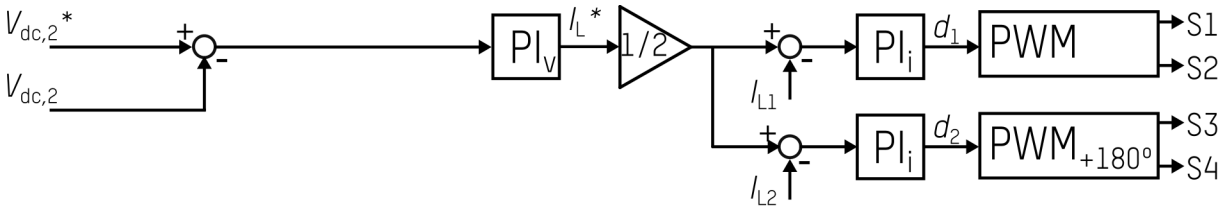

Figure 3.22. DC-DC voltage control closed-loop diagram based on PI regulators.

Increasing the proportional constant and/or reducing the integral time, a faster system response is obtained, but it gets more oscillating. It is worth mentioning that the PID regulator technology is directly discarded as its derivative component increases such noise.

The parameters of the PI regulators for the voltage and current loops are given, respectively, in Table 3.5.

As previously mentioned, this intermediate converter is composed of two paralleled buck converters. Each PWM in Fig. 3.22 is applied to its corresponding buck branch. A phase-shift of 180º is applied between both PWM carrier signals, obtaining two phase-shifted output current waveforms as depicted in Fig. 3.21. Therefore, the total current circulating through the output of the buck converter will result in half of the ripple.

Table 3.5. Proportional and integral constants for the DC-DC voltage control loops.

PI loop	Proportional constant, K_p	Integral constant, K_i
PI_v	0.2	100
PI_i	3.5	1667

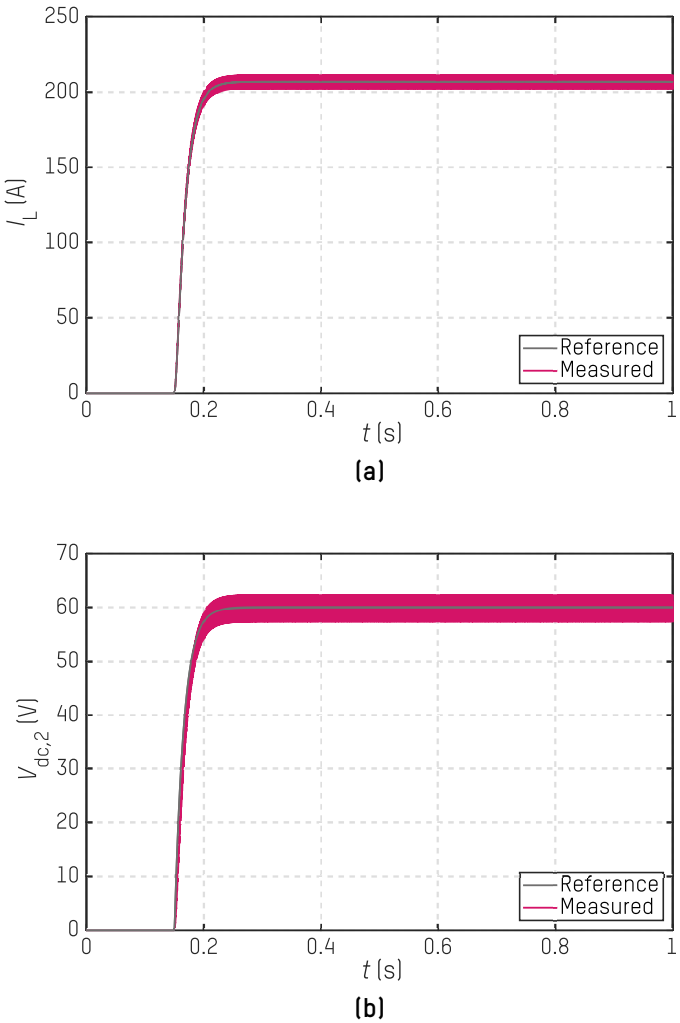

Figure 3.23. Dynamics of the voltage control of the buck converter: (a) currents through the DC-DC buck output, and (b) voltage at the output DC-bus.

In Fig. 3.23a, the transition of the output current control dynamics is plotted to see how accurately they follow the reference value. The regulated DC-bus voltage, $V_{dc,2}$, is obtained by means of the filtering provided by the bus capacitor. The regulated bus voltage, $V_{dc,2}$, dynamics, simulated in Fig. 3.23b, will be determined by the power cycle to be delivered in the hardening process.

3.2.3 H-Bridge Series-Resonant Inverter

Finally, the output stage comprises an H-bridge-type DC-AC switched inverter controlled to generate a square voltage at the output, which is connected to the resonant tank.

The inverter is designed to be easily configurable to provide a versatile machine able to operate with a wide range of loads. A double two-switch branches are employed to form a parallel half-bridge circuit or a simple full-bridge topology. The reason to employ the paralleled HB topology is the possibility to provide the same output currents through the inductor, with half of the currents, compared to the single FB configuration, circulating through each switch branch.

In Fig. 3.24, current and voltage waveforms of the resonant tank and induction load are extracted from the electrical simulations for the inverter's paralleled half-bridge configuration. With the aim of circulating around 500 A rms through the inductor, the constant voltage of 60 V on the input of the inverter has been computed. When paralleling branches on the HB configuration, half of the current is being circulated from each of the devices, i.e., 250 A rms.

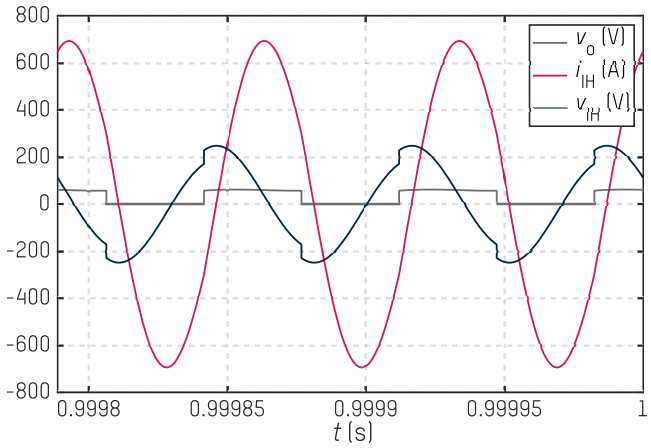

Figure 3.24. Waveforms in the resonant tank and induction load for the inverter's half-bridge configuration.

3.2.3.1 Series-resonant inverter's characteristics

A series LC-circuit has been selected as the resonant tank to optimize the delivered power. The resonant capacitance value is chosen to operate at the desired frequency of the heating process, as the inductive reactance is imposed by the load and wiring.

The resonant capacitor bank, which is located on the light-blue block in Fig. 3.16, is composed of commercial capacitors from CELEM, specially designed for induction heating applications, [199]. The two models employed are C500T and CSP300, respectively captured in Fig. 3.25a and Fig. 3.25b.

Different combinations of these capacitors can be made in order to cover the maximum working range of the series-resonant inverter. In Fig. 3.26, the three-dimensional ren-

(a) (b)

Figure 3.25. Resonant capacitors from CELEM: (a) C500T, and (b) CSP300. [199]

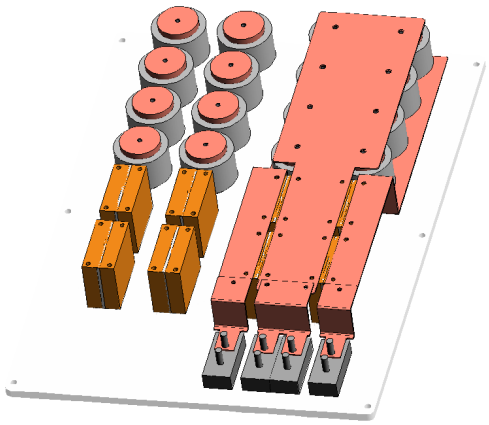

Figure 3.26. Rendering of the resonant capacitors tank.

dering of the board of the resonant capacitors is shown. For the same model, different capacitance values are employed, maintaining the same sizes, so they can be replaced between them to impose the desired resonance condition.

3.2.3.2 Control strategy

For simplicity reasons, the DC-AC inverter in this study will work at constant frequency and a constant duty cycle of 50 %. Working at a fixed switching frequency makes the operation of the inverter independent of the output power regulation, simplifying the control of the electronics; the transferred power is regulated by the intermediate DC-DC. Furthermore, a matching transformer may also be implemented to better adapt to the load's diversity.

3.2.4 Induction Heating Power Conversion System

For simplicity and versatility reasons, seven equal silicon-carbide MOSFET modules are employed to manufacture the power converter under study. The complete power converter detailed scheme is depicted in Fig. 3.27 with the inverter's paralleled half-bridge and full-bridge configurations, respectively drawn in Fig. 3.27a and Fig. 3.27b, [200].

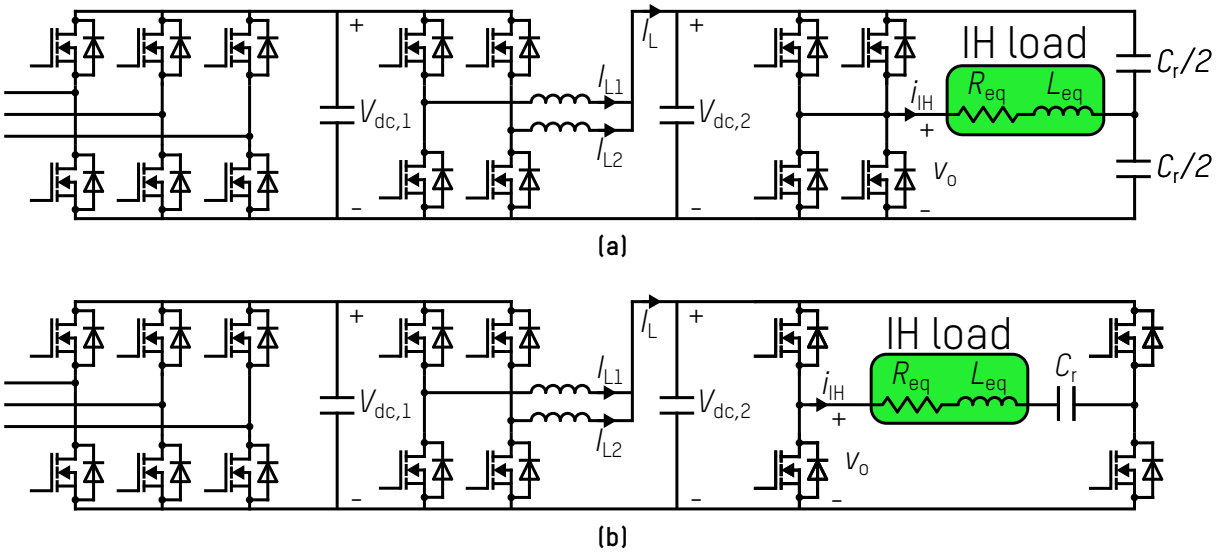

Figure 3.27. Power conversion stages detailed scheme, from left to right: 3-phase rectifier, DC-DC buck, and the inverter's (a) paralleled half-bridge and (b) full-bridge configurations.

3.2.5 Physical Implementation of the IH Test Bench

The complete power converter – the three power conversion stages – is composed of seven Wolfspeed CAB425M12XM3 1200 V and 425 A SiC modules captured in Fig. 3.28a, each implementing a half-bridge inverter composed of two MOSFETs with a drain-source resistance, R_{DS}, of 3.2 mΩ. One of the reasons for employing this module, apart from its high performance for the required electrical specifications, is that commercial driver boards are available to plug on top of the component, greatly simplifying the design of the equipment. In this case, a dual channel differential isolated gate driver XM3 CPM3 SiC in Fig. 3.28b connected to each module has been used to generate the trigger signals at a desired switching frequency on each stage.

On the other hand, the reason for homogenizing the components in all the power conversion stages is to reduce the cost and simplify the assembly – mechanical and thermal designs – of the converter. Bear in mind that we are working in an industrial system where the cost of engineering is large enough, higher than the component costs.

The whole induction heating test bench is captured in Fig. 3.29. In Fig. 3.29a, the front view of the test bench is shown, where the general control block and the induction load are observed. The back view is captured in Fig. 3.29b to focus the resonant capacitors and power converter elements; the blue element is the refrigeration circuit of the inductor.

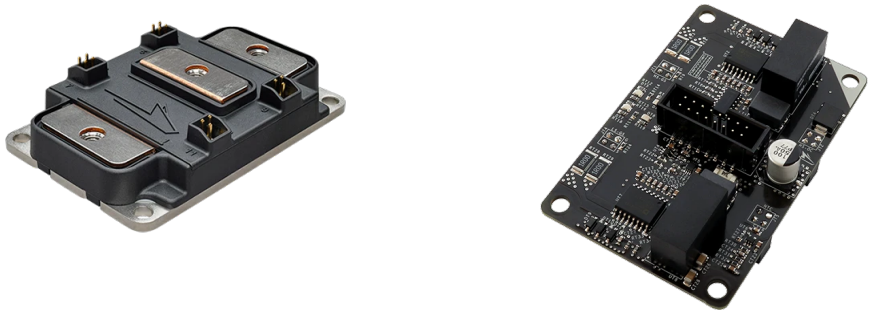

(a) (b)

Figure 3.28. Wolfspeed's power modules: (a) CAB425M12XM3 SiC module, [201], and (b) XM3 CPM3 SiC driver, [202].

(a) (b)

Figure 3.29. Induction heating test bench: (a) front view (load and general control electronics), and (b) back view (resonant capacitors tank in the bottom-left and the power converter in the bottom-right).

Then, those pictures are itemized according to the general power conversion diagram in Fig. 3.16.

The physical implementation of the power conversion stages – including the input filters, all the sensors, and the control board – is captured in Fig. 3.30 prior to being placed in its final location in Fig. 3.29b.

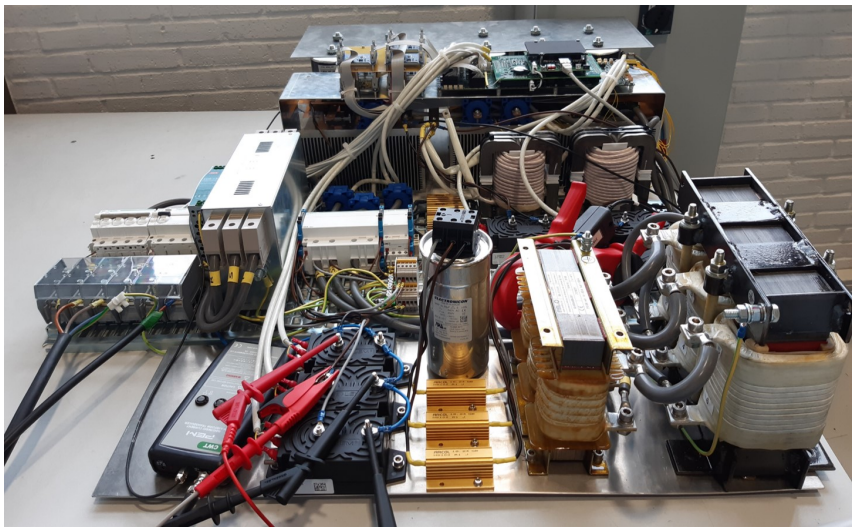

Figure 3.30. Implementation of the power electronics converter.

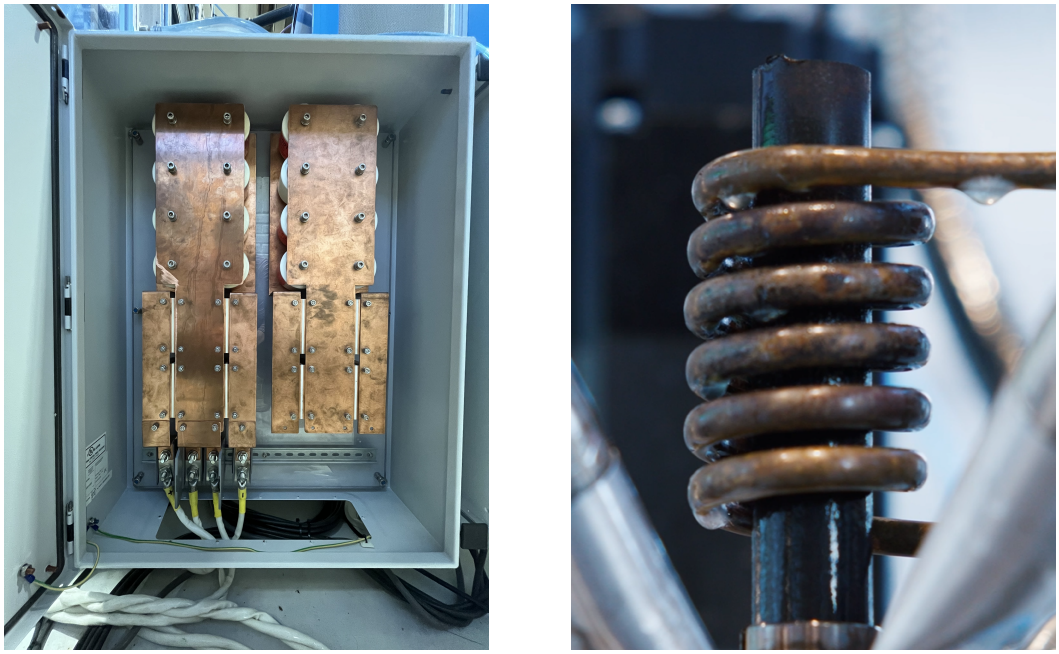

(a) (b)

Figure 3.31. Series resonant tank: (a) configurable resonant capacitor bank, and (b) induction load.

Figure 3.31 shows the practical implementation of the series-resonant tank. The resonant capacitor bank is captured in Fig. 3.31a, in which the configuration in Fig. 3.26 is implemented. Then, Fig. 3.31b presents the induction load, that is, the inductor-workpiece couple. Both the resonant capacitor bank and the IH load are connected to the power converter by means of 35 mm^2 litz wires – 70 μm $\times$ 16000 strands –, which can be observed in both pictures protected with a white-colored electrical insulating cover.

3.3 Series-Resonant Inverter's Versatility Analysis

In this section, the last component of the described induction power converter, i.e., the series-resonant inverter, is particularly analyzed. Various possible configurations are proposed and compared to explore the working ranges of the inverter, aiming for a versatile industrial induction heater.

3.3.1 Resonant Tank Components

In induction heating systems, the resistive and inductive components are imposed by the induction load and the wiring. At the same time, the capacitance value is configured to work in the preferred working conditions.

A typical industrial induction load will be placed at the output of the inverter under study, which consists of a cylindrical steel workpiece surrounded by a multiturn solenoid, as described in Chapter 2.

In every induction heating process, the induction load is represented as a resistor-inductor pair connected in series or parallel, depending on the application; in this case, a series connection is employed. There are different ways to obtain the electrical equivalence of such load. On the one hand, a small-signal measurement is realized by means of LCR meters, with which frequency-dependent *R-L* values are obtained. On the other hand, finite element simulations are carried out to characterize the load as in Chapter 2.

As analyzed in the Chapter 2, the behavior of the metals heated inductively is usually nonlinear; that is, their properties vary with the magnetic field levels. Moreover, temperature dependence is another factor to consider. However, this chapter deals mainly with the magnetic field's frequency dependence issue; therefore, for the sake of simplicity, the material's nonlinearities will not be taken into account.

Figure 3.32 shows the load's performance under small-signal excitation of 10 mA. In this measurement, apart from the coil-workpiece pair, litz wire terminals, whose impedance is significant when it comes to determining the resonance of the system, are included. To get an idea, the induction load itself has an inductance value of around 0.6 μH, and the resistance value does not exceed 5 mΩ at 100 kHz.

These equivalent resistance and inductance values will be employed to realize the inverter's analysis in this section, because this is the impedance that will be perceived from the converter's output.

The capacitive component of the tank is configured in the capacitor bank described in the previous section. This study combines various resonant capacitors from CELEM, [199], of different values; Table 3.6 details the reference material. This analysis employs all parallel combinations of these capacitors to cover the maximum working range of the series-resonant inverter. Likewise, the capacitors' limits will be considered, depending on the data provided by the manufacturer, see Fig. 3.33 and Fig. 3.34.

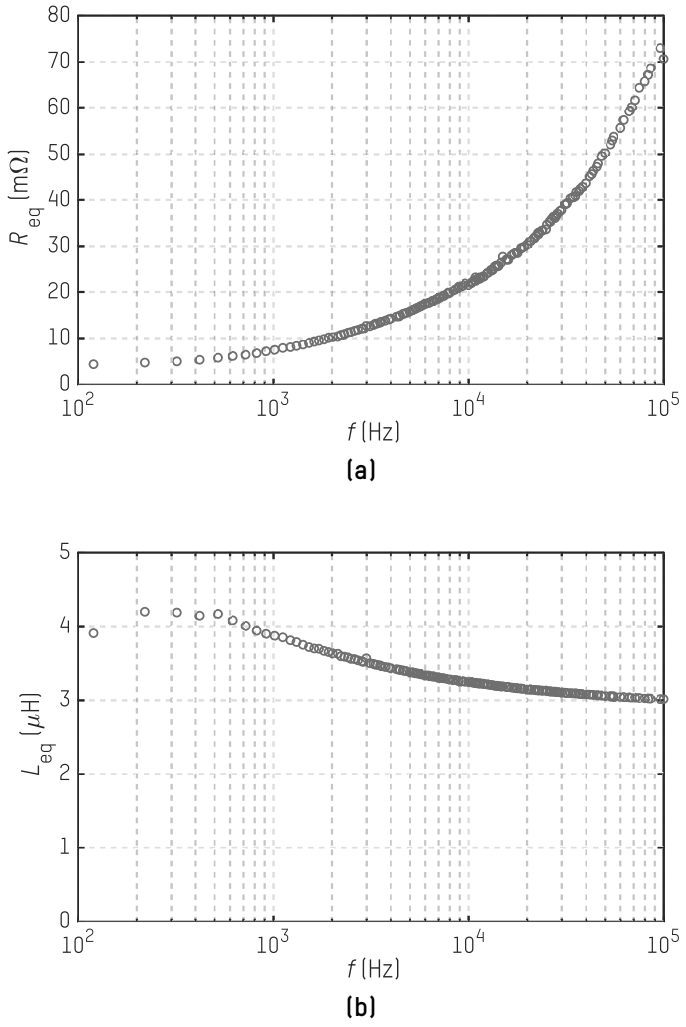

Figure 3.32. Small-signal measurements of the equivalent inductance of the induction load including the litz terminals: (a) equivalent resistance, and (b) equivalent inductance.

Table 3.6. Resonant capacitors under study.

Model	Rendering	Capacitance	Number	Identifier
C500T	Fig. 3.25a	1,4 μF	16	C1
CSP300	Fig. 3.25b	6,3 μF	8	C2
C500T	Fig. 3.25a	21 μF	8	C3
CSP300	Fig. 3.25b	21 μF	4	C4

Moreover, CELEM's MT500 matching transformer, also described in the previous section, is also implemented in this analytical analysis. The transformation ratio, *n*, of 6:1 is considered in this work.

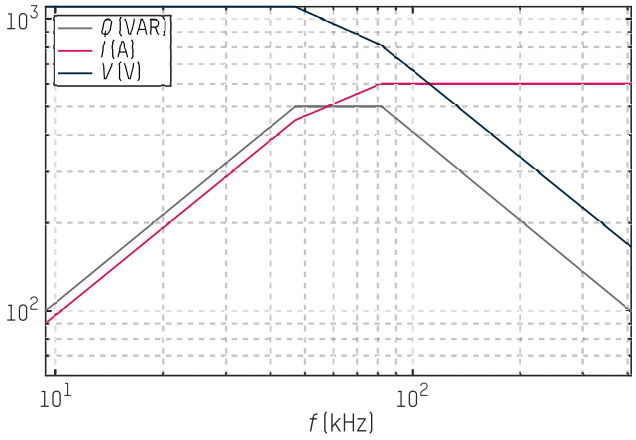

(a)

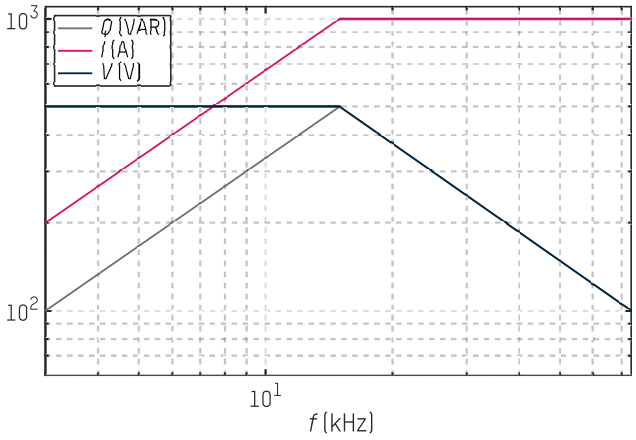

(b)

Figure 3.33. C500T capacitors limits: (a) C1, and (b) C3, [199].

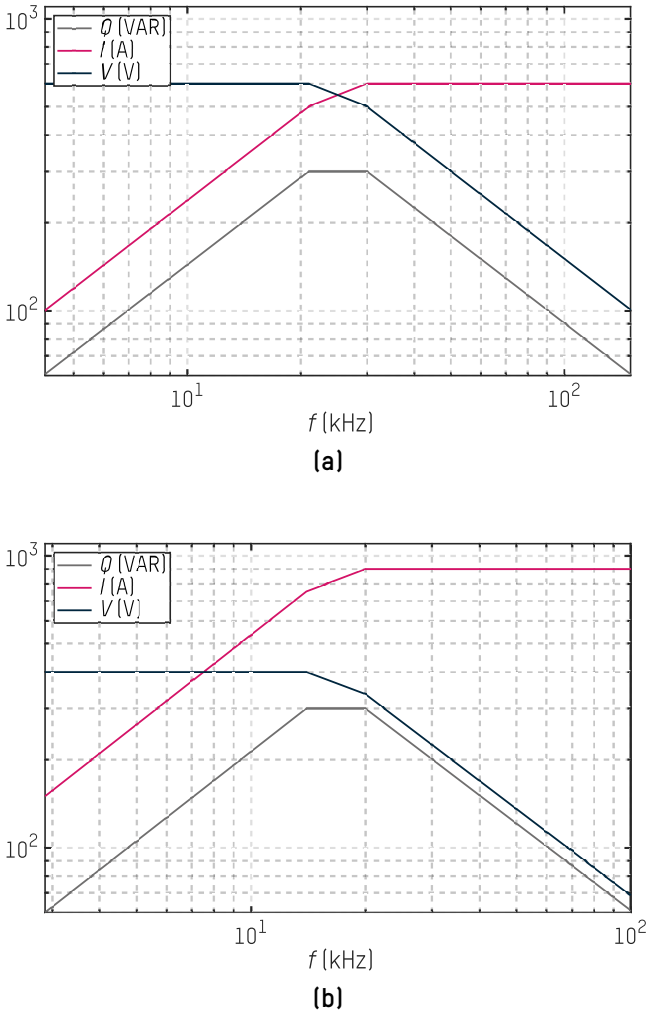

Figure 3.34. CSP300 capacitors limits: (a) C2, and (b) C4, [199].

3.3.2 Comparison of the Series-Resonant Inverter's Configurations

In this task, various configurations of a series-resonant inverter are compared to develop a versatile power converter for industrial induction heating applications.

Figure 3.35 shows the five configurations under study, all configured with two power SiC modules. In the case of the half-bridge (HB) configuration, both branches are paralleled, and the full-bridge (FB) comprises the same two modules. Both bridge-type topologies directly connected to the load are analyzed, and the matching transformer is also implemented; the resonant capacitors are positioned on both the primary and secondary sides of the transformer. It is worth mentioning that the half-bridge (HB) configuration with the resonant capacitor bank on the secondary side of the transformer is discarded because a DC voltage component, due to the topology's nature, saturates the transformer. That is the reason why only five configurations are studied.

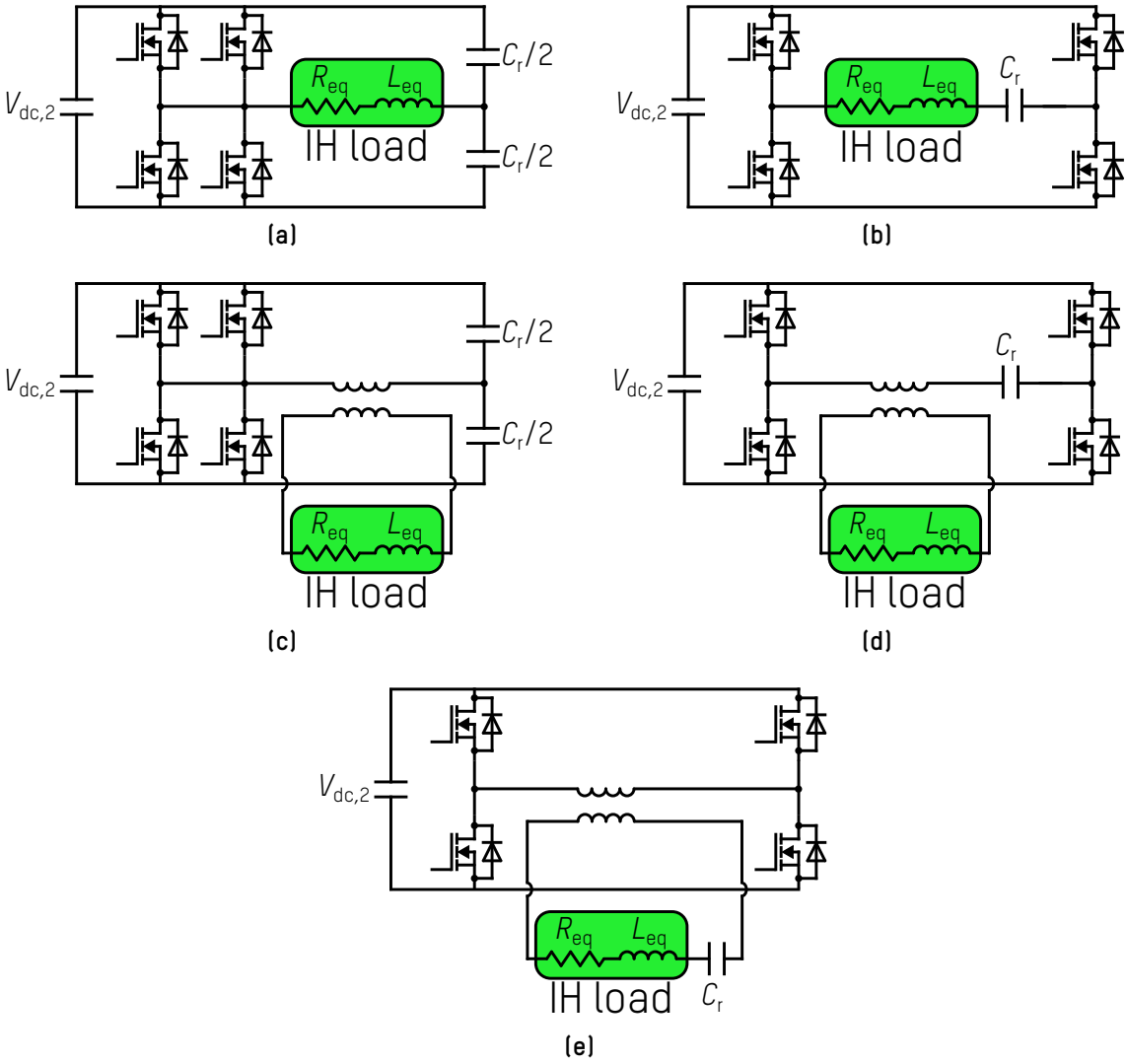

Figure 3.35. Series-resonant inverter's possible configurations: (a) half-bridge and (b) full-bridge configurations directly feeding the load, (c) HB with adapting transformer and C_r in primary side, (d) FB with adapting transformer and C_r in primary side, and (e) FB with adapting transformer and C_r in secondary side.

In Table 3.7, all the analyzed inverter configurations compiled in this work are summarized.

Table 3.7. Series-resonant inverter's configurations overview.

Bridge conf.	Transformer	C_r position	Conf. number	Scheme	P-f curves
half-bridge	no	-	1	Fig. 3.35a	Fig. 3.36a
full-bridge	no	-	2	Fig. 3.35b	Fig. 3.36b
half-bridge	yes	primary	3	Fig. 3.35c	Fig. 3.37a
full-bridge	yes	primary	4	Fig. 3.35d	Fig. 3.37b
full-bridge	yes	secondary	5	Fig. 3.35e	Fig. 3.38

3.3.3 Power-Frequency Curves

The output average active power dissipated in a series-resonant circuit is expressed with the well-known equation in terms of the effective current and voltage:

$$P_{out} = {I_{rms}}^2 R = \frac{{V_{rms}}^2}{Z} R. \tag{3.29}$$

Replacing the resonant tank impedance module, $|Z|$, obtained from (3.1) in (3.29), the complete expression of the output active power of the series-resonant circuit is obtained:

$$P_{out} = \frac{{V_{rms}}^2 R}{R^2 + \left(\omega L - \frac{1}{\omega C}\right)^2}. \tag{3.30}$$

All possible power-frequency curves are mapped in Fig. 3.36, Fig. 3.37, and Fig. 3.38 to explore the operating ranges that each configuration can work in. The five inverter configurations are compared, and their advantages and drawbacks are analyzed.

Several frequency-dependent output power curves are computed from (3.30), combining the capacitors in Table 3.6. The inverter's input DC-bus voltage has been set as a reference parameter to compare the five configurations. Input dc voltages from 10 to 600 V have been used, the latter being the maximum dc voltage limited by the previous conversion stage. All the points that exceed the maximum current set through the modules are not considered as working points. The nominal current, according to the SiC modules datasheet, [201], is 425 A. However, with a prior thermal analysis of the designed cooling circuit, the maximum branch current at steady state regime is estimated to be around 300 A. Moreover, the inverter's conduction losses are also considered for a drain-source resistance of 1.1 mΩ. An approached estimation of the switching losses is also considered in these power-frequency; as the worst case, switching-off losses have been computed assuming operation away from resonance, up to 50 W. In Appendix B, a detailed switching losses estimation is realized for the power converter under study; this analysis is published in [203].

The capacitive operation mode, which is caused when the inverter switches below the resonant frequency, f_r, is directly discarded in the power-frequency map. Therefore, inductive operation mode, above f_r, is considered an acceptable working range.

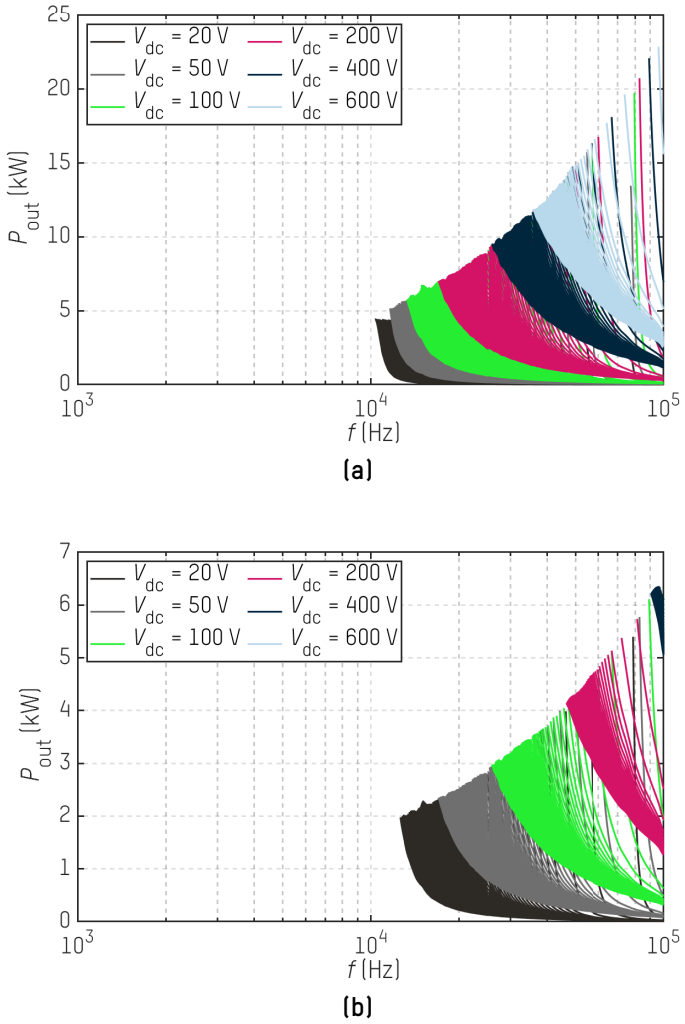

Figure 3.36. Frequency-dependent output power curves for a wide range of resonant capacitance values: (a) half-bridge, and (b) full-bridge configurations directly feeding the load.

Resonant capacitors limit graphs concerning the switching frequency are given by CE-LEM, [199]. The same manufacturer provides the transformer's limits. Each point that exceeds those limits is directly discarded from the plots.

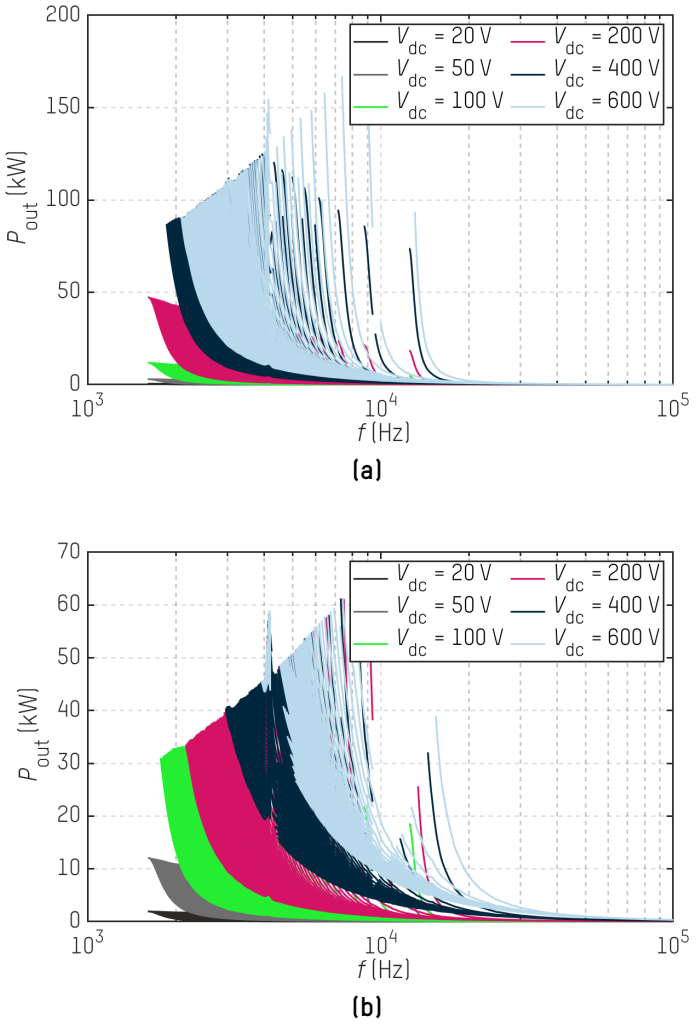

Figure 3.37. Frequency-dependent output power curves for a wide range of resonant capacitance values: (a) HB with transformer and C_r in primary side, and (b) FB with transformer and C_r in primary side.

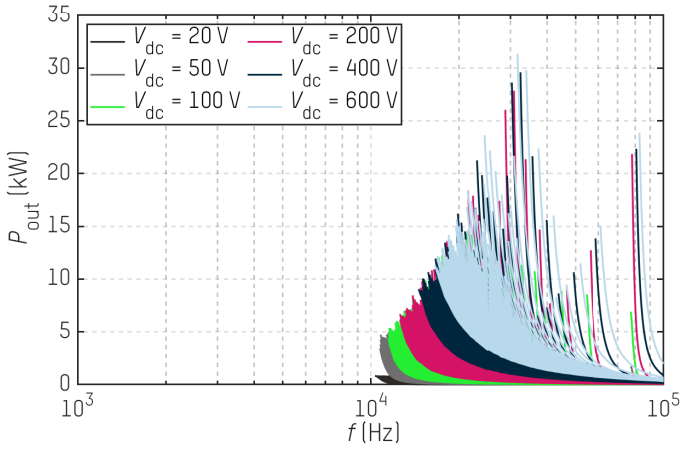

Figure 3.38. Frequency-dependent output power curves for a wide range of resonant capacitance values for the FB configuration with transformer and C_r in secondary side.

3.3.4 Comparison of the Inverter's Configurations

Regarding all the plotted power-frequency curves, it is clearly observed that the resonance condition is changed with the location of the resonant capacitors with respect to the transformer. If the capacitor bank is directly connected to the induction load, the resonant frequency is directly given by (3.2). However, if the transformer is located between the capacitors and the IH load, the capacitance value is multiplied by a factor of n^2, reducing the resonant frequency.

All the curves plotted in Fig. 3.37, Fig. 3.36, and Fig. 3.38 define a permissible working area for each inverter's configuration. All operating regions are plotted in Fig. 3.39 to better compare the five configurations.

This Fig. 3.39 also reflects the effect of placing the capacitors, in the case of using the transformer, on the opposite side of the induction load. When connecting the resonant capacitors on the primary side and the load on the secondary, the inverter can operate at lower frequencies. This can be advantageous for other types of heat treatments, such as tempering or melting, where lower frequencies are needed to penetrate the heat in the whole section of the workpiece.

Another clear conclusion extracted from Fig. 3.39 is that less power is transferred without the transformer. This is due to the MOSFET's channel current restrictions; the transformer allows higher currents to circulate through the load for the same channel current.

Comparing the half-bridge and full-bridge topologies employing the same configurations, i.e., Conf. 1 vs. Conf. 2 or Conf. 3 vs. Conf. 4, the higher output power is transferred to the induction load with the former topology. This happens because the half-bridge topology is developed by the two MOSFET modules connected in parallel, enabling double currents to circulate through the IH load.

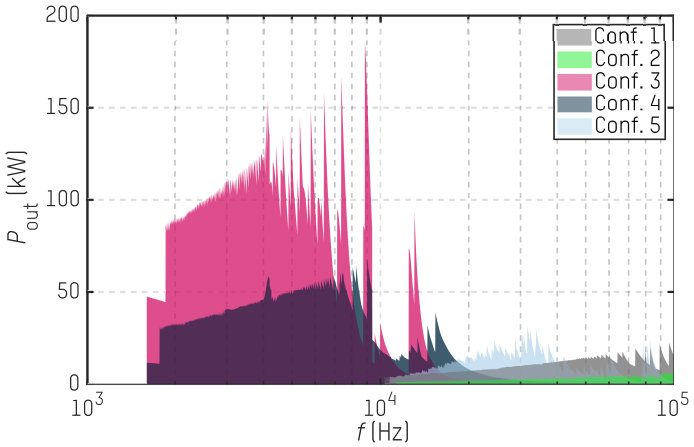

Figure 3.39. Desirable operating area for each configuration.

Finally, the last option places the resonant capacitors on the secondary side of the transformer, directly connected to the load. In this case, only the full-bridge topology is analyzed. The same frequency ranges as those without a transformer are covered, obtaining slightly higher output powers. It was supposed to transfer higher power amounts; however, due to placing the capacitors on the secondary side, all the power-frequency points that get near the resonance condition exceed the CELEM capacitors' limits, therefore, this configuration can easily work under unsafe conditions.

Chapter 4

Dynamic Modeling of the Induction Heating Process

This chapter describes a reduced-order dynamic model of an industrial induction heating system, working from ambient temperature beyond the Curie point and operated by a regulated input-voltage series-resonant inverter. A co-simulation model has been derived to ensure inverter control stability under the variable operating conditions intrinsically associated with the physical properties of the induction load. This model is based on applying a reduction of the parameters obtained from simulations carried out by employing a finite-element analysis tool to use the results in electrical simulation software.

4.1 Introduction to Dynamic Modeling of an Induction Heating Process

The induction heating system required for industrial hardening must work under a wide range of conditions to achieve accurate thermal processing of materials. This system involves a nonlinear light inductive load, where the equivalent impedance depends on both the workpiece's temperature distribution and the applied excitation level during processing.

A versatile inverter topology able to supply the required power to loads of varying characteristics while maintaining robust behavior is proposed to facilitate the control of the power converter. The power converter has to be able to control the power delivered to the load despite the change in its properties to modulate the metallurgical process in the workpiece. Moreover, it should cover a wide range of power levels to ensure proper operation. Additionally, the electronics has to be capable of handling inductive loads with a small resistive component, which may vary considerably throughout an induction heating process for hardening purposes. The basic structure of the proposed system is illustrated in Fig. 4.1.

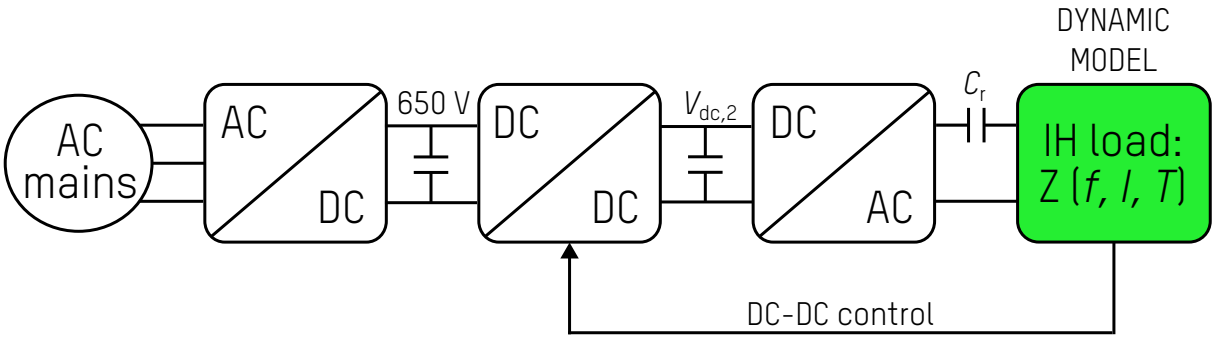

Figure 4.1. Diagram of the dynamic model: power conversion stages with the nonlinear inductive load.

The present modular design improves functionality and provides a clear pathway for upgrades and adjustments, making it a practical choice for various applications.

The induction heating system operates by supplying a medium-frequency current to the load. The heating element consists of a solenoidal-type coil with a few turns. When operating without a workload, the system load is mainly inductive with a small resistive component due to losses in the conductor of the coil. When the workpiece is inserted, the equivalent inductance of the system may change according to the temperature and magnetic conditions, and the system resistance increases due to power delivery to the load.

Above the Curie temperature, the material's magnetic properties are lost, and the induction heating process relies solely on the material's electrical conductivity. However, because the applied power densities are very high and heat diffusion in the workpiece is not instantaneous, significant temperature inhomogeneities can develop within the workpiece. As a result, even if some areas of the workpiece have surpassed the Curie temper-

ature, regions that remain below it can significantly influence the overall electrical behavior of the material. In cases where the Curie temperature has been reached in certain hot spots, but the total energy delivered is insufficient to exceed it throughout the entire workpiece, it becomes essential to model the electrical behavior of the workpiece accurately.

Induction heating generates high heat flux to the workpiece's surface, and therefore, controlling the delivered power enables the precise application of metallurgical treatment to the workpiece's superficial layer.

4.2 DC-DC Dynamic Control

A control strategy based on regulating the second DC-bus voltage level, $V_{dc,2}$, the input of the inverter feeding the induction load, is proposed, with the same final purpose of maintaining the envelope of the AC current through the coil constant. This bus is controlled through the intermediate DC-DC stage, whose closed-loop control schematic is shown in Fig. 4.2. Each loop employs a PI controller to follow the reference signal; from inner to outer loops, current through output inductors of the buck converter, I_{L1} and I_{L2}, is regulated to control the voltage in the output, $V_{dc,2}$, which is imposed to maintain the AC current through the coil, I_{IH}, constant.

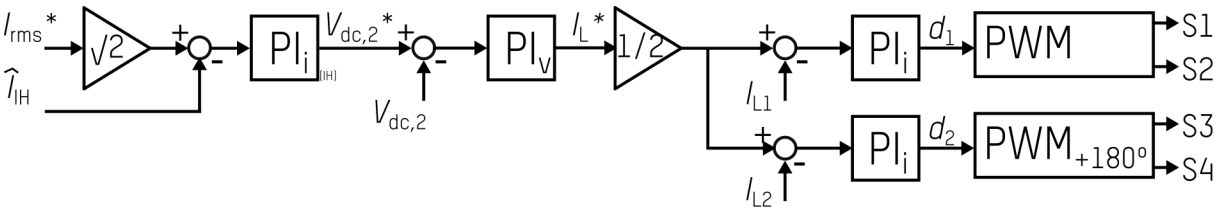

Figure 4.2. Three-loop DC-DC control diagram based on PI regulators to control the current through the coil.

A third current loop, PI_i, is added to this strategy, which may slightly delay the response of the control dynamics. Furthermore, with this strategy, the voltage in the second DC-bus is controlled.

The parameters of the PI regulators for the three voltage and current loops are given in Table 4.1.

Table 4.1. Proportional and integral constants for three-loop DC-DC control.

PI loop	Proportional constant, K_p	Integral constant, K_i
$PI_{i_{(IH)}}$	3	1
PI_V	0.2	100
PI_i	3.5	1667

4.3 Reduced-Order Dynamic Model

The results from Chapter 2 provide a good description but are not practical for predicting the entire system's performance because of the high computational cost. Combining the simulation results from the finite element analysis tool with electronic circuit simulation software like MATLAB®/Simulink, [204] can be beneficial. An accurate definition of the reduced-order model based on physical considerations for modeling the induction-workpiece load and its inclusion into the electronic simulation tool can be valuable. This reduced-order model was first published in [205], [206] and further developed in [207].

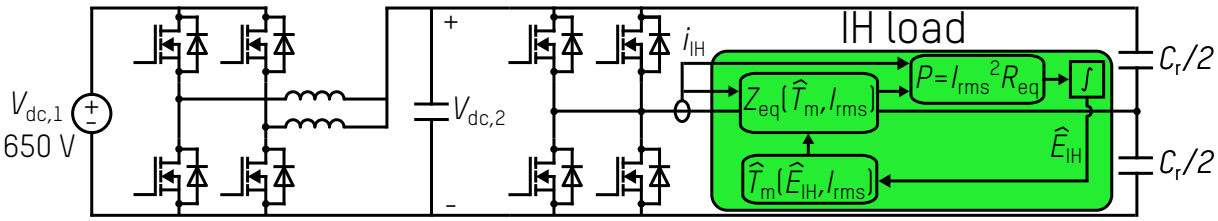

Figure 4.3. Schematic of the dynamic model of the IH system under study: power converter with the nonlinear load.

The equivalent impedance of the induction load with the workpiece has several parameter dependencies. Although it does not constitute a complete description of the electrical behavior, it is appropriate to indicate that the equivalent impedance can be determined as follows since it presents a good balance between complexity and descriptive power:

$$Z_{eq}\left(f, I_{rms}, \widehat{T}_m\right) = R_{eq}\left(f, I_{rms}, \widehat{T}_m\right) + j\omega L_{eq}\left(f, I_{rms}, \widehat{T}_m\right), \tag{4.1}$$

where f represents the working frequency, I_{rms} is related to the amplitude of the applied current, and $\widehat{T}_m$ is the estimated temperature of the central region of the workpiece.

The proposed reduced-order equivalent impedance at a fixed operating frequency, $f = f_{IH}$, will be represented as:

$$Z_{eq}\left(I_{rms}, \widehat{T}_m\right) = R_{eq}\left(I_{rms}, \widehat{T}_m\right) + j\omega L_{eq}\left(I_{rms}, \widehat{T}_m\right), \tag{4.2}$$

which is depicted inside the green highlighted area in Fig. 4.3.

The detailed procedure to estimate the equivalent impedance of the IH load $Z_{eq}\left(I_{rms}, \widehat{T}_m\right)$ will be detailed as follows.

4.3.1 Current Level and Estimated Temperature

In the proposed reduced-order model, the level of current feeding the inductor-workpiece system plays an important role. As mentioned in the aforementioned assumptions, when operating near resonance, the most significant current component is the one given

at its fundamental frequency. Therefore, being a practically sinusoidal waveform, the relationship between the current amplitude and its effective value, I_{rms}, is immediate, so both values can be used interchangeably. Note that the current I_{rms} will be determined by the operational conditions in the circuit simulation model.

On the other hand, the reduced-order model also depends on the temperature, T_m, in the key point given by the central region of the workpiece; and at the same time, T_m depends on the total energy delivered to the workpiece, $\widehat{E}_{IH}$, obtained from the integral of the delivered power at each moment. Moreover, a second factor related to the heating rate of the workpiece is also considered in the T_m estimation. The heating rate will be given by the amplitude of the current, I_{rms}, with which the load is fed, because the characteristic of the load depends on current level. In order to simplify the treatment, a factorization into two terms, each dependent on the estimation of the total energy, $\widehat{E}_{IH}$, and the current, I_{rms}, respectively, is proposed as follows::

$$\widehat{T}_m\left(\widehat{E}_{IH}, I_{rms}\right) = \widehat{T}_E\left(\widehat{E}_{IH}\right) \cdot \widehat{T}_I\left(I_{rms}\right), \tag{4.3}$$

where $\widehat{T}_E\left(\widehat{E}_{IH}\right)$ and $\widehat{T}_I\left(I_{rms}\right)$ are factors dependent on the provided energy to the workpiece and the current level, respectively.

The temperature of the workpiece has different dependencies according to the regions observed in Fig. 2.34; this approach considers two dependencies. The induction energy transfer process is more efficient below the Curie temperature, T_C, where the material possesses ferromagnetic properties. Above T_C, a phase transition occurs where the material no longer has magnetic properties, and the temperature rises slower. In order to capture this behavior, the following temperature factors are proposed concerning the estimated delivered energy based on the observed behavior:

$$\widehat{T}_E\left(\widehat{E}_{IH}\right) = \begin{cases} T_0 + C_{T_E}\widehat{E}_{IH}^{\,n_{T_E}} & T_m < T_C \\ T_{brk} + C'_{T_E}\left(\widehat{E}_{IH} - E_{brk}\right)^2 & T_m \geq T_C, \end{cases} \tag{4.4}$$

where T_0 is the initial temperature, n_{T_E} and C_{T_E} are the exponent and proportionality factor, respectively, fitted to a potential function for the dependence below the Curie temperature. E_{brk} is the cumulative energy to reach the breaking temperature, T_{brk}, close to the Curie point, and C'_{T_E} is the factor of proportionality of the quadratic dependence with excess energy from the Curie temperature, respectively.

Regarding the current-dependent factor $\widehat{T}_I\left(I_{rms}\right)$, a polynomial expression has been considered, including only the dependence below the Curie temperature, as follows:

$$\widehat{T}_I\left(I_{rms}\right) = \begin{cases} \frac{\sum_{i=0}^{2} C_{T_I,i} {I_{rms}}^i}{\sum_{i=0}^{2} C_{T_I,i} {I_{ref}}^i} & T_m < T_C \\ 1 & T_m \geq T_C, \end{cases} \tag{4.5}$$

where $C_{T_I,i}$ proportionality factors will be adjusted in the following lines.

The coefficients are adjusted by means of a curve fitting tool, and the results are afterward depicted in Fig. 4.4. The initial temperature, T_0, is set to the ambient temperature of 22 ºC.

For the equations below the Curie temperature, the exponent and proportionality factors, respectively, are $n_{T_E} = 0.6777$ and $C_{T_E} = 0.6055$. Instead, for above Curie expression, the proportionality factor C'_{T_E} takes the value of $4.0017 \cdot 10^{-8}$.

Moreover, according to the current dependence, the adjustment provides the coefficients $C_{T_I,0} = 621.1191$, $C_{T_I,1} = 0.6627$, and $C_{T_I,2} = 1.0691 \cdot 10^{-5}$, respectively. These coefficients are fitted for a reference current, I_{ref}, of 500 A rms.

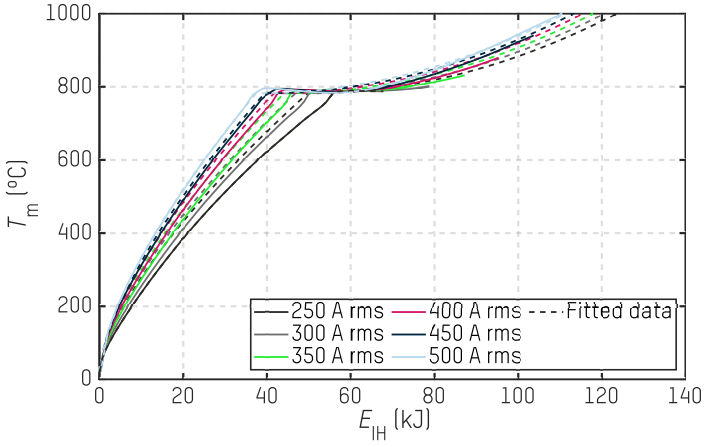

Figure 4.4. Comparison of simulated data and fitted curves for the middle point temperature of the billet's surface.

In Fig. 4.4, the comparison between fitted curves and simulation results in COMSOL® with respect to the temperature in the central region of the workpiece is shown. As can be seen, the fit is quite good. However, a more significant error is observed at the lowest current values, I_{rms}, due to the difficulty of accurately capturing the behavior with a small number of parameters. In any case, the accuracy achieved will be sufficient to obtain valid results.

4.3.2 Impedance Dependence on the Estimated Parameters

Polynomial expressions are used to model the equivalent impedance $Z_{eq}\left(I_{rms}, \widehat{T}_m\right)$ because they provide an analytical solution that can precisely capture an extended range of behaviors. The equivalent resistance, R_{eq}, and inductance, L_{eq}, expressions are dependent on the estimated temperature, $\widehat{T}_m$, and current level, I_{rms}. These expressions are obtained by factorizing each dependency equation, as it is provided as follows:

$$R_{eq}\left(I_{rms}, \widehat{T}_m\right) = R_T\left(\widehat{T}_m\right) \cdot R_I\left(I_{rms}\right) \tag{4.6}$$

and

$$L_{eq}\left(I_{rms}, \widehat{T}_m\right) = L_T\left(\widehat{T}_m\right) \cdot L_I\left(I_{rms}\right). \tag{4.7}$$

The expressions for (4.6) and (4.7) have a similar structure but with different coefficients. These coefficients are associated with the temperature, $\widehat{T}_m$, and current level, I_{rms} dependencies, respectively. The fitting is divided in the two regions delimited by the material's Curie Temperature, T_C: below and above the Curie temperature, T_C, with a transitional temperature ΔT to ensure stability in the simulation without sacrificing precision. Additionally, the temperature dependence requires a higher order polynomial compared to the current dependence to accurately approximate the behavior.

The factors for the temperature dependence are as follows:

$$R_T\left(\widehat{T}_m\right) = \begin{cases} \sum_{i=0}^{6} C_{R_T,i} \widehat{T}_m{}^i & \widehat{T}_m < T_C \\ \sum_{i=0}^{3} C'_{R_T,i} \widehat{T}_m{}^i & \widehat{T}_m \geq T_C + \Delta T \end{cases} \tag{4.8}$$

and

$$L_T\left(\widehat{T}_m\right) = \begin{cases} \sum_{i=0}^{6} C_{L_T,i} \widehat{T}_m{}^i & \widehat{T}_m < T_C \\ \sum_{i=0}^{3} C'_{L_T,i} \widehat{T}_m{}^i & \widehat{T}_m \geq T_C + \Delta T. \end{cases} \tag{4.9}$$

Conversely, no current level dependence, I_{rms}, is observed above the Curie temperature, T_C as the magnetic properties of the workload vanish, and consequently, the equivalent impedance loses its dependence on this parameter. As a result, the factor with respect to the current level, I_{rms}, can be expressed as:

$$R_I\left(I_{rms}\right) = \begin{cases} \frac{\sum_{i=0}^{2} C_{R_I,i} I_{rms}{}^i}{\sum_{i=0}^{2} C_{R_I,i} I_{ref}{}^i} & \widehat{T}_m < T_C \\ 1 & \widehat{T}_m \geq T_C \end{cases} \tag{4.10}$$

and

$$L_{\mathrm{l}}\left(I_{\mathrm{rms}}\right)=\begin{cases}\frac{\sum_{\mathrm{i}=0}^{2} C_{\mathrm{L_l,i}} {I_{\mathrm{rms}}}^{i}}{\sum_{\mathrm{i}=0}^{2} C_{\mathrm{L_l,i}} {I_{\mathrm{ref}}}^{i}} & \widehat{T}_{\mathrm{m}}<T_{\mathrm{C}} \\ 1 & \widehat{T}_{\mathrm{m}}\geq T_{\mathrm{C}}.\end{cases} \tag{4.11}$$

Table 4.2. Temperature-dependent coefficients for below Curie's point, $T_{\mathrm{m}} < T_{\mathrm{C}}$.

i	$C_{\mathrm{R_T,i}}$	$C_{\mathrm{L_T,i}}$
0	-0.0331	$-7.6398 \cdot 10^{-10}$
1	$5.1118 \cdot 10^{-4}$	$5.6922 \cdot 10^{-9}$
2	$-2.0662 \cdot 10^{-6}$	$-2.3673 \cdot 10^{-11}$
3	$4.6521 \cdot 10^{-9}$	$5.4237 \cdot 10^{-14}$
4	$-5.8262 \cdot 10^{-12}$	$-6.8645 \cdot 10^{-17}$
5	$3.8162 \cdot 10^{-15}$	$4.5309 \cdot 10^{-20}$
6	$-1.0197 \cdot 10^{-18}$	$-1.2184 \cdot 10^{-23}$

Table 4.3. Temperature-dependent coefficients for above Curie's point, $T_{\mathrm{m}} \geq T_{\mathrm{C}}$.

i	$C'_{\mathrm{R_T,i}}$	$C'_{\mathrm{L_T,i}}$
0	1.1953	$1.3487 \cdot 10^{-5}$
1	-0.0029	$-3.0867 \cdot 10^{-8}$
2	$2.3028 \cdot 10^{-6}$	$2.4655 \cdot 10^{-11}$
3	$-6.2056 \cdot 10^{-10}$	$-6.6043 \cdot 10^{-15}$

Table 4.4. Current-dependent coefficients for below Curie's point, $T_{\mathrm{m}} < T_{\mathrm{C}}$, for a reference current, I_{ref}, of 500 A rms.

i	$C_{\mathrm{R_l,i}}$	$C_{\mathrm{L_l,i}}$
0	0.0585	$1.1819 \cdot 10^{-6}$
1	$-7.3044 \cdot 10^{-5}$	$-1.4958 \cdot 10^{-9}$
2	$4.9189 \cdot 10^{-8}$	$1.2137 \cdot 10^{-12}$

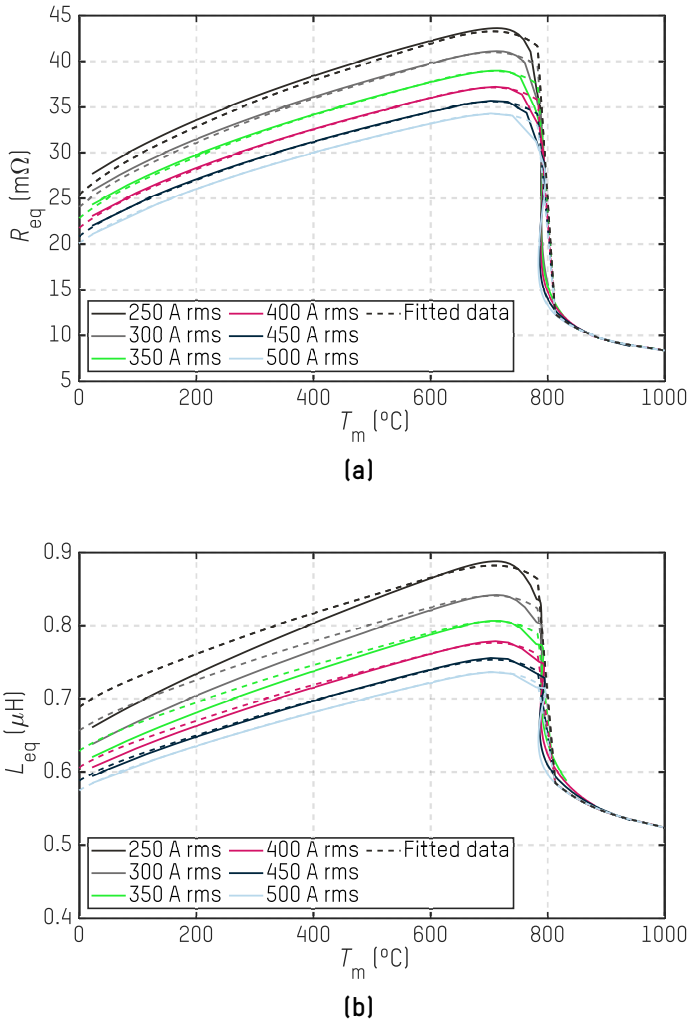

Figure 4.5. Comparison of simulated data and fitted curves: (a) equivalent resistance, and (b) equivalent inductance.

Table 4.2 and Table 4.3 present the coefficients to fit the temperature-dependent impedance below and above T_C, respectively. The order of the polynomials was determined by assessing whether the fitting error was acceptable. Above the Curie temperature, the behavior of the workpiece is more straightforward, and it is not necessary to use a polynomial of such a high order as is required for temperatures below the Curie temperature. On the other hand, in Table 4.4, current-dependent coefficients are shown for temperatures below T_C.

The polynomial curves obtained are depicted in Fig. 4.5a and Fig. 4.5b, along with their corresponding curves obtained from COMSOL Multiphysics®. As can be seen, the factorization of the equivalent resistance and inductance gives a pretty accurate representation of an extended range of parameters.

Furthermore, as can be observed in Fig. 4.5a and Fig. 4.5b, both R_{eq} and L_{eq} exhibit sharp and non-monotonic variations during the steep decrease after the Curie temperature. The

variations may be associated with instabilities in the model. To prevent convergence issues in the subsequent electrical simulation, this transition needs a negative linear slope for at least the following $\Delta T = 30$ °C above the Curie temperature T_C to ensure stability of the system.

4.4 Reduced-Order Dynamic Model's Implementation

The reduced equation-based dynamic model in the previous section has been implemented in the electrical simulation tool MATLAB®/Simulink, to simulate dynamically the power conversion stages of the induction heating power converter.

The model simulated through MATLAB®/Simulink software is summarized in Fig. 4.6. The simulation model starts from a DC voltage source of 650 V in the first DC-bus, $V_{dc,1}$, which will replace the three-phase PFC rectifier just for simplicity.

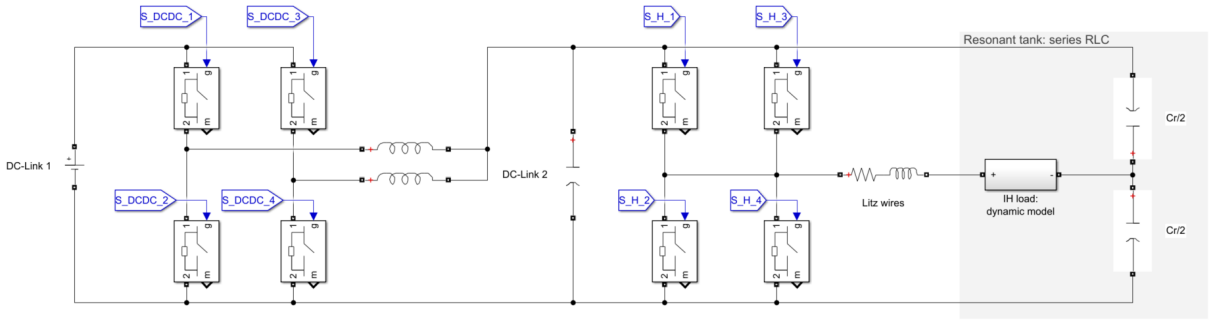

Figure 4.6. Capture of the simulated power conversion stages in MATLAB®/Simulink.

The objective of this work is to simulate the whole induction heating process to ensure that the working dynamics of the control loops are stable even if the Curie temperature is reached, as beyond this point, the load presents a rapid electrical characteristics variation.

The simulation is carried out for a specific operation point, which will afterward be replicated in the laboratory setup in Chapter 5. These working conditions are set to deliver a controlled constant current of 500 A rms and 14.2 kHz through the load, slightly above the self-resonant frequency of the output RLC tank. At this point, it is worth mentioning that the resonance is given in part by the inductance value of the litz wires that connect the voltage-fed inverter with the resonant tank. Therefore, the impedance of these wires is added in the electrical simulation connecting in series an R-L pair, measured in Chapter 5, to the IH load.

As captured in Fig. 4.6, ideal switch components represent the real SiC modules. However, the drain-source on-state resistance and package resistances are added, and the stray inductance of the modules is also considered in the electrical simulation.

According to the DC-DC regulation strategy, the same control parameters described in Chapter 3 are used. The values of the rest of the electrical components employed in the electrical simulation are taken from Chapter 3.

4.4.1 Temperature and Impedance Estimation from the Reduced Model

Fig. 4.7 shows the temperature evolution at the midpoint of the workpiece during the application of 500 A rms over a 30-second cycle time, incorporating a soft start in the first second. The graph indicates that the Curie temperature is reached after 5 seconds. Following this point, the rate of temperature increase slows significantly as the magnetic properties of the workpiece begin to disappear.

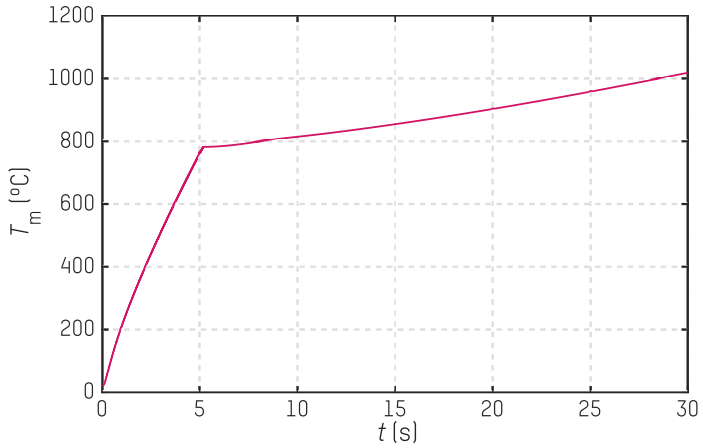

Figure 4.7. Estimated temperature in the middle point of the billet's surface, $\widehat{T}_m$, during a transient of time extracted by electrical simulation.

In Fig. 4.8, it can be seen that between room temperature and the Curie temperature, both resistance and inductance increase due to the temperature dependence of the physical properties of the material. After 5 seconds, both values start to decrease because a larger region of the material reaches the Curie temperature. This trend continues until around 10 s, when the material becomes magnetically saturated in the area where power dissipation occurs, as a result of exceeding the Curie temperature. Beyond 10 seconds, the changes in both components of the impedance are primarily influenced by the increase in electrical conductivity as the temperature rises.

As can be observed in Fig. 4.8, the Curie temperature is reached at around $t = 5$ s, just when the equivalent resistance, in Fig. 4.8a, and the inductance, Fig. 4.8b, start to decline.

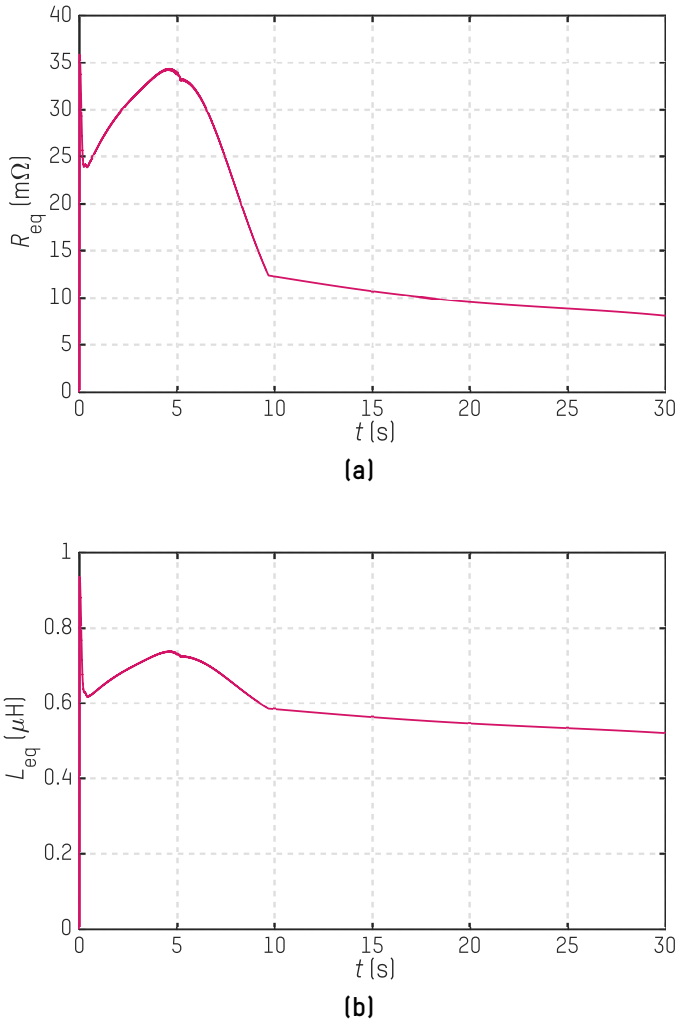

Figure 4.8. Equivalent impedance during a transient of time extracted by electrical simulation: (a) resistance, and (b) inductance.

4.4.2 Electrical Simulation Results

From Fig. 4.9, the designed current control dynamics are considered fast enough to maintain a stable current in the load during the initial transient and rapid impedance variation as the Curie temperature in the workpiece is exceeded. The simulated effective current, I_{rms}, correctly follows the 500 A rms set as a reference, I_{rms}*, with a slight ripple.

In Fig. 4.10, the reference and simulated voltages on the second DC-bus are depicted, respectively, $V_{dc,2}$* and $V_{dc,2}$. Two transitions are clearly marked on the simulated voltage buck's output voltage, related to the same transitions resulting in the equivalent resistance. This is due to the temperature-dependent expression of the equivalent resistance, divided into three ranges. As detailed in the previous section, the resistance below Curie temperature is modeled as a polynomial; then, there is a transition where a linear dependence is assumed, and for higher temperatures, its descent slope is modeled as another

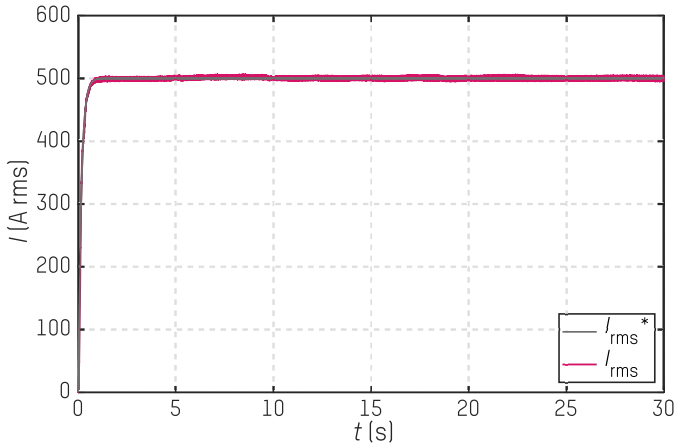

Figure 4.9. Simulated effective current through the induction coil.

polynomial of lower order. In other words, this transient voltage shape is equal to the resistance ones, because the current is maintained constant during the thirty seconds.

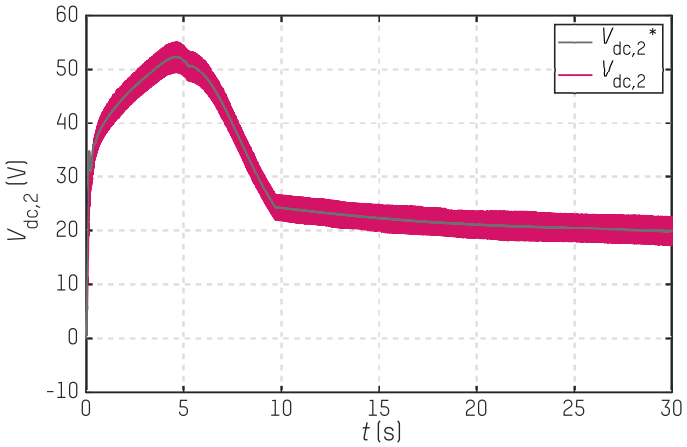

Figure 4.10. Simulated second DC-bus voltage through the induction coil.

Output currents through the DC-DC buck converter's output two branches are plotted in Fig. 4.11. In this figure, almost constant and equal DC currents are observed, which have been used to control this intermediate DC-DC stage.

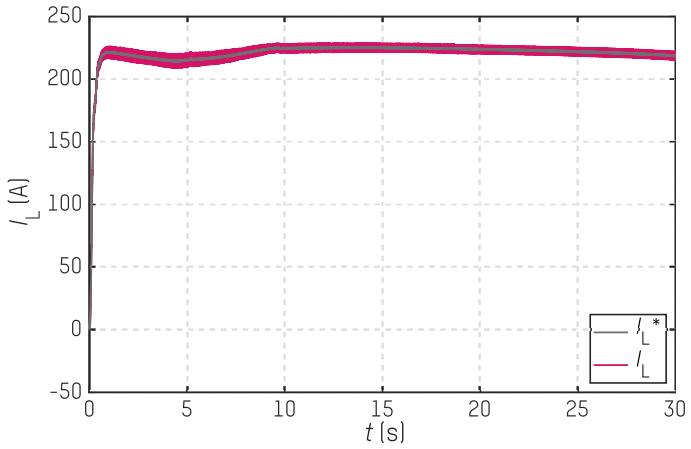

Figure 4.11. Simulated current through the DC-DC buck output inductor, I_L.

The simulated inductor currents, I_L, adequately follow the reference created by the selected control strategy, I_L*. Moreover, the sum of those currents is multiplied by the voltage in Fig. 4.10 to compute the DC-DC converter's output power, which, at the same time, is the input power of the series resonant inverter.

Then, Fig. 4.12 represents active power balance on each power stage. $P_{inv,in}$ and $P_{inv,out}$ are, respectively, the input and output powers of the inverter, and the P_{ind} is the induced power, in other words, the active power delivered into the workpiece.

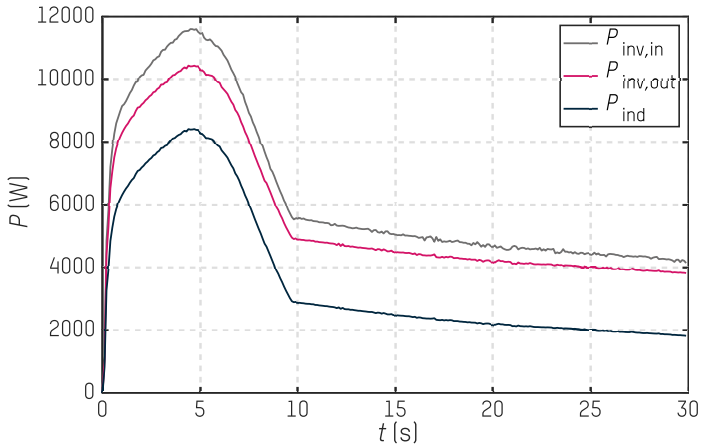

Figure 4.12. Itemized simulated active power balance.

The power losses in the inverter and the resonant tank are drawn in Fig. 4.13. The former is the difference of the inverter's input and output powers, $P_{inv,in}$ - $P_{inv,out}$. Instead, the latter corresponds to the difference between the inverter's output power and the induced active

power to the load, $P_{inv,out}$ - P_{ind}, which corresponds to power losses in litz wire terminals, [208], resonant capacitors, and the induction coil.

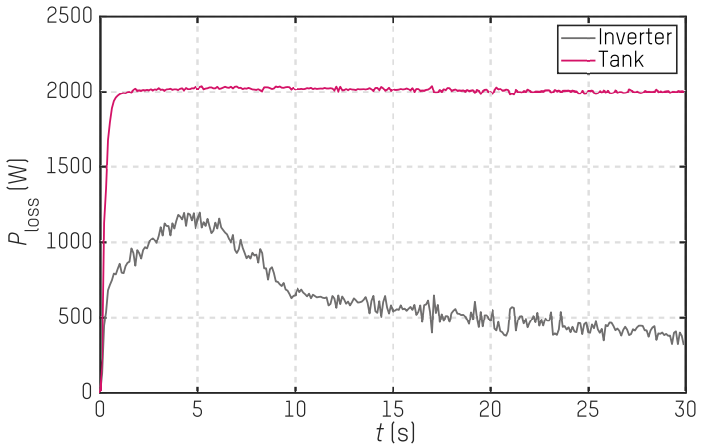

Figure 4.13. Power losses computed by electrical simulation.

After itemizing those power losses, the efficiency of the induction system is computed in Fig. 4.14. The system's efficiency reaches 70 % of value at the maximum point just before the Curie temperature, and it varies with the induction load's electrical characteristic variation, decreasing its value below 50 % at the end of the heating.

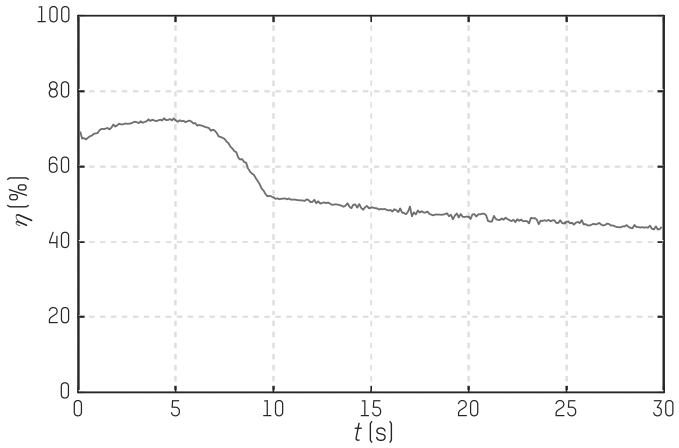

Figure 4.14. Efficiency analysis extracted by electrical simulation.

4.5 Comparison between Cases of Interest

In this section, two different cases of interest are studied with the dynamic model to electrically simulate different heating processes. These two new simulations differ depending on the current reference to be followed.

First, a lower current reference is given as input. In this way, the superficial areas of the billet last longer to reach the Curie temperature, while the heat is penetrating through the inner areas. Thus, lower current amplitudes result in higher hardened layers. To lower the current can be interesting for a through-hardening process.

Different heat treatments than hardening can be realized with different input recipes. For instance, the annealing process needs to maintain the temperature constant at a certain level significantly below the Curie point. Therefore, an option, while using the power converter topology analyzed in this dissertation, is to use a pulsed-current reference.

In both of them, the same simulation time of 30 seconds has been used. Those two cases directly affect the heating process of the billet, which will obtain different mechanical properties.

4.5.1 Different Constant Current Levels

In a first step, some constant current references are introduced in Fig. 4.15, but also applying a soft start to protect the components of the inverter. Three different configurations at current levels of 350 A rms, 450 A rms, and 500 A rms have been simulated in order to give a comparison of the main parameters. As can be seen, the control is able to provide the desired current in all the cases.

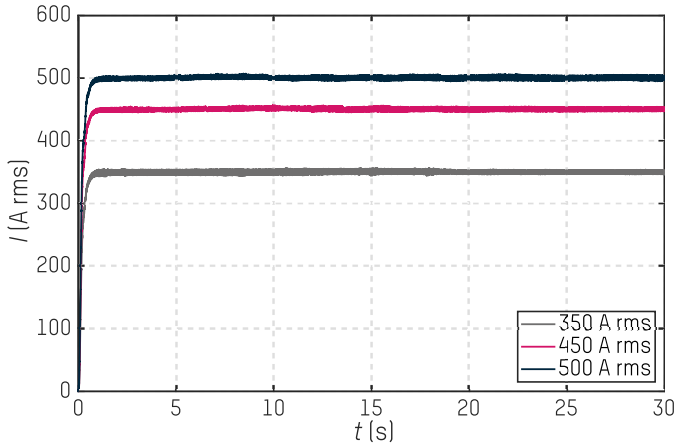

Figure 4.15. Current levels applied to the induction coil.

As shown in Fig. 4.16, at all current levels, there is a rapid increase in temperature at the midpoint up to the Curie temperature, above which the temperature increases slowly due to a decrease in power transfer to the surface of the part. Obviously, the instant at which this Curie temperature is reached depends largely on the level of current applied because at higher current values, the phase transition occurs earlier, resulting in the loss of the material's magnetic properties.

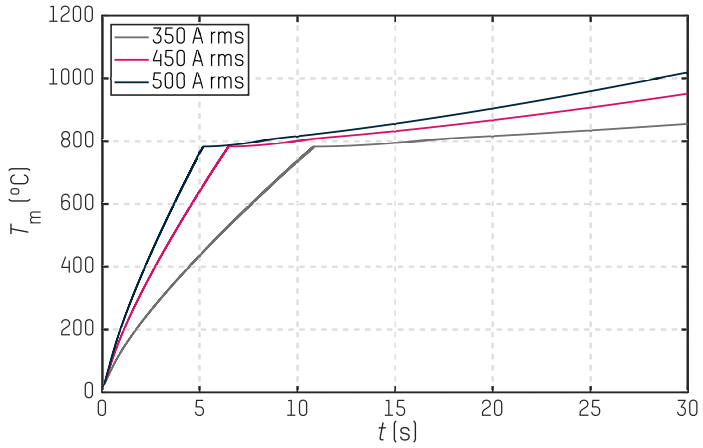

Figure 4.16. Estimated temperature in the middle point of the billet's surface, $\widehat{T}_m$, during a transient of time extracted by electrical simulation.

In Fig. 4.17, it can be observed that, compared with its equivalent of 500 A rms reference, the phase transition is delayed in time because it depends on the power transferred to the workpiece. This delay is due to slowing down the billet's superficial mid-point temperature evolution while delivering lesser power levels. In addition, it can be observed that the impedance levels reached are higher because a lower power level is associated with slower heating of the part, but with greater homogeneity in the temperature distribution.

The power transferred to the workpiece, as shown in Fig. 4.18, exhibits a smoother profile as the applied current decreases. This suggests that if strong temperature gradients are to be applied to the workpiece material, it is advisable to use higher current levels. Moreover, the induction system's efficiency is plotted in Fig. 4.19 for different current levels, which significantly reduces after reaching the Curie temperature. This Fig. 4.19 shows that the efficiency depends on the temperature in the load. Lower currents through the inductor deliver lower power to the load, so the heating is slower, and efficiency is maintaind higher for more time.

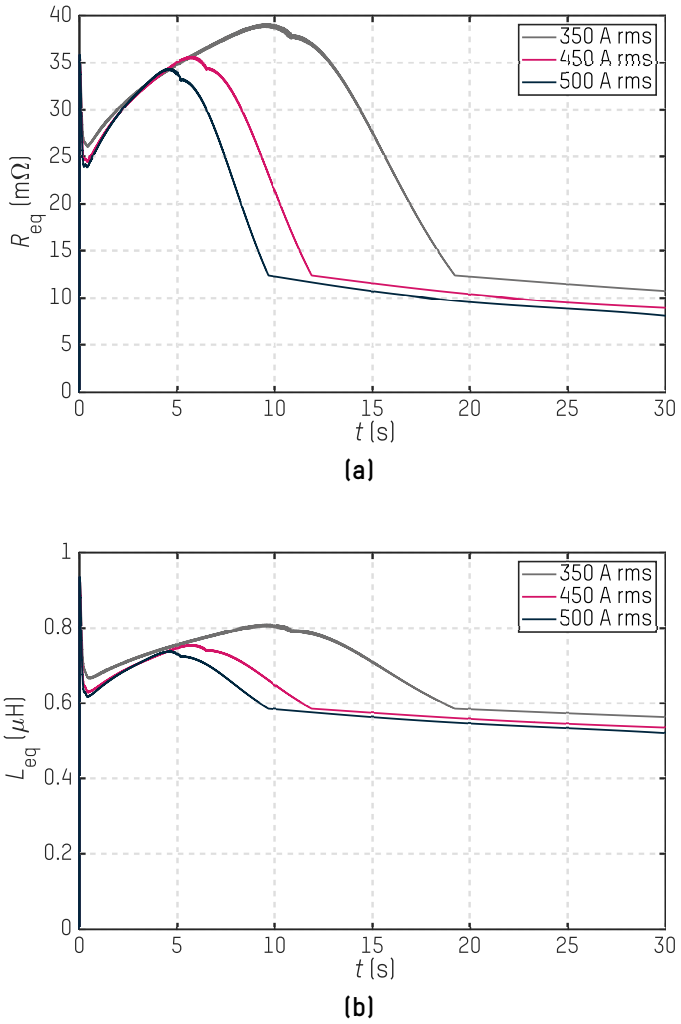

Figure 4.17. Equivalent impedance during a transient of time extracted by electrical simulation: (a) resistance, and (b) inductance.

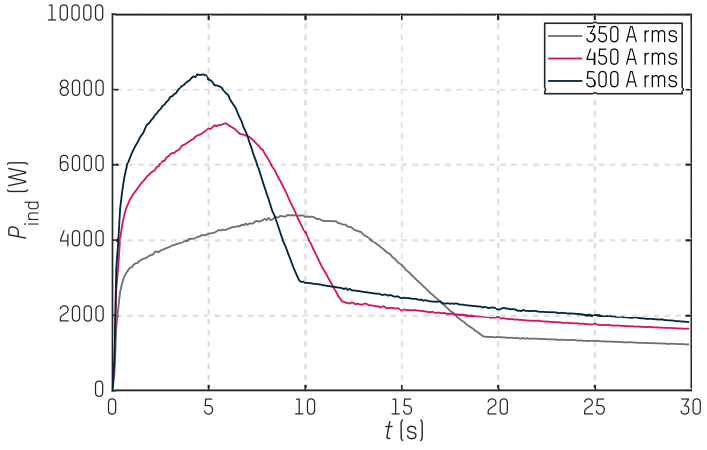

Figure 4.18. Power delivered to the induction load.

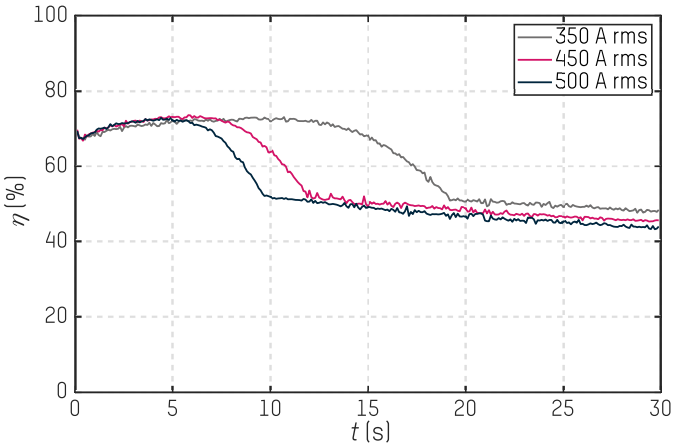

Figure 4.19. Induction heating system's efficiency.

4.5.2 Comparison of Pulsated Current Level and Constant Current

Then, the input reference is switched between 200 A rms and 50 A rms in a ten-second period with a duty-cycle of 60 %, as shown in Fig. 4.20, where soft current transitions have been defined to protect the converter. Moreover, the results are compared when applying a constant current with an effective value of 158.11 A rms, which correspond to the constant level of the current.

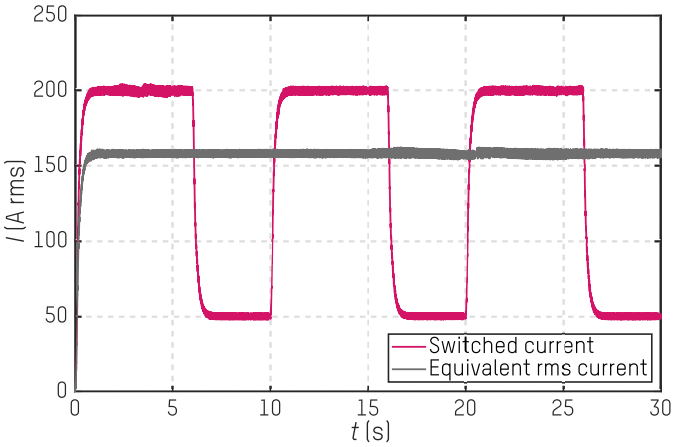

Figure 4.20. Simulated effective current through the induction coil.

In Fig. 4.21, the reduced-order equations-based estimated temperature is depicted. It can be observed that the temperature increases when power is applied to the workpiece, but when the power is pulse to a lower level, the temperature decreases because the temperature of the workpiece becomes more uniform. In both configurations, a similar temperature increase is observed over time; however, in the case of pulsing the delivered current, a smoother profile is observed.

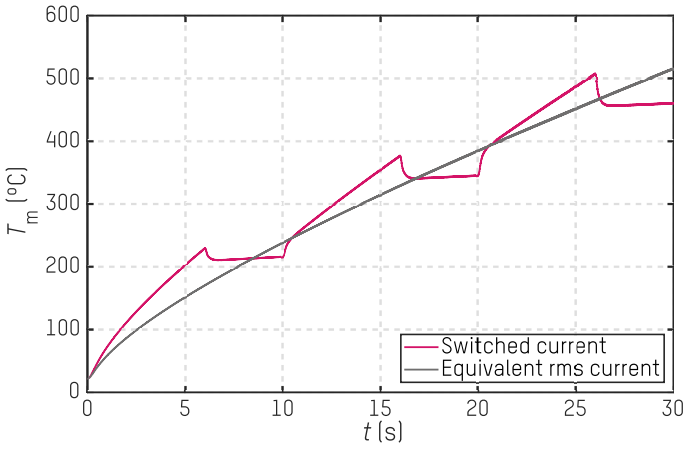

Figure 4.21. Estimated temperature in the middle point of the billet's surface, $\widehat{T}_m$, during a transient of time extracted by electrical simulation.

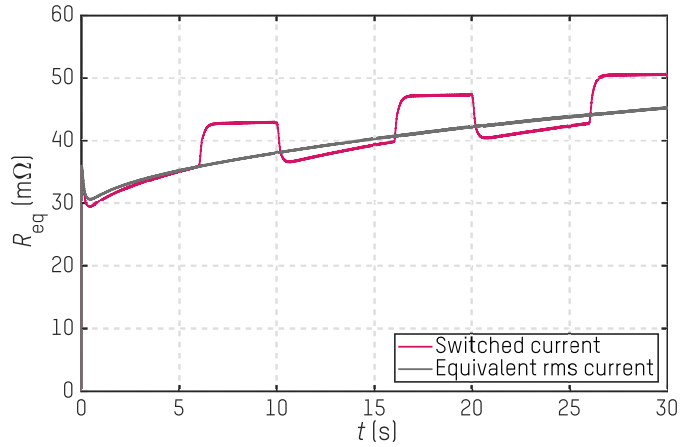

(a)

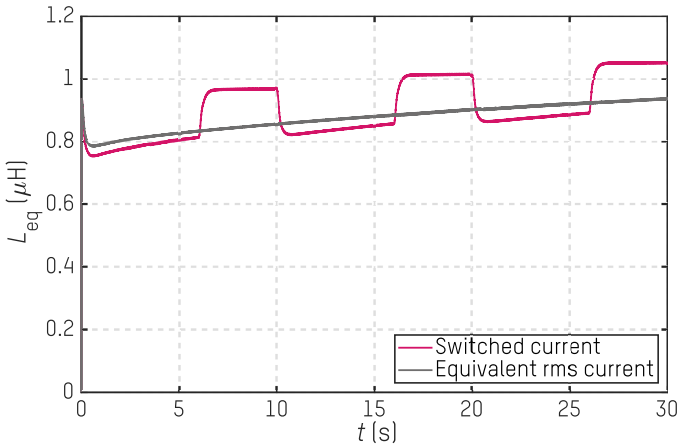

(b)

Figure 4.22. Equivalent impedance during a transient of time extracted by electrical simulation: (a) resistance, and (b) inductance.

In Fig. 4.22, it is clearly observed how the impedance changes the resistive and inductive values with the current level along the cycles. As it was expected, pulsating the current implies a similar pattern in the resistive and inductive components of the equivalent impedance. Note that constant current excitation implies similar equivalent impedances to values at higher current in the pulsating strategy.

With regard to the power delivered to the workpiece, shown in Fig. 4.23, an increase is observed throughout the cycle applied. This increase is associated with the behavior of the resistance in the workpiece along time.

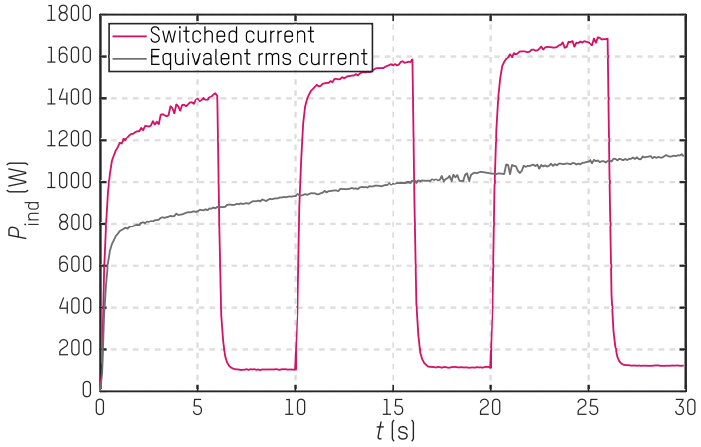

Figure 4.23. Comparison of power delivered into the workpiece between applying pulsating current and equivalent constant current.

Chapter 5

Experimental Validation

In this chapter, the simulation results will be experimentally validated. First, the impedance of the induction load will be measured in the small-signal regime with an LCR meter to compare the finite-element electromagnetic simulation results with the measured values. Then, to validate the coupled electromagnetic-thermal FEM simulation, an induction heating experiment under typical operational conditions is realized and recorded with a thermal camera. Moreover, the electrical behavior will also be validated by measuring current and voltage signals at different power conversion stages.

5.1 Context of the Experimental Measurements Validation

This chapter presents experimental measurements carried out in two distinct regimes. On the one hand, we use the small-signal regime to determine the system's impedance across various frequency ranges, utilizing a high-precision LCR meter for this purpose. This regime is used to characterize the induction system for the induction load working with linear conditions. On the other hand, we establish a complete experimental setup to evaluate the system's performance in front of large signals. Different processes under different excitation profiles can be tested in this test bench. This second regime yields a variety of measurements, including currents and voltages at all power stages, as well as the temperature cycle in the billet. Moreover, after treating the workpieces, they are also mechanically tested to ensure that they obtain the desired properties. However, in this work, only the electrical and thermal measurements are provided; the mechanical issue covers other technological fields.

Therefore, the numerical models using the finite element method will be experimentally validated. First, the electromagnetic simulation results in the frequency domain are compared with LCR meter measurements in small-signal regime. Then, under large-signal conditions, the thermal camera records an induction heating process to somehow validate the thermal model. Finally, as power conversion stages are monitored, these electrical measurements validate the proposed dynamic model.

5.2 Small-Signal Regime

LCR meters are small signal-measuring instruments that measure impedance, Z, from the current circulating through the measurement target and the voltage on its terminals. The resulting impedance is a complex vector, so the LCR meters measure current and voltage values and the phase shift between them. LCR meters have three measurement signal modes depending on which parameter is set: open-voltage mode, constant-voltage mode, and constant-current mode, [209].

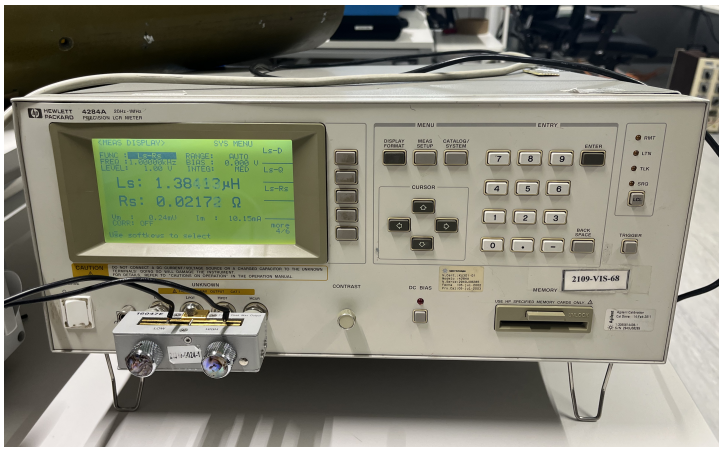

Figure 5.1. Agilent 4284A LCR meter.

In this thesis, small-signal measurements are performed with a high-precision Agilent 4284A LCR meter, captured in Fig. 5.1, to analyze the system's impedance, [210]. This instrument can excite frequencies from 20 Hz to 1 MHz, with a large amount of intermediate selectable frequencies at the current level.

5.2.1 Small-Signal Measurements

Different impedances are measured with the LCR, and frequency ranges from 20 Hz to 100 kHz are analyzed. In this case, as the measuring elements may exhibit current dependence, the LCR meter is set to operate at constant-current mode, setting its value at 10 mA. The integration time has been set to long format in order to achieve high accuracy in the measurement values, slightly increasing the measuring time.

In Table 5.1, the measuring configurations are summarized. The excitation current amplitude and frequency ranges are exposed for each case study. In that table, the configurations named 'ZTD' and 'LSRS' are mentioned, which are related to the information format given by the LCR meter. The former means that the measured impedance is expressed with its absolute value and phase angle in degrees. Instead, the latter provides the impedance as an equivalent series resistor-inductor pair.

Table 5.1. Small-signal measuring parameters.

Measuring element	Excitation current	Frequency range	Configuration
Coil in air	10 mA	20 Hz÷100 kHz	LSRS
IH load	10 mA	20 Hz÷100 kHz	LSRS
Resonant tank with coil in air	10 mA	20 Hz÷100 kHz	ZTD
Resonant tank with IH load	10 mA	20 Hz÷100 kHz	ZTD

The first two measurements in Table 5.1, coil in air and IH load, are used to validate the electromagnetic finite-element simulations in Chapter 2. First, the coil's impedance is measured without the workpiece, i.e., coil in air; then, the steel billet is introduced in the center of such coil. At that point, the series equivalent circuit is configured to obtain the series inductance and resistance values. The 'LSRS' configuration mode is selected because the focus is on the induction load from an electromagnetic point of view, so the electrical equivalence of the IH load is measured.

However, the 'ZTD' configuration is employed to measure the impedance module and phase of the complete resonant tank, which is composed of the mentioned induction load, resonant capacitor bank, and litz terminals. This measurement will give the impedance of the whole resonant tank from the point of view of the electronics. Here again, the coil in air and the coil-billet pair are measured separately. The aim of these latter measurements is to find the exact resonance point of the system seen from the inverter's output.

5.2.2 Validation of the Electromagnetic Simulations

In a first place, the focus is on the induction load, whose geometrical characteristics are detailed in Chapter 2. The coil is constructed with 6 tubular copper turns, as a water-cooling system is necessary to limit the maximum working temperature of this component. The tube has a cross-section consisting of an outer circle with a diameter of 6 mm and a hollow section with an inner diameter of 4 mm. Actually, the coil is a spiral, but the simulation model is approximated to six equal rings with an inner radius of 15 mm, and equally separated by 9 mm along a common rotational axis. The workpiece is a cylindrical billet with a radius of 10 mm and a length of 75 mm. Figure 5.2 shows two screenshots of the COMSOL Multiphysics® interface with the simulated current density at 100 kHz in a revolved geometry; in Fig. 5.2a, the six-turn coil in air is captured, and in Fig. 5.2b, the cylindrical steel billet is centered inside the coil.

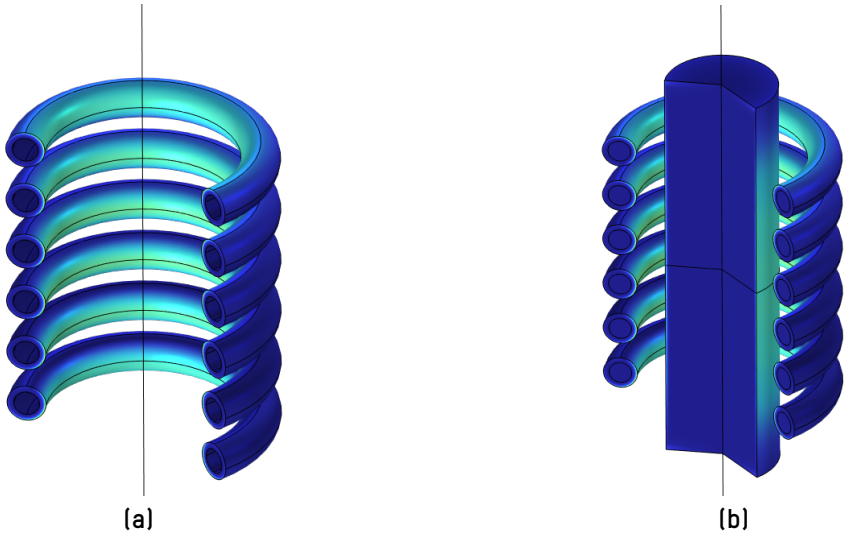

Figure 5.2. COMSOL®-based simulated current density for the induction load's revolved geometry: (a) coil in air, and (b) including workpiece.

The LCR meter is configured to obtain the series L-R parameters of such load. Again, the measurements are performed, positioning the billet inside and outside the coil. These measurements are afterward compared in Fig. 5.3 and Fig. 5.4 with the results obtained from finite-element simulation models.

Small-signal electromagnetic modeling is performed in the frequency domain to compute the electromagnetic field and induced power density in the billet. These models aim to validate the system's geometry by verifying with LCR meter measurements.

First, the billet is dismissed, and the focus is on the coil. In Fig. 5.3, the coil's equivalent resistance and inductance values are depicted in the frequency spectrum. As can be seen, the agreement between experimental measurements and simulation data is quite good, validating the geometrical modeling of the coil. There is a slight error in L_{eq} of around 0.1 μH, possibly because the spiral geometry is not precisely represented with the axisymmetric domain.

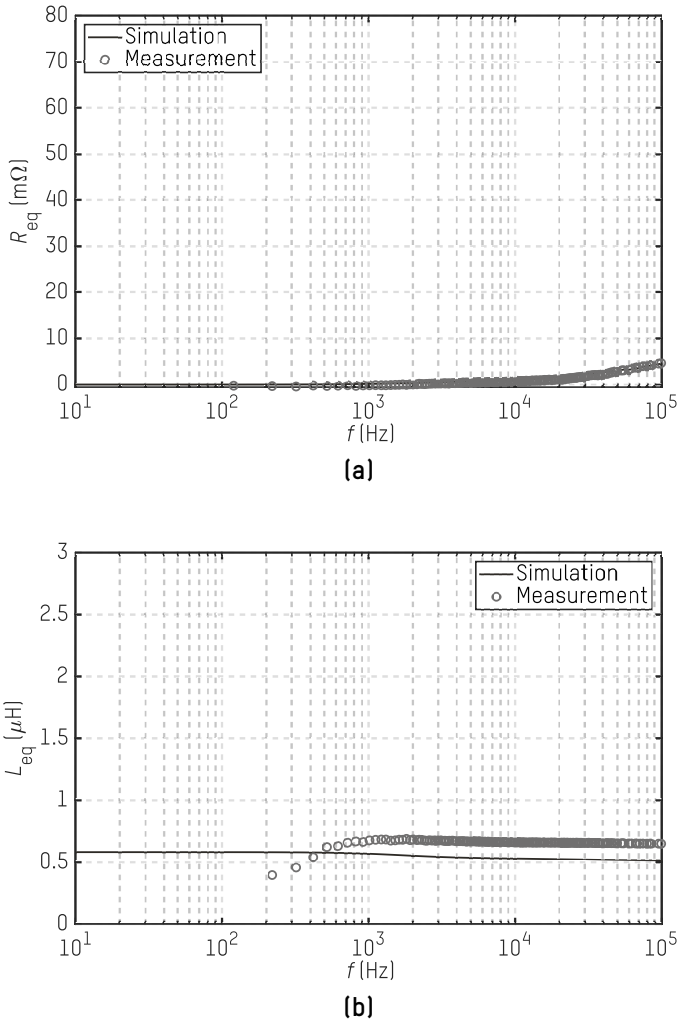

Figure 5.3. Comparison of simulation and small-signal measured equivalent impedance, Z_{eq}, of the heating coil: (a) equivalent resistance, R_{eq}, and (b) equivalent inductance, L_{eq}.

In Chapter 2, the DC resistance value of the copper coil is computed to be 0.75 mΩ. Figure 5.3a shows the resistance value of the induction coil depending on excitation frequency. The value at low frequencies should be close to R_{dc} value of such coil.

Regarding Fig. 5.3b, it can be seen that the L_{eq} values around 100 Hz and below are not represented; for lower frequencies, the precision results are inadequate. LCR meters lack on accuracy at low frequencies when measuring small inductance values (< 1 μH), [209]. These points have been neglected because they are not representative due to the device's accuracy with so small inductance values.

When the steel bar is placed in the center of the coil, the equivalent resistance and inductance values rise significantly. Resistance R_{eq} and inductance L_{eq} dependencies with frequency are shown in Fig. 5.4a and Fig. 5.4b, respectively. The material properties are supposed to be linear because the coil is excited with a small amplitude current. Exactly, the model with linear conductivity $\sigma = 1$ MS/m and permeability $\mu_r = 100$ is the one that best approaches the measured impedance, resulting in a σ/μ_r ratio of 10^4 S/m.

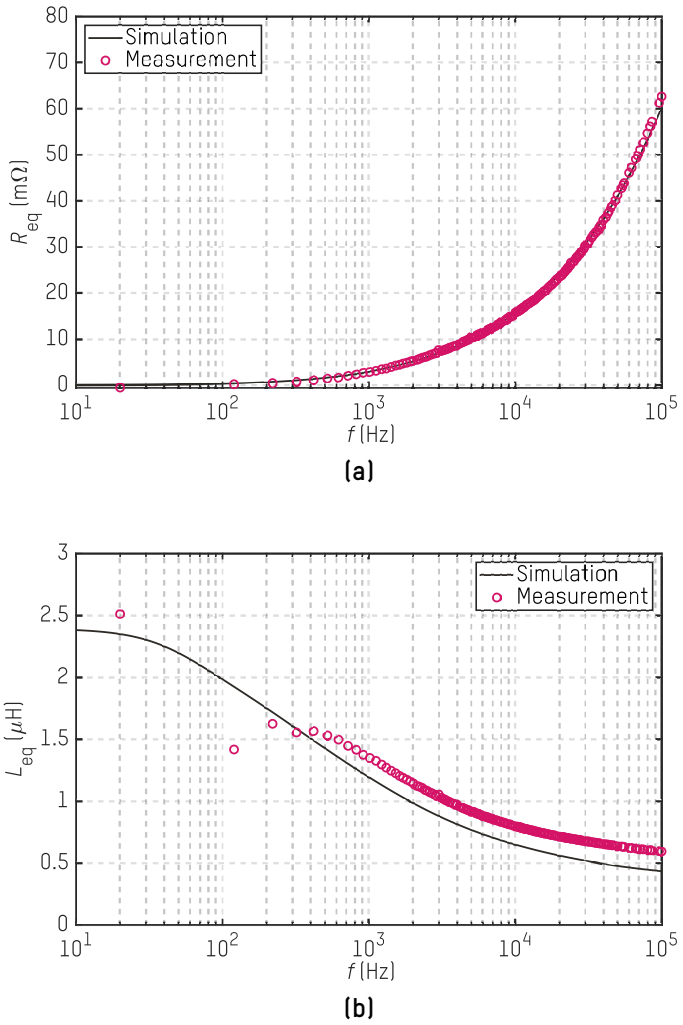

Figure 5.4. Comparison of simulation and small-signal measured equivalent impedance, Z_{eq}, of the induction load: (a) equivalent resistance, R_{eq}, and (b) equivalent inductance, L_{eq}.

The low-frequency equivalent resistance value should match the DC resistance, R_{dc}, value of the coil, which comes to be the DC resistance of the induction load, as there is no power induced to the billet in DC condition, i.e., low frequencies.

5.2.3 Measurement of the Resonant Tank

Then, the full RLC series-resonant tank is measured. As previously mentioned, the resistive and inductive components are given by the induction load and litz-wire terminals connecting the converter with this IH load. Instead, the capacitive component is configured by the resonant capacitors bank; in this case, it is composed of four capacitors of 6.3 μF and eight of 1.4 μF, obtaining, in total, 36.4 μF of capacitance in the resonant tank.

In Fig. 5.5 and Fig. 5.6, the series-resonant tank's impedance module and argument are depicted. Respectively, two measurements are realized and compared: on the one hand, the induction coil in air is measured, and on the other hand, the resonant tank is measured, centering the cylindrical steel billet inside such coil, i.e., the loaded coil is measured.

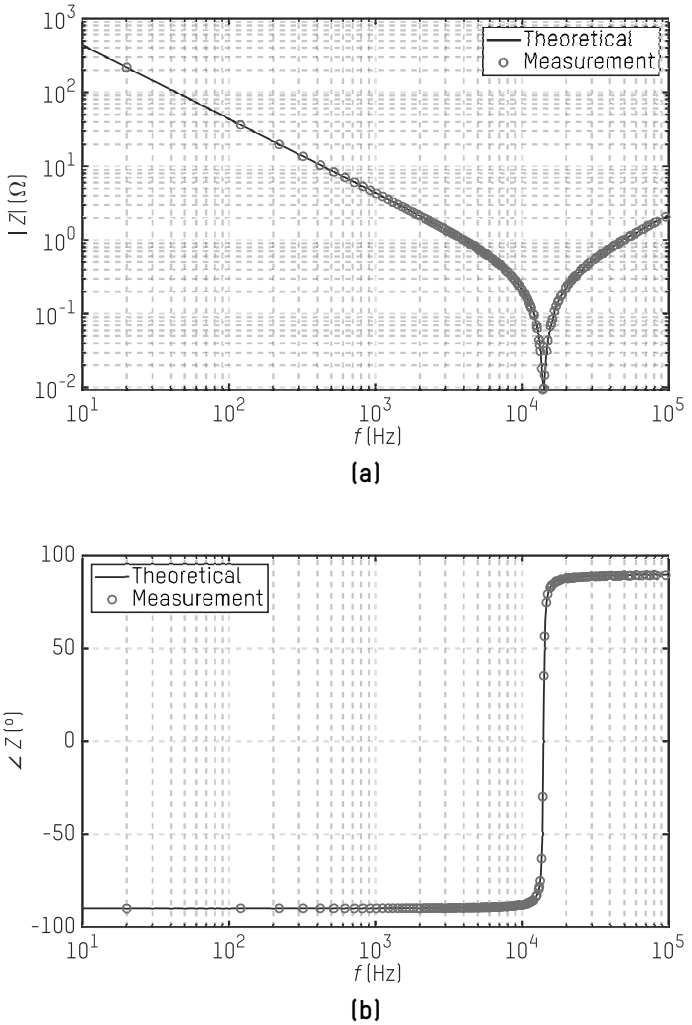

Figure 5.5. Measured impedance (a) module and (b) argument of the whole resonant tank: resonant capacitors bank, litz terminals, and IH load with the coil in air.

A slight difference can be observed in Fig. 5.5a and Fig. 5.6a. When the steel billet is introduced, the impedance of the resonant tank increases. However, both impedances have

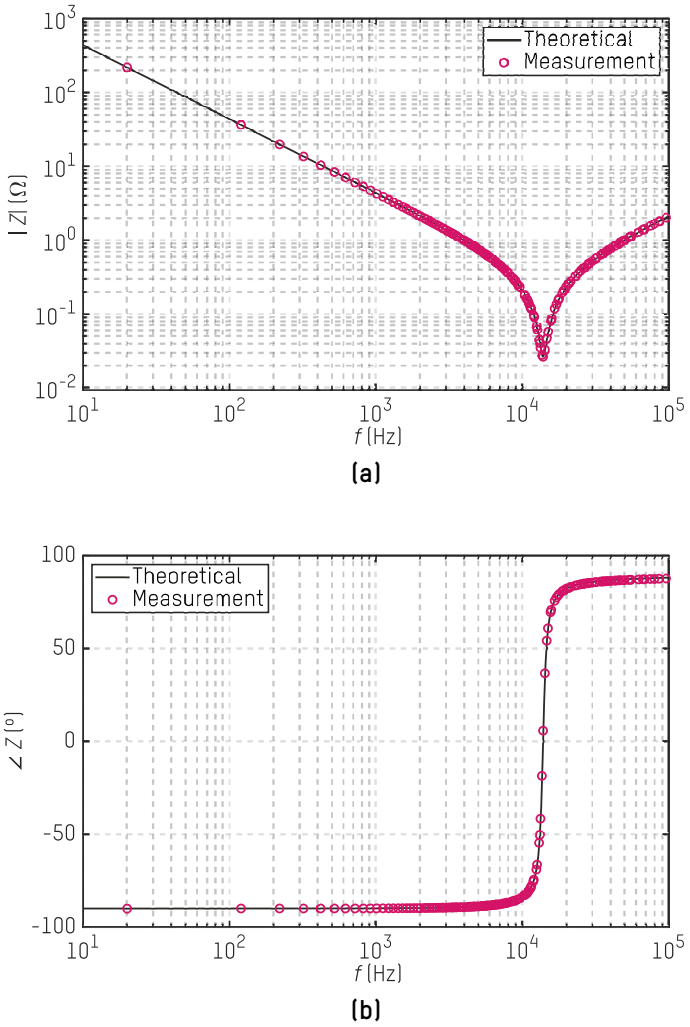

Figure 5.6. Measured impedance (a) module and (b) argument of the whole resonant tank: resonant capacitors bank, litz terminals, and IH load including the steel workpiece.

no large difference because of the impact of the litz terminals, whose inductive component prevails in front of the induction load. Exactly, for the system with the coil in air, the resonance condition is reached switching at 14.12 kHz, while when the steel billet is introduced, the resonant frequency drops to 13.89 kHz. Indeed, these litz terminals have around 8 mΩ of resistance and 3 μH inductance.

5.3 Large-Signal Regime

In this section, the 42CrMo4 steel billet is heated by electromagnetic induction for hardening purposes; the process is captured in Fig. 5.7. First, the billet is heated while it centered inside the coil. The billet needs to be heated up relatively quickly, exceeding the Curie temperature, T_C, which is around 800 ºC. Therefore, large-signal alternating current is needed. Then, after reaching the austenizing temperature of the material, around 50 ºC above T_C, the heated workpiece is immediately cooled down to be properly quenched.

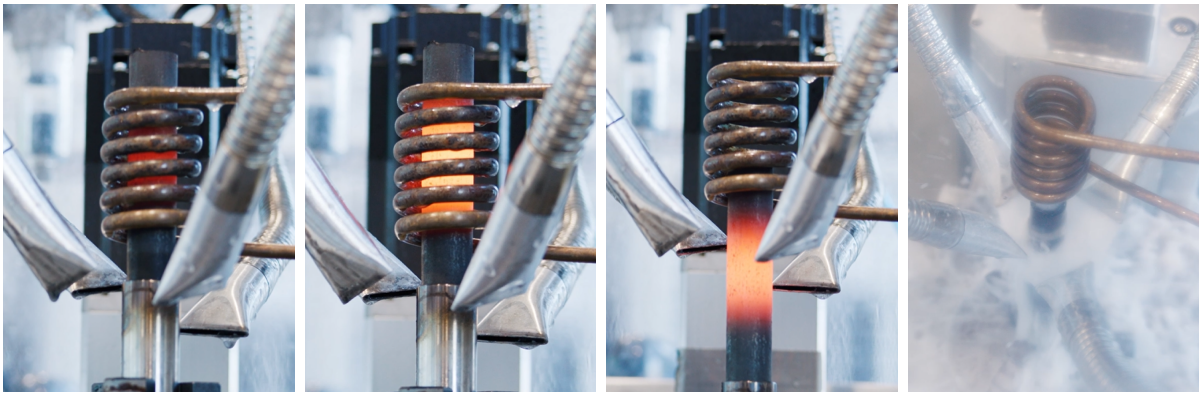

Figure 5.7. Captured images while hardening a cylindrical 42CrMo4 steel billet by induction heating: (a) heating the billet, (b) at austenizing temperature, (c) going down after reaching the desired temperature, and (d) quenching process.

The experimental setup in the laboratory for induction heating processes is presented in Fig. 5.8. The induction heating test bench is captured at the top, which includes all the power converters described in Chapter 3.

On the one hand, there is the input AC-DC power converter fed with a 3-phase AC mains of 50 Hz, with EMC and LCL filters on its entrance. It includes all the power conversion stages, rectifier, buck, and inverter, composed of SiC half-bridge modules, as detailed in Chapter 3. The control board is also integrated in the electronics, with the sbRio which communicates the general control of the test bench through CAN protocol.

On the other hand, there is the steel billet to be heated and the heat source coil, forming the induction load; the resonant capacitors, which will compose the series-resonant tank, are placed in another box. Both the resonant capacitor bank and the IH load are connected to the power converter utilizing 35 mm^2 Litz wires. These wires play a very important role when it comes to analyzing the resonance of the system, as the system's self-resonant frequency is mainly determined by their impedance. Therefore, it is crucial to measure this impedance before launching any heating.

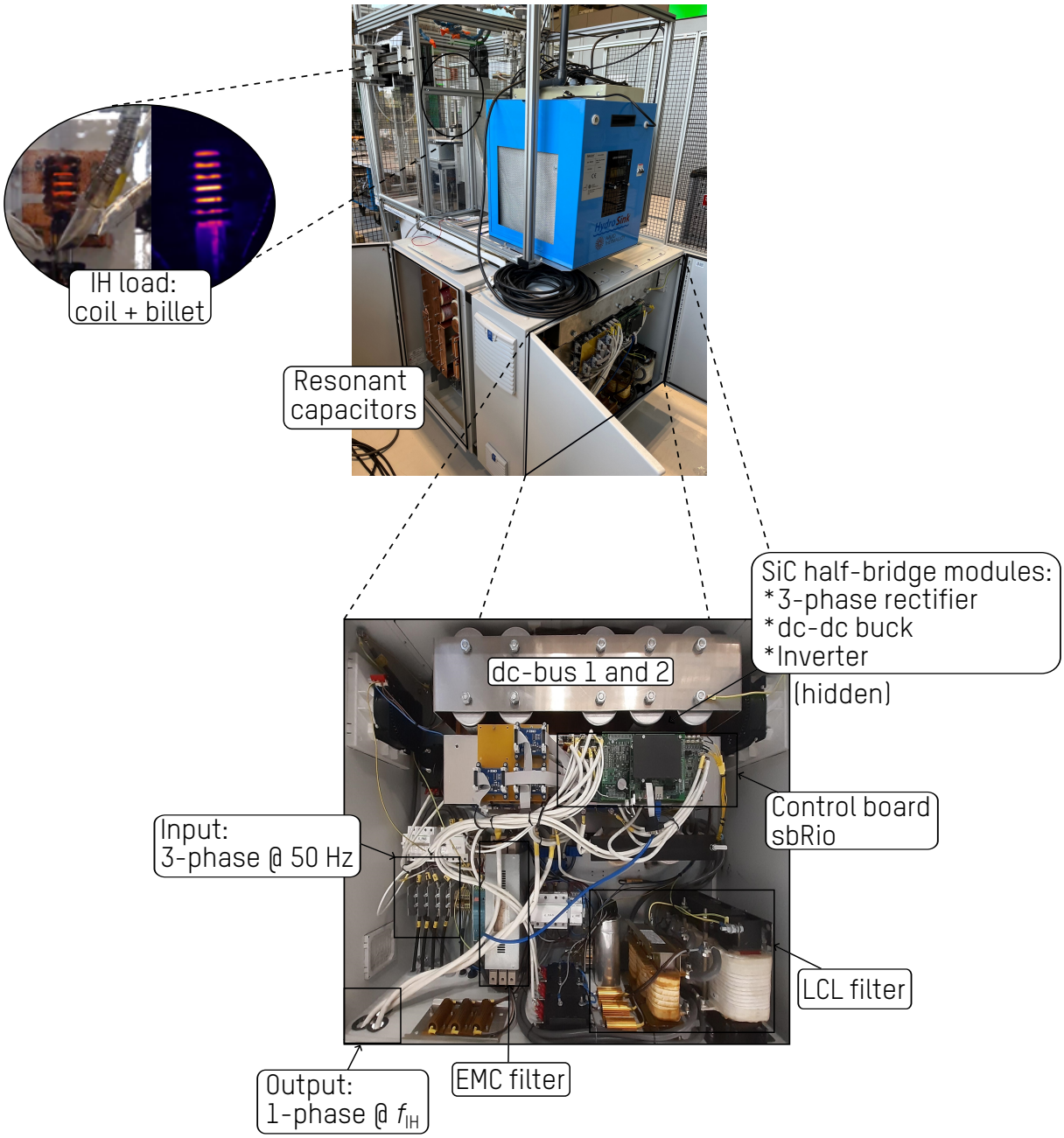

Figure 5.8. Experimental setup.

5.3.1 Sensing System

The entire system was controlled using a digital system implemented in a National Instruments sbRio 9607 embedded controller, [211], which is inserted in the power converter captured on the bottom of Fig. 5.8. The trigger signals for the 3-phase rectifier were generated from the measurements of the current and voltage signals of each phase and the output voltage $V_{dc,1}$. We used a 200 A rms LEM LF 210-S current transformer, [212], for the current measurements and a LEM DVL 250 voltage transducer, [213], for the voltage measurements of each phase of the mains, respectively. The voltage at the output of the 3-phase rectifier was monitored with a LEM DVL 750-UI voltage transducer, [214].

To generate the regulated DC-bus, $V_{dc,2}$, through the DC-DC buck, different control variables can be applied: the voltage in the second DC-bus or the current delivered to the load, i_{IH}, was used as the control variable. The voltage or current setpoint, $V_{dc,2}^*$ and I_{rms}^*, is provided through a CAN-bus communication in an open-loop system, allowing flexibility in the cycle to be applied depending on the type of workpiece under treatment. Additionally, the current supplied by each branch of the DC-DC buck stage is monitored by two 200 A rms LEM LF 210-S current transformers. The DC-bus voltage $V_{dc,2}$ was provided by a LEM DVL 750-UI voltage transducer. The current delivered to the load was determined by measuring the peak current of each of the two modules using a 300 A rms LEM LF 306-S Hall current probe, [215]; two Peak Detector Circuit (PDC)s are inserted in the hardware. In paralleled half-bridge mode, the current through the load is the sum of the two measurements, while for the full-bridge configuration, the current is obtained by averaging them. The trigger signals were generated by two PWMs of the same frequency as the 3-phase rectifier and out of phase by 180º to reduce the interference generated by the system when applying interleaving of the two branches.

Finally, the symmetric gating signals of the inverter's two modules are generated with a fixed duty cycle of 50% and frequency, f_{IH}, which is high enough to ensure the ZVS conditions at the interest heating treatments despite the existing slight inductance variations.

Table 5.2 defines the specifications of the analog inputs that receive the monitorized information.

Table 5.2. Specifications of the analog inputs.

Variable	Number	Unit	Nominal range	Maximum range
Phase voltage, v_{ac}	3	V	-325:325	-356:356
Phase current, i_{ac}	3	A	-102.5:102.5	-120:120
DC-bus voltage, V_{dc}	2	V	0:650	0:650
Buck current, I_{dc}	2	A	0:150	0:175
Inverter's output current, I_{IH}	2	V	-375:375	-400:400

The specific definition of the power cycle to be applied will be defined in the future for each of the workpieces to be treated, ensuring the repeatability of the process. The proposed control includes overcurrent and phase-shift protections so that the modulation in the inverter is suppressed when a malfunction is detected.

5.3.2 Validation of the Electromagnetic-Thermal Simulation

This section compares the finite-element electromagnetic-thermal model with an experiment realized on the induction hardening test bench. The heating process was recorded with a FLUKE RSE300 thermal camera, [216], to compare the simulated and real temperature distributions during the heating process. The experimental setup to thermally record the induction heating process is captured in Fig. 5.9.

Both the FEM simulation and thermal test are carried out under 500 A rms and 14.2 kHz coil's current excitation. The configured capacitance value is 36.4 μF, resulting in a resonance of around 14 kHz. With those working conditions, the steel billet should be heated for 30 seconds to reach the desired temperature in the central areas of the billet's surface. The temperature distribution of the system for the captured instants is shown in Fig. 5.10.

The information recorded in the thermal camera is processed with SmartView® software from FLUKE. The software gives the graph captured in Fig. 5.11, which depicts the temperature values captured by the thermal camera in a longitudinal path that covers the whole billet for the instant $t = 10$ s.

(a) (b) (c)

Figure 5.9. Experimental arrangement to record temperature of the IH process: (a) general view of the thermal measurement setup, (b) thermal camera, and (c) frame captured by the thermal camera.

While heating the steel probe with a spiral coil that surrounds it, the magnetic field density is longitudinal, leading to the strongest fields in the central area, in the z axis, of the coil. Therefore, the hottest areas are also those near the mid-surface point of the metallic piece. Then, as the temperature distribution is not homogeneous, the magnetic, electrical, and thermal properties are not equal throughout the piece, resulting in different power densities applied to different workpiece areas; this effect is clearly observed in this Fig. 5.11. However, the captured maximum temperature at the central point of the billet at $t = 10$ s differs from the value it should take, i.e., around 800 ºC, due to the constant emissivity factor applied to the recording. The emissivity is a key parameter to obtain accurate measurements but it is difficult to calibrate.

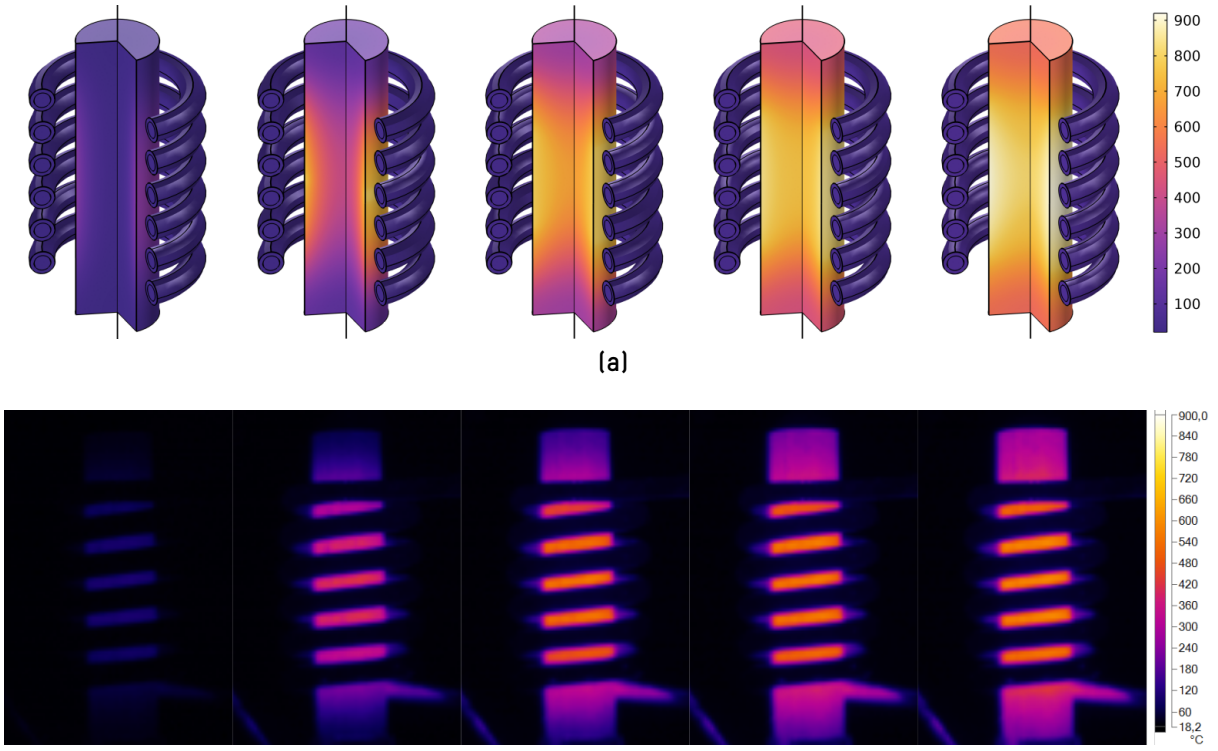

Figure 5.10. Temperature distribution through the billet with 500 A rms and 14.2 kHz coil's current at t = 1, 5, 10, 15, and 20 s, respectively: (a) COMSOL®-based thermal simulation, and (b) thermal camera captures during the experimental heating process.

The temperature distribution on the surface of the workpiece, as illustrated in both Fig. 5.10a and Fig. 5.10b, is notably inhomogeneous. However, it exhibits a clear pattern where the maximum temperature is found in the central zone of the billet. Temperatures significantly above the Curie temperature are not observed, primarily due to magnetic saturation, which implies lower power transference, and, to a lesser extent, the increased heat capacity. In capturing images with the thermal camera, a behavior that performs as a gray body of the workpiece is assumed, with properties that remain consistent throughout the process. This means that the emissivity is considered independent of the wavelength and remains constant with temperature.

As shown in Fig. 5.10, there is a considerable correlation between the simulation and experimental results, indicating that the electromagnetic-thermal simulation has been validated. The same temperature scale is employed to compare both the simulation and experimental temperature distributions. The emissivity of the workpiece changes as its color varies at around 600 °C, but while capturing the temperature images, we use a constant emissivity. That is why the thermal camera does not capture temperatures above 650 °C, and it is already known that the heated material can reach temperatures beyond it.

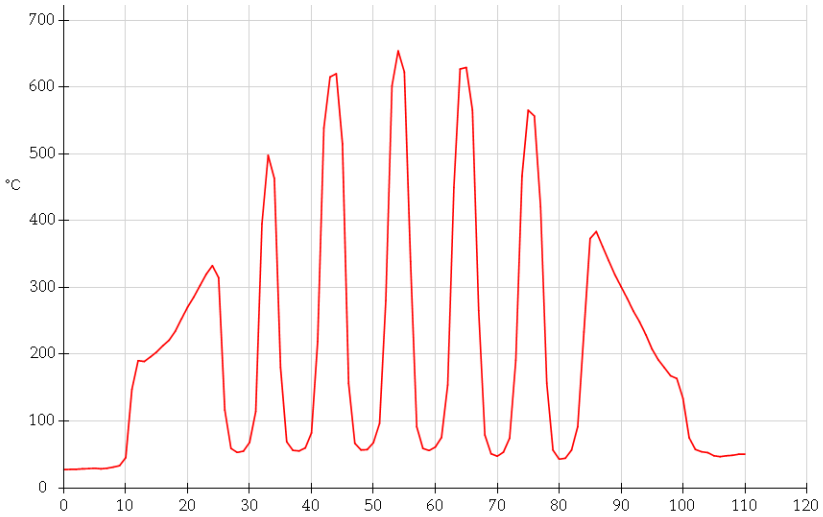

Figure 5.11. Temperature distribution through a billet's vertical path captured with the thermal camera with 500 A rms and 14.2 kHz coil's current at instant $t = 10$ s.

Furthermore, the temperature of a superficial point of the billet has been measured in several experiments by means of K-type thermocouples. In Fig. 5.12, three temperature measurements are compared with FEM simulation results during a transient of 30 seconds feeding the coil with 500 A rms constant current.

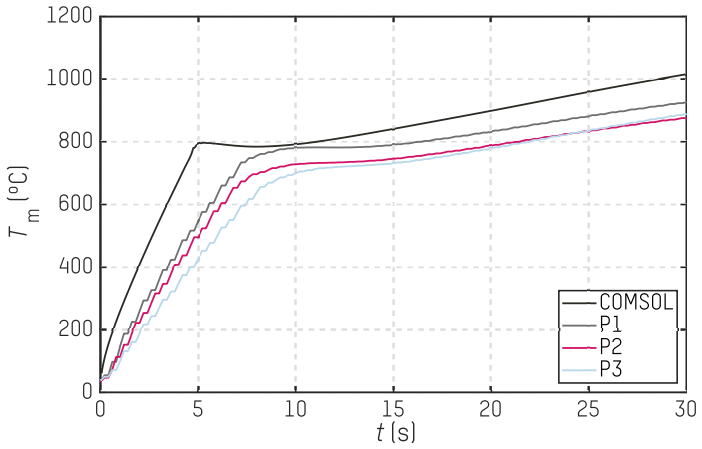

Figure 5.12. Comparison of COMSOL® simulation results and experimentally measured temperatures at the boundary middle point of the billet, T_m, during three induction heating tests of 30 seconds exciting the coil with a current of 500 A rms and 14.2 kHz.

The measured temperature appears to differ from the simulated results. It is worth mentioning that it is not easy to have accurate temperature measurements in this kind of process as very high temperatures are reached. This can be clearly observed in Fig. 5.12, where the three measurements show different temperature responses, even the Curie temperature – the point where the tendency is changed – seems to vary, which cannot be real.

First, the thermocouples are welded to the billet's surface so the measurement can be distorted due to the non-magnetic welding material. Moreover, a slight offset in the position modifies the time dependence of the temperature at the supposed measured point; in this case, it is intended to measure the temperature on the middle point of the billet's surface, T_m. Furthermore, since thermocouples exhibit a degree of inertia, they may introduce a time lag in rapidly changing temperature situations, which happens in the induction heating process under study.

5.4 Validation of the Dynamic Model

Experimental validation of the dynamic model's results has been performed using the setup shown in Fig. 5.8. The abovementioned conditions – 500 A rms at 14.2 kHz – were applied to obtain the results shown in this section.

All the experimental results displayed in this section are sensed as specified in Table 5.2 and monitored by LabVIEW®, [217].

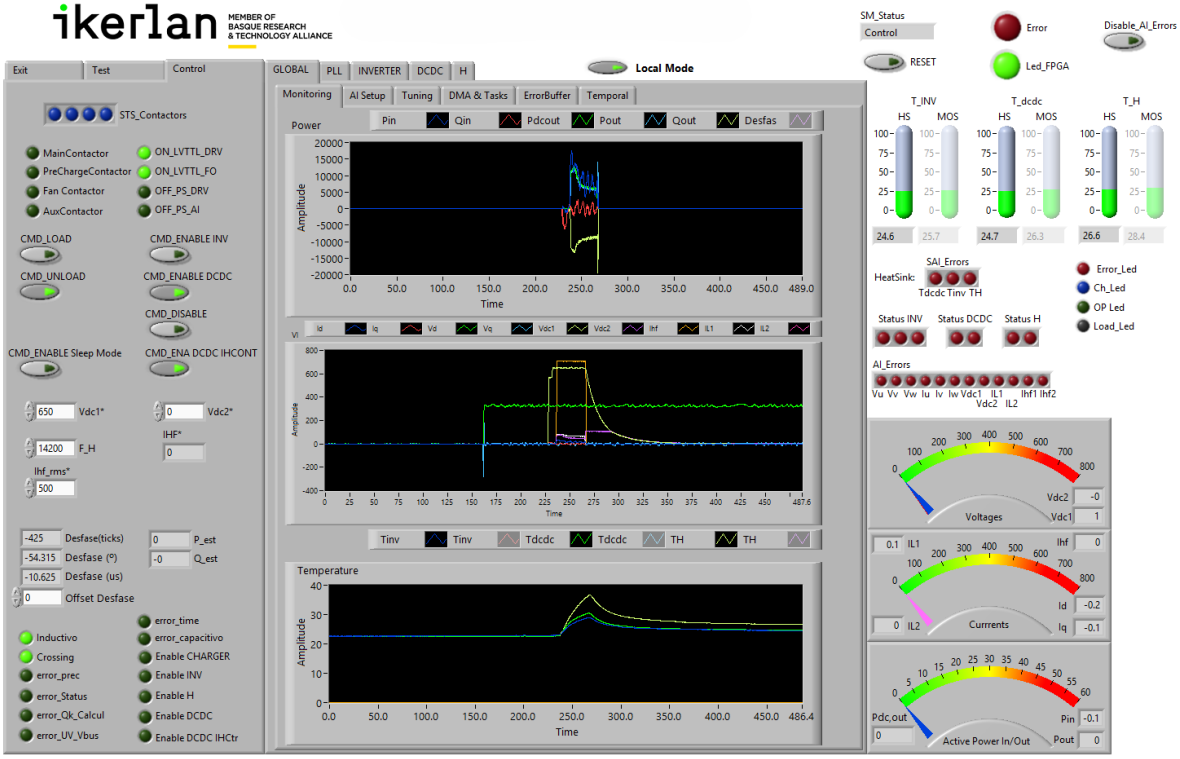

Figure 5.13. LabVIEW®interface capture to monitor real-time currents and voltages during the induction heating process.

As depicted in Fig. 5.14, the current control dynamics are fast enough to maintain a stable high current through the load during the initial transient and rapid impedance variation as the Curie temperature in the workpiece is exceeded. The simulated current follows the 500 A rms set as reference correctly with a slight ripple, which cannot be captured on the

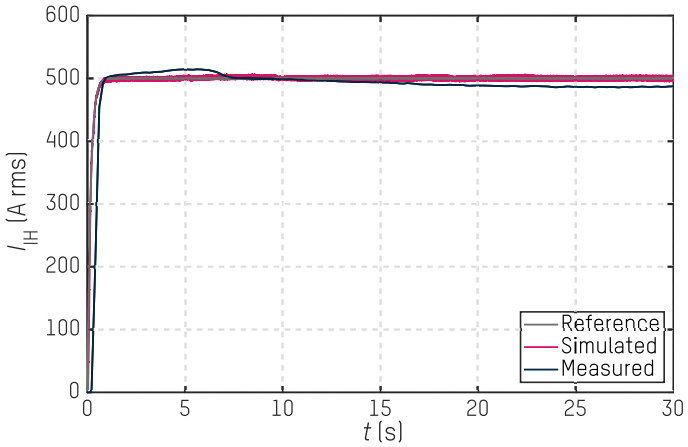

Figure 5.14. Effective current through the induction coil: dynamic simulation results vs experimental measurements.

measured signal due to the bandwidth of the current sensors and sample ratio. A current overshoot is observed at around 5 seconds, just when the middle point of the billet reaches the Curie temperature, the error on the peak is 3.4 %; and after it, the current drops slightly until it reaches a negative error of 2.8 % at the end of the process. These inaccuracies are within the acceptable tolerance range for this industrial process. We see that after 30 seconds, the current would continue dropping, but at this point, the workpiece has already reached the desired temperature, and the process will always be stopped before the current decreases significantly. That is why we have considered it an acceptable level of accuracy.

On the other hand, in Fig. 5.15, a ripple is also observed in the measured voltage signal, which can be due to the noise effects of such small amplitudes. Comparing the evolution of the DC-bus voltage with simulation results, it is concluded that it is reasonably well-regulated, considering the simplifications of the reduced model. The simulated equivalent induction load is divided into three parts through three analytical equations, which is why the transition at around t = 10 s is sharper than in experiments; the load's dynamics are smoother. Therefore, it is assumed that the simulated general variable behavior of the load is correctly modeled, considering all its inconsistencies.

Furthermore, these parameters are measured in the experimental test, and it is concluded that the tendency of the simulations is reasonably followed. Half-bridge inverter's input power is also measured in the same experiment, see Fig. 5.16, reaching around 12 kW at the maximum value of $V_{dc,2}$.

Previous power conversion stages measurements are also monitored by LabView® and displayed in Appendix C.

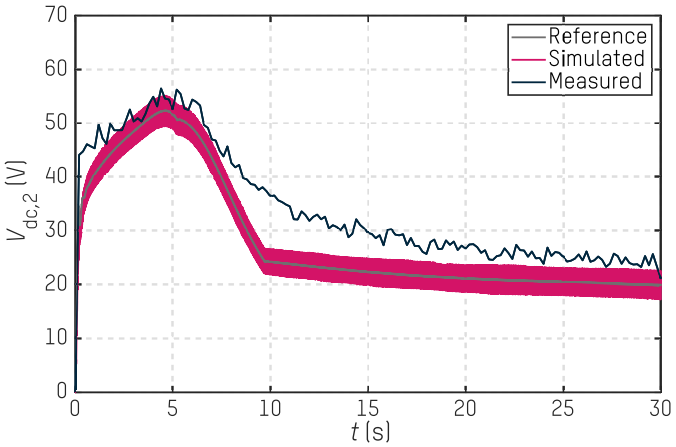

Figure 5.15. Regulated voltage in the second DC-bus, $V_{dc,2}$: dynamic simulation results vs experimental measurements.

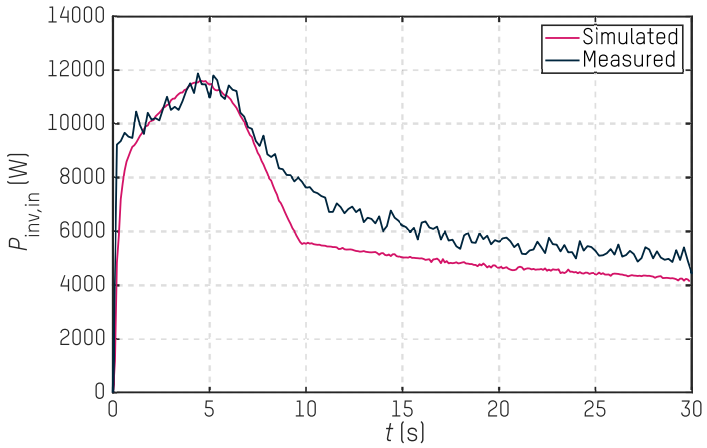

Figure 5.16. Input power of the inverter, $P_{inv,in}$: dynamic simulation results vs experimental measurements.

5.4.1 Oscilloscope Measurements

Finally, some oscilloscope measurements are captured to further validate the induction heating process. MDO3054 model from Tektronix, [218], was used to capture the voltage and current on the output of the series resonant inverter. A differential voltage probe is used to measure the switched voltage, and a Rogowski coil is used for the current. In Fig. 5.17, the measurement setup is presented.

Figure 5.18 shows the voltage in the resonant tank, v_o, as well as the output through the induction load, i_{IH}, waveforms just before reaching the Curie point and at the end of the process, verifying the proper operational conditions of the power converter. The Zero Voltage Switching (ZVS) condition is ensured in both process instants.

Figure 5.17. Voltage and current waveforms measurement setup with Tektronix MDO3054 oscilloscope.

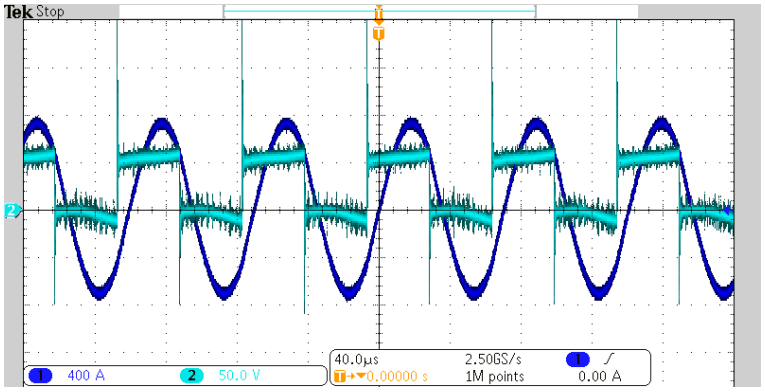

(a)

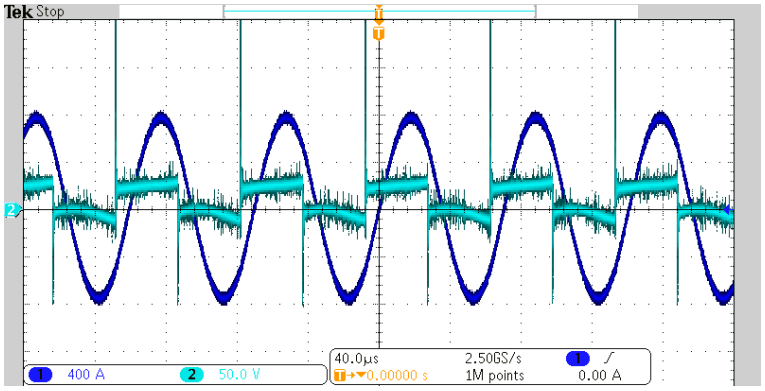

(b)

Figure 5.18. Measured waveforms of the voltage in the resonant tank, v_o, and the load current, i_{IH}, at $f_{sw} = 14.2$ kHz: (a) $t = 5$ s and (b) $t = 25$ s.

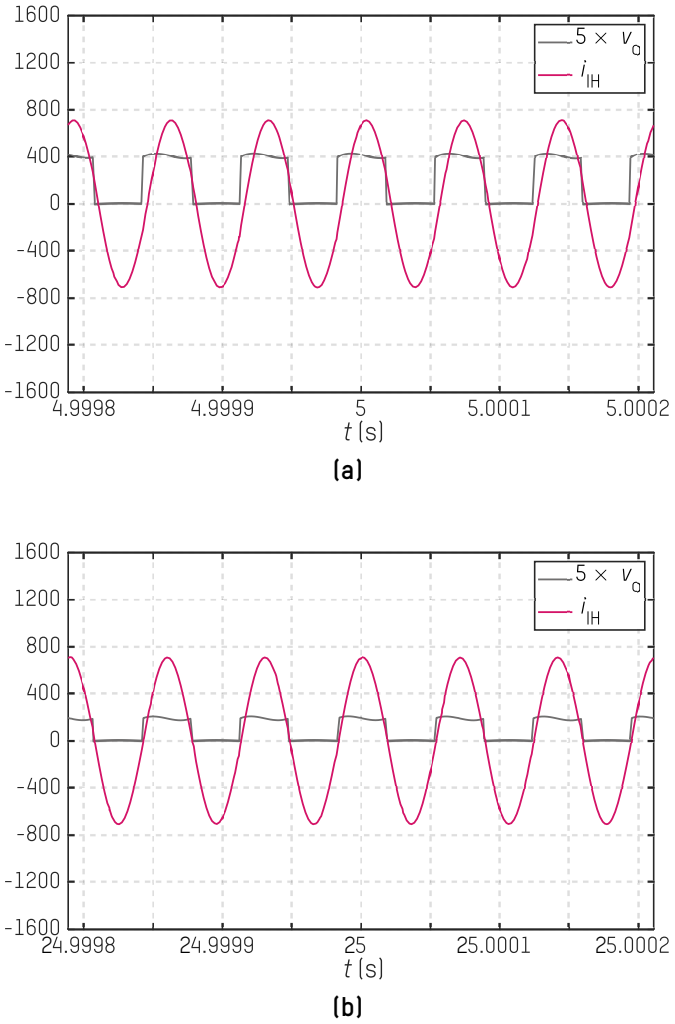

Figure 5.19. Simulated waveforms of the voltage in the resonant tank, v_o, and the load current, i_{IH}, at $f_{sw} = 14.2$ kHz: (a) $t = 5$ s and (b) $t = 25$ s.

In Fig. 5.18a, the square waveform of v_o and the sinusoidal of i_{IH} are captured for the instant $t = 5$ s. The v_o voltage takes 0 and $V_{dc,2}$ values, and comparing it with Fig. 5.15 at that specific instant, both of them are slightly higher than 50 V. However, in Fig. 5.18b, the $V_{dc,2}$ value captured at the instant $t = 25$ s is around 25 V, which also matches with the voltage value measured and processed via LabVIEW® in Fig. 5.15. The same waveforms are plotted in Fig. 5.19 obtained from the simulated dynamic model in Chapter 4; in order to maintain a comparable scale in Fig. 5.18, the output voltage has been multiplied by 5.

Moreover, it is confirmed that the current amplitude remains constant at both instants, barely higher than the 500 A rms set as a reference, but always inside the tolerance range.

Chapter 6

Conclusions and Future Lines

The final chapter aims to summarize the various research activities conducted in this thesis, highlighting the main findings, contributions, and discussing the results while also identifying the study's limitations and opportunities for future work.

This chapter is structured as follows. First, it summarizes the different research activities undertaken in this thesis. It evaluates the extent to which the objectives and hypotheses stated in the introduction have been achieved. Next, the key contributions of the thesis are presented, and the results obtained throughout the various chapters are discussed. Finally, the main limitations of the research are identified, and some suggestions for future work are proposed.

6.1 Summary

This thesis analyzes the behavior of the electromagnetic-thermal induction heating process applied to a workpiece undergoing metallurgical treatment. The aim is to capture the behavior under different operating conditions in order to obtain the electrical equivalent of the inductor-workpiece system for use in time simulation, with the ultimate goal of obtaining an electrical simulation model of the inductor-workpiece system acting as a load on the power stage that feeds it. In this way, it will be possible to capture the dynamic behavior of the system over time in order to optimize the different types of industrial processes that can be applied by induction heating.

The work carried out has focused on the use of a power converter that can be used to power light inductive loads, whose impedance varies significantly throughout the applied power cycle. The variations in the impedance of the induction load are associated with the dependence of the physical parameters of the workpiece under treatment, which are linked to both the significant temperature variation and the different excitation levels applied, given that it exhibits strong non-linear behavior.

6.2 Contributions

The main findings from the research conducted during this thesis are summarized below:

- **Electromagnetic-thermal simulation of the inductor-workpiece system.**

  This thesis employs finite element simulations to accurately describe the behavior of an inductive-type load, which consists of an inductor system and a workpiece. The study emphasizes the strong nonlinear behavior of the load, primarily due to its significant dependence on magnetic properties under varying temperature conditions and levels of excitation. A key contribution of this work is the successful modeling of the electromagnetic behavior of the workpiece using a nonlinear boundary impedance condition, which provides reliable results at a reasonable computational cost.

- **Dynamic model of the electronic converter and non-linear inductive-type light load.**

  A reduced-order model has been developed in this thesis to capture the dynamics of the IH load. This model facilitates the extraction of valuable insights from the system, which includes the electronic power stage and the inductor-workpiece assembly. The aim is to optimize various industrial processing techniques applied to metal components.

- **Experimental validation of the dynamic model.**

  The primary numerical outcomes from the proposed dynamic model have been validated through experimental measurements. These measurements encompass both electrical tests, conducted in the small-signal regime where the induction load behaves linearly under manageable conditions, and in the large-signal regime, where the proposed power converter effectively supplies power to the inductor-workpiece

system. Additionally, temperature measurements were taken throughout the power cycle delivered to the workpiece. Despite challenges in obtaining these measurements, they essentially validated the computational results obtained earlier.

6.3 Future Work

Firstly, among the potential tasks to be undertaken, it can be considered applying the proposed methodology to obtain simulation results for metallurgical processes under various conditions, including materials with different properties than those previously considered. It is important to previously conduct an experimental characterization of the physical properties of the workpiece material.

In order to validate the reduced-order model more comprehensively, it would be beneficial to compare the results obtained from this model under different conditions with co-simulation results. This would involve integrating a finite element simulation tool with the MATLAB®/Simulink electrical simulator. While the co-simulation would incur a high computational cost, leading to longer simulation times, it would allow for an assessment of the accuracy achieved with the reduced-order models.

Additionally, it is proposed to investigate improvements to the converter for light inductive loads, which is the focus of this thesis. This could be accomplished by using an adaptation transformer between the power stage output and the inductor-load system. A fully functional prototype of a power transformer that meets the required specifications is available at this moment.

Chapter 7

Conclusiones y Líneas Futuras

El capítulo final pretende resumir las diversas actividades de investigación realizadas en esta tesis, destacando las principales conclusiones, contribuciones y debatiendo los resultados, al tiempo que se identifican las limitaciones del estudio y las oportunidades de trabajo futuro.

Este capítulo está estructurado de la siguiente manera. En primer lugar, se resumen las distintas actividades de investigación realizadas en esta tesis. Se evalúa en qué medida se han alcanzado los objetivos e hipótesis enunciados en la introducción. A continuación, se presentan las principales aportaciones de la tesis y se discuten los resultados obtenidos a lo largo de los distintos capítulos. Por último, se señalan las principales limitaciones de la investigación y se proponen algunas sugerencias para futuros trabajos.

7.1 Resumen

En esta tesis se analiza el comportamiento del proceso de calentamiento por inducción electromagnético-térmico aplicado a una pieza sometida a tratamiento metalúrgico. El objetivo es capturar el comportamiento bajo diferentes condiciones de operación para obtener el equivalente eléctrico del sistema inductor-pieza para su uso en simulación temporal, con el fin último de obtener un modelo de simulación eléctrica del sistema inductor-pieza actuando como carga sobre la etapa de potencia que lo alimenta. De esta forma, será posible captar el comportamiento dinámico del sistema a lo largo del tiempo con el fin de optimizar los diferentes tipos de procesos industriales que pueden aplicarse mediante calentamiento por inducción.

El trabajo realizado se ha centrado en la utilización de un convertidor de potencia que permite alimentar cargas inductivas ligeras, cuya impedancia varía significativamente a lo largo del ciclo de potencia aplicado. Las variaciones en la impedancia de la carga inductiva están asociadas a la dependencia de los parámetros físicos de la pieza a tratar, que están ligados tanto a la importante variación de temperatura como a los diferentes niveles de excitación aplicados, dado que presenta un fuerte comportamiento no lineal.

7.2 Contribuciones

Las principales conclusiones de la investigación realizada durante esta tesis se resumen a continuación:

- **Simulación electromagnética-térmica del sistema inductor-pieza.**

  Esta tesis emplea simulaciones de elementos finitos para describir con precisión el comportamiento de una carga inductiva, que consiste en un sistema inductor y una pieza de trabajo. El estudio enfatiza el fuerte comportamiento no lineal de la carga, principalmente debido a su significativa dependencia de las propiedades magnéticas bajo condiciones variables de temperatura y niveles de excitación. Una contribución clave de este trabajo es la modelización satisfactoria del comportamiento electromagnético de la pieza de trabajo utilizando una condición de impedancia de frontera no lineal, que proporciona resultados fiables a un coste computacional razonable.

- **Modelo dinámico del convertidor electrónico y ligera carga inductiva no lineal.**

  En esta tesis se ha desarrollado un modelo de orden reducido para capturar la dinámica de la carga de inducción. Este modelo facilita la extracción de información valiosa del sistema, que incluye la etapa de electrónica de potencia y el conjunto inductor-pieza. El objetivo es optimizar diversas técnicas de procesamiento industrial aplicadas a componentes metálicos.

- **Validación experimental del modelo dinámico.**

  Los principales resultados numéricos del modelo dinámico propuesto se han validado mediante mediciones experimentales. Estas mediciones abarcan tanto prue-

bas eléctricas, realizadas en el régimen de pequeña señal, en el que la carga de inducción se comporta linealmente en condiciones manejables, como en el régimen de gran señal, en el que el convertidor de potencia propuesto suministra potencia eficazmente al sistema inductor-pieza. Además, se realizaron mediciones de temperatura durante todo el ciclo de potencia suministrada a la pieza de trabajo. A pesar de las dificultades para obtener estas mediciones, esencialmente validaron los resultados computacionales obtenidos anteriormente.

7.3 Trabajos Futuros

En primer lugar, entre las posibles tareas a realizar, se puede considerar la aplicación de la metodología propuesta para obtener resultados de simulación de procesos metalúrgicos en diversas condiciones, incluyendo materiales con propiedades diferentes a las consideradas anteriormente. Es importante realizar previamente una caracterización experimental de las propiedades físicas del material de la pieza.

Para validar el modelo de orden reducido de forma más exhaustiva, sería beneficioso comparar los resultados obtenidos a partir de este modelo en diferentes condiciones con los resultados de la co-simulación. Para ello habría que integrar una herramienta de simulación de elementos finitos con el simulador eléctrico MATLAB®/Simulink. Aunque la co-simulación supondría un elevado coste computacional, con el consiguiente aumento del tiempo de simulación, permitiría evaluar la precisión alcanzada con los modelos de orden reducido.

Además, se propone investigar mejoras del convertidor para cargas inductivas ligeras, que son el foco de esta tesis. Esto podría lograrse utilizando un transformador de adaptación entre la salida de la etapa de potencia y el sistema inductor-pieza. En este momento se dispone de un prototipo totalmente funcional de un transformador de potencia que cumple las especificaciones requeridas.

List of Publications

Journal Articles (JCR)

- A. Mendi-Altube, I. Villar, C. Carretero, and J. Acero, "Reduced-Order Dynamics of a DC-Bus Voltage-Regulated Inverter for Steel Hardening Beyond Curie Point Temperature," *IEEE Transactions on Industry Applications*, vol. 61, 4, pp. 6581-6592, 2025.
  doi: 10.1109/TIA.2025.3549736

- A. Mendi-Altube, I. Villar, C. Carretero, and J. Acero, "Electro-Thermal Modeling of an Induction Heating Process of 42CrMo4 Steel Probe," *International Journal of Applied Electromagnetics and Mechanics*, vol. 75, pp. 169-178, 2024.
  doi: 10.3233/JAE-230182

International Conferences

- A. Mendi-Altube, I. Villar, I. Landaburu, C. Carretero, and J. Acero, "Exploring Power-Frequency Ranges in Series Resonant Inverters: Study of a Versatile Industrial Induction Heater," *PCIM Europe 2025; International Exhibition and Conference for Power Electronics, Intelligent Motion, Renewable Energy and Energy Management*, Nuremberg, Germany, 2025, pp. 1303-1309.
  doi: 10.30420/566541169

- A. Mendi-Altube, I. Villar, C. Carretero, and J. Acero, "Dynamic DC-Bus Voltage Control of Induction Hardening System Under Load Temperatures from Ambient to Beyond Curie Point," *IEEE Applied Power Electronics Conference and Exposition, APEC 2024*, Long Beach, 2024, pp. 1669-1674.
  doi: 10.1109/APEC48139.2024.10509197

- A. Mendi-Altube, I. Villar, C. Carretero, and J. Acero, "Electro-Thermal Modelling of Induction Hardening Process of 42CrMo4 Steel Probe," *International Conference on Heating by Electromagnetic Systems, HES-23*, Padova, 2023.

- A. Mendi-Altube, F. Gonzalez-Hernando, I. Villar, C. Carretero, and J. Acero, "Switching Losses Estimation Considering Device Parasitics in SiC-Based Industrial Induction Heaters," *PCIM Europe 2023; International Exhibition and Conference for Power Electronics, Intelligent Motion, Renewable Energy and Energy Management*, Nuremberg, Germany, 2023, pp. 1799-1804.
  doi: 10.30420/566091248

National Conferences

- A. Mendi-Altube, I. Villar, C. Carretero, and J. Acero, "Modeling and Design of Induction Heating Systems," *Jornada de Jóvenes Investigadores del I3A*, Zaragoza, 2024.
  doi: 10.26754/jjii3a.202410580

- A. Mendi-Altube, I. Villar, C. Carretero, and J. Acero, "Modelado electrotérmico de un proceso de calentamiento por inducción para aplicaciones industriales," *Jornada de Jóvenes Investigadores del I3A*, Zaragoza, 2023.
  doi: 10.26754/jjii3a.20239020

- A. Mendi-Altube, I. Villar, C. Carretero, and J. Acero, "SiC Based Power Converter for Industrial Induction Hardening of Steel Probes," *Jornada de Jóvenes Investigadores del I3A*, Zaragoza, 2022.
  doi: 10.26754/jjii3a.20226985

Bibliography

[1] D. Fessler, "A burning desire: Steps toward an evolutionary psychology of fire learning," *Journal of Cognition and Culture*, vol. 6, pp. 429–451, 3-4 2006. DOI: 10.1163/156853706778554986.

[2] J. A. Gowlett, "The discovery of fire by humans: A long and convoluted process," *Philosophical Transactions of the Royal Society B: Biological Sciences*, vol. 371, 1696 2016. DOI: 10.1098/RSTB.2015.0164.

[3] K. G. Frank, "Progress in the iron and steel industry and the electric furnace," *Proceedings of the American Institute of Electrical Engineers*, vol. 34, pp. 2547–2554, 10 1915. DOI: 10.1109/PAIEE.1915.6590245.

[4] Impensustained, *Plate detailing equations affixed to rear of plinth on which statue of James Clerk Maxwell statue sits*, Licensed under Creative Commons BY-SA 3.0, 2013. [Online]. Available: https://commons.wikimedia.org/wiki/File:James_Clerk_Maxwell_Statue_Equations.jpg.

[5] O. Lucía, P. Maussion, E. J. Dede, and J. M. Burdío, "Induction heating technology and its applications: Past developments, current technology, and future challenges," *IEEE Transactions on Industrial Electronics*, vol. 61, pp. 2509–2520, 5 2014. DOI: 10.1109/TIE.2013.2281162.

[6] V. Rudnev, "Evolution of induction heating and heat treating as a subject of mathematical modeling, optimization and design," in *2019 XXI International Conference Complex Systems: Control and Modeling Problems (CSCMP)*, 2019, pp. 43–47. DOI: 10.1109/CSCMP45713.2019.8976826.

[7] J. Acero, R. Alonso, J. M. Burdio, L. A. Barragan, and D. Puyal, "Analytical equivalent impedance for a planar circular induction heating system," *IEEE Transactions on Magnetics*, vol. 42, pp. 84–86, 2006. DOI: 10.1109/TMAG.2005.854443.

[8] V. Nemkov, *Online induction heating course*, Accessed: 2024/09/13. [Online]. Available: https://fluxtrol.com/education-online-induction-heating-course.

[9] S. Lupi, *Fundamentals of Electroheat*. Springer, 2017.

[10] E. J. Rothwell and M. J. Cloud, *Electromagnetics*. CRC Press, 2001.

[11] J. Egalon, S. Caux, P. Maussion, M. Souley, and O. Pateau, "Multiphase system for metal disc induction heating: Modeling and RMS current control," *IEEE Transactions on Industry Applications*, vol. 48, pp. 1692–1699, 5 2012. DOI: 10.1109/TIA.2012.2210176.

[12] B. Nacke and A. Dietrich, "Potentials of single stage induction heating for press hardening of steel blanks," in *IOP Conference Series: Materials Science and Engineering*, vol. 424, Institute of Physics Publishing, 2018. DOI: 10.1088/1757-899X/424/1/012058.

[13] M. Schulze, A. Nikanorov, and B. Nacke, "Hierarchical shape optimization of one-sided transverse flux heating induction coil," *COMPEL - The International Journal for Computation and*

Mathematics in Electrical and Electronic Engineering, vol. 39, pp. 73–80, 1 2020. DOI: 10.1108/COMPEL-05-2019-0214.

[14] A. Dietrich and B. Nacke, "Numerical investigation of effects on blanks for press hardening process during longitudinal flux heating," in *IOP Conference Series: Materials Science and Engineering*, vol. 355, Institute of Physics Publishing, 2018. DOI: 10.1088/1757-899X/355/1/012014.

[15] P. Vishnuram, G. Ramachandiran, T. S. Babu, and B. Nastasi, "Induction heating in domestic cooking and industrial melting applications: A systematic review on modelling, converter topologies and control schemes," *Energies*, vol. 14, p. 6634, 20 2021. DOI: 10.3390/en14206634.

[16] T. Thosdeekoraphat, K. Tanthai, K. Lhathum, S. Kotchapradit, S. Santalunai, and C. Thongsopa, "The design of a large-scale induction heating power source for organic waste digesters to produce fertilizer," *Energies 2023, Vol. 16, Page 2123*, vol. 16, p. 2123, 5 2023. DOI: 10.3390/EN16052123.

[17] Y. Design, *Induction iron*, Accessed: 2025/02/04. [Online]. Available: https://www.yankodesign.com/2009/07/24/induction-iron/.

[18] ENRX, *Induction heating - Automotive*, Accessed: 2024/12/03. [Online]. Available: https://www.enrx.com/en/Industries/Induction-heating/Automotive.

[19] E. Plumed, S. Member, I. Lope, J. Acero, S. Member, and J. M. Burdío, "Domestic induction heating system with standard primary inductor for reduced-size and high distance cookware," *IEEE Transactions on Industry Applications*, vol. 58, pp. 7562–7571, 6 2022. DOI: 10.1109/TIA.2022.3193107.

[20] W. Zhang, C. Wu, and S. R. P. Silva, "Proposed use of self-regulating temperature nanoparticles for cancer therapy," *Expert Review of Anticancer Therapy*, vol. 18, pp. 723–725, 8 2018. DOI: 10.1080/14737140.2018.1483242.

[21] R. K. Gilchrist, R. Medal, W. D. Shorey, R. C. Hanselman, J. C. Parrott, and C. B. Taylor, "Selective inductive heating of lymph nodes," *Annals of surgery*, vol. 146, pp. 596–606, 4 1957. DOI: 10.1097/00000658-195710000-00007.

[22] E. C. García-Galán, M. Medel-Plaza, J. J. Pozo-Kreilinger, *et al.*, "In vivo reduction of biofilm seeded on orthopaedic implants," *Bone & Joint Research*, vol. 13, pp. 695–702, 12 2024. DOI: doi:10.1302/2046-3758.1312.BJR-2024-0111.R2.

[23] UltraFlex Power Technologies, *Induction heating application viewbook*, 2018.

[24] L. Rising, D. Gibeaut, F. Wilson, J. Millard, and E. Fouche, "A review on energy management in textile industry," *TechApplication*, 1 1995.

[25] J. Kimme, J. Gruner, A. Fröhlich, and M. Kroll, "Study of an additive manufacturing technology using pulsed inductive wire melting," *International Journal of Applied Electromagnetics and Mechanics*, vol. 75, pp. 119–130, 2024. DOI: 10.3233/JAE-230183.

[26] W. Raza, G. S. Ko, and Y. C. Park, "Induction heater based battery thermal management system for electric vehicles," *Energies 2020, Vol. 13, Page 5711*, vol. 13, p. 5711, 21 2020. DOI: 10.3390/EN13215711.

[27] P. Bocher, D. Mingardi, B. Larregain, F. Bridier, F. Dughiero, and M. Spezzapria, "Simulation of fast induction surface heating and comparison with experimental full-field surface temperature measurements," *International Conference on Heating by Electromagnetic Sources*, pp. 99–108, 2013.

[28] I. Villar, U. Iruretagoyena, A. Cardenas, and F. Redondo, "Induction application to aircraft ice protection system," *2019 IEEE Energy Conversion Congress and Exposition, ECCE 2019*, pp. 4201–4206, 2019. DOI: 10.1109/ECCE.2019.8912552.

[29] A. Ahmad, M. S. Alam, and R. Chabaan, "A comprehensive review of wireless charging technologies for electric vehicles," *IEEE Transactions on Transportation Electrification*, vol. 4, pp. 38–63, 1 2017. DOI: 10.1109/TTE.2017.2771619.

[30] R. E. Haimbaugh, *Practical Induction Heat Treating*, 2nd ed. ASM International, 2015. DOI: 10.31399/asm.tb.piht2.9781627083119.

[31] O. Lucia, J. Acero, C. Carretero, and J. M. Burdío, "Induction heating appliances: Toward more flexible cooking surfaces," *IEEE Industrial Electronics Magazine*, vol. 7, pp. 35–47, 3 2013. DOI: 10.1109/MIE.2013.2247795.

[32] GH Group, *Induction solutions for your industry*, Accessed: 2024/08/26. [Online]. Available: https://ghinduction.com/en/.

[33] E. Baake and V. A. Shpenst, "Recent scientific research on electrothermal metallurgical processes," *Journal of Mining Institute*, vol. 240, pp. 660–668, 2019. DOI: 10.31897/PMI.2019.6.660.

[34] V. Rudnev, D. Loveless, and R. Cook, *Handbook of Induction Heating*, 2nd ed. CRC Press, 2017. DOI: 10.1201/9781315117485.

[35] Leflambela, *Inducteur à roue dentée*, Licensed under Creative Commons BY-SA 3.0, 2007. [Online]. Available: https://commons.wikimedia.org/wiki/File:HE_097_Zahnraderw%C3%A4rmung_Applikationslabor,_Spule_beleuchtet.jpeg.

[36] M. Fisk, L. E. Lindgren, W. Datchary, and V. Deshmukh, "Modelling of induction hardening in low alloy steels," *Finite Elements in Analysis and Design*, vol. 144, pp. 61–75, 2018. DOI: 10.1016/j.finel.2018.03.002.

[37] P. Z. Cao, G. Z. Liu, and K. Wu, "Study of heat treatment parameters for large-scale hydraulic steel gate track," *Water Science and Engineering*, vol. 6, pp. 423–432, 4 2013. DOI: 10.3882/j.issn.1674-2370.2013.04.006.

[38] J. P. Oleaga, *TTT diagram of the isothermal transformations of a hypoeutectoid carbon steel*, Licensed under Creative Commons BY-SA 4.0, 2020. [Online]. Available: https://commons.wikimedia.org/wiki/File:TTT_diagram-20201210-isothermal_transformations_in_steels.svg.

[39] G. Krauss, *Steels: Processing, Structure, and Performance*. ASM International, 2015. DOI: 10.31399/asm.tb.spsp2.9781627082655.

[40] C. Simsir, "Modeling and simulation of steel heat treatment—prediction of microstructure, distortion, residual stresses, and cracking," in *Steel Heat Treating Technologies*. ASM International, 2014, pp. 409–466. DOI: 10.31399/asm.hb.v04b.a0005950.

[41] S. M. Muyskens, T. I. Eddir, and R. C. Goldstein, "Improving induction tube welding system performance using soft magnetic composites," *COMPEL - The International Journal for Computation and Mathematics in Electrical and Electronic Engineering*, vol. 39, pp. 185–191, 1 2020. DOI: 10.1108/COMPEL-06-2019-0232.

[42] T. Steinberg, E. Baake, W. Kollenberg, *et al.*, "Additive manufactured magnetic flux concentrators for induction heating applications," *International Journal of Applied Electromagnetics and Mechanics*, vol. 63, S31–S39, S1 2020. DOI: 10.3233/JAE-209119.

[43] Y. Pleshivtseva, M. Baldan, A. Popov, A. Nikanorov, E. Rapoport, and B. Nacke, "Effective methods for optimal design of induction coils on example of surface hardening," *COMPEL - The International Journal for Computation and Mathematics in Electrical and Electronic Engineering*, vol. 39, pp. 90–99, 1 2020. DOI: 10.1108/COMPEL-05-2019-0216.

[44] S. Schubotz and B. Nacke, "Approaches for increasing the lifetime of single-shot coils," *COMPEL - The International Journal for Computation and Mathematics in Electrical and Electronic Engineering*, vol. 39, pp. 166–176, 1 2020. DOI: 10.1108/COMPEL-06-2019-0228.

[45] M. Schulze, A. Nikanorov, and B. Nacke, "Design of an one-sided transverse flux induction coil by using a numerical optimization algorithm," in *IOP Conference Series: Materials Science and Engineering*, vol. 424, Institute of Physics Publishing, 2018. DOI: 10.1088/1757-899X/424/1/012065.

[46] J. Acero, C. Carretero, R. Alonso, and J. M. Burdio, "Quantitative evaluation of induction efficiency in domestic induction heating applications," *IEEE Transactions on Magnetics*, vol. 49, pp. 1382–1389, 4 2013. DOI: 10.1109/TMAG.2012.2227495.

[47] G. Martín-Segura, "Induction heating converter's design, control and modeling applied to continuous wire heating," Ph.D. dissertation, Universitat Politècnica de Catalunya, 2012.

[48] V. Esteve, "Influencia de los componentes parásitos en el análisis y diseño de inversores resonantes paralelo para aplicaciones de calentamiento por inducción," Ph.D. dissertation, Universitat de Valencia, 1999.

[49] F. Forest, S. Faucher, J.-Y. Gaspard, D. Montloup, J.-J. Huselstein, and C. Joubert, "Frequency-synchronized resonant converters for the supply of multiwinding coils in induction cooking appliances," *IEEE Transactions on Industrial Electronics*, vol. 54, 1 2007. DOI: 10.1109/TIE.2006.888797.

[50] C. Carretero, O. Lucia, J. Acero, R. Alonso, and J. M. Burdio, "Frequency-dependent modelling of domestic induction heating systems using numerical methods for accurate time-domain simulation," *IET Power Electronics*, vol. 5, pp. 1291–1297, 8 2012. DOI: 10.1049/iet-pel.2012.0113.

[51] F. de Leon and A. Semlyen, "Time domain modeling of eddy current effects for transformer transients," *IEEE Transactions on Power Delivery*, vol. 8, pp. 271–280, 1 1993. DOI: 10.1109/61.180346.

[52] R. Asensi, R. Prieto, J. A. Cobos, and J. Uceda, "Modeling high-frequency multiwinding magnetic components using finite-element analysis," *IEEE Transactions on Magnetics*, vol. 43, pp. 3840–3850, 10 2007. DOI: 10.1109/TMAG.2007.903162.

[53] G. V. Kopcsay, B. Krauter, D. Widiger, A. Deutsch, B. J. Rubin, and H. H. Smith, "A comprehensive 2-D inductance modeling approach for VLSI interconnects: Frequency-dependent extraction and compact circuit model synthesis," *IEEE Transactions on Very Large Scale Integration (VLSI) Systems*, vol. 10, pp. 695–711, 6 2002. DOI: 10.1109/TVLSI.2002.801574.

[54] D. Puyal, C. Bernal, J. M. Burdio, I. Millan, and J. Acero, "A new dynamic electrical model of domestic induction heating loads," in *2008 Twenty-Third Annual IEEE Applied Power Electronics Conference and Exposition*, 2008, pp. 409–414. DOI: 10.1109/APEC.2008.4522754.

[55] F. Forest, E. Labouré, F. Costa, and J. Y. Gaspard, "Principle of a multi-load/single converter system for low power induction heating," *IEEE Transactions on Power Electronics*, vol. 15, p. 223, 2 2000.

[56] C. Carretero, O. Lucía, J. Acero, and J. M. Burdío, "FEA tool based model of partly coupled coils used in domestic induction cookers," in *IECON 2011 - 37th Annual Conference of the IEEE Industrial Electronics Society*, 2011, pp. 2533–2538. DOI: 10.1109/IECON.2011.6119708.

[57] J. Serrano, J. Acero, I. Lope, C. Carretero, J. M. Burdio, and R. Alonso, "Modeling of domestic induction heating systems with non-linear saturable loads," *Conference Proceedings - IEEE Applied Power Electronics Conference and Exposition - APEC*, pp. 3127–3133, 2017. DOI: 10.1109/APEC.2017.7931144.

[58] C. Carretero, J. Acero, R. Alonso, J. M. Burdío, and F. Monterde, "Temperature influence on equivalent impedance and efficiency of inductor systems for domestic induction heating appliances," in *APEC 07 - Twenty-Second Annual IEEE Applied Power Electronics Conference and Exposition*, 2007, pp. 1233–1239. DOI: 10.1109/APEX.2007.357672.

[59] J. Barglik, A. Smalcerz, A. Smagór, and P. Paszek, "Analysis of continuous induction hardening of steel cylinder element made of steel 38mn6," *Archives of Metallurgy and Materials*, No 4 December 2015. DOI: 10.1515/amm-2015-0457.

[60] S. Ali, Q. Mohammed, and J.-W. Jung, "A state-of-the-art review on soft-switching techniques for DC-DC, DC-AC, AC-DC, and AC-AC power converters," *IEEE Transactions on Industrial Informatics*, vol. 17, p. 6569, 10 2021. DOI: 10.1109/TII.2021.3058218.

[61] M. Buffolo, D. Favero, A. Marcuzzi, *et al.*, "Review and outlook on GaN and SiC power devices: Industrial state-of-the-art, applications, and perspectives," *IEEE Transactions on Electron Devices*, 2024. DOI: 10.1109/TED.2023.3346369.

[62] Infineon Technologies, *Silicon Carbide CoolSiC™ MOSFETs - Infineon Technologies*, Accessed: 2025/05/14. [Online]. Available: https://www.infineon.com/cms/en/product/power/mosfet/silicon-carbide/.

[63] Infineon Technologies, *Gallium Nitride (GaN) - Infineon Technologies*, Accessed: 2025/02/14. [Online]. Available: https://www.infineon.com/cms/en/product/power/gallium-nitride/?redirId=294997.

[64] A. Lidow, M. de Rooij, J. Strydom, D. Reusch, and J. Glaser, "GaN technology overview," in *GaN Transistors for Efficient Power Conversion*. John Wiley & Sons, Ltd, 2019, pp. 1–23. DOI: https://doi.org/10.1002/9781119594406.ch1.

[65] E. J. Dede, J. Jordán, and V. Esteve, "The practical use of SiC devices in high power, high frequency inverters for industrial induction heating applications," in *2016 IEEE 2nd Annual Southern Power Electronics Conference (SPEC)*, 2016, pp. 1–5. DOI: 10.1109/SPEC.2016.7846163.

[66] E. J. Dede, J. Jordan, and V. Esteve, "SIC induction smart welder integrated in an industry 4.0 network," in *IECON 2017 - 43rd Annual Conference of the IEEE Industrial Electronics Society*, 2017, pp. 3797–3800.

[67] H. Sarnago, J. M. Burdío, and O. Lucía, "High-frequency GaN-based induction heating versatile module for flexible cooking surfaces," in *2019 IEEE Applied Power Electronics Conference and Exposition (APEC)*, 2019, pp. 448–452.

[68] J. Acero, J. M. Burdío, L. A. Barragan, *et al.*, "Domestic induction appliances," *IEEE Industry Applications Magazine*, vol. 16, pp. 39–47, 2 2010. DOI: 10.1109/MIAS.2009.935495.

[69] J. W. Kolar and T. Friedli, "The essence of three-phase PFC rectifier systems—Part I," *IEEE Transactions on Power Electronics*, vol. 28, pp. 176–198, 1 2013. DOI: 10.1109/TPEL.2012.2197867.

[70] T. Friedli, M. Hartmann, and J. W. Kolar, "The essence of three-phase PFC rectifier systems—Part II," *IEEE Transactions on Power Electronics*, vol. 29, pp. 543–560, 2 2014. DOI: 10.1109/TPEL.2013.2258472.

[71] H. P. Ngoc, H. Fujita, K. Ozaki, and N. Uchida, "Phase angle control of high-frequency resonant currents in a multiple inverter system for zone-control induction heating," *IEEE Transactions on Power Electronics*, vol. 26, pp. 3357–3366, 11 2011. DOI: 10.1109/TPEL.2011.2146278.

[72] H. W. E. Koertzen, J. A. Ferreira, and J. D. V. Wyk, "A comparative study of single switch induction heating converters using novel component effectivity concepts," in *23rd Annual IEEE Power Electronics Specialists Conference PESC '92 Record*, 1992. DOI: 10.1109/PESC.1992.254659.

[73] H. Sarnago, J. M. Burdío, and O. Lucia, "Dual-output extended-power-range quasi-resonant inverter for induction heating appliances," *IEEE Transactions on Power Electronics*, vol. 38, pp. 3385–3397, 3 2023. DOI: 10.1109/TPEL.2022.3226497.

[74] C. Chen, Y. Chen, Y. Li, Z. Huang, T. Liu, and Y. Kang, "An SiC-based half-bridge module with an improved hybrid packaging method for high power density applications," *IEEE Transactions on Industrial Electronics*, vol. 64, pp. 8980–8991, 11 2017. DOI: 10.1109/TIE.2017.2723873.

[75] T. Mishima, C. Takami, and M. Nakaoka, "A new current phasor-controlled ZVS twin half-bridge high-frequency resonant inverter for induction heating," *IEEE Transactions on Industrial Electronics*, vol. 61, pp. 2531–2545, 5 2014. DOI: 10.1109/TIE.2013.2274420.

[76] P. Savary, M. Nakaoka, and T. Maruhashi, "A high-frequency resonant inverter using current-vector control scheme and its performance evaluations," *IEEE Transactions on Industrial Electronics*, vol. IE-34, pp. 247–256, 2 1987. DOI: 10.1109/TIE.1987.350961.

[77] N. J. Park, D. S. Lee, and D. Y. Hyun, "A power-control scheme with constant switching frequency in class-D inverter for induction-heating jar application," *IEEE Transactions on Industrial Electronics*, vol. 54, pp. 1252–1260, 3 2007. DOI: 10.1109/TIE.2007.892741.

[78] E. J. Dede, J. V. Gonzalez, J. A. Linares, J. Jordan, D. Ramirez, and P. Rueda, "25-kW/50-kHz generator for induction heating," *IEEE Transactions on Industrial Electronics*, vol. 38, pp. 203–209, 3 1991. DOI: 10.1109/41.87588.

[79] A. Shenkman, B. Axelrod, and V. Chudnovsky, "Assuring continuous input current using a smoothing reactor in a thyristor frequency converter for induction metal melting and heating applications," *IEEE Transactions on Industrial Electronics*, vol. 48, pp. 1290–1292, 6 2001. DOI: 10.1109/41.969415.

[80] J. M. E. Huerta, E. J. D. G. Santamaría, R. G. Gil, and J. Castelló-Moreno, "Design of the L-LC resonant inverter for induction heating based on its equivalent SRI," *IEEE Transactions on Industrial Electronics*, vol. 54, pp. 3178–3187, 6 2007. DOI: 10.1109/TIE.2007.905928.

[81] V. Esteve, J. Jordán, E. J. Dede, *et al.*, "Optimal LLC inverter design with SiC MOSFETs and phase shift control for induction heating applications," *IEEE Transactions on Industrial Electronics*, vol. 69, pp. 11 100–11 111, 11 2022. DOI: 10.1109/TIE.2021.3121730.

[82] V. Esteve, J. Jordán, E. J. Dede, P. J. Martinez, K. J. Ferrara, and J. L. Bellido, "Comparative analysis and improved design of LLC inverters for induction heating," *IET Power Electronics*, vol. 16, pp. 1754–1764, 10 2023. DOI: 10.1049/pel2.12484.

[83] M. A. Dzieniakowski, "Power electronics converters in induction heating-the survey," in *Progress in Applied Electrical Engineering (PAEE)*, 2017.

[84] P. Guillen, H. Sarnago, J. M. Burdío, and O. Lucía, "Single-ended direct AC-AC converter for domestic induction heating based on a bidirectional GaN-FET," in *Conference Proceedings - IEEE Applied Power Electronics Conference and Exposition - APEC*, Institute of Electrical and Electronics Engineers Inc., 2024, pp. 1659–1663. DOI: 10.1109/APEC48139.2024.10509398.

[85] S. Komeda and H. Fujita, "A phase-shift-controlled direct AC-to-AC converter for induction heaters," *IEEE Transactions on Power Electronics*, vol. 33, pp. 4115–4124, 5 May 2018. DOI: 10.1109/TPEL.2017.2712281.

[86] R. C. M. Gomes, M. A. Vitorino, D. A. Acevedo-Bueno, and M. B. D. R. Correa, "Multiphase resonant inverter with coupled coils for AC-AC induction heating application," *IEEE Transactions on Industry Applications*, vol. 56, pp. 551–560, 1 2020. DOI: 10.1109/TIA.2019.2955661.

[87] S. Inami and S. Komeda, "A three-phase AC input induction heating system with heat distribution control capability," *IEEE Transactions on Industrial Electronics*, pp. 1–11, 2024. DOI: 10.1109/tie.2024.3440478.

[88] H. Fujita, N. Uchida, and K. Ozaki, "A new zone-control induction heating system using multiple inverter units applicable under mutual magnetic coupling conditions," *IEEE Transactions on Power Electronics*, vol. 26, pp. 2009–2017, 7 2011. DOI: 10.1109/TPEL.2010.2101084.

[89] R. C. M. Gomes, M. A. Vitorino, D. A. Acevedo-Bueno, and M. B. D. R. Correa, "Three-phase AC-AC converter with diode rectifier for induction heating application with improved input current quality and coil modeling," *IEEE Transactions on Industry Applications*, vol. 57, pp. 2673–2681, 3 2021. DOI: 10.1109/TIA.2021.3065629.

[90] P. Guillen, H. Sarnago, O. Lucia, and J. M. Burdío, "GaN-based matrix resonant power converter for domestic induction heating," *IEEE Transactions on Power Electronics*, vol. 38, pp. 6769–6773, 6 2023. DOI: 10.1109/TPEL.2023.3239160.

[91] Y. Kawaguchi, E. Hiraki, T. Tanaka, *et al.*, "A comparative evaluation of DCM control and CCM control for soft-switching PFC converter," *IECON Proceedings (Industrial Electronics Conference)*, pp. 250–255, 2010. DOI: 10.1109/IECON.2010.5675018.

[92] Y. Wang, O. Lucia, Z. Zhang, S. Gao, and D. Xu, "A review of high frequency power converters and related technologies," *IEEE Open Journal of the Industrial Electronics Society*, vol. 1, pp. 247–260, 2020. DOI: 10.1109/OJIES.2020.3023691.

[93] E. Spateri, F. Ruiz, and G. Gruosso, "Modelling and simulation of quasi-resonant inverter for induction heating under variable load," *Electronics (Switzerland)*, vol. 12, 3 2023. DOI: 10.3390/electronics12030753.

[94] S. Wang, K. Izaki, I. Hirota, H. Yamashita, and H. Omori, "Induction-heated cooking appliance using new quasi-resonant ZVS-PWM inverter with power factor correction," *IEEE Transactions on Industry Applications*, vol. 34, pp. 705–712, 4 1998. DOI: 10.1109/28.703961.

[95] V. Esteve, J. Jordán, E. J. Dede, and J. L. Bellido, "Enhanced asymmetrical modulation for half-bridge series resonant inverters in induction heating applications," *IET Power Electronics*, vol. 16, pp. 2482–2491, 15 2023. DOI: 10.1049/pel2.12573.

[96] B. Meziane and H. Zeroug, "Comprehensive power control performance investigations of resonant inverter for induction metal surface hardening," *IEEE Transactions on Industrial Electronics*, vol. 63, pp. 6086–6096, 10 2016. DOI: 10.1109/TIE.2016.2581145.

[97] Z. Ye and Z. Liang, "Modeling and design of a pulse phase modulated resonant inverter system," in *INTELEC 2008 - 2008 IEEE 30th International Telecommunications Energy Conference*, 2008.

[98] A. Mendi-Altube, I. Landaburu, I. Villar, C. Carretero, and J. Acero, "Exploring power-frequency ranges in series resonant inverters: Study of a versatile industrial induction heater," in *PCIM Conference 2025; International Exhibition and Conference for Power Electronics, Intelligent Motion, Renewable Energy and Energy Management*, 2025. DOI: 10.30420/566541169.

[99] P. K. Jain, J. R. Espinoza, and S. B. Dewan, "Self-started voltage-source series-resonant converter for high-power induction heating and melting applications," *IEEE Transactions on Industry Applications*, vol. 34, pp. 518–525, 3 1998.

[100] L. A. Barragán, D. Navarro, J. Acero, I. Urriza, and J. M. Burdío, "FPGA implementation of a switching frequency modulation circuit for EMI reduction in resonant inverters for induction heating appliances," *IEEE Transactions on Industrial Electronics*, vol. 55, pp. 11–20, 1 2008. DOI: 10.1109/TIE.2007.896129.

[101] V. Esteve, E. Sanchis-Kilders, J. Jordán, *et al.*, "Improving the efficiency of IGBT series-resonant inverters using pulse density modulation," *IEEE Transactions on Industrial Electronics*, vol. 58, pp. 979–987, Mar. 2011. DOI: 10.1109/TIE.2010.2049706.

[102] H. Fujita and H. Akagi, "Pulse-density-modulated power control of a 4 kW, 450 kHz voltage-source inverter for induction melting applications drain to source voltage drain current on-

state resistance input capacitance output capacitance turn-on delay time rise time," *IEEE Transactions on Industry Applications*, vol. 32, 2 1996.

[103] J. Zerad, S. Riachy, P. Toussaint, and J. P. Barbot, "Novel phasor transformation for feedback control design of induction heating systems with experimental results," *IEEE Transactions on Industrial Electronics*, vol. 62, pp. 6478–6485, 10 2015. DOI: 10.1109/TIE.2015.2424394.

[104] G. Martín-Segura, C. Ferrater-Simón, J. López-Mestre, D. Montesinos-Miracle, and J. Bergas-Jané, "Simulation of an induction hardening system during Curie temperature transition considering converter's performance," *COMPEL - The international journal for computation and mathematics in electrical and electronic engineering*, vol. 32, pp. 396–411, 1 2013. DOI: 10.1108/03321641311293957.

[105] J. L. Bellido, V. Esteve, and J. Jordán, "Efficiency optimization in parallel LLC resonant inverters with current-controlled variable-inductor and phase shift for induction heating," *Electronics (Switzerland)*, vol. 13, 13 2024. DOI: 10.3390/electronics13132593.

[106] P. Pal, D. Roy, A. Datta, P. K. Sadhu, and A. Banerjee, "A closed-loop power controller model of series-resonant-inverter-fitted induction heating system," *Archives of Electrical Engineering*, vol. vol. 65, pp. 827–841, No 4 December 2016. DOI: 10.1515/aee-2016-0058.

[107] Z. F. Li, J. C. Hu, M. S. Huang, Y. L. Lin, C. W. Lin, and Y. M. Meng, "Load estimation for induction heating cookers based on series RLC natural resonant current," *Energies*, vol. 15, p. 1294, 4 2022. DOI: 10.3390/EN15041294.

[108] M. S. Huang, J. C. Hu, Y. M. Chen, Z. F. Li, and C. W. Lin, "Simple power control method for induction heating cookers using fundamental frequency power under asymmetrical pulse-width modulation," *IEEE Transactions on Power Electronics*, 2024. DOI: 10.1109/TPEL.2024.3521397.

[109] M. Popescu, A. Bitoleanu, and V. Suru, "Control of the power in induction heating systems with L-LC resonant voltage source inverters," *2013 4th International Symposium on Electrical and Electronics Engineering, ISEEE 2013 - Proceedings*, 2013. DOI: 10.1109/ISEEE.2013.6674344.

[110] P. Herasymenko and O. Yurchenko, "An extended pulse-density-modulated series-resonant inverter for induction heating applications," *2020 IEEE 61st Annual International Scientific Conference on Power and Electrical Engineering of Riga Technical University, RTUCON 2020 - Proceedings*, 2020. DOI: 10.1109/RTUCON51174.2020.9316617.

[111] A. Bitoleanu, M. Popescu, and V. Suru, "Shift phase power control in induction heating systems with voltage resonant inverter," *2014 International Conference on Applied and Theoretical Electricity, ICATE 2014 - Proceedings*, 2014. DOI: 10.1109/ICATE.2014.6972649.

[112] K. L. Nguyen, O. Pateau, S. Caux, P. Maussion, and J. Egalon, "Robustness of a resonant controller for a multiphase induction heating system," *IEEE Transactions on Industry Applications*, vol. 51, pp. 73–81, 1 2015. DOI: 10.1109/TIA.2014.2354405.

[113] J. S. Artal-Sevil, F. Rivases, J. Beyza, and M. A. Evangelista, "Design and implementation of a high-power resonant converter for an induction steel-melting furnace," *2021 23rd IEEE International Autumn Meeting on Power, Electronics and Computing, ROPEC 2021*, 2021. DOI: 10.1109/ROPEC53248.2021.9668081.

[114] M. K. Artur and Y. E. Pleshivtseva, "Synthesis of feed-back system of optimal control for numerical model of induction heating process of steel cylindrical billets," *2018 International Russian Automation Conference, RusAutoCon 2018*, 2018. DOI: 10.1109/RUSAUTOCON.2018.8501784.

[115] C. Carretero, J. Lasobras, R. Alonso, E. Carretero, and E. Imaz, "Radiation heat measurement model for temperature estimation in induction heating appliances," in *IECON 2014 - 40th Annual Conference of the IEEE Industrial Electronics Society*, 2014, pp. 3265–3269. DOI: 10.1109/IECON.2014.7048979.

[116] F. Aki, T. Loi, H. Saito, and K. Mitobe, "Examination of the influence on precision of the wireless temperature measurement induction heating system by 37 °C constant temperature environment," *IEEE Transactions on Magnetics*, vol. 54, pp. 1–3, 6 2018. DOI: 10.1109/TMAG.2018.2815028.

[117] M. Chatterjee and P. Y. Nabhiraj, "Capturing the temperature of the workpiece in an induction heating system using thermocouple with minimal error," in *2021 5th International Conference on Electronics, Materials Engineering & Nano-Technology (IEMENTech)*, 2021, pp. 1–5. DOI: 10.1109/IEMENTech53263.2021.9614759.

[118] D. Kaiser, B. de Graaff, S. Dietrich, and V. Schulze, "A novel procedure to account for high temperature gradients in an induction dilatometer sample during rapid heating," *Thermochimica Acta*, vol. 646, pp. 8–15, 2016. DOI: 10.1016/j.tca.2016.10.014.

[119] X. Zhe and P. Sanqiang, "Temperature optimal control of the casting billet induction heating process based on the BP prediction model," *Proceedings of the 2013 IEEE Symposium on Computational Intelligence in Control and Automation, CICA 2013 - 2013 IEEE Symposium Series on Computational Intelligence, SSCI 2013*, pp. 163–167, 2013. DOI: 10.1109/CICA.2013.6611678.

[120] D. Lowther, V. Ghorbanian, M. H. Mohammadi, and I. Ibrahim, "Design tools for electromagnetic-driven multi-physics systems using high performance computing," *COMPEL - The International Journal for Computation and Mathematics in Electrical and Electronic Engineering*, vol. 39, pp. 198–205, 1 2020. DOI: 10.1108/COMPEL-06-2019-0234.

[121] M. Spezzapria, M. Forzan, and F. Dughiero, "Numerical simulation of solid-solid phase transformations during induction hardening process," *IEEE Transactions on Magnetics*, vol. 52, 3 2016. DOI: 10.1109/TMAG.2015.2484388.

[122] J. Y. Jang and Y. W. Chiu, "Numerical and experimental thermal analysis for a metallic hollow cylinder subjected to step-wise electro-magnetic induction heating," *Applied Thermal Engineering*, vol. 27, pp. 1883–1894, 11-12 2007. DOI: 10.1016/j.applthermaleng.2006.12.025.

[123] M. Fernández-Torrijos, C. Sobrino, J. A. Almendros-Ibáñez, C. Marugán-Cruz, and D. Santana, "Inverse heat problem of determining unknown surface heat flux in a molten salt loop," *International Journal of Heat and Mass Transfer*, vol. 139, pp. 503–516, 2019. DOI: 10.1016/j.ijheatmasstransfer.2019.05.002.

[124] D. Desisa, A. Smalcerz, V. Kotlan, J. Barglik, A. Smagor, and I. Dolezel, "Mathematical modelling of thermal stresses of induction surface hardening in axi-symmetric formulation," *Surface and Coatings Technology*, vol. 479, 2024. DOI: 10.1016/j.surfcoat.2024.130516.

[125] V. Bukanin, A. Ivanov, and A. Zenkov, "Investigation of heating and melting in ELTA programs," *COMPEL - The International Journal for Computation and Mathematics in Electrical and Electronic Engineering*, vol. 39, pp. 117–124, 1 2020. DOI: 10.1108/COMPEL-05-2019-0219.

[126] F. Bay, V. Labbe, Y. Favennec, and J. L. Chenot, "A numerical model for induction heating processes coupling electromagnetism and thermomechanics," *INTERNATIONAL JOURNAL FOR NUMERICAL METHODS IN ENGINEERING*, vol. 58, pp. 839–867, 6 2003. DOI: 10.1002/nme.796.

[127] M. Areitioaurtena, U. Segurajauregi, V. Akujärvi, M. Fisk, I. Urresti, and E. Ukar, "A semi-analytical coupled simulation approach for induction heating," *Advanced Modeling and Simulation in Engineering Sciences*, vol. 8, 1 2021. DOI: 10.1186/s40323-021-00199-0.

[128] K. Ishibashi, "Eddy current analysis of induction heating by boundary element method," *Electrical Engineering in Japan*, vol. 104, pp. 109–117, 1 1984. DOI: https://doi.org/10.1002/eej.4391040115.

[129] K. S. Ismail and R. A. Marzouk, "Iterative hybrid finite element-boundary element method for the analysis of induction heating system with nonlinear charge," *IEEE Transactions on Magnetics*, vol. 32, pp. 3212–3218, 4 PART 2 1996. DOI: 10.1109/20.508384.

[130] J. M. Bergheau and P. Conraux, "FEM-BEM coupling for the modelling of induction heating processes including moving parts," *Journal of Shanghai Jiaotong University (Science)*, vol. E-5, pp. 91–99, 2000.

[131] E. Baake, A. Umbrashko, and A. Jakovics, "Numerical simulation of turbulent flows, heat and mass transfer in metallurgical induction processes," *Steel Research International*, vol. 78, pp. 413–418, 5 2007. DOI: 10.1002/SRIN.200705913.

[132] J. P. A. Bastos and N. Sadowski, *Electromagnetic Modeling by Finite Element Methods*. CRC Press, 2003.

[133] J. C. Maxwell, *A treatise on electricity and magnetism*. Oxford University Press, 1973, vol. 1.

[134] M. Fisk, M. Ristinmaa, A. Hultkrantz, and L. E. Lindgren, "Coupled electromagnetic-thermal solution strategy for induction heating of ferromagnetic materials," *Applied Mathematical Modelling*, vol. 111, pp. 818–835, 2022. DOI: 10.1016/j.apm.2022.07.009.

[135] D. Schlesselmann, B. Nacke, A. Nikanorov, and S. Galunin, "Coupled numerical multiphysics simulation methods in induction surface hardening," in *VI International Conference on Computational Methods for Coupled Problems in Science and Engineering*, 2015.

[136] A. Nikanorov, E. Baake, H. Brauer, and C. Weil, "Approaches for coupled numerical simulation of high frequency tube welding process," in *VI International Conference on Computational Methods for Coupled Problems in Science and Engineering*, 2015.

[137] P. Das, J. I. Asperheim, B. Grande, T. Petzold, and D. Hömberg, "Three-dimensional numerical study of heat-affected zone in induction welding of tubes," *COMPEL - The International Journal for Computation and Mathematics in Electrical and Electronic Engineering*, vol. 39, pp. 213–219, 1 2020. DOI: 10.1108/COMPEL-06-2019-0238.

[138] E. Mannanov, S. Galunin, M. Yermekova, A. Nikanorov, and B. Nacke, "Numerical simulation, investigation and development of induction systems for heating of disks with complex profile," in *2019 IEEE Conference of Russian Young Researchers in Electrical and Electronic Engineering (ElConRus)*, 2019.

[139] K. Blinov, A. Nikanorov, B. Nacke, and M. Klöpzig, "Numerical simulation and investigation of induction through-heaters in dynamic operation mode," *COMPEL - The international journal for computation and mathematics in electrical and electronic engineering*, vol. 30, F. Dughiero, E. Baake, and M. Forzan, Eds., pp. 1539–1549, 5 2011. DOI: 10.1108/03321641111152694.

[140] J. Barglik, "Mathematical modeling of induction surface hardening," *COMPEL: The International Journal for Computation and Mathematics in Electrical and Electronic Engineering*, vol. 35, S. Gratkowski and M. Ziolkowski, Eds., pp. 1403–1417, 4 2016. DOI: 10.1108/COMPEL-09-2015-0323.

[141] D. Hömberg, Q. Liu, J. Montalvo-Urquizo, *et al.*, "Simulation of multi-frequency-induction-hardening including phase transitions and mechanical effects," *Finite Elements in Analysis and Design*, vol. 121, pp. 86–100, 2016. DOI: 10.1016/j.finel.2016.07.012.

[142] B. Nacke and A. Dietrich, "Optimal design of induction heating process for hot metal forming of steel blanks," in *2019 XXI International Conference Complex Systems: Control and Modeling Problems (CSCMP)*, 2019. DOI: 10.1109/CSCMP45713.2019.8976825.

[143] M. Baldan, A. Nikanorov, and B. Nacke, "Hierarchical optimization approaches in designing surface hardening induction systems," in *IOP Conference Series: Materials Science and Engineering*, vol. 424, Institute of Physics Publishing, 2018. DOI: 10.1088/1757-899X/424/1/012067.

[144] M Baldan and A Nikanorov and B Nacke, "A novel multi-surrogate multi-objective decision-making optimization algorithm in induction heating," *COMPEL - The International Journal for Computation and Mathematics in Electrical and Electronic Engineering*, vol. 39, pp. 144–157, 1 2020. DOI: 10.1108/COMPEL-05-2019-0222.

[145] M. Baldan, A. Nikanorov, and B. Nacke, "A parallel multi-fidelity optimization approach in induction hardening," *COMPEL - The International Journal for Computation and Mathematics in Electrical and Electronic Engineering*, vol. 39, pp. 133–143, 1 2020. DOI: 10.1108/COMPEL-05-2019-0221.

[146] Y. Pleshivtseva, E. Rapoport, B. Nacke, *et al.*, "Design concepts of induction mass heating technology based on multiple-criteria optimization," *The International Journal for Computation and Mathematics in Electrical and Electronic Engineering*, vol. 36, pp. 386–400, 2 2017. DOI: 10.1108/COMPEL-05-2016-0216.

[147] Y. Pleshivtseva, E. Rapoport, B. Nacke, *et al.*, "Design and control of electrotechnological systems: A multi-objective optimization approach," *The International Journal for Computation and Mathematics in Electrical and Electronic Engineering*, vol. 39, pp. 239–247, 1 2020. DOI: 10.1108/COMPEL-11-2019-0454.

[148] H. Kurose, D. Miyagi, N. Takahashi, N. Uchida, and K. Kawanaka, "3-D eddy current analysis of induction heating apparatus considering heat emission, heat conduction, and temperature dependence of magnetic characteristics," *IEEE Transactions on Magnetics*, vol. 45, pp. 1847–1850, 3 2009. DOI: 10.1109/TMAG.2009.2012829.

[149] F. Preisach, "Über die magnetische nachwirkung," *Zeitschrift für Physik*, vol. 94, pp. 277–302, 5 1935. DOI: 10.1007/BF01349418.

[150] E. C. Stoner and E. P. Wohlfarth, "A mechanism of magnetic hysteresis in heterogeneous alloys," *Philosophical Transactions of the Royal Society of London. Series A, Mathematical and Physical Sciences*, vol. 240, pp. 599–642, 826 Jan. 1997. DOI: 10.1098/rsta.1948.0007.

[151] D. C. Jiles and D. L. Atherton, "Theory of ferromagnetic hysteresis," *Journal of Magnetism and Magnetic Materials*, vol. 61, pp. 48–60, 1-2 1986. DOI: 10.1016/0304-8853(86)90066-1.

[152] D. C. Jiles and J. B. Thoelke, "Theory of ferromagnetic hysteresis: Determination of model parameters from experimental hysteresis loops," *IEEE Transactions on Magnetics*, vol. 25, pp. 3928–3930, 5 1989. DOI: 10.1109/20.42480.

[153] M. Schwenk, J. Hoffmeister, and V. Schulze, "Experimental determination of process parameters and material data for numerical modeling of induction hardening," *Journal of Materials Engineering and Performance*, vol. 22, pp. 1861–1870, 7 2013. DOI: 10.1007/s11665-013-0566-3.

[154] M. Schwenk, M. Fisk, T. Cedell, J. Hoffmeister, V. Schulze, and L.-E. Lindgren, "Process simulation of single and dual frequency induction surface hardening considering magnetic nonlinearity," *Materials Performance and Characterization*, vol. 9, pp. 1–20, 4 2012. DOI: 10.1520/ACEM104374.

[155] V. Akujärvi, T. Cedell, K. Frogner, and M. Andersson, "Mapping of magnetic properties for simulations of high-temperature electromagnetic applications," *COMPEL - The International Journal for Computation and Mathematics in Electrical and Electronic Engineering*, vol. 36, pp. 546–554, 2 2017. DOI: 10.1108/COMPEL-05-2016-0217.

[156] S. H. Chai, J. H. Kim, S. I. Kim, and J. P. Hong, "Extrapolating B–H curve data using common electrical steel characteristics for high magnetic saturation applications," *Journal of Magnetics*, vol. 20, pp. 258–264, 3 2015. DOI: 10.4283/JMAG.2015.20.3.258.

[157] F. C. Trutt, E. A. Erdelyi, and R. E. Hopkins, "Representation of the magnetization characteristic of dc machines for computer use," *IEEE Transactions on Power Apparatus and Systems*, vol. PAS-87, pp. 665–669, 3 1968. DOI: 10.1109/TPAS.1968.292178.

[158] M. Dadic, M. Jurcevic, and R. Malaric, "Approximation of the nonlinear B-H curve by complex exponential series," *IEEE Access*, vol. 8, pp. 49 610–49 616, 2020. DOI: 10.1109/ACCESS.2020.2979866.

[159] D. Labridis and P. Dokopoulos, "Calculation of eddy current losses in nonlinear ferromagnetic materials," *IEEE Transactions on magnetics*, vol. 25, pp. 2665–2669, 3 1989.

[160] C. P. Steinmetz, *Transient Electric Phenomena and Oscillations*, 3rd. Wexford College Press, 2003.

[161] C. Carretero, J. Acero, and J. M. Burdio, "Normalized nonlinear impedance boundary condition in anhysteretic magnetic material for eddy current problems," *IEEE Transactions on Magnetics*, 2024. DOI: 10.1109/TMAG.2024.3395924.

[162] D. Coupard, T. Palin-luc, P. Bristiel, V. Ji, and C. Dumas, "Residual stresses in surface induction hardening of steels: Comparison between experiment and simulation," *Materials Science and Engineering A*, vol. 487, pp. 328–339, 1-2 2008. DOI: 10.1016/j.msea.2007.10.047.

[163] S. Wiak and E. Napieralska-Juszczak, *Computational Methods for the Innovative Design of Electrical Devices*. Springer, 2010, vol. 327, pp. 247–250.

[164] M. Baldan, P. D. Barba, and B. Nacke, "Magnetic properties identification by using a bi-objective optimal multi-fidelity neural network," *IEEE Transactions on Magnetics*, vol. 57, 6 2021. DOI: 10.1109/TMAG.2021.3068705.

[165] A. Canova, F. Dughiero, F. Fasolo, *et al.*, "Simplified approach for 3-D nonlinear induction heating problems," *IEEE Transactions on Magnetics*, vol. 45, pp. 1855–1858, 3 2009. DOI: 10.1109/TMAG.2009.2012831.

[166] A. Canova, F. Dughiero, F. Fasolo, *et al.*, "Identification of equivalent material properties for 3-D numerical modeling of induction heating of ferromagnetic workpieces," *IEEE Transactions on Magnetics*, vol. 45, pp. 1851–1854, 3 2009. DOI: 10.1109/TMAG.2009.2012830.

[167] E. Grüneisen, "Die abhängigkeit des elektrischen widerstandes reiner metalle von der temperatur," *Annalen der Physik*, vol. 408, pp. 530–540, 5 1933. DOI: 10.1002/andp.19334080504.

[168] S. Koley, T. Ray, I. Mohanty, S. Chatterjee, and M. Shome, "Prediction of electrical resistivity of steel using artificial neural network," *Ironmaking and Steelmaking*, vol. 46, pp. 383–391, 4 2019. DOI: 10.1080/03019233.2017.1403109.

[169] D. T. Pierce, G. Muralidharan, A. Trofimov, *et al.*, "Evaluation of thermal processing and properties of 422 martensitic stainless steel for replacement of 4140 steel in diesel engine pistons," *Materials and Design*, vol. 214, 2022. DOI: 10.1016/J.MATDES.2021.110373.

[170] J. H. L. V and J. H. L. IV, *A Heat Transfer Textbook*, 6th ed. PhlogistonPress, 2024.

[171] G. Fang and P. Zeng, "Finite element simulation of metal quenching," *Tsinghua Science and Technology*, vol. 9, pp. 555–559, 5 2004.

[172] D. N. Passarella, A. Aparicio, F. Varas, *et al.*, "Heat transfer coefficient determination of quenching process," *Mecánica Computacional*, vol. XXXIII, pp. 2009–2021, 2014.

[173] H. S. Hasan, M. J. Peet, J. M. Jalil, and H. K. D. H. Bhadeshia, "Heat transfer coefficients during quenching of steels," *Heat and Mass Transfer/Waerme- und Stoffuebertragung*, vol. 47, pp. 315–321, 3 2011. DOI: 10.1007/s00231-010-0721-4.

[174] Y. C. Chen and J. A. Worden, "Evaluation of microalloyed steel for articulated piston applications in heavy duty diesel engines," *SAE Technical Papers*, 2000. DOI: 10.4271/2000-01-1232.

[175] M. Areitioaurtena, U. Segurajauregi, M. Fisk, M. J. Cabello, and E. Ukar, "Numerical and experimental investigation of residual stresses during the induction hardening of 42CrMo4 steel," *European Journal of Mechanics, A/Solids*, vol. 96, p. 104 766, June 2022. DOI: 10.1016/j.euromechsol.2022.104766.

[176] E. Öztürk, "FEM and statistical-based assessment of AISI-4140 dry hard turning using microtextured insert," *Journal of Manufacturing Processes*, vol. 81, pp. 290–300, 2022. DOI: 10.1016/j.jmapro.2022.06.060.

[177] I. Yilmaz, E. Durna, and M. Ermis, "Design and implementation of a hybrid system for the mitigation of pq problems of medium-frequency induction steel-melting furnaces," *IEEE Transactions on Industry Applications*, vol. 52, pp. 2700–2713, 3 2016. DOI: 10.1109/TIA.2016.2530707.

[178] I. Yilmaz, Ö. Salor, M. Ermiş, and I. Çadirci, "Field-data-based modeling of medium-frequency induction melting furnaces for power quality studies," *IEEE Transactions on Industry Applications*, vol. 48, pp. 1215–1224, 4 2012. DOI: 10.1109/TIA.2012.2199732.

[179] D. M. Choudhary and C. D. Kotwal, "Analysis of load dynamics in induction melting furnace and improved power quality with phase shift modulated llc resonant igbt inverter," *IEEE Journal of Emerging and Selected Topics in Power Electronics*, vol. 11, pp. 4681–4692, 5 2023. DOI: 10.1109/JESTPE.2023.3292144.

[180] G. Huang, F. Ma, H. Ding, Q. Yang, R. Fan, and L. Wang, "Dual fundamental frequency HSS-based reduced order impedance modeling of AC/AC modular multilevel converter for tundish heating," *IEEE Transactions on Power Delivery*, vol. 39, pp. 1749–1760, 3 2024. DOI: 10.1109/TPWRD.2024.3377807.

[181] Y. J. Kim and J. Wang, "Power hardware-in-the-loop simulation study on frequency regulation through direct load control of thermal and electrical energy storage resources," *IEEE Transactions on Smart Grid*, vol. 9, pp. 2786–2796, 4 2018. DOI: 10.1109/TSG.2016.2620176.

[182] Y. Mu, Y. Xu, J. Zhang, *et al.*, "A data-driven rolling optimization control approach for building energy systems that integrate virtual energy storage systems," *Applied Energy*, vol. 346, 2023. DOI: 10.1016/j.apenergy.2023.121362.

[183] D. Wang, M. Li, M. Guo, *et al.*, "Modelling variable refrigerant flow system for control purpose," *Energy & Buildings*, vol. 292, p. 113 163, 2023. DOI: 10.1016/j.enbuild.2023.113163.

[184] S. Hu, W. Huang, M. Yu, *et al.*, "An active inertia control strategy of motor load for islanded microgrid frequency regulation," in *12th International Conference on Renewable Power Generation (RPG 2023)*, 2023. DOI: 10.1049/icp.2023.2152.

[185] COMSOL, *The AC/DC module user's guide*, Accessed: 2024/10/11, 2023. [Online]. Available: www.comsol.com/blogs.

[186] K. F. Wang, S. Chandrasekar, and H. T. Y. Yang, "Finite-element simulation of induction heat treatment," *Journal of Materials Engineering and Performance*, vol. 1, pp. 97–112, 1 1992. DOI: 10.1007/BF02650041.

[187] A. Mohsen, "On the impedance boundary condition," *Applied Mathematical Modelling*, vol. 6, pp. 405–407, 5 1982. DOI: https://doi.org/10.1016/S0307-904X(82)80109-1.
[188] D. C. Ludwigson and F. C. Schwerer, "The effect of composition on the resistivity of carbon steel sheet," *Metallurgical Transactions*, vol. 2, pp. 3500–3501, 1971.
[189] X. Fu, B. Wang, X. Tang, H. Ji, and X. Zhu, "Study on induction heating of workpiece before gear rolling process with different coil structures," *Applied Thermal Engineering*, vol. 114, pp. 1–9, 2017. DOI: 10.1016/j.applthermaleng.2016.11.192.
[190] M. C. Song and Y. H. Moon, "Coupled electromagnetic and thermal analysis of induction heating for the forging of marine crankshafts," *Applied Thermal Engineering*, vol. 98, pp. 98–109, 2016. DOI: 10.1016/j.applthermaleng.2015.11.129.
[191] O. Lahuerta, J. Ortega, C. Carretero, J. P. Martínez, and J. Acero, "Fröhlich model characterization of magnetic properties of the induction heating load," *COMPEL - The international journal for computation and mathematics in electrical and electronic engineering*, vol. 43, pp. 1127–1138, 6 2024. DOI: 10.1108/COMPEL-09-2023-0427.
[192] A. Mendi-Altube, I. Villar, C. Carretero, and J. Acero, "Electro-thermal modeling of an induction heating process of 42CrMo4 steel probe," *International Journal of Applied Electromagnetics and Mechanics*, vol. 75, pp. 169–178, 2 2024. DOI: 10.3233/JAE-230182.
[193] A. Mendi-Altube, I. Villar, C. Carretero, and J. Acero, "Modelado electrotérmico de un proceso de calentamiento por inducción para aplicaciones industriales," *Jornada De Jóvenes Investigadores Del I3A*, vol. 11, 2023. DOI: 10.26754/jjii3a.20239020.
[194] N. Mohan, T. M. Undeland, and W. P. Robbins, *Power Electronics: Converters, Applications, and Design*, 3rd ed. Wiley, 2002.
[195] R. W. Erickson and D. Maksimović, *Fundamentals of Power Electronics*, 3rd ed. Springer Cham, 2020. DOI: 10.1007/978-3-030-43881-4.
[196] H. I. Hsieh, C. C. Kuo, and W. T. Chang, "Study of half-bridge series-resonant induction cooker powered by line rectified dc with less filtering," *IET Power Electronics*, vol. 16, pp. 1929–1942, 11 2023.
[197] Plexim, *PLECS user manual*, Accessed: 2024/12/28, 2024. [Online]. Available: https://www.plexim.com/download/documentation.
[198] G. Abad, *Power Electronics and Electric Drives for Traction Applications*. John Wiley & Sons (UK), 2017.
[199] CELEM, *CELEM Power Capacitors*, Accessed: 2024/09/17. [Online]. Available: https://www.celem.com/.
[200] A. Mendi-Altube, I. Villar, C. Carretero, and J. Acero, "SiC based power converter for industrial induction hardening of steel probes," *Jornada De Jóvenes Investigadores Del I3A*, vol. 10, 2022. DOI: 10.26754/jjii3a.20226985.
[201] Wolfspeed, *1200 V, 425 A All-Silicon Carbide Switching-Optimized, Half-Bridge Module*, 2020.
[202] Wolfspeed, *Dual Channel Differential Isolated Gate Driver XM3 CPM3 SiC Half-Bridge Module Companion Tool*, 2020.
[203] A. Mendi-Altube, F. Gonzalez-Hernando, I. Villar, C. Carretero, and J. Acero, "Switching losses estimation considering device parasitics in SiC-based industrial induction heaters," in *PCIM Europe 2023; International Exhibition and Conference for Power Electronics, Intelligent Motion, Renewable Energy and Energy Management*, 2023, pp. 1799–1804. DOI: 10.30420/566091248.
[204] MathWorks, *Simulink® user's guide R2024a*, Accessed: 2024/09/23, 2024. [Online]. Available: www.mathworks.com.

[205] A. Mendi-Altube, I. Villar, C. Carretero, and J. Acero, "Dynamic dc-bus voltage control of induction hardening system under load temperatures from ambient to beyond curie point," in *Conference Proceedings - IEEE Applied Power Electronics Conference and Exposition - APEC*, Institute of Electrical and Electronics Engineers Inc., 2024, pp. 1669–1674. DOI: 10.1109/APEC48139.2024.10509197.

[206] A. Mendi-Altube, I. Villar, C. Carretero, and J. Acero, "Modeling and design of induction heating systems," *Jornada De Jóvenes Investigadores Del I3A*, vol. 12, 2024. DOI: 10.26754/jjii3a.202410580.

[207] A. Mendi-Altube, I. Villar, C. Carretero, and J. Acero, "Reduced-order dynamics of a dc-bus voltage-regulated inverter for steel hardening beyond curie point temperature," *IEEE Transactions on Industry Applications*, vol. 61, pp. 6581–6592, 2025. DOI: 10.1109/TIA.2025.3549736.

[208] C. D. Manolopoulos, M. F. Iacchetti, A. C. Smith, I. P. Miller, and I. Mark, "Litz wire loss performance and optimization for cryogenic windings," *IET Electric Power Applications*, vol. 17, pp. 487–498, 4 2022. DOI: 10.1049/elp2.12279.

[209] Hioki, *How to use LCR meters, impedance analyzers, capacitance meters*, Accessed: 2024/11/28. [Online]. Available: https://www.hioki.com/global/learning/usage.

[210] Agilent Technologies, *Specifications Agilent 4284A precision LCR meter*, Accessed: 2025/03/18, 2004. [Online]. Available: https://www.agilent.com/.

[211] National Instruments, *NI sbRIO-9607 User Manual*, Accessed: 2024/09/25. [Online]. Available: www.ni.com.

[212] LEM, *Current Transducer LF 210-S*, Accessed: 2024/09/25, 2015. [Online]. Available: www.lem.com.

[213] LEM, *Voltage Transducer DVL 250*, Accessed: 2024/09/25, 2017. [Online]. Available: www.lem.com.

[214] LEM, *Voltage Transducer DVL-UI Series*, Accessed: 2024/09/25, 2020. [Online]. Available: www.lem.com.

[215] LEM, *Current Transducer LF 306-S*, Accessed: 2024/09/25, 2007. [Online]. Available: www.lem.com.

[216] FLUKE, *Cámaras de infrarrojos RSE300 y RSE600*, Accessed: 2025/04/02. [Online]. Available: https://www.fluke.com/es-es/producto/camara-termografica/rse300.

[217] National Instruments Corporation, *LabVIEW fundamentals*, Accessed: 2025/02/14, 2025. [Online]. Available: https://www.ni.com/docs/en-US/bundle/labview/page/user-manual-welcome.html.

[218] Tektronix, *Mixed domain oscilloscopes MDO3000 series datasheet*, Accessed: 2025/04/02. [Online]. Available: www.tektronix.com/MDO3000.

[219] M. Baldan, M. H. Stolte, B. Nacke, and F. Nurnberger, "Improving the accuracy of fe simulations of induction tempering toward a microstructure-dependent electromagnetic model," *IEEE Transactions on Magnetics*, vol. 56, 10 2020. DOI: 10.1109/TMAG.2020.3013562.

[220] J. Rabkowski, M. Zdanowski, F. Gonzalez-Hernando, I. Villar, and U. Larranaga, "Experimental study on turn-off process of medium voltage SiC MOSFET modules," in *PCIM Europe 2022; International Exhibition and Conference for Power Electronics, Intelligent Motion, Renewable Energy and Energy Management*, 2022, pp. 1–8. DOI: 10.30420/565822110.

[221] J. Rabkowski, F. Gonzalez-Hernando, M. Zdanowski, I. Villar, and U. Larrañaga, "Measurement of Coss-V characteristic of the 1.7kV/900A SiC power module and estimation of the channel current," in *2022 24th European Conference on Power Electronics and Applications (EPE'22 ECCE Europe)*, 2022, pp. 1–9.

[222] J. Rabkowski, F. Gonzalez-Hernando, M. Zdanowski, I. Villar, and U. Larrañaga, "Real EOFF as a factor in design of soft-switched DC-DC converters with SiC MOSFET power modules," in *2022 IEEE Energy Conversion Congress and Exposition (ECCE)*, 2022, pp. 1–6. DOI: 10.1109/ECCE50734.2022.9947303.

Appendix A

Model Comparison of Material's Nonlinear Magnetic Characteristic

When modeling induction heating systems, anhysteretic BH-curves are employed for sake of simplicity. However, the complexity comes from the saturation of the material's magnetic characteristic, which cannot be ignored, according to field levels and temperature. In this appendix, different equations proposed to model the nonlinear BH-curves in literature will be compared. To adjust the models and verify their accuracy, the measurement data of 42CrMo4 steel studied in this thesis are employed in the fitting.

A.1 Material's BH-Curve Models Comparison

In this first section, the anhysteretic BH-curve of a 42CrMo4 steel probe will be modeled at ambient temperature. Several equations have been proposed in the literature to reflect the relation between the magnetic flux density and the magnetic field. Going from the simplest to the more complex ones, Table A.1 summarizes the models that are compared afterward.

Table A.1. BH-curve models overview.

Model name	Equation	References
Potential	(A.1)	[158]
Inverse tangent	(A.2)	[158]
Inverse tangent & potential	(A.3)	[219]
Fröhlich-Kenelly	(A.4)	[126], [158]–[160], [191]
Langevin function	(A.5)	[161]
Analytic saturation curve	(A.8)	[153]–[155], [162], [163]
Analytic saturation with knee adjustment	(A.9)	[163], [164]

A.1.1 Simple Potential Model

The simplest BH-curve model found in literature is the simple potential model, which does not consider the saturation of the material but include a nonlinear dependence:

$$B(H) = aH^n. \tag{A.1}$$

A.1.2 Inverse Tangent Model

The inverse tangent model takes into account the saturation:

$$B(H) = a_1 \arctan(a_2 H). \tag{A.2}$$

A.1.3 Inverse Tangent and Potential Model

A kind of combination of the above two models, the inverse tangent of the potential function, is proposed in [219], in order to catch properly the saturation on middle field dependence:

$$B(H) = a_1 \arctan(a_2 H^n). \tag{A.3}$$

A.1.4 Fröhlich-Kenelly Model

Other works emphasize Fröhlich-Kenelly model's accuracy and simplicity:

$$B(H) = \frac{\alpha}{\beta + H} H. \tag{A.4}$$

A.1.5 Langevin Model

The Langevin function is used to determine anhysteretic magnetization in the Jiles-Atherton model:

$$B(H) = \mu_0 M_{\text{an}}(H) + \mu_0 H, \tag{A.5}$$

where

$$M_{\text{an}}(H) = M_{\text{s}} \left(\coth\left(\frac{H}{a}\right) - \frac{1}{H/a} \right) \tag{A.6}$$

and

$$M_{\text{s}} = \frac{B_{\text{s}}}{\mu_0}. \tag{A.7}$$

A.1.6 Analytic Saturation Curve Model

More complex approximations than the Fröhlich-Kenelly model are proposed in [163]. The first one is the Analytic Saturation Curve (ASC), which was first used by [162]. This model is also employed by [153]–[155]. It is a combination of a straight line and an arctangent curve:

$$B(H, T) = \mu_0 H + \frac{2B_{\text{s}}}{\pi} \arctan\left(\frac{\pi \mu_{\text{r,i}} \mu_0 H}{2B_{\text{s}}} \right). \tag{A.8}$$

A.1.7 Analytic Saturation Curve Model with Knee Adjustment

The second proposal of [163] is the ASC with knee adjustment. It is the same straight line and the arctangent curve as in (A.8), but with a coefficient, a, adjusting the shape of the curve knee for a better approximation:

$$B(H) = \mu_0 H + B_{\text{s}} \frac{H_{\text{a}} + 1 - \sqrt{(H_{\text{a}} + 1)^2 - 4H_{\text{a}}(1 - a)}}{2(1 - a)}, \tag{A.9}$$

where

$$H_{\text{a}} = \mu_0 H \frac{\mu_{\text{r,i}} - 1}{B_{\text{s}}}. \tag{A.10}$$

A.1.8 Fitting BH-Curve Models

In Fig. A.1, the measured BH-curve for 42CrMo4 steel, [153], is used as a reference to fit all the following equations, with the aim of comparing them.

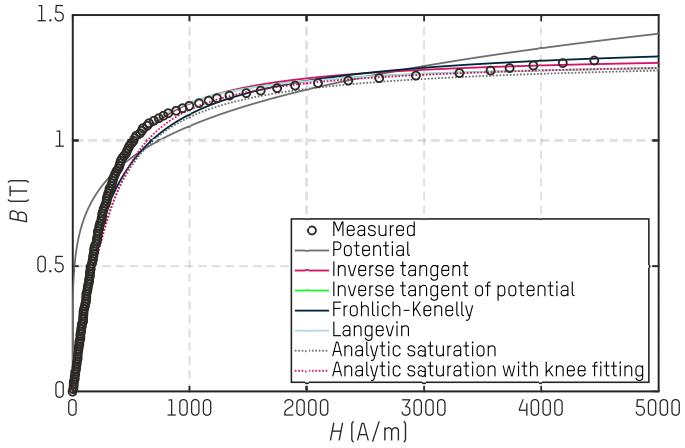

Figure A.1. BH-curve models fitted to measurements at ambient temperature.

The first two models are the simplest ones. The potential model does not saturate at all, and it will continue increasing for higher H values; the inverse tangent model follows the measured data properly. The third one, indeed, is a combination of the previous two models, and it also agrees with the measured BH-curve. The Fröhlich-Kenelly and Langevin models behave similarly as both saturate at an exact value. Regarding the last two models, which are based on analytic saturation curves, they approach satisfactorily the reference measured BH-curve. Moreover, they do consider the magnetic properties as model parameters.

To conclude, all the analyzed models except the simple potential one are adequate to capture the nonlinear magnetic behavior of the material.

A.2 Temperature Dependence of Magnetization Characteristic

The two most employed functions in previous and recent literature are the power and exponential functions of temperature, respectively:

$$f(T) = 1 - \left(\frac{T}{T_C}\right)^{\gamma} \tag{A.11}$$

and

$$f(T) = 1 - e^{(T-T_C)/C}, \tag{A.12}$$

where T is the current temperature of the billet at a point, and T_C is the Curie point of the material. In (A.11), the power coefficient, γ, is the temperature sensitivity parameter which depends on the material. On the second function, there is a temperature constant, C, which determines the inflection point of the two exponentials defined by (A.12). For $T < T_C$ values, when $f(T)$ ranges from 1 to 0.1, the exponential has a negative curvature; however, for temperatures near Curie point, or $f(T)$ is between 0.1 and 0, the curvature will be positive.

The potential function is employed in [126], [164], while the exponential expression is used by [153]–[155]. Each BH-curve model can be multiplied by each of the two functions to reflect the temperature dependence.

A.3 Selected Model

One of the most used functions in literature to model nonlinear inductive loads BH-curves is the product of equations (A.8) and (A.12), as it is given as follows, [127], [134], [154], [155]:

$$B(H,T) = \mu_0 H + \frac{2B_s}{\pi} \arctan\left(\frac{\pi \mu_{r,i} \mu_0 H}{2B_s}\right)\left(1 - e^{(T-T_C)/C}\right). \tag{A.13}$$

The result is shown in Fig. A.2, compared to experimentally measured data:

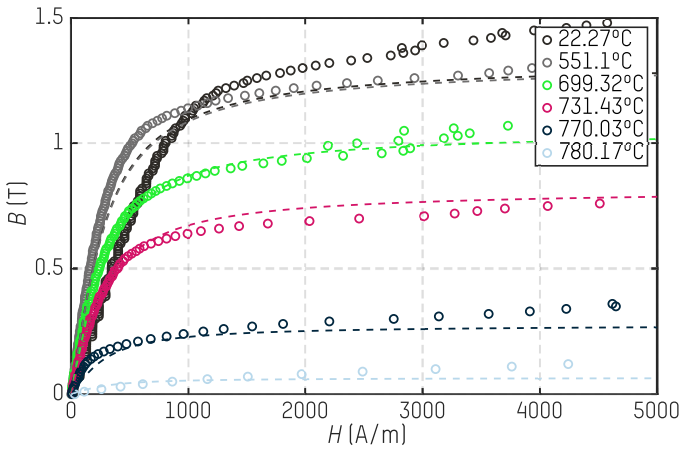

Figure A.2. Nonlinear temperature-dependent BH-curve model compared to experimental measurements.

Appendix B

Switching Losses Estimation Considering Device Parasitics in SiC-Based Industrial Induction Heaters

This appendix proposes a method to compute switching off energy losses of SiC MOSFETs in ZVS conditions. Switching power losses estimated in this way are lower and more precise than traditional methods, and consequently, a more realistic total power loss analysis is carried out. The determined switching energies are employed in calculating the power losses of a series-resonant inverter designed for industrial induction heating applications assuming ZVS operation. This work was presented in PCIM Europe 2023; International Exhibition and Conference for Power Electronics, Intelligent Motion, Renewable Energy and Energy Management in Nuremberg, Germany, and is published in the conference proceedings in IEEEXplore, [203].

B.1 Introduction to Switching Losses Estimation

In the design process of such power converters, an accurate estimation of power losses is required in view of the proper sizing of the cooling system. Considering that IH inverters usually operate at Zero Voltage Switching (ZVS), energy dissipated during the switching-off of semiconductors is indispensable to estimate the whole system's power losses.

SiC devices, compared to their Si-based peers, stand to benefit when working in higher frequency ranges, making this technology very attractive for high-frequency IH inverters [65]. Therefore, the estimation of switching losses is more critical than ever. However, this estimation process is not as simple as in Si-based ones, due to the parasitic components, operation modes, and other parameters that change the input transfer characteristic.

In [220], factors that most influence this transfer characteristic are studied. Moreover, in [221] the capacitive current of parasitic capacitance is reconstructed to estimate the real current in the MOSFET channel. Furthermore, turn-off losses in SiC devices are more realistically estimated in [222], considering the displacement current through the parasitic capacitors and voltage drop in the internal stray inductance of the package.

B.2 Accurate Estimation of the SiC Switching-Off Energy Losses

Switching-off energy losses are typically obtained either from the datasheet or experimentally. In the second case, it is required to measure the drain current, i_D, and drain-source voltage, v_{DS}, in double-pulse tests, and integrating their product energy dissipated is calculated. However, as mentioned in the introduction, two parasitic components in Fig. B.1 affect the energy loss estimation of the SiC MOSFETs. On the one hand, part of i_D flows through the output parasitic capacitance, C_{oss}), causing the channel current, i_{CH}, to be smaller and consequently reducing the energy losses since this channel current is the primary source of the switching energies. On the other hand, the package's stray inductance, L_{stray}, applies a negative voltage drop – that is, a voltage growth in the device – due to the negative derivative of the switched current so that losses could be increased.

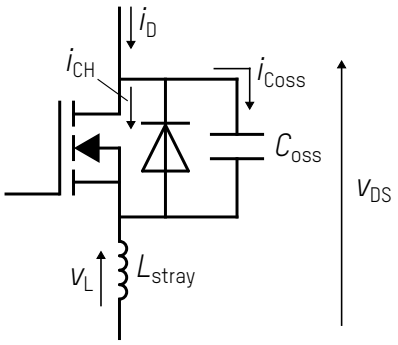

Figure B.1. SiC MOSFET scheme with parasitic components.

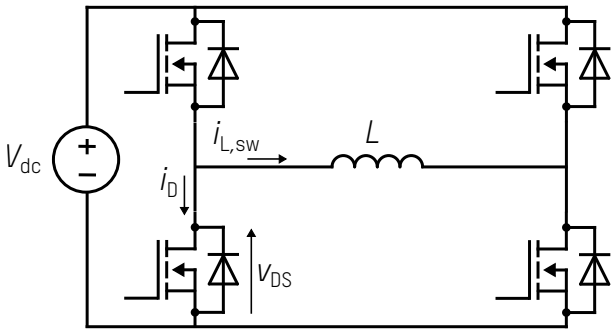

Figure B.2. Circuit used for energy loss characterization.

An H-Bridge inverter in Fig. B.2 with a highly inductive load, L = 330 μH, has been used to study the switching-off energy losses of CAB425M12XM3 SiC modules, [201]. The switches are controlled to generate a rectangular voltage in the inductor from -V_{dc} to +V_{dc} with a duty cycle of 50 %, and the current is almost a pure triangular waveform obtained at different switching frequencies according to (B.1). In this way, the turn-off currents range from 25 A to 275 A with a fixed dc voltage V_{dc} of 600 V. This control ensures ZVS in the device under test.

$$i_{L,sw} = \frac{V_{dc}}{4 \cdot f_{sw} \cdot L} \tag{B.1}$$

In Fig. B.3, the measured switching-off drain currents and drain-source voltages are displayed, followed by their product, which is afterward integrated to compute the energy dissipated during the switching process. Figure B.4 shows the effect of the parasitic elements previously presented. First, i_{CH} is obtained from the subtraction of i_D and i_{Coss} with (B.2), the latter one being calculated by (B.3), and C_{oss} obtained from the datasheet characteristic [201] in function of v_{DS}. In addition, the stray inductance voltage v_L has been determined from (B.4), also considering the stray inductance value indicated in the same datasheet. The result is a negative and low voltage drop due to the negative derivative of the module's current and small stray inductance, respectively. This negative voltage needs to be added to the voltage measured from the outside of the module as in (B.5).

$$i_{CH} = i_D - i_{Coss} \tag{B.2}$$

$$i_{Coss} = C_{oss} \cdot \frac{dv_{DS}}{dt} \tag{B.3}$$

$$v_L = L_{stray} \cdot \frac{di_D}{dt} \tag{B.4}$$

$$v_{DS,L} = v_{DS} + v_L \tag{B.5}$$

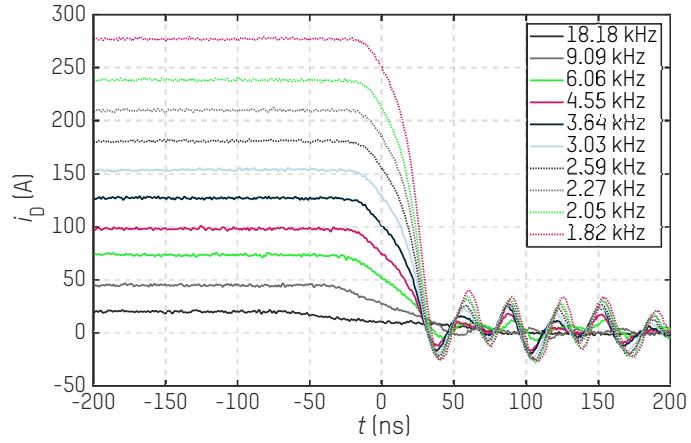

(a)

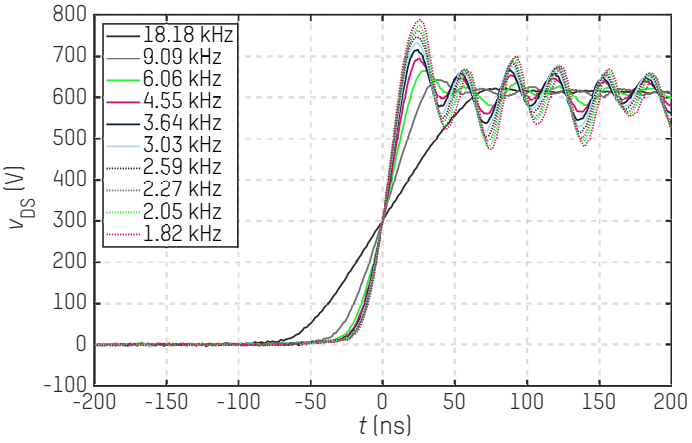

(b)

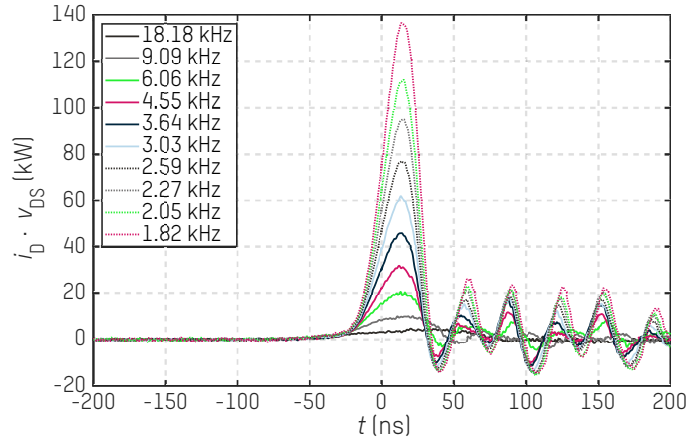

(c)

Figure B.3. Measured i_D and v_{DS} for different frequencies: (a) i_D, (b) v_{DS}, and (c) product of (a) and (b).

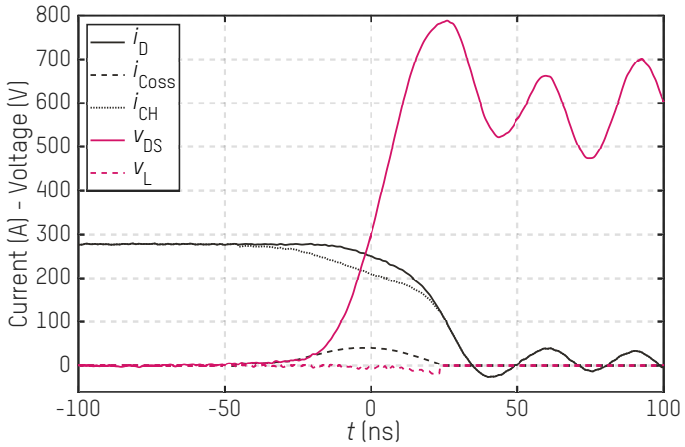

Figure B.4. Itemized i_{Coss} and v_L for 1.82 kHz.

Consequently, the energy dissipated in the SiC MOSFET has been estimated considering the cited components and the results are compared with the overestimated ones in Fig. B.5. As recent literature and previous experiments have shown, energy losses measured in the real setup vary from the ones provided by the manufacturer in the datasheet because the layout employed is different. In this section, the semiconductor's energy dissipation is characterized by employing the same layout as in the final application, bringing them as close to reality as possible.

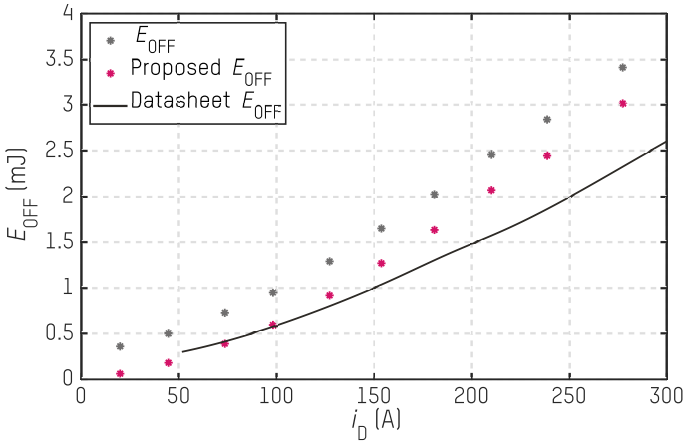

Figure B.5. Switching-off energy losses estimation for v_{DS} = 600 V.

B.3 Experimental Results

Chapter 3 describes the power converter under study. This specific study is focused on the last inverter stage for its half-bridge (HB) configuration.

This analysis was realized before inserting the converter into its final box, and the resonance condition was then slightly modified. Different operating points of the ZVS HB inverter have been studied to compare the power losses in the turn-off process of the SiC MOSFETs computed using both E_{OFF} and the proposedE_{OFF} calculation method. An inductive load with variable impedance, whose resistance and inductance values for ambient temperature are, respectively, in the order of 10 mΩ and slightly smaller than 5 μH, has been employed in the tests. A resonant capacitor bank of 36.4 μF has been placed in series, resulting in a resonant frequency of 11.9 kHz as measured in Fig. B.6.

The high-frequency inverter is controlled with three different switching frequencies, all of them higher than the resonant frequency, to ensure ZVS in the power devices. Different currents have been conducted through the heating coil to further analyze the inverter's performance. All the tests carried out for this analysis are displayed in Fig. B.7, Fig. B.8, and Fig. B.9; current and voltage waveforms of the series resonant tank are displayed in each figure. Realize that the current is equally paralleled in both half-bridge branches, each carrying half of the load's current.

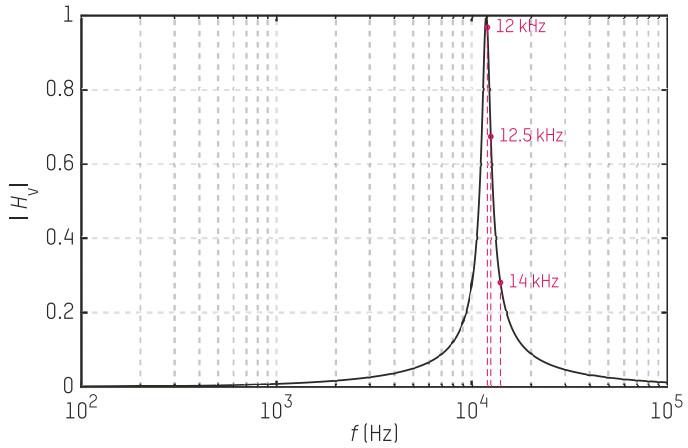

Figure B.6. Voltage gain of the IH load measured by an LCR meter.

Switching-off power losses have been computed for all these operating points; energy loss for each current has been obtained from Fig. B.5 and extrapolated to the voltage applied in the input dc bus; then, power losses are computed by multiplying these energies by the switching frequency. On the other hand, conduction losses have been analyzed for the same cases, obtaining the total power losses of the whole inverter in Fig. B.10.

Various observations can be conducted from this last figure. On the one hand, a drop is noticed in the estimated switching-off losses when using the proposed E_{OFF} calculation method; the error decreases with the coil's current increase. However, this is not very meaningful at switching frequencies close to the circuit's resonant frequency, as the conduction losses exceed the sum of the total power losses. This occurs due to high current amplitudes and low voltages, which is the basis of the resonant circuits. Indeed, as the switching frequency increases, distancing from the resonant frequency, the switching losses get higher, and the proposed method will result in a more accurate estimation.

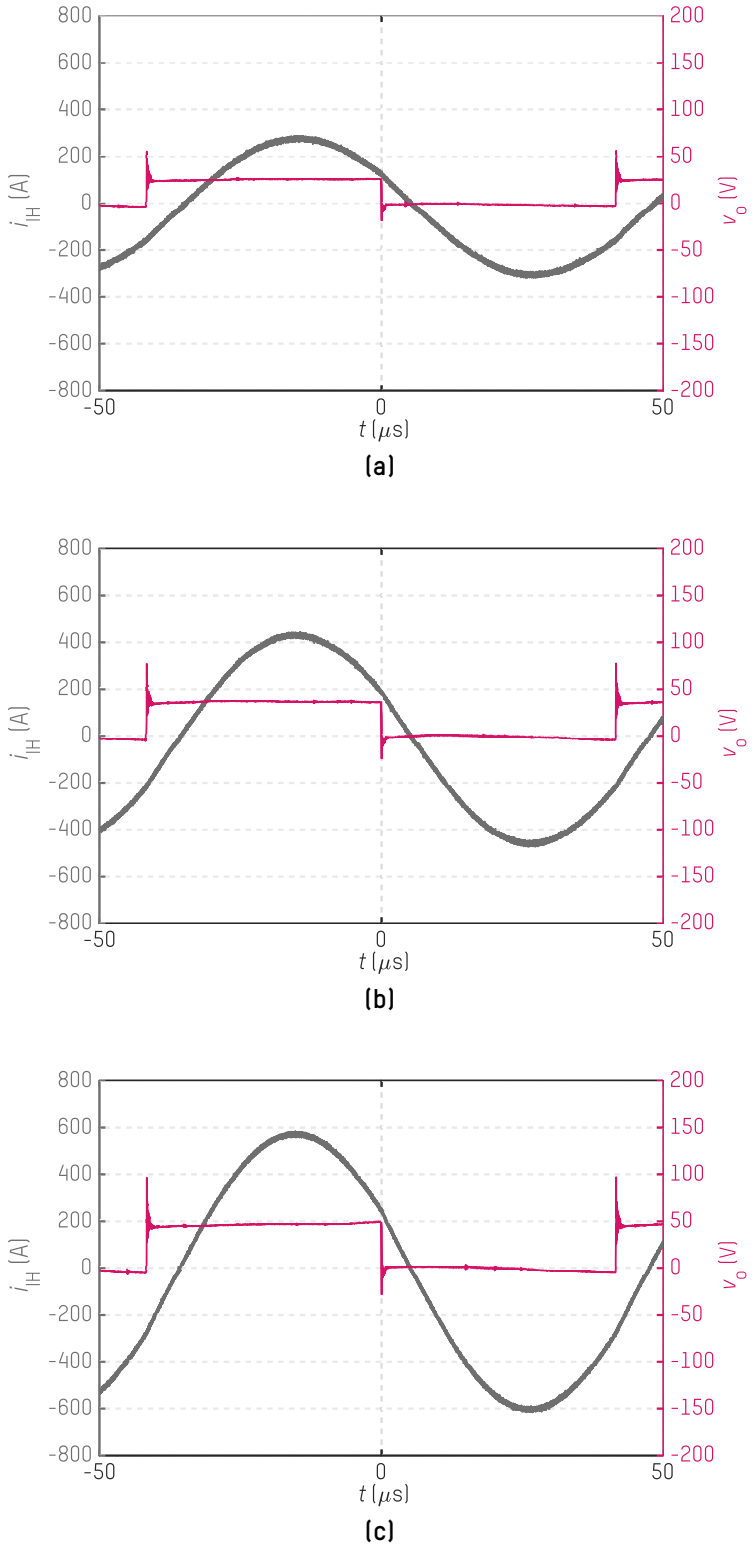

Figure B.7. i_{IH} current and v_o voltage waveforms in the resonant tank at ambient temperature for different inductor's current effective values and switching frequency of 12 kHz: (a) 200 A rms, (b) 300 A rms, and (c) 400 A rms.

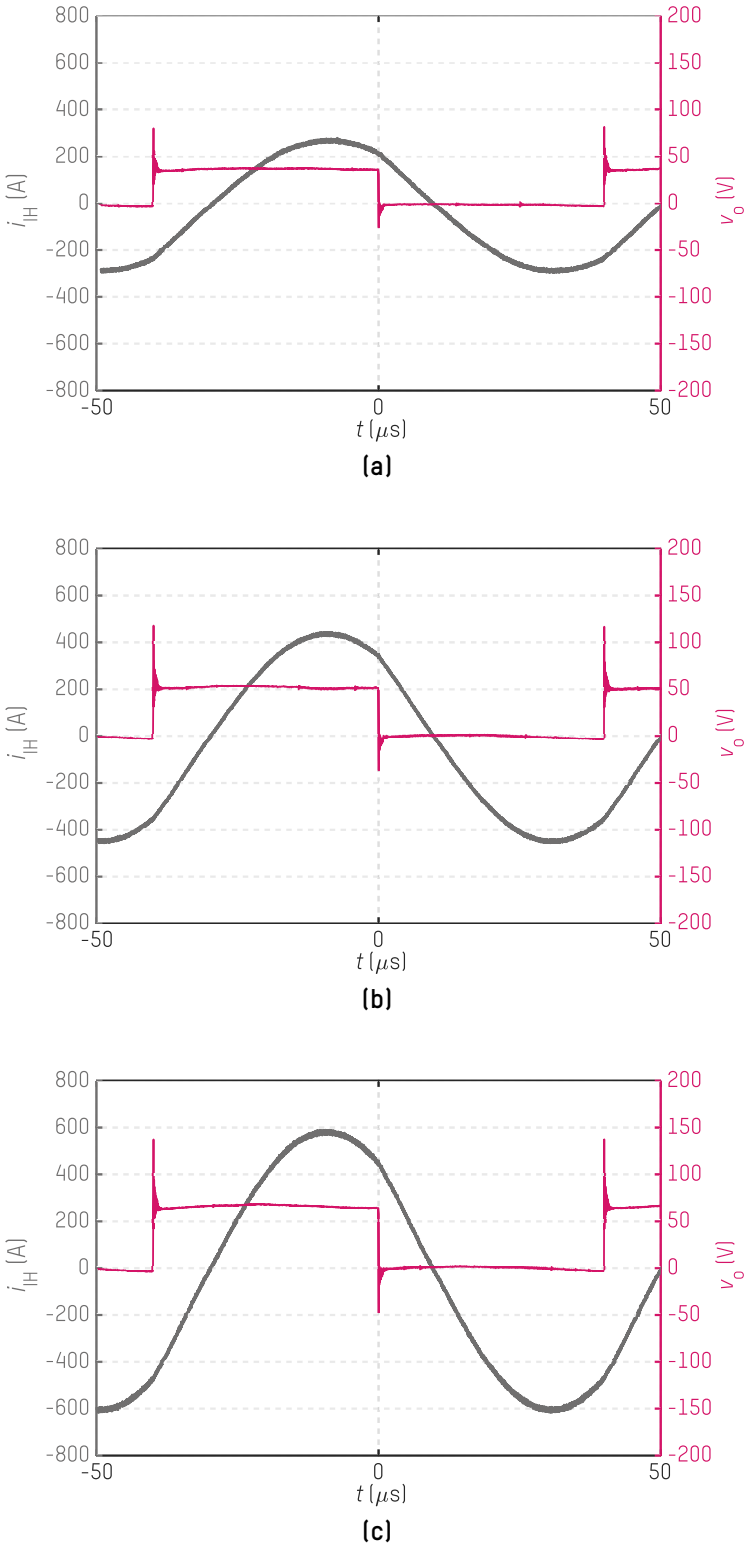

Figure B.8. i_{IH} current and v_o voltage waveforms in the resonant tank at ambient temperature for different inductor's current effective values and switching frequency of 12.5 kHz: (a) 200 A rms, (b) 300 A rms, and (c) 400 A rms.

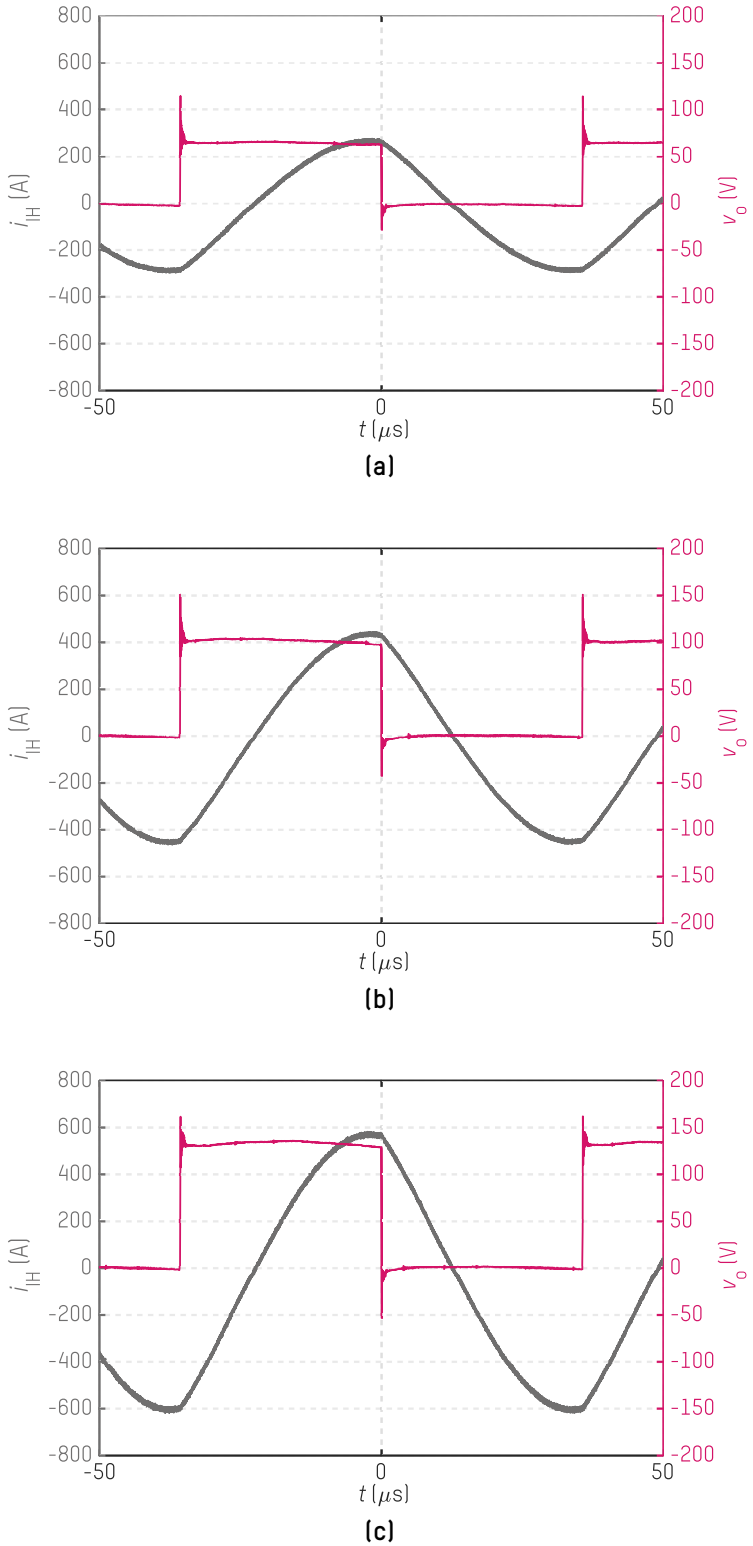

Figure B.9. i_{IH} current and v_o voltage waveforms in the resonant tank at ambient temperature for different inductor's current effective values and switching frequency of 14 kHz: (a) 200 A rms, (b) 300 A rms, and (c) 400 A rms.

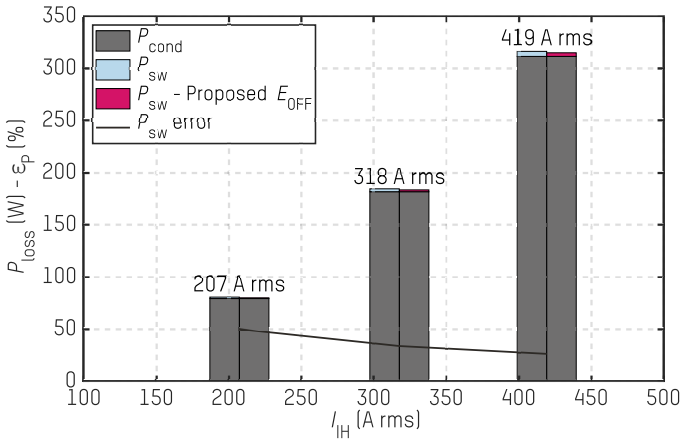

(a)

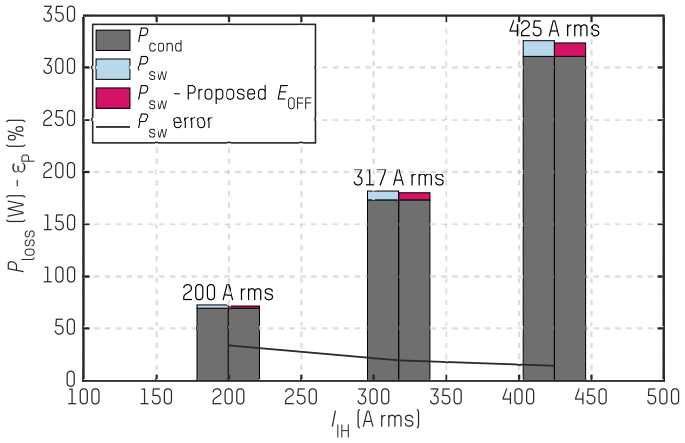

(b)

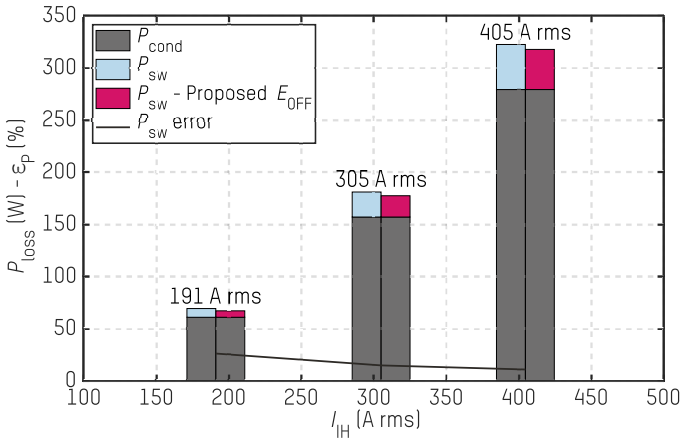

(c)

Figure B.10. Comparison of switching-off and conduction power losses for the full inverter – 4 semiconductors – with different coil's current values (200, 300, and 400 A rms) and frequencies: a) 12 kHz, b) 12.5 kHz, and c) 14 kHz.

Appendix C

Experimental Measurements in the Power Converter

In this Appendix, some other parameters recorded and processed via LabVIEW® during the experimental induction heating test are displayed and commented.

C.1 Experimental Measurements of Previous Power Conversion Stages

First, Fig. C.1 shows the measured grid currents and voltages in *dq* components, obtained by applying the Park transformation to the three-phase grid currents and voltages. This *dq* reference frame is the one employed for the vector control of the three-phase boost rectifier.

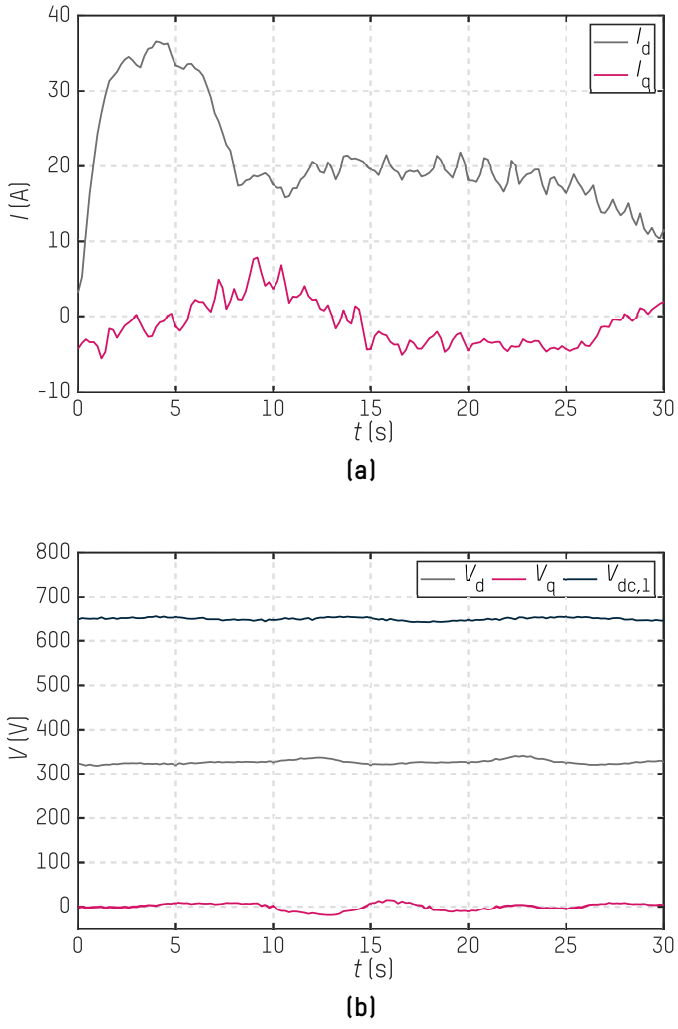

Figure C.1. Experimentally measured three-phase rectifier grid-side *dq* currents and voltages, during the induction heating test of 30 seconds exciting the coil with a current of 500 A rms and 14.2 kHz.

Regarding Fig. C.1a, at first glance, the grid currents i_{dg} and i_{qg} may seem unsteady. However, further analyzing them, it is observed that the *q* component of the current oscillates around 0, which has been imposed to ensure the unity power factor. The *d* component, however, takes a similar transient behavior as the dynamics of the load. This means that

almost null reactive power is absorbed from the mains grid.

Simulated currents through the DC-DC buck converter's output are plotted in Fig. C.2. From Fig. C.2a and Fig. C.2b, it is assumed that the output DC current is equally distributed between both branches.

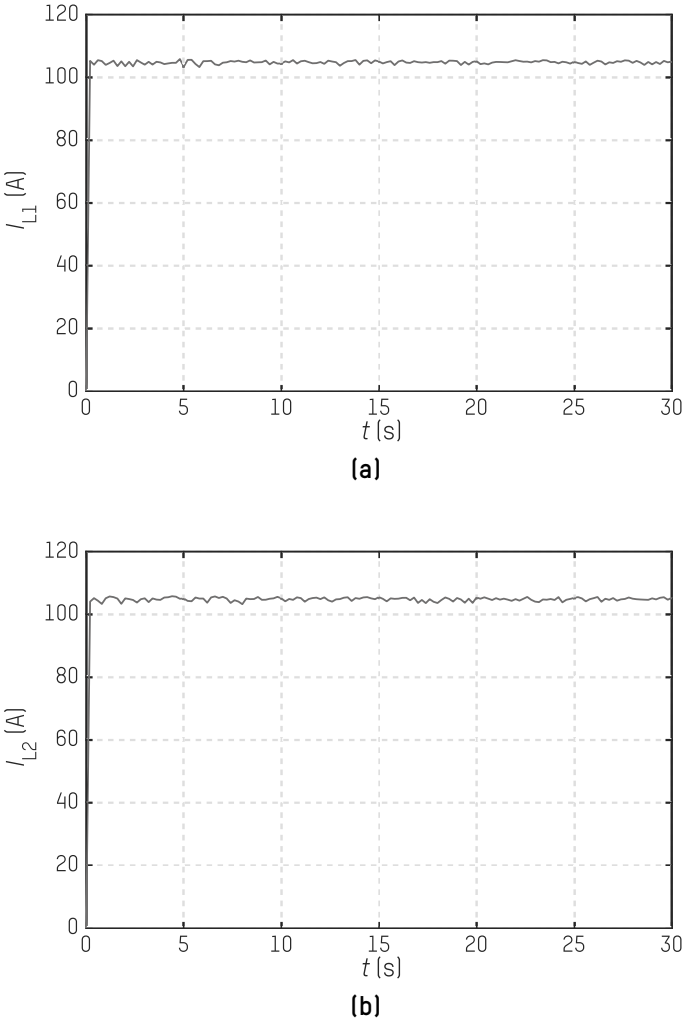

Figure C.2. Experimentally measured DC-DC buck output currents, I_{L1} and I_{L2}, during the induction heating test of 30 seconds exciting the coil with a current of 500 A rms and 14.2 kHz.

Constant *d* and *q* voltages are depicted in Fig. C.1b. As the grid voltage vector, $\mathbf{v}_g$, is aligned with the *d* axis, the *q* component of the voltage is null. Instead, the *d* component is the amplitude of the mains phase voltage. Additionally, the $V_{dc,1}$ voltage is also measured, and it is observed that constant 650 volts are regulated adequately in this first DC-bus, i.e., the desired DC voltage is rectified in the first stage.

Moreover, Fig. C.3 shows the phase shift between the inverter's output switched voltage and current during the same induction heating test. This phase shift is measured by implementing a zero-crossing detector to the current waveform.

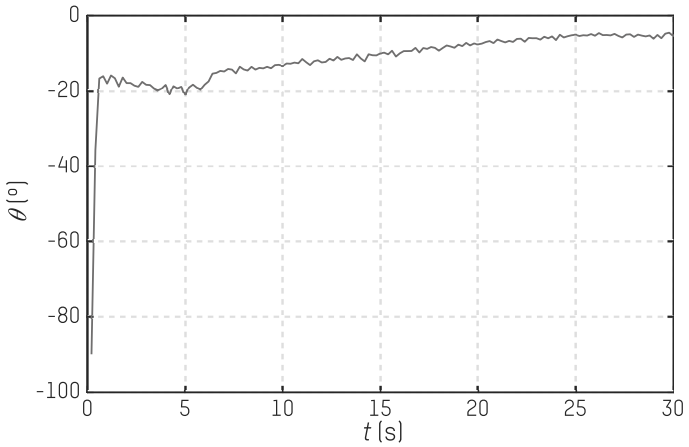

Figure C.3. Experimentally measured phase shift, Φ_{shift}, between inverter's output switched voltage, v_o, and current, i_{IH}, during the induction heating test of 30 seconds, exciting the coil with a current of 500 A rms and 14.2 kHz.

Here again, the inductive operation mode is ensured as the current is delayed according to the voltage. The phase-shift trend is directly linked to the variation of the equivalent inductance with temperature, as the resonant capacitance value is maintained constant.